Scratching the Hinuera Surface: Cryptic faulting in the late Quaternary alluvial plain, Te Tātua o Wairere Fault Zone

A thesis submitted in partial fulfilment

of the requirements for the degree of

Master of Science (Research) in Earth Sciences

at

The University of Waikato

by

George Robert McQuillan

THE UNIVERSITY OF
WAIKATO
Te Whare Wānanga o Waikato

2021

Abstract

Between *c.* 20,000 and 15,000 years BP, precursors to the modern Waikato River deposited alluvium of the Hinuera Formation throughout the Hamilton Basin – a *c.* 1,600 km^2 terrestrial sedimentary basin in the centre-north of New Zealand's North Island (Māori: *Te Ika-a-Māui*). Together with clayey silt beds of overlying late Quaternary tephras, the sand and gravel dominated Mid-Pleistocene to Holocene Hinuera Formation infills much of the basin to form the Hinuera Surface, a large alluvial plain, often referred to as a low-angle alluvial fan. Rising above the Hinuera Surface are the low (<*c.* 100 m) Hamilton Hills, formed of Early to Mid-Pleistocene primary and reworked volcanic sequences, also overlain by late Quaternary tephras.

Recent studies have established the presence of paleoliquefaction within the Hinuera Formation – evidence of seismic disturbance – and fault deformation of the adjoining Hamilton Hills. The most recent fault activity identified to date, <*c.* 50,000 years BP, is within Te Tātua o Wairere Fault Zone, a zone broadly defined by an approximately N-S line of hills across the south-eastern margins of Hamilton City and including portions of the Hinuera Surface. Whilst deformation has been confirmed in cohesive materials of the fault zone's hills, this study is the first to attempt identification of faulting within the younger, unconsolidated, granular sediments of the <*c.* 20 ka Hinuera Formation. The study combined desktop analysis of digital models, gravity anomalies, earthquake datasets, and historic aerial imagery with results from field surveys, including geomorphic mapping and electrical resistivity tomography (ERT), and paleoseismic trenching of the Hinuera Surface.

Basin-scale digital modelling showed that Te Tātua o Wairere Fault Zone marks a slight but significant change in Hinuera Surface slope, inferred to mark the eastern boundary of an uplifted fault block. This change is near-coincident with geomorphic evidence for paleochannel constriction and abrupt directional changes, subtle linear breaks in surface elevation, and apparent offsets across paleochannel banks. The same modelling inadvertently highlighted the ultra-low, almost nil angle

of slope inherent to the Hinuera Surface (consistently <0.1°) and it is considered that application of a term such as braid-plain is more appropriate to that of alluvial fan.

Gravity anomaly analysis did not yield significant results but interrogation of earthquake datasets highlighted a cluster of earthquakes in the Puketaha/Ruakura area – in the fault zone's extreme north – and seismic reflection survey maps from the 1960s/1970s highlighted prior interpretations of proximal deep (pre-Hinuera Formation) faults. Historic aerial photographs suggested the possibility of fault scarps having once been visible within the fault zone, since obscured or modified beyond recognition by construction of the University of Waikato campus and adjacent developments. ERT surveys established an off-fault reference section which highlighted the essentially planar nature of undisturbed Hinuera Formation and late Quaternary strata at Ruakura. Against the reference section, a number of significant sub-surface resistivity anomalies were identified, including; discontinuities with subtle vertical offsets in shallow high resistivity zones; vertical/sub-vertical zones of low resistivity, and; discrete areas of high resistivity at depth, accompanied by a lack of planar continuity. These ERT anomalies not only aligned with one another but also with known faulting in hills to the south and a hypothesised approximate N-S fault.

Investigations concluded with excavation of a paleoseismic trench on the AgResearch Ruakura Research Farm, exposing a discrete, *c.* 4 m wide zone of deformation within the upper Hinuera Formation. This deformation was extremely similar to that observed across a confirmed fault scarp within near-identical lithostratigraphy in the Hauraki Basin and includes small listric (normal) fault segments, cryptic granular deformation, and paleoliquefaction. The absence of a through-going fault (pseudo-)plane negates deformation being interpreted as the hypothesised fault-proper but comparison with fault propagation models through granular materials suggests deformation is co-seismic in origin and near-fault. Movement on a deeper, basement fault (possibly identified in the 1960s/1970s but not since explored in any detail) is likely to have been accommodated in a diffuse manner within the Hinuera Formation, with deformation not necessarily following the true fault-plane.

The study concludes that evidence of co-seismic deformation within the uppermost Hinuera Formation and for seismic influence of Hinuera Surface geomorphology indicates disturbance must have occurred <*c.* 15,000 years BP; Te Tātua o Wairere Fault Zone has been active more recently than previous evidence suggested. From the cumulative range of data gathered, an inferred line of faulting is presented which links the deformation at Ruakura with known fault offsets in the south-east of Hamilton City, at Hillcrest Road and Cobham Drive. Significant ERT anomalies and likely tectonogeomorphic expressions in the northern Ruakura area and east of the trenched location remain unresolved and require further investigation to confirm the hypothesised main line of strike. A greater understanding of the nature of Te Tātua o Wairere Fault Zone would be beneficial to seismic hazard risk planning in the area and there is scope for future research to consider the interplay between deeper local fault systems and distributed surface deformation.

Acknowledgements

Amongst a global pandemic, car crashes and a myriad other conundrums during the study period, it seemed at many times as if this project would never get off (or beneath) the ground, let alone reach completion. Yet in the end, it did come to fruition and that is wholly due to the support provided by a wonderfully wide-ranging sphere of people. To commence the thanks, I express gratitude to my supervisor Dr Vicki Moon, whose down to earth, practical teaching style is especially appreciated and something to aspire to – all the best in your 'retirement'. Thanks also to second supervisor Dr Adrian Pittari, who was particularly helpful during the early planning stages and with negotiating the administrative requirements of postgraduate study. Dr David Lowe was an enthusiastic supporter of the research and a font of invaluable Hamilton Basin-related knowledge while Dr Willem de Lange provided essential help with trench surveying and digital data collection, sincere thanks to them both.

Tēnā rawa atu koe / thank you very much to university Research Associate Wiremu Puke (Ngāti Wairere, Ngāti Waikai, Ngāti Mahuta, Ngāti Whaawhakia) for kindly facilitating mana whenua permission to undertake excavations within the rohe of Ngāti Parekirangi. A special thank you also to Dr Pilar Villamor and Dr Kelvin Berryman for journeying from Wellington to provide advice and expertise in logging our paleoseismic trench, it was fantastic to meet and learn from you. None of the fieldwork could have been accomplished without the kind support granted by landholders and infrastructure project partners: Tim Hale (AgResearch), Mark Jackways and Shane Hill (Tainui Group Holdings), Bob Connell (Fulton Hogan), Raj Ramgobin (CityEdge Alliance), I thank you not only for being key links in the chain but also for your receptiveness and enthusiasm.

The climax of it all was of course excavation of the trench but this was no sure thing until funding was made available by Waikato Regional Council and some wonderful contractors stepped up at the last minute – Rick Liefting (Waikato Regional Council), Innes Fisher (Utility Location Services), the two Tims and a Ben (Broughton Contracting), you were all project-saviours and I really cannot thank you

enough. I was also honoured that The University of Waikato's scholarships committee felt I was worthy of personal financial support by way of Taught Postgraduate and Research Masters Scholarships, for which I am most grateful.

Earth Sciences technical staff of the university went above and beyond throughout the course of the study and were a joy to spend time with – Annette Rodgers, Kirsty Vincent and Chris Morcom, thank you so much. Alongside Chris in particular, special thanks to 'honorary Earther' Stephanie Watson who was tagged-in as part of the resistivity Dream Team – I am indebted to you both for those back-breaking, cable-wrangling days. Whether it be in the field, over weird video morning teas during lockdown, or in the office generally flailing about pretending we knew how to put "science in action", I am of course also extraordinarily grateful to my friends and fellow graduate students for their support, companionship and inspiration. Amongst the crew I must particularly acknowledge (in no particular order) Francesca Spinardi, Tom Robertson, Anya Podrumac, Ashley Cave, Oliver McLeod, Miriam Namaliu, Vittoria Gibbons and Jordanka Chaneva. Special thanks are also due to the School of Science office staff, Gloria, Fiona and Vicki, who never failed to cheerfully find the answer to some question or take care of all the little odd bits and pieces. If per chance I have neglected to mention anyone else I can only apologise – you know how it goes when you get to this stage!

Lastly but most importantly of all, my immense gratitude and love to my family and loved ones who have never failed to support me along the road. Mum, Dad and Nana especially, thank you for being there and particularly to Mum for always ensuring I had a decent meal and a roof over my head. To Helen and the late Murray Dreyer, none of this could ever have happened without your friendship and mentorship being such a fundamental part of my life, and your support when I decided to abandon the nuts, bolts and washers for textbooks and essays.

To you all, *go raibh maith agat / may you have goodness.*

G. R. McQuillan, June 2021

Not without respect, you would have thought it a pile of academic horse manure so this one's for you, Murray. Thanks for helping me get here.

Rest in peace.

Table of Contents

List of Figures

List of Tables

1. Introduction, Study Area and Background Information

1.1. Introduction

By New Zealand definition, where a fault has ruptured or deformed the earth's surface within the last 125,000 years then it is classified as active, incorporated in the New Zealand Active Faults Database, and may be fed into relevant seismic hazard models (Langridge *et al.* 2016). With relatively contiguous and seemingly undisturbed sequences of thick, unconsolidated, Quaternary alluvium, the Hamilton Basin on New Zealand's North Island has historically been regarded as lacking any surface faults and relatively seismically inactive. Such an assumption of seismic quiescence has been sound enough for GNS scientists to publicly regard the city of Hamilton, in the central basin, as "the most geologically sound city in New Zealand" (Leonard 2011 cited in 'Where is the safest place to live in NZ?' 2011).

The apparent absence of Hamilton Basin surface faulting has been called into question as a result of recent investigations, particularly following the discovery of paleoliquefaction features within the <*c.* 20,000 year old Hinuera Formation by Kleyburg (2015) and evidence for fault structures through the Pliocene–Pleistocene Hamilton Hills presented by Campbell (2017), Moon and de Lange (2017), and Spinardi (2017). In Hamilton City during 2019 and 2020, earthworks for a residential development on Hillcrest Road and an extension of the Hamilton Ring Road at Cobham Drive exposed new evidence for faulting in beds of the Hamilton Ash Formation. Dated to ≤*c.* 125,000 years old at Hillcrest Road and ≤*c.* 50,000 years old at Cobham Drive, both of these fault locations were within hills of the recently proposed Te Tātua o Wairere Fault Zone.

As a result of the Cobham Drive and Hillcrest Road investigations, Te Tātua o Wairere Fault Zone is slated to be incorporated as an active fault in the forthcoming update to the New Zealand Community Fault Model (Moon, V. 2020, pers. comm.). Since it is now clear that earlier assumptions were incorrect and intra-basin faulting has certainly occurred at least mid-Quaternary, the question then arises as to whether faulting has continued into the late Quaternary. To answer this, attention must be turned towards even younger geological formations than those found in the hills.

Being formed upon unconsolidated, readily eroded alluvial sediments of the Hinuera Formation, deposited *c.* 20,000–*c.* 15,000 years BP (before present), means the young plains of the Hinuera Surface are unlikely to exhibit fault evidence often seen in cohesive or indurated strata, such as planes, scarps and offset beds (Kear & Schofield 1978; Selby & Lowe 1992; McCraw 2011). As a consequence of this challenging tectonomorphic environment, a multi-disciplinary approach is essential in order to identify hidden seismic deformation structures, utilising traditional field techniques, geophysical data and digital modelling. Presenting the results of such an analysis of the Hinuera Surface in the Ruakura area, this study will utilise the findings of geomorphological, geophysical and geological investigations to answer the specific research question:

Has Te Tātua o Wairere Fault Zone been active within the past 20,000 years?

1.1.1. Study Aim and Objectives

This study aims to determine if Te Tātua o Wairere Fault Zone has been active during the very late Quaternary Period, by seeking evidence for seismic deformation of the Hinuera Surface. In order to achieve this aim, four key objectives are identified:

a) Review background literature pertaining to Hamilton Basin geology and geomorphology, as well as fault studies in similar stratigraphic environments elsewhere to identify suitable investigative methods;
b) Identify any broad relationships between Te Tātua o Wairere Fault Zone, Hinuera Surface geomorphology, basin-scale geophysics and earthquake data, by way of non-intrusive desktop analyses;

c) Resolve stratigraphic structure of the Hinuera Surface at a location identified as likely to exhibit seismic deformation by completion of b), using geophysical surveys and excavation of a trench, and;
d) If evidence of structural deformation is forthcoming as a result of c), give consideration to possible alternative explanations.

1.2. Study Area

Comprising an at times rather arbitrarily defined area of approximately 1,600 km^2, the Hamilton Basin is a terrestrial sedimentary basin located between the Lower Waikato Basin to the north and Waipa Basin in the central Waikato region (Figure 1.1). Bounded by uplifted hills and ranges formed upon Triassic–Jurassic volcaniclastic sedimentary rocks, and infilled with extra-basin late Quaternary volcanogenic sediments, the basin's surface topography comprises a series of low relief hills (the Hamilton Hills, <*c.* 100 m high) and flat plains (the Hinuera Surface) (Selby & Lowe 1992; McCraw 2011). Nomenclatural confusion may arise due to the Hamilton Basin having also been somewhat interchangeably termed the Hamilton Lowlands or Middle Waikato Basin across various works (e.g. McCraw 1967; Hume *et al.* 1975; Selby & Lowe 1992; Jeong & Wotherspoon 2019) however this study adopts the geographically- and geologically-apt title preferred by McCraw (2011).

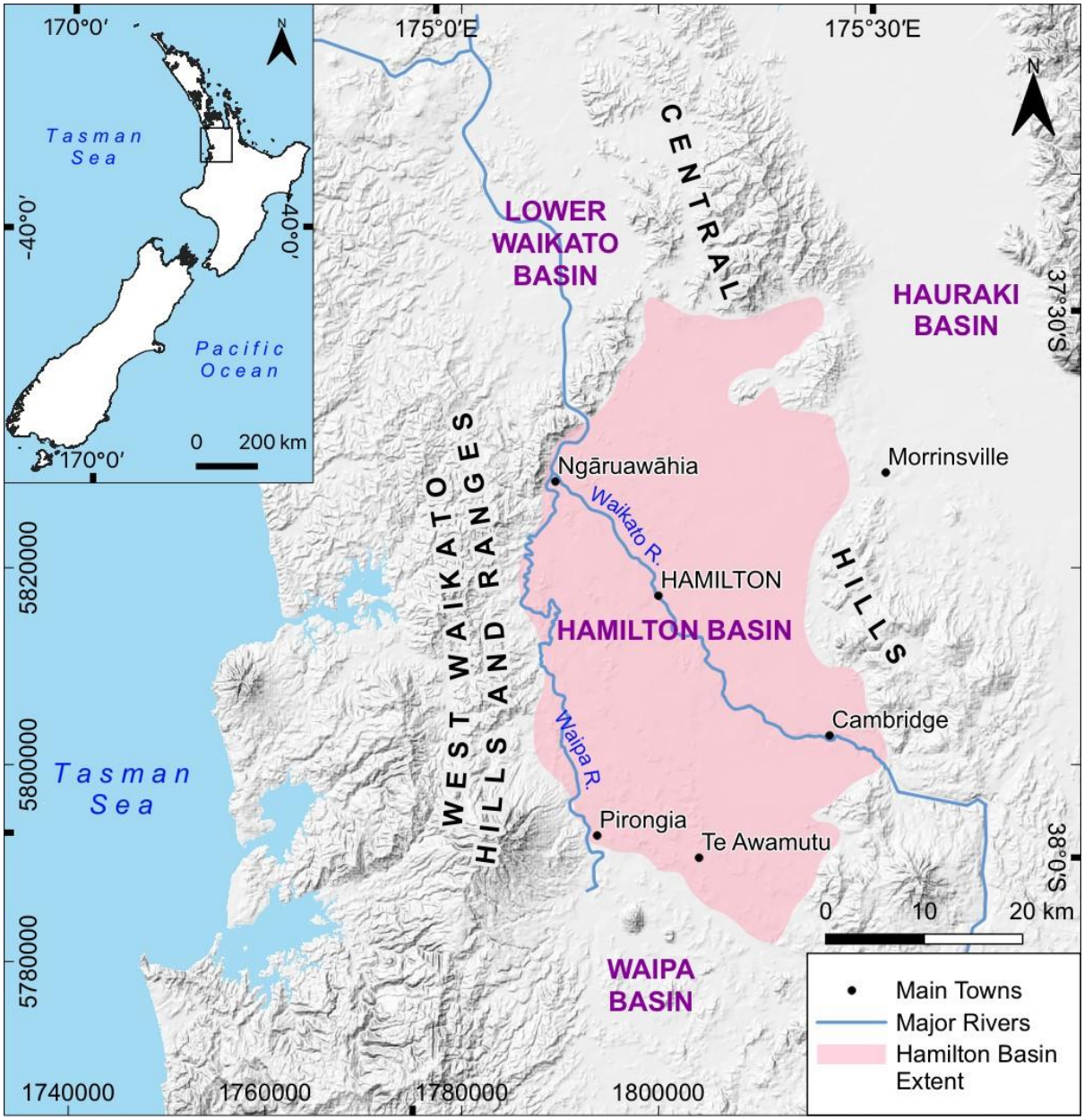

Figure 1.1. Hillshade relief map showing extent of Hamilton Basin and relationship to neighbouring geomorphic areas, redrawn from McCraw (2011). VE=2.5x, illumination from NW. Note that the map utilises the West Waikato Hills and Ranges name of Edbrooke (2005) in place of McCraw's Western Uplands but retains McCraw's boundary with the Waipa Basin (Edbrooke placed it further south). Inset shows location of map area on New Zealand's North Island.

Describing an approximately N-S trace across both the low hills and flat plains of Hamilton City's south-eastern suburbs, Te Tātua o Wairere Fault Zone was the southernmost of four major fault zones indicated within the central Hamilton Basin by Moon and de Lange (2017) (Figure 1.2). Encompassing a variety of land-use and terrain covers, ranging from pasture and stock grazing to urban residential and industrial developments, Te Tātua o Wairere Fault Zone also intersects major road and rail transport corridors (Figure 1.3). A number of key features, infrastructure and reference points are located within the zone, including:

- The University of Waikato main campus;
- AgResearch Ruakura Research Farm and Waikato Innovation Park;
- Ruakura Superhub/Inland Port development;
- Southern Links/Wairere Drive extension of the Hamilton Ring Road and Hamilton Section of the Waikato Expressway (under construction);
- Transpower National Control Centre and Hamilton Substation;
- Hamilton City Water Treatment Plant;
- East Coast Main Trunk Railway;
- Hamilton Gardens.

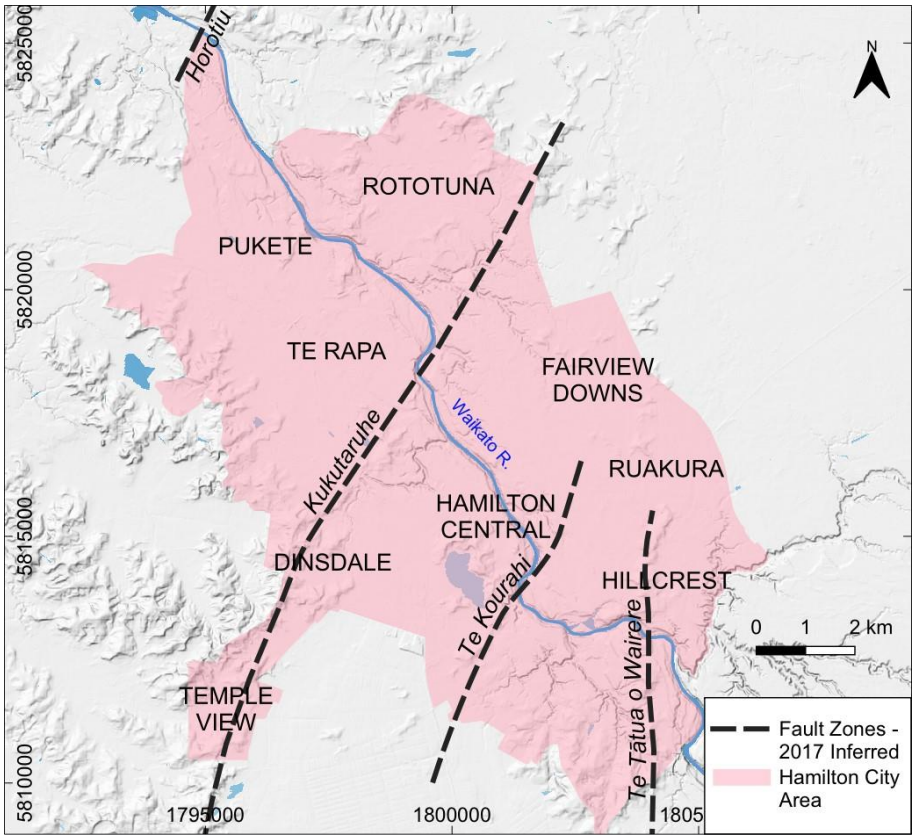

Figure 1.2. Hillshade relief map of the Hamilton City area showing the four main fault zones inferred by Moon and de Lange (2017), with selected suburbs annotated for context. Redrawn from Moon and de Lange (2017). VE=2.5x, illumination from NW.

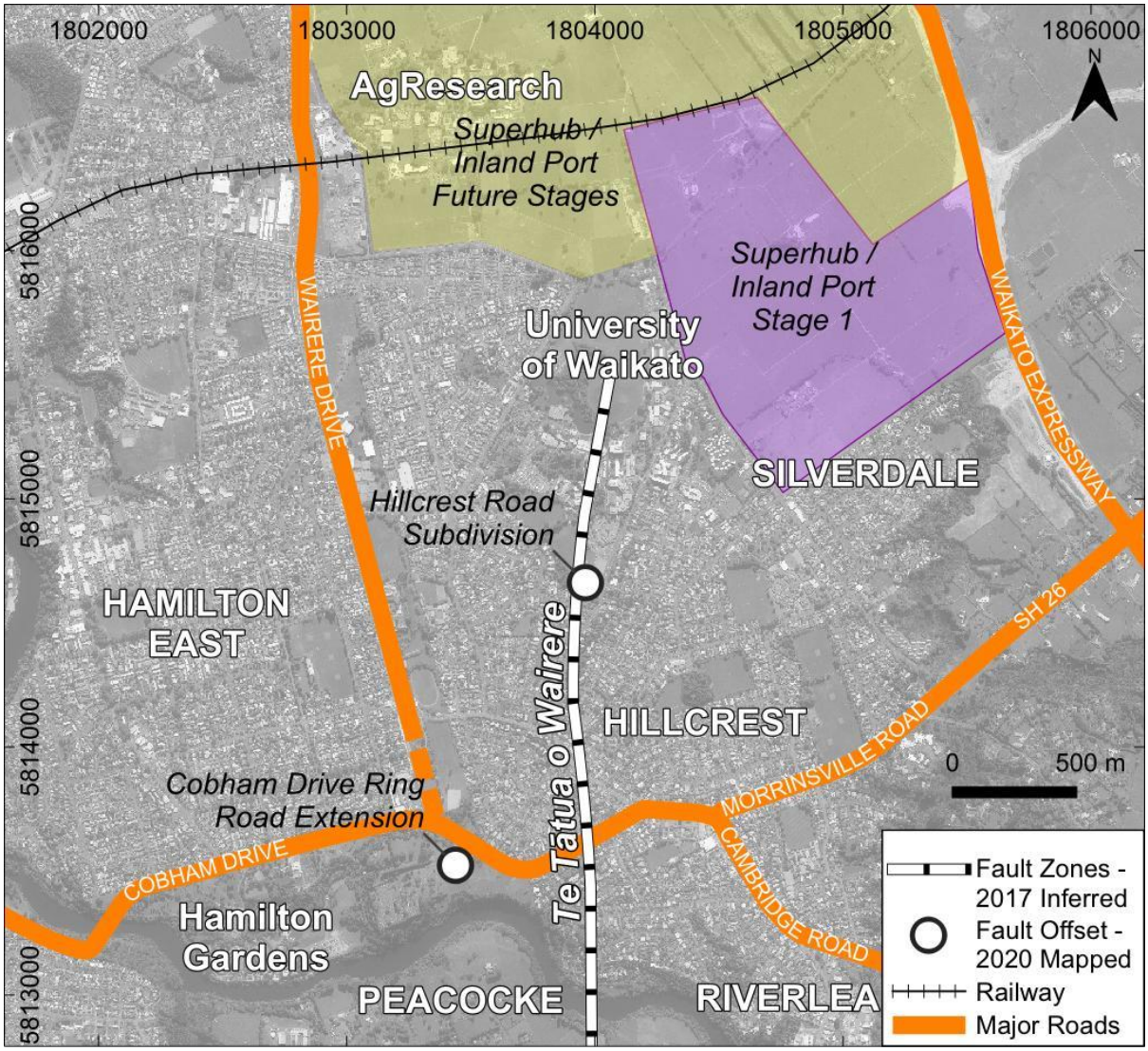

Figure 1.3. Northern section of Te Tātua o Wairere Fault Zone where it intersects major urban areas and transport links, overlaid on a low-contrast greyscale aerial photo. Note the two locations where evidence of fault offset was discovered in 2020; all of the Hamilton fault zones have degrees of uncertainty and do not indicate a definitive fault trace but should be viewed as indicating a generally related zone of deformation. Waikato 0.3m Rural Aerial Photos (2016-2019) sourced from the LINZ Data Service and licenced for reuse under CC BY 4.0.

1.3. Hamilton Basin Geology

Petrography and lithostratigraphic relationships within the Hamilton Basin have been described in several seminal works such as Hume *et al.* (1975), Kear and Schofield (1978), Selby and Lowe (1992), Edbrooke (2005) and McCraw (2011); as a consequence, a review and summation of these publications (among others) provides the basis for this section. Whilst this study is specifically concerned with surficial and shallow depth features of the Quaternary Period, the section commences with a summary of pre-Quaternary units generally only encountered at depth in drill holes for complete stratigraphic context.

1.3.1. Geological Naming Convention

Within the New Zealand geological community there is a generally accepted hierarchy of stratigraphic lexicon, similar in outline to biological taxonomy. As the relationship between stratigraphic units, groupings of units, and geomorphic names can become rather complex, it is helpful to summarise this hierarchical structure. Formal geological names are always expressed with a capitalised suffix such as Group, Sub-Group, Formation, Member or X---stone. Overarching sub-continental scale groupings (i.e. Murihiku Terrane) and landscape geomorphology names (i.e. Hamilton Hills) are also capitalised but the lack of any of the aforementioned terms or a textural descriptor indicates they do not denote a lithological unit.

It is pertinent to note not all divisions or subdivisions may necessarily occur within a group. For example, units belonging to the Te Kuiti Group (which includes formations and members spanning the mid to late Paleogene Period) are not placed into sub-groups. Conversely, the Hinuera Formation (which dates from the Late Pleistocene Epoch) has no formally defined subordinate members but is grouped with the Taupō Pumice Alluvium, which does, and they both belong to the Piako Sub-Group (spanning the Pleistocene and Holocene Epochs). Table 1.1 presents the key geological units that are found within the Hamilton Basin, illustrating this system of ranking. For clarification regarding geological time, the reader is directed to the *New Zealand Geological Timescale* reproduced in Appendix A.

Table 1.1. Stratigraphic hierarchy of key geological units encountered within the Hamilton Basin and discussed in Section 1.3, in order of relative age from oldest to youngest. Dashes indicate where a particular subdivision has either not been formally described or allocated, or where named units do exist but are not found within the basin; italicised names are units that have been described or reported but are not discussed in detail as they are of minor relevance. Compiled from Kear and Schofield (1978), Lowe *et al.* (2001), Edbrooke (2005) and Edbrooke *et al.* (2009).

Group	**Sub-Group/s**	**Formation/s**	**Member/s**
Manaia Hill Group	*Undifferentiated Manaia Hill Group*	-	-
Te Kuiti Group	-	*Unknown – reported from drill holes but not defined*	*Unknown – mudstone and limestone reported but uncorrelated*
Waitemata Group	*Meremere Sub-Group*	*Waikawau Sandstone*	*Unknown – fine to coarse lithologies reported but uncorrelated*
		Units A, B, C (informal, uncorrelated)	-
Tauranga Group	Frankton Sub-Group	*Kaawa Formation*	*Aberfoyle Siltstone*
			Koromatua Blacksand
		Whangamarino Formation	*Frankton sequence (informal)*
	Walton Sub-Group	Puketoka Formation	-
		Karapiro Formation	-
	Piako Sub-Group (including undifferentiated units)	Hinuera Formation	-
		Taupō Pumice Alluvium	*Melville Pumice Member*
			Hopuhopu Pumice Member
-	-	Kauroa Ash Formation[1]	K1–K15
-	-	Hamilton Ash Formation[1]	H1–H7
-	-	Late Quaternary tephras (informal) [1]	-

[1] Can be syndepositional and intercalate with Piako Sub-Group.

1.3.2. Pre-Pleistocene Geology

1.3.2.1. Late Jurassic Basement of the Manaia Hill Group

Basement refers to the lowermost igneous or metamorphic strata that underlie sedimentary cover beds ('Basement' 2003) but in New Zealand basement is regarded as all Early Cretaceous and older rocks (>100.5 Ma), and may not strictly meet the igneous or metamorphic criterion (Bradshaw 1993; Johnston 2019). Regionally, basement has in the past been referred to as the Hokonui System or Hokonui Facies (e.g. Kear & Schofield 1978; Kear 1993), however, more recent studies have re-classified New Zealand's basement into a series of tectonostratigraphic terranes. Each terrane is a constituent member of either the Western Province, Eastern Province, or the dividing Median Tectonic Zone (Bradshaw 1993; Briggs *et al.* 2004; Johnston 2019). As a consequence of terrane classification the Hokonui name is no longer applied, although rare attempts have been made towards resurrection by way of the 'Hokonui Assemblage', referring to a proposed amalgamation of the Eastern Province's Brook Street, Murihiku, and Dun Mountain-Matai Terranes (e.g. Landis *et al.* 1999; Noda *et al.* 2004).

Positioned within the Eastern Province's Waipapa Composite Terrane, the Hamilton Basin is underlain by Late Jurassic basement comprised of massive, volcaniclastic, sandstones, siltstones and argillites belonging to the Manaia Hill Group (Kear 1993; Briggs *et al.* 2004; Edbrooke 2005). Approximately 60 Ma after earliest deposition of the Manaia Hill, during the middle Cretaceous, the Waipapa Composite Terrane became sutured to other terranes in an accretionary prism off the coast of the Gondwanan supercontinent. Shortly after suturing, *c.* 100 Ma BP, rifting began to separate the amalgamated terranes from Gondwana, forming the proto-continent of Zealandia (Spörli 1978; Briggs *et al.* 2004; Johnston 2019). Basement rocks of the Waipapa Composite Terrane (and others) are often collectively referred to as 'greywacke' but as Johnston (2019) mentioned, this is imprecise and lithologically inappropriate, given only a small number of units are actually greywackes.

Rare exposures in anomalously shallow outcrops and logs from a number of petroleum exploration drill holes have established the presence of the Manaia Hill Group throughout the Hamilton Basin (Kear & Schofield 1978; Edbrooke 2005). A basement surface contour map presented by Edbrooke *et al.* (2009) shows a north-west deepening of basement across the basin, from *c.* 200 m depth in the south-east to >1,600 m nearest the Hakarimata Range in the north-west (Figure 1.4). Results from recent work to geophysically model basement depth and structure utilising the horizontal-to-vertical (H/V) spectral ratio method, by Jeong and Wotherspoon (2019) and Cave (2020), reflect this basement deepening in a general sense but show a greater SW-NE oriented depth profile than Edbrooke's contours (Figure 1.5). This later work agrees with a seismograph survey report by Petty Geophysical Engineering Company (1963), which stated "the deepest part of the basin is near… Gordonton", a village about 6 km N of the Hamilton city limit.

External to, but defining the basin boundaries in the west and north-west, are uplifted Triassic–Early Jurassic sandstones and siltstones of the Murihiku Terrane's Newcastle Group, while Permian–Triassic ultramafic ophiolites of the Dun Mountain-Matai Terrane are not exposed in outcrop but have been geomagnetically inferred between the Waipapa Composite and Murihiku Terranes (Hatherton & Sibson 1970; Kear 1993; Sutherland 1999; Eccles *et al.* 2005). Referred to as the Junction Magnetic Anomaly (JMA), this feature has also been inferred as being coincident or near-coincident with the Waipa Fault which is discussed further in Section 1.4.

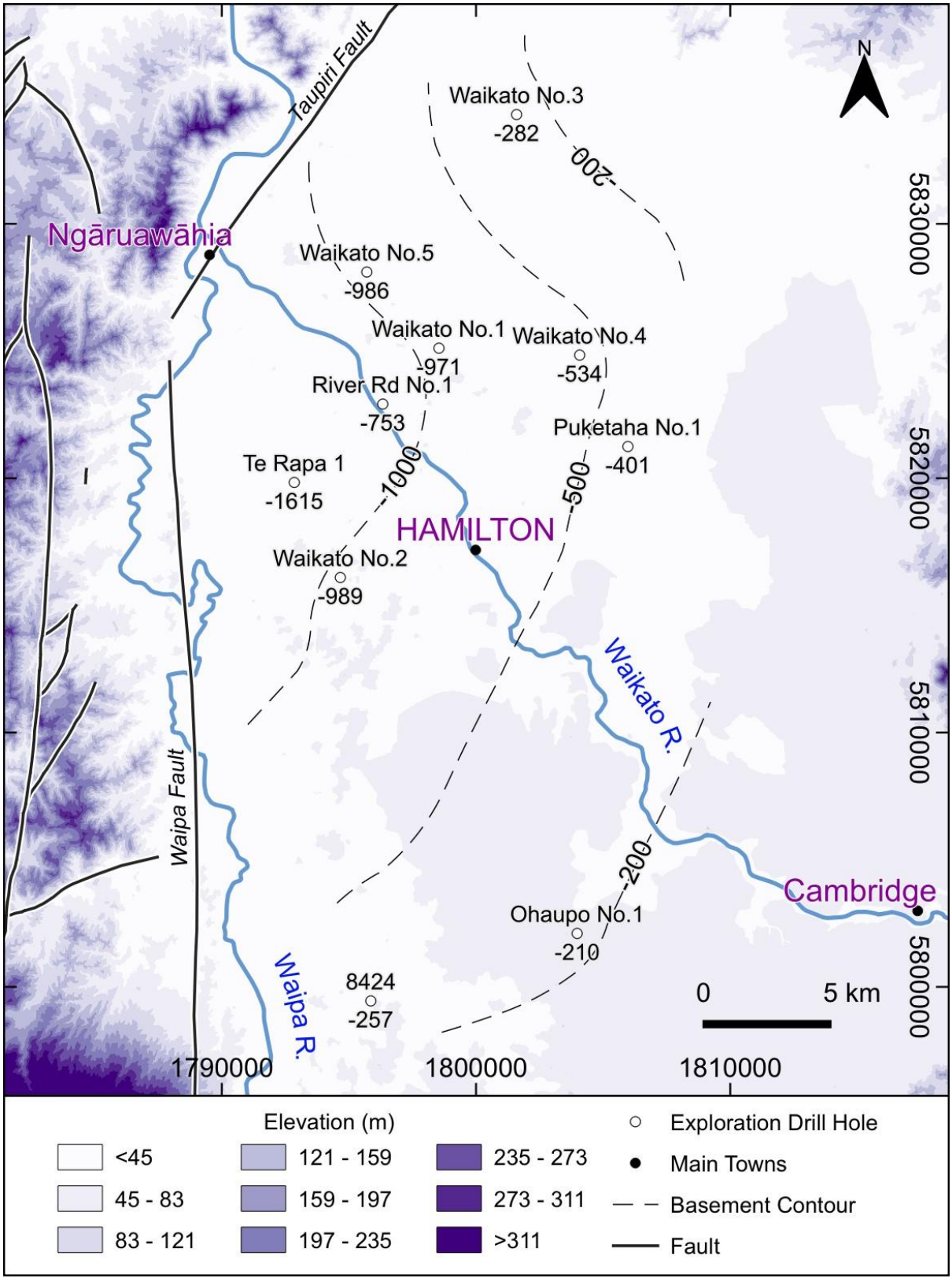

Figure 1.4. Hamilton Basin basement surface contours interpolated from exploration drill hole logs with nearby faults shown (Waipa and Taupiri Faults annotated) and overlaid on a digital elevation model. Redrawn from Edbrooke *et al.* (2009, p. 35, Figure 6.1). Note King's (1991, cited in Spinardi 2017) proposed Taupiri Fault was included but did not appear in Edbrooke's 2005 map, which has become a standard reference work.

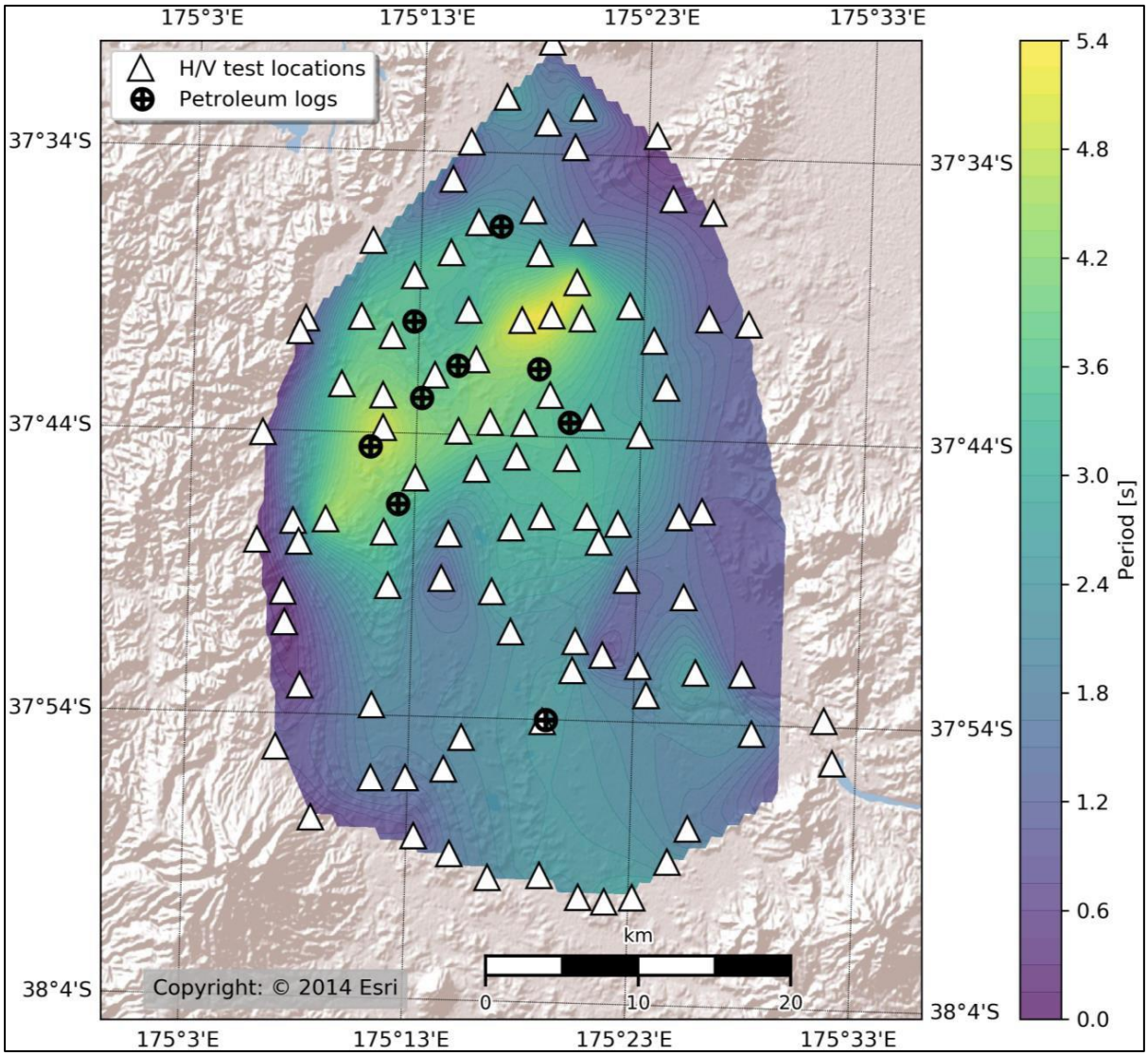

Figure 1.5. Hamilton Basin fundamental site period (T_0) interpolation map from ambient seismic vibrations, where time is a proxy for depth to basement, overlaid on a hillshade relief (VE unknown, illuminated from NW). Light (yellow) shades indicate greater depth, dark (purple) shades are shallower. While similar to Figure 1.4, note the greater depth in the basin's north, producing a depth profile effectively parallel to the NW basin boundary. Reproduced from Jeong and Wotherspoon (2019, p. 5, Figure 3).

1.3.2.2. Mid-Eocene to Pliocene Marine Transition Strata of the Te Kuiti Group, Waitemata Group and Frankton Sub-Group

Described by Kear and Schofield (1978) as "a classical lithological sequence" (p. 48), the Te Kuiti Group lies unconformably upon the Late Jurassic Manaia Hill Group. Deposition of Te Kuiti Group sediments commenced Late Eocene, which defines a hiatus in the order of *c.* 102 Ma (Kear & Schofield 1978; Kamp *et al.* 2014). With a progression from basal coal measures through claystones, siltstones, sandstones, and limestones, the distribution and stratigraphy of Te Kuiti Group units both throughout the basin and across the uplifted bordering ranges provides evidence for marine transgression prior to a period of major faulting and structural change (Kear & Schofield 1978; Selby & Lowe 1992; McCraw 2011). Whilst Te Kuiti Group outcrops are frequently encountered in hills and ranges outside the basin, variably thick units remain buried within it, ranging from 30 m to 228 m in thickness but generally thinning with distance from west to east (Edbrooke *et al.* 2009). In conjunction with the succeeding Waitemata Group, the Te Kuiti Group's presence within the basin is known only from exploratory drilling.

Following cessation of Te Kuiti Group sedimentation and a subsequent period of erosion when the paleo-basin was inverted for a time, sediments of the less contiguous Waitemata Group began to be deposited during the Early Miocene (Kear & Schofield 1978; Edbrooke *et al.* 2009; Kamp *et al.* 2014). The siltstones, sandstones, and tuffs of the Waitemata Group are indicative of a shallowing marine environment, reflected by progressively greater inclusion of terrigenous inputs towards the top of the group (Kear & Schofield 1978). Whilst not as widely distributed as the underlying Te Kuiti Group, the generally relatable extent and overlying position of Waitemata Group both intra- and extra-basin provides evidence of substantial regional faulting mechanisms post-Late Miocene; the subsequent unconformity between the Waitemata Group and succeeding Frankton Sub-Group is an expression of the Kaikoura Orogeny which commenced around that time and continued until the Early Pliocene (Landis & Coombs 1967; Stipp & Thompson 1971; Selby & Lowe 1992).

Lying unconformably atop eroded Waitemata Group and being comprised of varying shallow marine sediments and terrestrial sedimentary strata (with inclusions of extra-basin Late Pliocene-Early Pleistocene Alexandra Volcanics), the Frankton Sub-Group reflects a fluctuating near-shore continental facies, deposited as relative sea level fell and the basin transitioned to a continental environment (Kear & Schofield 1978). Being the basal unit of the same Tauranga Group in which Quaternary strata that form the Hamilton Hills and Hinuera Surface are placed, the Frankton Sub-Group also represents an epoch transition from Pliocene to Pleistocene. Half the members of the Frankton Sub-Group have been found only in Hamilton Basin drill holes at depths ≥50 m below present sea level and lack any corresponding outcrops outside the basin, resulting in the sub-group's true distribution being unknown (Kear & Schofield 1978; Petch & Marshall 1988).

1.3.3. Quaternary Geology

1.3.3.1. Early to Mid-Pleistocene Volcanogenic Deposits of the Walton Sub-Group

The moderately consolidated clayey deposits of the Tauranga Group's Walton Sub-Group unconformably overlie the Frankton Sub-Group and date from Early to Mid-Pleistocene (*c.* 2.4–0.13 Ma) (Kear & Schofield 1978; Selby & Lowe 1992; Edbrooke 2005). Within the basin, the sub-group may be divided into the Puketoka Formation and Karapiro Formation, although in-field distinction between them can be rather subjective and is perhaps more academic in nature than practical; a sub-group unit derived from locally weathered basement hills, the Waeranga Gravels, does not occur in any significance within the Hamilton Basin (Kear & Schofield 1978).

Described by Kear and Schofield (1978) as a "pure" pumiceous formation of lacustrine, fluviatile and ignimbritic origins, Puketoka Formation is lighter in colour than Karapiro Formation; the former being white to light grey whereas the latter may be any or all of the same as well as orange, pink, red or brown. Kear and Schofield (1978) postulated the latter's colouration could possibly be due to a higher abundance of ferromagnesian minerals. Whilst Puketoka Formation has been recognised as incorporating both subaqueous and subaerial depositional forms, both Kear and Schofield (1978) and Selby and Lowe (1992) inferred that only the latter,

being the weathered remains of unwelded, distal ignimbrites, is typically found within the basin. This unsorted, massive, moderately consolidated formation incorporates glass shards (commonly argillized), sand-sized pumice fragments, and broken phenocrysts of angular quartz, which may make up to approximately 25% of the deposit (Kear & Schofield 1978).

As distinct from the massive, dominantly pumiceous Puketoka Formation, the Karapiro Formation comprises fluvial and lacustrine current-bedded coarse sands and grits with greater lithic rhyolite content (Kear & Schofield 1978; Selby & Lowe 1992). Notably, Kear and Schofield (1978) mentioned that aside from a higher degree of weathering, Karapiro Formation deposits "are identical" (p. 105) to those of the much younger Hinuera Formation, which suggests very similar sediment supply and depositional environments. Kear and Schofield (1978) also stated that Puketoka Formation, being *c.* 2.4–0.34 Ma in age, is the basin's oldest Quaternary strata but also suggested the same age and period of weathering for Karapiro Formation. This age range overlaps with deposition of the Kauroa Ash Formation and the upper margin of error for Hamilton Ash Formation, indicating that whilst the depositional events may have been distinct they cannot be viewed as temporally discrete – there must have been significant overlap across geological processes.

The Hamilton Basin's geological depositional continuum is reinforced by way of both Walton Sub-Group formations being interbedded with peats, containing numerous unconformities and, more often than not, inter-fingering with one another (Kear & Schofield 1978). Any clear distinction between the two is somewhat difficult and indeed, Kear and Schofield (1978) made the specific point that "differentiation of the… formations may not be wholly satisfactory, [but] their separation is convenient for purposes of correlation and discussion" (p. 100). Puketoka Formation can potentially on occasion be distinguished, however, due to a propensity for forming bluffs where localised case hardening has taken place (Kear & Schofield 1978). Although not a formal geological name in itself, the Hamilton Hills is a useful geomorphic descriptor referring to the low rolling basin hills formed upon units of the Walton Sub-Group.

1.3.3.2. Early to Mid-Pleistocene Tephras of the Kauroa Ash Formation, Hamilton Ash Formation, and Late Quaternary Sequences

A series of highly weathered, clayey tephras, called the Kauroa Ash Formation, Hamilton Ash Formation, and "late Quaternary tephras", form widely but variably distributed covers across the Hamilton Hills (Selby & Lowe 1992). Notably, these are regarded as formations in their own right and have not been placed within the Tauranga Group (or any other). Although the terms *shower bedding* and *airfall ashes* have largely fallen out of contemporary usage these descriptors are apt in indicating ash-sized pyroclasts settling across the paleo-basin surface from distal eruption plumes. The oldest of these fine-grained tephras, originating from the Coromandel Volcanic Zone and/or Taupō Volcanic Zone, the Kauroa Ash Formation (members referred to as K-beds) consists of 15 highly weathered rhyolitic ash beds with numerous disconformities and paleosols; a very distinct, topmost, reddish-brown, blocky paleosol separates them from the overlying Hamilton Ash Formation (where present) (Selby & Lowe 1992). Though not all 15 K-beds are always found at any locality, the oldest (K1) has been dated at 2.24 ± 0.19 Ma and the youngest (K15) at *c.* 0.78 Ma (Lowe *et al.* 2001).

Overlying the K-beds, the Hamilton Ash Formation (members referred to as H-beds) is similar to the former in being rhyolitic, with a number of paleosols but constitutes fewer beds (seven) and is more widespread, having been logged onshore as far afield as Auckland, Wellington, Raglan and Gisborne (Selby & Lowe 1992). Lowe *et al.* (2001) dated the basal H-beds (H1/H2) at 0.38 ± 0.04 Ma, approximating previously calculated ages of *c.* 0.35 Ma, and estimated the topmost (H6/H7) to be *c.* 0.18–0.08 Ma. Earlier work by Ward (1967) had described nine H-beds, including an overlying Mairoa Ash Formation (H9), but the number of beds was revised down when Lowe *et al.* (2001) correlated H8/H9 with the *c.* 64 ka Rotoehu Ash, leading to those beds incorporation within the "late Quaternary tephras". Importantly, whilst they were unable to definitively attribute a source for the younger H-beds (though did suggest the Taupō Volcanic Zone being highly plausible), Lowe *et al.* (2001) were able to correlate H1 with the Whakamaru Caldera-derived Rangitawa Tephra.

Not only does the Rangitawa Tephra mark the re-commencement of substantial tephra deposition within the Hamilton Basin after a hiatus in the order of 400 ka but its' in situ characteristics make it most suitable for use as both a stratigraphic and structural marker bed (Ward 1967; Selby & Lowe 1992). Unlike the darker red/brown hues of under- and over-lying clay-rich beds, the silty H1 bed/Rangitawa Tephra is distinctively pale pinkish to brownish grey, with a yellowish coarse sandy layer at the base, containing quartz crystals and prominent manganese staining (Ward 1967; Selby & Lowe 1992). Where Rangitawa Tephra is recognised in the field, the observer is readily able to determine underlying units as being >*c.* 350 ka while those above must be <*c.* 350 ka, and should the tephra be offset, then movement must have been within the last *c.* 350 ka.

The final tephra formation within the Hamilton Basin lacks a formal geological name, comprising >40, thin and oft-indistinguishable members, collectively referred to as "late Quaternary tephras" (Selby & Lowe 1992). As Selby and Lowe (1992) described, these distal rhyolitic and andesitic deposits originate from volcanic centres *c.* 70–200 km from the basin and are generally thicker south and east of Hamilton City (≥1 m) than to the west and north (≤0.5 m). The basal member of this formation is the Rotoehu Ash, dated at 64 ± 4 ka and modern volcanism (e.g. Taupō *c.* AD 232, Ruapehu AD 1995–1996) continues to build upon the youngest, soil-forming beds (Selby & Lowe 1992; Lowe *et al.* 2001). Of these late Quaternary tephras then, the oldest may be found atop the Hamilton Ash Formation but beneath or indeed intercalated with the Piako Sub-Group, whilst the youngest can mantle both.

1.3.3.3. Late Pleistocene to Holocene Alluvium of the Piako Sub-Group

Youngest of the Tauranga Group subordinates, the Piako Sub-Group incorporates extensive alluvial and colluvial deposits of the Hinuera Formation, with lesser tracts of Taupō Pumice Alluvium (the Hauraki Clay also belongs to the sub-group but is only deposited in the Hauraki Basin) (Kear & Schofield 1978; Edbrooke 2005). Aside from the Walton Sub-Group and Quaternary ashes, the Hinuera Formation is the predominant geological unit of the Hamilton Basin, forming sequences up to 90 m thick in the paleo-valleys between hills. A characteristic feature

of the Hinuera Formation is the great lateral and vertical variation in texture and structure, ranging from rhyolitic sands and gravels to pumice silts, sands and gravels, interbedded with minor peats; bedding is sometimes planar and massive (most often in lower sequences), at other times strongly current bedded (Kear & Schofield 1978; Edbrooke 2005). Loose ferromagnesian (or heavy) minerals are common, often forming a lag that is useful in identifying bedsets (Schofield 1965; Hume *et al.* 1975).

The Hinuera Formation was deposited in two main periods as the forebear of today's Waikato River alternated courses between the proto-Hauraki and Hamilton Basins, aggradationally depositing volcanogenic sediments originating from the Taupō Volcanic Zone (Schofield 1965; Edbrooke 2005). The first depositional period (culminating in Schofield's "Hinuera-1 Surface") was believed to have occurred between *c.* 50,000 and 20,000 years BP, while the second ("Hinuera-2 Surface"), was a much more active period between *c.* 20,000 and 15,000 years BP as a combined result of increased sediment from the *c.* 26,500 years BP Oruanui eruption, and increased erosion due to a cool, dry climate (Kear & Schofield 1978; Edbrooke 2005).

Radiocarbon dating of organic material within the Hinuera Formation later refined the beginning of the first depositional phase to *c.* 64,000–45,000 years BP and ending *c.* 24,000 years BP, while the second phase occurred *c.* 19,000–15,000 years BP (Selby & Lowe 1992). It is noted that some later authors have adopted a rather simplified view of the Hinuera Formation, implying that it *is* 20 ka old or that deposition ceased *c.* 17,000–18,000 years BP (e.g. Kleyburg 2015; Spinardi 2017) but this is incorrect. 20 ka is only an approximate age for second-phase deposition commencing and although the bulk of deposition did take place >17,000 years BP, it did not cease entirely until a few thousand years later (Selby & Lowe 1992).

McCraw (2011) apparently disagreed with the earlier postulation of two-phase deposition, stating there is "little evidence" to suggest the proto-Waikato River flowed through the Waikato Basin after cessation of Karapiro Formation deposition *c.* 1.0 Ma and before influx of Oruanui materials "a few thousand years after [the 26.5 ka eruption]" (p. 19). As opposed to the river alternating its flow between basins over a

c. 50 ka period, McCraw (2011) favoured the concept of a discrete break-out flood. McCraw suggested that following outflow for almost 1 Ma through the Hauraki Valley (proto-Hauraki Basin) to the Thames Estuary, choking of the river at Piarere by Oruanui pyroclasts caused it to breach the divide with the Waikato Valley (proto-Hamilton Basin) and quickly adopt the course of an existing stream. Earlier authors had also agreed with the basic break-out flood hypothesis as an explanation for second-phase deposition but quite why McCraw disagreed with the concept of an earlier first-phase is unclear.

Validation of the valley-switching hypotheses is a matter for debate outside the scope of this study but in either case, proponents of both arguments all agreed that from *c.* 20,000–15,000 years BP, a redirected, volcanic sediment-laden Waikato River flowed beyond the Piarere Gap (Schofield's "Hinuera disjunction") as an extensive braided river system (Schofield 1965; Hume *et al.* 1975; Edbrooke 2005; McCraw 2011). Schofield (1965) adopted the name Hinuera Surface for the extensive plains formed upon the topmost deposits of the Hinuera Formation, which he also concluded was a very low angle alluvial fan, formed from the overlapping of innumerable smaller fans laid down by the wandering river. Notably, most works subsequent to Hume *et al.* (1975) allude to the Hinuera Surface forming a fan of ≤1°, however, whilst technically not incorrect, this is effectively an order of magnitude greater than that stated by the authors, who gave a mere 0.1°.

Alluvial fans are typically recognised as having slopes in the order of 1–6° although some works refer to ultra-low angle "megafans" or "braided fluvial fans" of <1° (McPherson *et al.* 1987; Saito & Oguchi 2005; Bowman 2019). As the Hinuera Surface forms flat plains with a gradient so slight as to have allowed earlier Waikato River iterations to meander so haphazardly, perhaps consideration should be given as to whether the Hinuera Formation is best called an alluvial fan at all. McPherson *et al.* (1987) drew a distinction between cone-shaped *fan-deltas* – alluvial fans at a highland/standing water interface – and *braid-deltas* – deposited by prograding braided river systems to form sheet-like, ultra-low gradient *braid-plains*. The braid-delta/braid-plain concept seems to capture key qualities of the Hinuera Surface.

Post-Hinuera Formation deposition, a combination of a warmer climate enabling pedological development, forestation and soil stabilisation, concurrent with a reduction in sediment supply, resulted in the Waikato River downcutting a permanent channel through the formation (Kear & Schofield 1978; Edbrooke 2005; McCraw 2011). Aside from sporadic inputs of tephra from distal volcanic eruptions, the only Holocene geological units in the Hamilton Basin are members of the Taupō Pumice Alluvium (TPA) (or Taupō Formation, after Edbrooke 2005), deposited <*c.* 1.8 ka by the river within the confines of its own recently entrenched channel (Kear & Schofield 1978). Within the Hamilton Basin these unconsolidated, highly pumiceous to pure pumice silts and sands do not extend to the Hinuera Surface (*cf.* the Lower Waikato Basin where the TPA forms more significant deposits) (Selby & Lowe 1992; Edbrooke 2005; Hogg *et al.* 2012).

1.4. Early Interpretations of Hamilton Basin Structures

1.4.1. The Waipa Fault

Effectively delineating the western boundary of the Hamilton Basin, the approximately N-S striking Waipa Fault separates uplifted Murihiku Terrane and overlying Eocene–Miocene groups on the western margin of the basin from low-lying Waipapa Composite Terrane and Pliocene–Pleistocene deposits to the east (Kear & Schofield 1978; Edbrooke 2005) (refer Figure 1.4). Although it is perhaps the greatest structural feature within the study area, direct evidence of the Waipa Fault – aside from inferred differences in elevation – is only exposed south of the basin and any surface expression dies out beneath Pirongia Volcano (Kamp & Lowe 1981; Spinardi 2017).

A northward trace of the Waipa Fault has been inferred beneath Pirongia, the Hakarimata Range and bending westward through the Auckland and Northland regions, from a geomagnetic anomaly called the Junction Magnetic Anomaly (JMA), thought to be coincident or near-coincident with the fault (Hatherton & Sibson 1970; Kear 1993; Eccles *et al.* 2005; Edbrooke 2005) (Figure 1.6A). The JMA is believed to result from the presence of Dun Mountain-Matai Terrane ultramafics, from which

serpentinite has been rotated to vertical and exposed near Piopio, further south along the fault (Hatherton & Sibson 1970; Kear 1993). Whilst most authors make a Waipa Fault/JMA association, Selby (1967) did not extend it to the north, instead mapping it geomorphically across the southern edge of the Hakarimata Range (Figure 1.6B). King (1991, cited in Spinardi 2017) proposed a near identical fault trace but rather than as a continuation of the Waipa Fault, suggested a separate – yet not unrelated – Taupiri Fault (Figure 1.4).

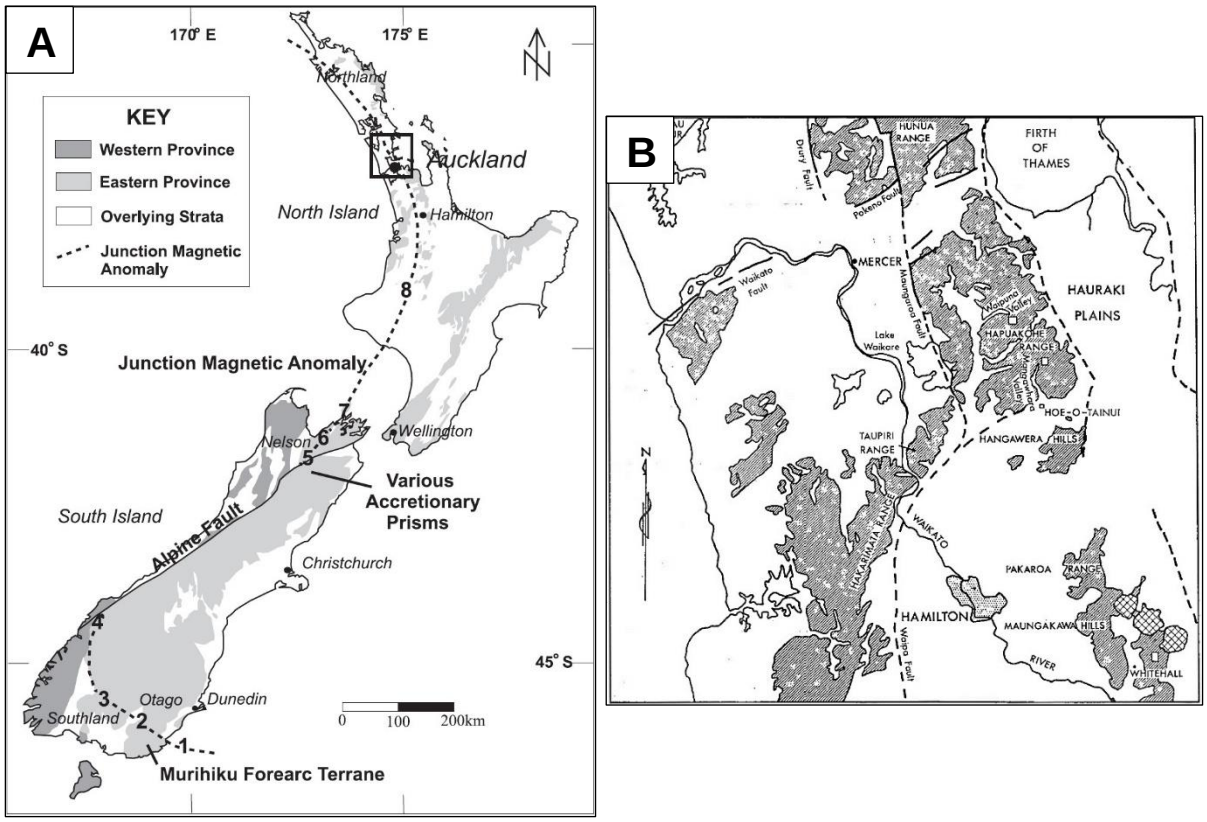

Figure 1.6. (A) Junction Magnetic Anomaly map of Eccles *et al.* (2005, p. 724, Figure 1), showing the line of anomaly which most studies infer as approximating the Waipa Fault; **(B)** Extract of Selby's (1967) map extending the Waipa Fault along the southern Hakarimata Range (dashed line curving to northeast from bottom centre), akin to King's (1991, cited in Spinardi 2017) proposed Taupiri Fault.

Age, magnitude and form of last activity on the Waipa Fault is undetermined but O'Brien and Rodgers (1973) surmised the Wairere Serpentinite near Piopio provided evidence of diapiric intrusion due to compressive stress, with a (topographically-inferred) fault plane dipping steeply to the west. In seismic contour maps produced by Petty Geophysical Engineering Company (1963), the Waipa Fault

is labelled as a "major transcurrent fault" and Kear (1993) stated that it is certainly a fault with at least some strike-slip aspect, as opposed to marking a simple terrane suture, but had previously suggested (in Kear & Schofield 1978) that it may have most recently (re)activated as a reverse fault.

Whilst no firm consensus on the Waipa Fault's age or motion has yet been reached, Kear (1993) has described how Triassic clasts of the Newcastle Group (Murihiku Terrane) are incorporated within Late Jurassic rocks of the Manaia Hill Group (Waipapa Composite Terrane). Such cross-terrane inclusions indicate older rocks were eroded from a landward mass and deposited as younger sediments in a deeper offshore basin, which Kear took to suggest the Waipa Fault was an active controlling feature at least *c.* 164 Ma (Kear 1993).

1.4.2. Petroleum Exploration Insights

No written report or discussion was provided but a compilation of unpublished petroleum exploration data by Liles (1971) included two detailed Hamilton Basin maps, showing Late Oligocene–Early Miocene (Figure 1.7) and Late Miocene–Early Pliocene (Figure 1.8) structural horizons. These were interpreted from an array of seismic sections (source unspecified but perhaps incorporating earlier work by Petty Geophysical Engineering Company (1963)) and calibrated against exploration drill logs; the absence of a legend or accompanying text does, however, make interpretation a little difficult. Complex systems of faults are readily apparent in both maps but the symbology used is more usually associated with thrust faults. Edbrooke *et al.* (2009) did explicitly state, however, that they are normal faults and the variable spacing between parallel/sub-parallel lines seems to support this premise, with spacing appearing to indicate degree of displacement and line convergence or divergence corresponding to a reduction or increase in displacement along-fault.

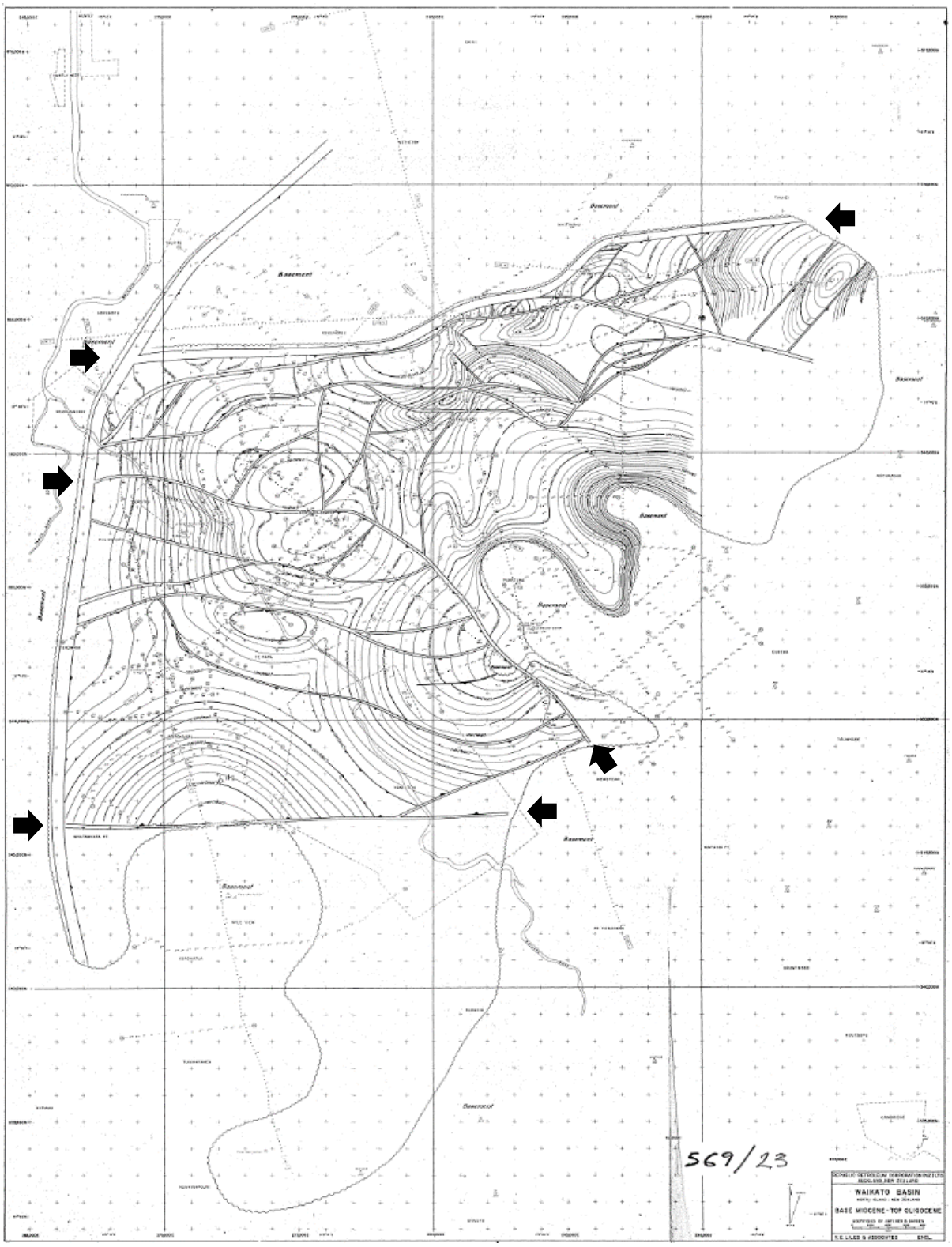

Figure 1.7. Oligocene–Miocene horizon map from Liles (1971). Note the three distinctive intra-basin faults also appearing in Figure 1.8 (arrows added for clarity); a fault striking approximately west-east in the north, a central fault arcing from west to south-east, and a southern fault striking almost due west-east.

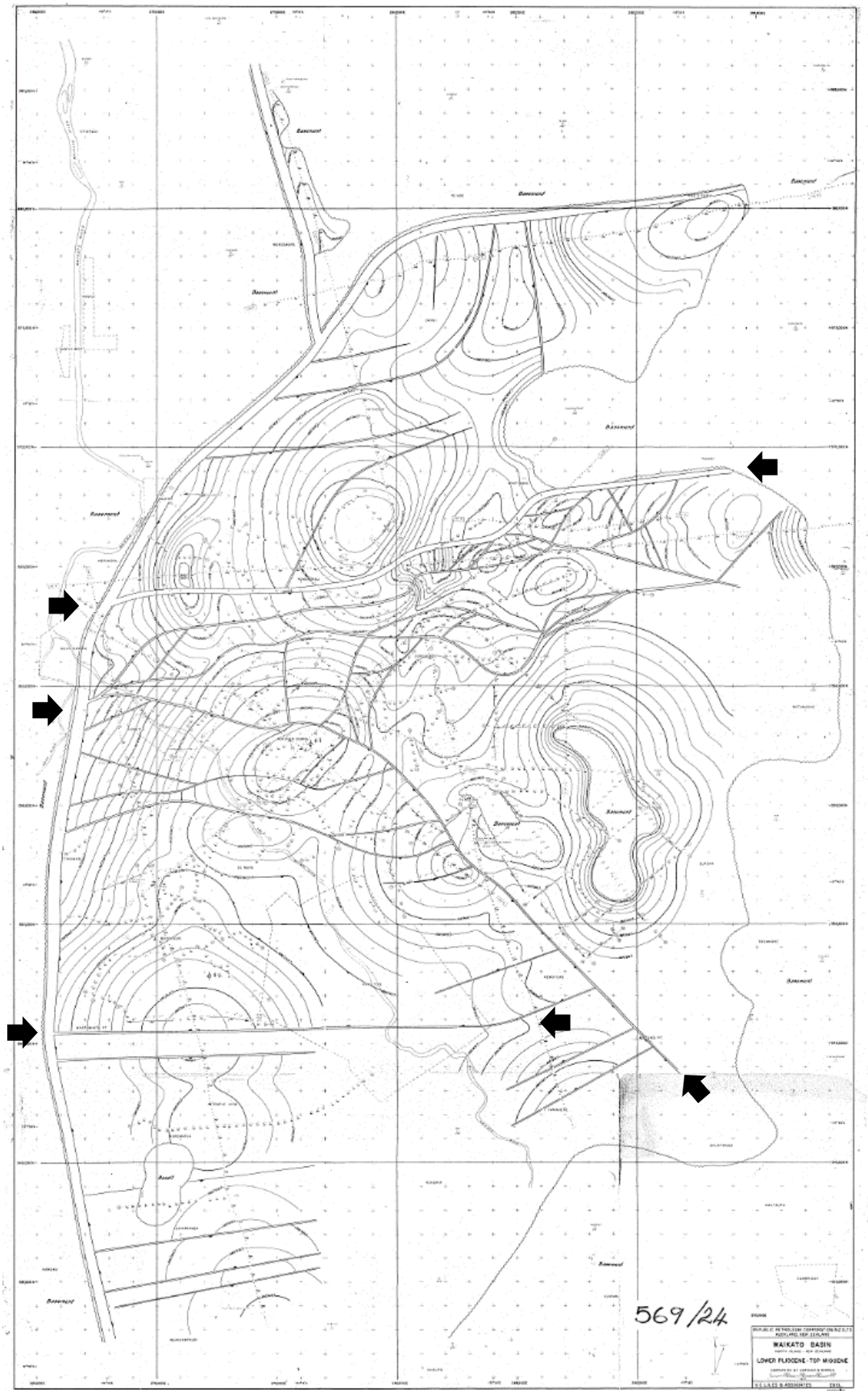

Figure 1.8. Miocene–Pliocene horizon map from Liles (1971). Note the three distinctive intra-basin faults as described in Figure 1.7 (arrows added for clarity).

While there are subtle differences between Liles' two maps, two key features are seen in both that are of particular relevance to tectonic studies. The first of these are three major normal faults cutting both horizons, seen in the same positions of both Figure 1.7 and Figure 1.8. The northernmost of these major faults strikes approximately west-east across the northern third of the basin, downthrown to the south, while the second describes a rough arc from west to southeast across the middle of the basin, downthrown to the south and west. The third major fault crosses almost due west-east across the basin's south and is downthrown to the north.

Second of the maps' key features are a series of shorter faults striking ENE within the central basin, truncated to the east by the major mid-basin fault. In Figure 1.8 particularly, these faults can be seen to step down to the south within the north of the basin while to the south they step down to the north, forming a classic horst and graben model. This is noteworthy as the modern basin has been referred to as a graben within a similar model (Selby 1967) albeit with a different orientation; today's horsts are to the west (West Waikato Hills and Ranges) and east (Central Hills) of the basin, giving an approximate N-S axis but in Liles' pre-Pleistocene model the internal structure is almost perpendicular, orientated WSW–ENE. The shorter, central-basin faults of Liles (1971) are also more numerous in the Miocene–Pliocene horizon, indicating their cutting units of both the Waitemata Group and early Tauranga Group, which would indicate displacement within, at most, 5.33 Ma.

Whether or not Liles' work was at least partly based upon earlier seismic data produced by Petty Geophysical Engineering Company (1963) (PGEC), the PGEC work is particularly noteworthy for a comment regarding the present-day Waikato River. PGEC's (1963) written report is very brief, chiefly concerned with survey procedural aspects and the lack of a map grid or scale makes precise spatial placement difficult but in enclosure 9 (one of eight seismic contour maps), at a point somewhere between Hamilton City and the Hakarimata Range, an annotation reads "it is possible the Waikato River is fault controlled" (Figure 1.9). Numerous intra-basin faults appear throughout the PGEC maps but unlike those of Liles (1971) the maps do not distinguish horizons so fault chronostratigraphy is unknown.

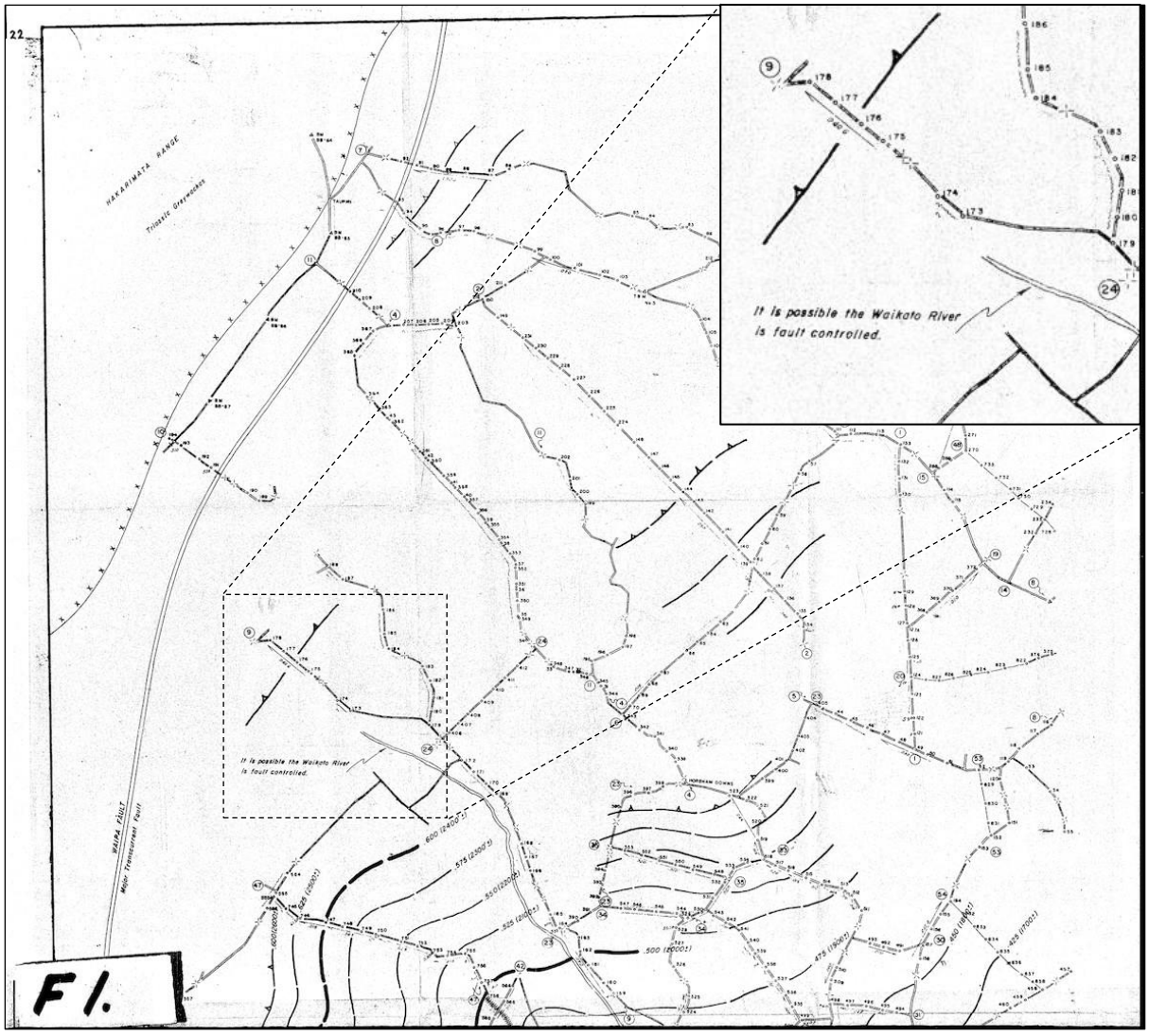

Figure 1.9. Enclosure 9, F1, seismic contour map reproduced from Petty Geophysical Engineering Company (1963). The map lacks coordinates but the (added) exploded view of the annotation regarding fault control of the Waikato River is between Hamilton City to the southeast (not visible in F1 but shown in F3, not reproduced) and the Hakarimata Range to the northeast.

Apparent intra-basin faulting and a specific observation by PGEC (1963) regarding modern fault-controlled geomorphology seems, as with Liles' analysis, not to have been widely circulated or explored in any detail. Few published works appear to cite either author and a Google Scholar search returned only three citations for Liles, with one of these (Edbrooke *et al.* 2009) also being the sole work citing PGEC. This is perhaps unsurprising given the commercial nature of the studies but, in any case, when detailed work relating to basin Quaternary geology was completed (often related to soil mapping), the only obvious fault – the Waipa – was considered long inactive and seemingly no researchers had detailed any surface fault structures.

1.4.3. The Erosion Hypothesis

In their conference field trip guide, Kamp and Lowe (1981) made a brief comment that "[n]ormal faults with 1 to 2 m of throw and trending N or NE are sometimes observed to displace Pleistocene strata [within the Hamilton Basin]" (p. 15) but provided no further emphasis, detail or reference. This rather specific statement does not seem to have reappeared or been repeated in any later work – perhaps their observations were subsequently considered implausible and not progressed further. Whether or not that was the case, contemporary conclusions were that the Hamilton Basin was tectonically benign and the surface hills were simply the result of erosional processes degrading essentially planar Walton Sub-Group materials (i.e. McCraw 1967; Kear & Schofield 1978; Selby & Lowe 1992).

McCraw (2011) and Selby and Lowe (1992) illustrated the apparently unquestioned erosion hypothesis particularly well in a series of diagrams which showed a Pliocene proto-Hamilton Basin being filled by ignimbritic sheets of Puketoka Formation, subsequently incised by fluvial action and infilled with re-worked Karapiro Formation. Later still, further erosion carved valleys through the younger Karapiro Formation and deposited the Hinuera Formation in their wake. Figure 1.10 reproduces the relevant portion of McCraw's cartoon in illustration of the concept. Such conclusions were logical in the absence of other evidence for alternative explanations (or non-progression of investigation towards it) but by 2015 new data was emerging that provided grounds to consider revision of this simplified tectonomorphic framework. This evidence, including paleoliquefaction, geomorphic analysis and direct exposure of fault structures, is discussed in Section 1.5.

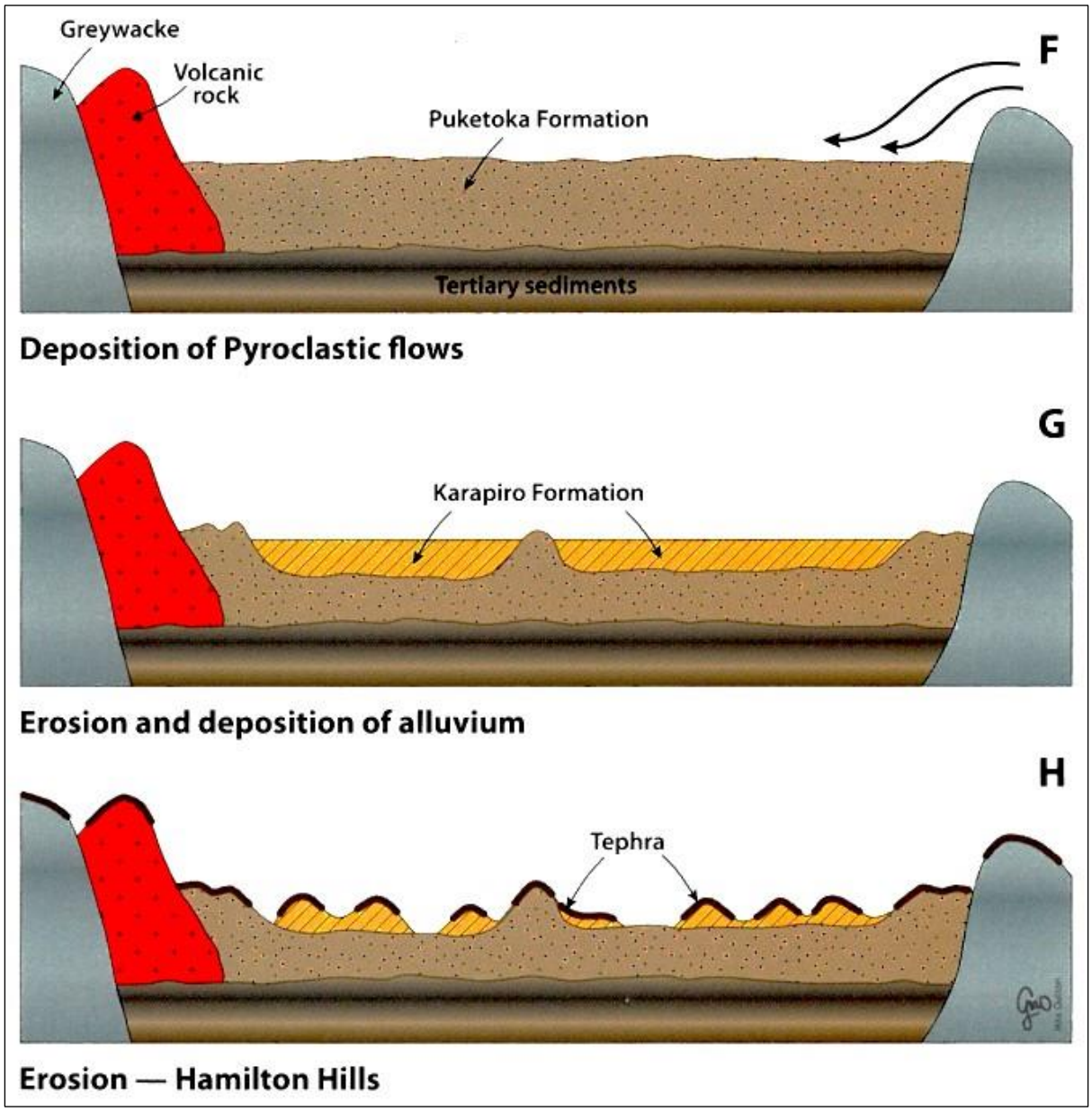

Figure 1.10. Panels F, G and H from a time series cartoon by McCraw (2011, p. 14) illustrating the popular theory of the Hamilton Hills being erosional features. The "volcanic rock" represents the Alexandra Volcanic Group to the west of the Hamilton Basin.

1.5. Revising the Hamilton Basin's Paleoseismic Framework

1.5.1. Paleoliquefaction Clues

Paleoliquefaction structures – preserved intra-stratal lobes of fine sediments remobilised and injected into surrounding strata due to a stress-induced increase in pore water pressure – had been described within the Hamilton Basin as early as the 1930s but it appears little consideration was given to their originating mechanism being seismic (Tonkin 1970). Tonkin (1970) argued that what had previously been described as concretions or differential weathering at the base of the Hamilton Ash Formation, was in fact liquefaction induced by earthquakes. However, Tonkin's hypothesis ascribed this liquefaction specifically to earthquakes associated with volcanic eruptions and did not give consideration to intra-basin fault rupture. Remarkably, shortly after Tonkin presented this research, Hume *et al.* (1975) described similar liquefaction structures within the Hinuera Formation but postulated their resulting from forces related to streambank erosion and differential loading, associated with periods of elevated groundwater conditions. As with Tonkin (1970), Hume *et al.* (1975) appears not to have considered a link between this evidence of cyclic stress with any movement of faults.

It would be a further 40 years after Tonkin's and Hume's studies before Hamilton Basin paleoliquefaction was revisited in a substantial way, when Kleyburg (2015) provided an alternative explanation, by way of facies and deformation analysis, for Hinuera Formation seismites having been emplaced as a result of earthquake shaking. By applying radiocarbon dating to organic sediments cross-cut by injection seismites, Kleyburg established a 95% probability of seismic activity having occurred, with sufficient energy to cause localised liquefaction, <19,964 ± 222 years BP. Whether such seismic activity had been generated from a local or distal source remained an unanswered question but serious consideration of the possibility for the former began to gain traction with a burst of new information coming to light shortly afterward.

1.5.2. Documented Faulting in Hills

A small (4 m wide) cutting made in 2015 for a residential development in the Hamilton suburb of Rototuna provoked interest from geologists at The University of Waikato, as apparent faulting was directly exposed for the first time (at least, for the first documented time since Kamp and Lowe's (1981) singular remark). Due to the upper layers having been mechanically removed prior to investigation, the complete structure and offset was unable to be determined but Moon and de Lange (2017) tentatively proposed normal fault movement <250,000 years BP, based on apparent offset of the Kauroa Ash Formation with fractures in-filled by younger sequences of Hamilton Ash Formation. The fault at Rototuna comprised 4 main and numerous minor strands with widely varying strike and dip orientations, forming a complex zone of deformation that precluded identification of a simple fault plane (as Campbell (2017) would also later find) (Figure 1.11).

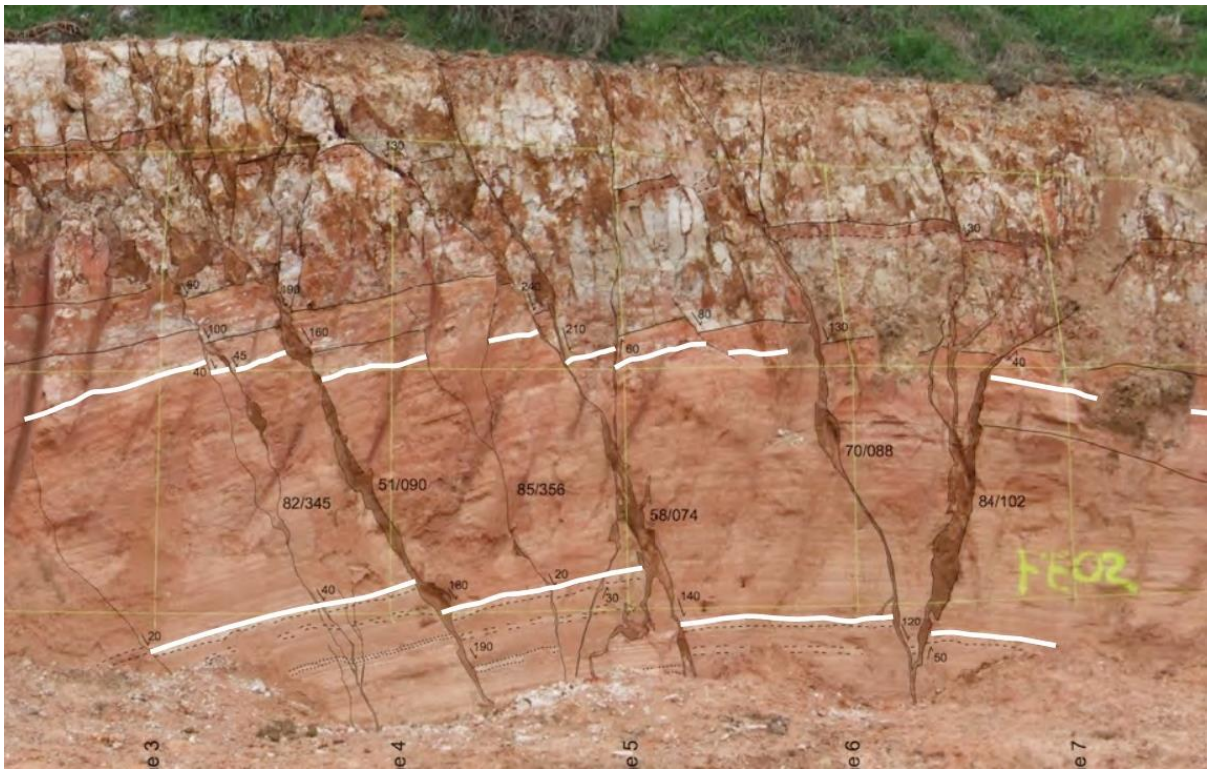

Figure 1.11. Enlarged and cropped photograph from Moon and de Lange (2017, p. 15, Figure 17) showing the central portion of the 2015 Rototuna fault exposure, illustrating the complex multi-strand nature of displacement – white lines added to emphasise offset of marker beds. Very small black text annotations are various dip/dip direction measurements.

Concurrent with both a shallow seismic survey of the Waikato River by Moon and de Lange (2017) and logging of a second fresh exposure by Campbell (2017), Spinardi (2017) undertook city-scale geomorphic analysis using a regional-scale digital elevation model (DEM). This digital analysis was combined with riverbank outcrop mapping and re-analysis of seismic reflectors from the 1970s and echo sounding scans of the Waikato River from 2006, leading Spinardi (2017) to identify 14 faults intersecting the river. The 14 faults were spread unevenly from the vicinity of Tamahere on the city's southern boundary to Pukete in the north, which Spinardi grouped into two zones of multiple strands exhibiting a general SSW-NNE trend (per Figure 1.2).

Kukutaruhe Fault Zone was posited as passing from the Ngāhinapōuri/Temple View area, southwest of the city limits, across the city's centre-north and out beyond Rototuna to the northeast. Te Tātua o Wairere Fault Zone was shown further south, with a trace from the Rukuhia/Hamilton Airport area, through south-eastern suburbs and along the Hillcrest ridge but unable to be inferred beyond Ruakura/Silverdale, as seen in Figure 1.2. Spinardi (2017) showed that, geomorphically, many of the individual fault strands within these zones coincided with lineaments of low ridges of the Hamilton Hills and abrupt, near right-angled bends in the Waikato River channel. Of the visible offset in outcrops along the riverbank, most were within cohesive and readily identifiable Walton Sub-Group materials. Spinardi (2017) did suggest there may be deformed Hinuera Formation sediments but acknowledged the difficulty in conclusively identifying this as not simply being reworked or fluvially incised deposits. In a paradigm shift regarding the accepted geological setting, Spinardi (2017) also suggested that the previously proposed Taupiri Fault was an essential structural feature to explain the geomorphology within an "[active] transtensional pull apart basin" (p. 134).

A study by Campbell (2017) marked the first investigation of major visible faulting within the Hamilton Basin, exposed in a fresh hillside road cutting at Kay Road on the northern outskirts of Hamilton City. Campbell established the presence of a complex fault zone within the Walton Sub-Group and Kauroa Ash Formation,

with clear intra-stratal deformation and offset to the top of the K-beds. Significantly, there was no deformation of the overlying Hamilton Ash Formation H1 bed, placing a limit on fault activation being >350 ka (Campbell 2017). Although this zone exhibited a complicated structure of antithetic, synthetic, and rotated blocks rather than a single fault plane, using stereonet and 3D computer model analysis Campbell (2017) concluded that this was a normal fault with a total 7.41 m downthrow to the south. Campbell also noted that a measured strike of 010° in the north-western face of the cutting aligned with one of the geomorphically inferred faults of Spinardi (2017). Given the similarity in location, stratigraphy and nature of faulting, it would be reasonable to suggest both a structural and temporal relationship to the 2015 fault at Rototuna, with Moon and de Lange's (2017) postulated age of <250 ka likely being too young.

1.5.3. Ongoing Accumulation of Evidence

A little less convincingly than with the Kay Road fault but not unimportantly, Campbell (2017) also produced some evidence for an apparent reverse fault rollover zone in the Hinuera Formation just north of the city at Osborne Road, Horsham Downs. This second zone was initially hypothesised from the existence of a linear, scarp-like slope break of 2 m that aligned with a ridgeline offsetting the Waikato River, though without including a map showing this ridge, it is a little difficult to visualise the proffered line of evidence. Geomorphic mapping, soil hand auger logs and electrical resistivity tomography (ERT) was used to identify a zone of low resistivity in the central area of the ERT array consistent with finer grained materials. Campbell (2017) surmised the change from high to low resistivity (reflected in a change from coarse to fine grained sediments) was likely to be the result of fault offset. The possibility was not discussed in Campbell's study but without conclusive intrusive investigations it could also be possible these stratigraphic changes may have been due to normal fluvial deposition variations.

Drawing upon all aspects of the 2015–2017 research, Moon and de Lange (2017) undertook a synthesis of central-basin faulting, focusing on the Hamilton city area. The inclusion of a waterborne shallow seismic survey along the length of the Waikato River from Cambridge to Taupiri led to their increasing the number of suspected fault strands from 14 to 25 and fault zones from two to four (Moon & de Lange 2017). Horotiu Fault Zone was added at the very northern edge of the Hamilton city boundary and Te Kourahi Fault Zone across the middle of the city, midway between the Kukutaruhe and Te Tātua o Wairere Fault Zones (Figure 1.2). Notably, both of the newer hypothesised fault zones exhibited a similar SW-NE trend to the original two and, if indeed they are also normal fault systems, would support the concluding premise of Spinardi (2017).

Whilst by 2017 the presence of Pliocene faulting within the Hamilton Basin had been established, no decisive evidence had been found for faulting <350,000 years BP. During 2019 and 2020, however, major deformation was unearthed during construction activities in Hamilton city. The first of these was at a residential development off Hillcrest Road and the second at an extension of the Hamilton Ring Road, very close to the Waikato River. Separate masterate (Gibbons 2020) and doctorate (Spinardi, F., in preparation) theses detail investigations of these fault complexes but together they illustrate deformation and displacement of the Hamilton Ash Formation (Figure 1.12). At Cobham Drive in particular, this displacement has been traced to H-beds dated at *c.* 50,000 years BP, substantially bringing forward the timeframe of last known fault activity within Te Tātua o Wairere Fault Zone. Given that the collective geological understanding of the Hamilton Basin has rapidly progressed in recent years from no known surface faults to complex fault networks with activity to at least 50 ka, it is certainly reasonable to continue investigations and ascertain whether faulting continues into even younger strata – namely that forming the Hinuera Surface.

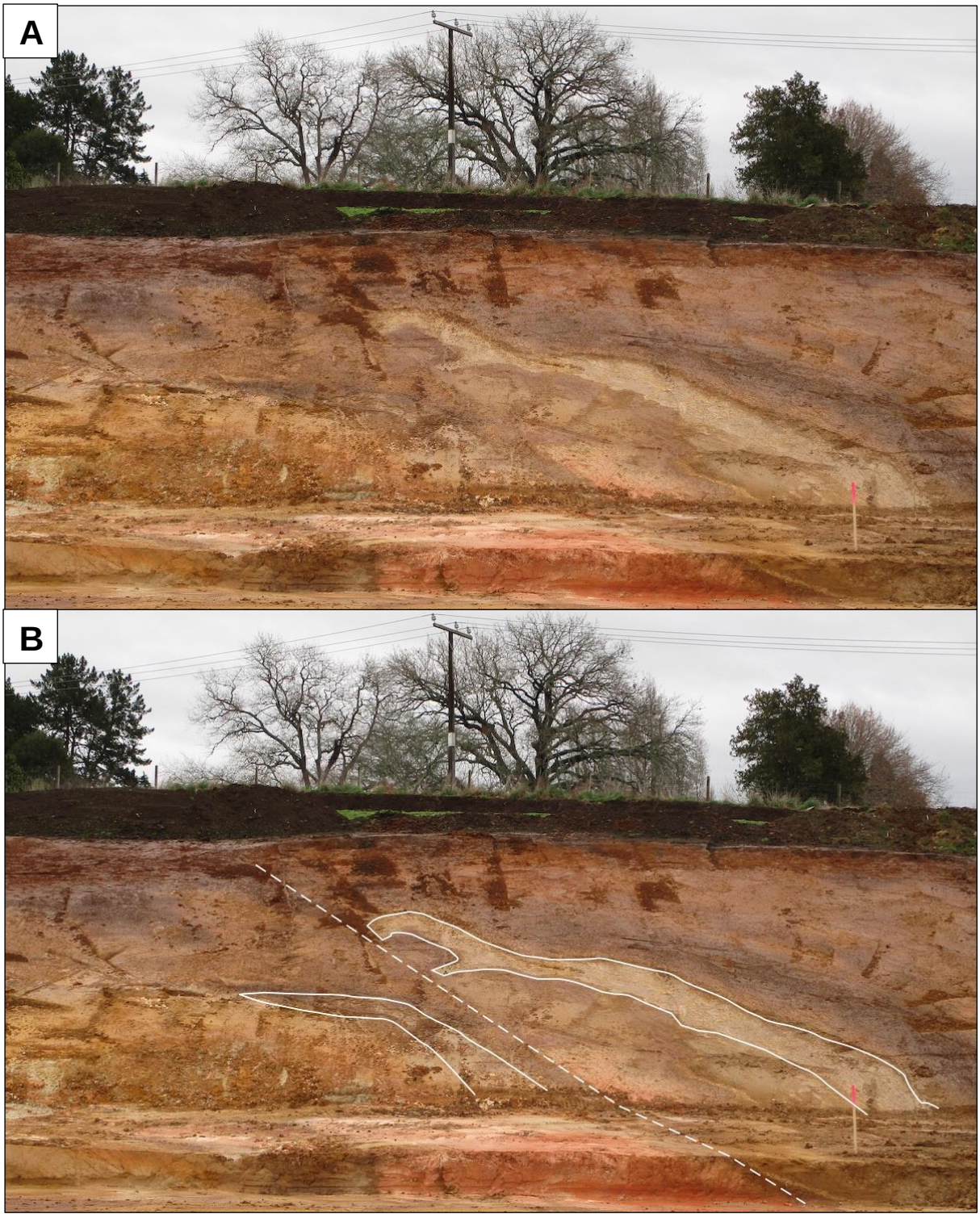

Figure 1.12. Deformation in a road cutting for the Wairere Drive extension of the Hamilton Ring Road at Cobham Drive, Hillcrest. **(A)** Photograph showing offset and disruption of prominent yellowish grey layer which is the *c*. 350 ka H1 bed/Rangitawa Tephra; **(B)** same photograph with inferred fault plane dashed and Rangitawa Tephra outlined. Offset continues through to younger H-beds dated at *c*. 50 ka, constraining last movement to ≤*c*. 50,000 years BP.

1.6. Identifying Cryptic Faults in Alluvial Basins

Whilst *cryptic* fault appears to be a term not as common in relevant literature as the (arguably) synonymous *blind* fault – meaning a fault which does not breach and leave a trace on Earth's surface – it is certainly not without precedent. Gold *et al.* (2013) used the term in reference to hidden strike-slip fault traces in alluvium and the 2020 Annual Meeting of the Seismological Society of America devoted a technical session to the subject, which broadly defined cryptic faults as fault systems incorporating any or all of; slow slip rates (<5 mm yr^{-1}), distributed fault networks, and blind faults ('SSA 2020 Annual Meeting' 2020). Given the complex and distributed nature of faulting within the Hamilton Basin, which remains hidden until physically exposed through excavation, cryptic faulting is considered an apt phrase and is adopted for this study.

It is a recognised phenomenon that faults within non-lithified sediments (cryptic or otherwise) such as those common to alluvial basins do not tend to propagate along simple fault planes in an entirely predictable manner. Scaled centrifuge and numerical modelling of alluvial soil compressive reverse faulting by Roth *et al.* (1981) showed how linear displacement can develop through deeper beds but strain may dissipate by grain displacement throughout unconsolidated upper beds, with the only resulting surface expression being a shallow monoclinal fold. Models of extensional regimes where normal faulting would be expected, such as those summarised in Burbank and Anderson (2001), demonstrate that all manner of antithetic faults (dipping in an opposite direction to the master fault), synthetic faults (dipping in the same direction), transfer zones and relay structures may develop to prevent simple linear displacement.

In reviewing literature regarding cryptic fault studies it quickly became apparent there are multiple challenges inherent to attempting tectonomorphological and paleoseismic investigations of complex fault zones in populated, alluvial basins in temperate climes. Kuebler *et al.* (2016) summarised these challenges well, describing how many relevant research methods and techniques such as geomorphic mapping, remote sensing and geophysical data analysis were developed in, are well

suited to, and regularly applied to arid (often desert) environments that are highly seismically active. Unfortunately the natural erosion, surface runoff, soil development and vegetation growth inherent to more humid regions (such as New Zealand) is likely to subdue or entirely supress physical seismogenic evidence (Kuebler *et al.* 2016). These concealing effects are exacerbated where earthquake recurrence intervals are long and/or seismic slip rates are low and, as Kuebler *et al.* (2016) remarked, land clearance, building and infrastructure development additionally disturbs or destroys natural geomorphology.

Despite the complex challenges presented, Kuebler *et al.* (2016) successfully applied a multidisciplinary approach to identify normal faulting and complex fault zone deformation within Holocene alluvium of the Lower Rhine Graben, Central Europe. The Lower Rhine Graben study utilised a combination of geographic information systems, electromagnetic mapping, electrical resistivity tomography, ground penetrating radar, core logging and trench excavation. Characteristic evidence of the cryptic fault zones reported by Kuebler *et al.* (2016) included:

- Very subtle topographic profiles with some fault scarps *c.* 0.3 m in height that only became obvious with a x 10 vertical exaggeration;
- Electromagnetic conductivity zone breaks parallel to fault traces which were reflected in vegetation (pasture) colour;
- Breaks in otherwise continuous shallow high resistivity zones and "upward-directed bends" of moderate resistivity, mirrored in GPR reflectors;
- Distributed fault zones without obvious fault planes, and cumulative offset being accommodated across many small (centimetre scale) fractures;
- Sediment deformation characterised by clasts being post-depositionally rotated, offset and fractured;
- Sill-like coseismic paleoliquefaction structures that may be truncated by more recent fine-grained channel fill.

Comments on the issues faced in their search for cryptic faults in a temporally and depositionally similar basin to the Hamilton Basin by Gold *et al.* (2013) reinforce those of Kuebler *et al.* (2016), particularly with regard to where faulting may incorporate strike-slip motion. In low-relief basins of poorly/unconsolidated sediments, the lack of "classic" geomorphic fault expressions such as scarps, beheaded streams, and shutter ridges means Quaternary fault traces simply cannot be inferred from visual clues in any telling way (Gold *et al.* 2013). Gold *et al.* (2013) also applied a combined methodology approach to their investigations of the Grizzly Valley fault system in California but utilised shallow seismic (*P*-wave) reflections instead of conductivity or resistivity surveys. Using a very high resolution (0.25 m) DEM and tremendous vertical exaggeration (x 75), Gold *et al.* (2013) identified very subtle topography they inferred to be "tectonic ridges". Clear breaks and offsets in the seismic reflectors could be seen at depths ≥*c.* 55 m, indicating faults that when extended to the surface correlated with the tectonic ridges, yet the signals were not apparent <*c.* 55 m (Gold *et al.* 2013). Such a relationship lends credence both to the insights provided by shallow-depth fault dissipation models and the unreliability of relying solely on geophysical observations.

1.7. Summary

Within the Hamilton Basin the oldest, basement-forming rocks originated as sediments eroded from continental Triassic rocks and transported across the Waipa Fault to be deposited in a deep marine basin during the Late Jurassic. Post-diagenesis, from Mid-Eocene, these rocks of the Manaia Hill Group underwent uplift and subaerial erosion prior to a marine transgression. Oligocene faulting then preceded a period of paleo-basin inversion, followed by major Miocene–Pliocene structural changes which saw the bounding basement ranges uplifted around the present day basin. Following an apparent cessation of major tectonism and with falling sea levels, the Hamilton Basin transitioned to a shallower marine environment with increasing terrigenous inputs during the Pliocene, evidenced by deposition of the first strata of the Tauranga Group, the Frankton Sub-Group.

As relative sea level continued to fall, the Frankton Sub-Group was superseded Early to Mid-Pleistocene by primary and fluvially re-worked volcanics of the Walton Sub-Group. Mid–Late Pleistocene sedimentary deposits are represented by the Piako Sub-Group, which in-fills paleo-valleys between Walton Sub-Group hills. Both pre- and post-Piako Sub-Group deposition, a series of distal rhyolitic and andesitic tephra ashes settled across the basin landscape. The oldest tephras are those of the Kauroa Ash Formation, separated from the succeeding Hamilton Ash Formation by *c.* 40 ka. Late Quaternary volcanism continues to sporadically but incrementally build upon the surface tephra covers.

Whilst the major Waipa Fault has long been recognised, the orientation and timing of its movement is still unclear, though it has possibly been inactive for millions of years after at least some form of strike-slip motion. Seismic surveys and drill holes for petroleum exploration in the 1960s and 1970s produced evidence for apparent faulting within the Hamilton Basin from the Oligocene into at least the earliest Pliocene and even hinted at fault control of the modern Waikato River. The results of these exploratory studies do not appear, however, to have been widely received or investigated in any detail and, in the apparent absence of any contradictory data, contemporary studies surmised that modern basin topography was purely erosional in origin.

Although a range of lithologies may be encountered within the Hamilton Basin and most are potentially faulted, only Quaternary Period formations are especially relevant to determining modern seismic activity. The Walton Sub-Group's Puketoka and Karapiro Formations form the core of the basin's hills and buried paleotopography, mantled with Kauroa and Hamilton Ash Formations which provide good marker beds. Paleoliquefaction features of the Hamilton Ash Formation were identified as far back as the 1930s but, even following a revised interpretation of their origins in the 1970s – alongside contemporaneous discovery of seismites in the alluvial Hinuera Formation – it was not until 2015 that their significance was recognised. Offset and deformation of the ashes have recently been used as evidence that the Hamilton Hills are complex fault structures rather than erosional features

and were recently active <*c.* 50,000 years BP, while dating of Hinuera Formation paleoliquefaction provides evidence for significant earthquake shaking within the Hamilton Basin <*c.* 20,000 years BP.

Comparable international studies have established that it is possible to identify cryptic faults in Quaternary alluvial basins but only through a multidisciplinary approach. Non-intrusive geophysical data cannot be relied upon to provide the complete picture and digital models must be ground-truthed to establish their validity. No evidence has yet been recorded of faults within the loose, unconsolidated sediments of the Hinuera Surface, the basin's youngest geomorphic unit, but that is primarily because no one has previously looked.

2. Methodology

2.1. Introduction

In lieu of being able to observe direct evidence of faulting upon the Hinuera Surface, a range of methodologies were necessary in order to investigate and draw together insights from potential topographic patterns and shallow subsurface stratigraphy. An investigative process was set out by way of three key stages, progressing firstly from remote data analysis and low intensity walkover survey, to non-intrusive geophysical survey and, finally, intensive intrusive exploration. The results of each stage helped determine the location of where the next would occur, this chapter is therefore presented in three sections in the same order as each stage took place, being:

- Desktop study and field survey
- Electrical resistivity tomography
- Paleoseismic trenching

2.2. Desktop Study and Field Survey

A preliminary desktop study was undertaken to identify areas of focus for the primary field survey which although largely centred upon digital analysis also drew heavily upon analogue resources (e.g. stereopair imagery) and traditional field methodologies (e.g. field sketches). The initial broad area of interest was determined by assuming a topological relationship between faults identified at Cobham Drive and Hillcrest Road, and extending a line of strike north-north-east, along and beyond the Hillcrest ridge – a linear approximation reflecting Moon and de Lange's (2017) proposed Te Tātua o Wairere Fault Zone. Within this zone, the AgResearch and Tainui Group Holdings farms provided large, easily accessible tracts of land formed upon the Hinuera Surface, well-suited to detailed examination. To make an initial

determination of focus areas within the farm boundaries, a range of first-pass digital maps and models were assembled utilising the ArcGIS suite from Esri.

Commonly forming the basis for analyses using Geographic Information Systems (GIS), Digital Elevation Models (DEMs) provide a 'bare Earth' view of Earth's surface by smoothing out interference from the likes of trees, buildings, power lines, etc., which would otherwise obscure natural topography. High resolution DEMs also allow detailed analysis of topological relationships and inspection of very small topographic differences that would otherwise be unobservable in lower resolution datasets or imagery. First-pass GIS analyses were based on a 1 m^2/pixel DEM provided to the university c. 2017 by Waikato Regional Council.

The 2017 DEM had been assembled using the NZGD2000 ellipsoidal geodetic datum and NZTM2000 projection from point clouds collected in the early/mid-2010s by airborne Light Detection and Ranging (LiDAR) surveys (exact density of original data unknown but ≤4 pts/m^2). In mid-2020 a new high-resolution DEM was released by Hamilton City Council and Land Information New Zealand (LINZ), built from LiDAR gathering flights over Hamilton City and Ngāruawāhia in November 2019 (Hamilton City Council & LINZ 2020). Using the same spatial reference systems and 1 m^2/pixel cell-size as the 2017 dataset, the 2020 DEM incorporated point density of 13.24 pts/m^2, substantially increasing city-scale GIS modelling quality. As a consequence, some models were re-built using the 2020 DEM and comparisons between the two DEMs also provided useful visualisation of topographic changes (primarily anthropogenic) over the intervening *c.* 5 years.

ArcGIS maps and models were analysed and refined at a range of scales, extents, classifications and breaks using ArcMap and ArcScene, including; elevation, hillshade (bare and overlaid as transparencies), gravity anomalies, historic earthquake distributions and orthographic 3D visualisation. Some maps and models were also prepared using QGIS 3.10, when access to a computer with ArcGIS was problematic. For thoroughness, slope and basin (hydrological) models were also produced, however these proved unsuitable due to the extreme subtleness inherent

in the alluvial surface and were disregarded as a consequence. Similarly, a manually georeferenced overlay of aeromagnetic intensity from Meyers (2010) was examined but, being of poor quality and low resolution, was not incorporated in any further modelling. Slope profile plots were created by exporting linear X,Y coordinates from ArcMap as text files and importing to Microsoft Excel. Slope angle in degrees was then calculated using the formula (DEGREES(ATAN(SLOPE(Y:Y,X:X))), where Y = elevation and X = along-line distance.

Georeferenced JPEG aerial photographs were downloaded from the LINZ Data Service (https://data.linz.govt.nz/). Source ASCII files for gravity anomalies (free air and topographically corrected) were obtained via the GNS Online Shop (http://shop.gns.cri.nz/nzrgg/) and raw earthquake data was obtained from the GeoNet Quake Search catalogue (https://quakesearch.geonet.org.nz/) by searching for all earthquakes >M_L 2.0 within the Waikato region. Earthquake catalogues were exported as CSV files and imported as XY data to ArcMap. Earthquake depth contours were interpolated from the XY data using kriging and natural neighbour methods within the Spatial Analyst Tools toolbox. All non-original digital source data was used in accordance with Creative Commons 4.0 International (CC BY 4.0).

A Sokkisha MS27 stereoscope was used with black and white stereopair photographs downloaded and printed from the Retrolens Historical Image Resource (http://retrolens.nz/) to supplement and, in a number of cases, validate, digital data. In particular, these historic stereopairs were necessary to determine whether apparent lineaments in the modern DEMs were anthropogenic modifications such as relict ditches or swamp drains and to identify features now partially obscured or buried by construction activity. The MapsPast project (http://www.mapspast.org.nz/) was also used as a historic reference in determining areas of peat bog and lake drainage, particularly via the early to mid-twentieth century NZMS13, NSMZ15 and NZMS1 map series. Numerous borehole, test pit, hand auger and CPT logs from a variety of construction projects logged in the New Zealand Geotechnical Database (https://www.nzgd.org.nz/) were also reviewed, as well as graphic long-sections for the under-construction Waikato Expressway, provided by the CityEdge Alliance.

Following identification of target areas via the desktop study, permission was obtained from relevant land holders to undertake field reconnaissance on foot. Initial walkover surveys were undertaken with the objective of ground-truthing apparent topographic features seen in DEMs, such as paleochannels and embankments, and to identify other micro-topography that may not be visible in digital format. Relevant notes and sketches were recorded by hand, with photographs taken on a 20MP Canon IXUS 185 digital camera and some initial coarse GPS points obtained using a handheld Garmin eTrex 10. Observations taken from elevated points a little after sunrise were necessary, when the sun was low to the east and cast long shadows, to identify extremely subtle features that would otherwise go unnoticed. Upon completion of the field survey, observations were used to refine the digital models and identify areas of particular interest for geophysical examination using electrical resistivity tomography.

2.3. Electrical Resistivity Tomography

Electrical resistivity tomography (ERT) is a popular method for geophysical analysis of soils and subsurface geology. In comparison with techniques such as boreholes or exploration wells, ERT is valued for its non-destructive, relatively non-intrusive nature, and variety of deployment variations capable of offering subsurface insight from depths of a few metres to hundreds of kilometres (Storz *et al.* 2000; Samouëlian *et al.* 2005). A typical ERT survey – and that used in this study – utilises dual-paired electrodes in a dipole-dipole arrangement to measure the apparent potential differences in resistivity to an induced electrical current in the soil space between them (Storz *et al.* 2000; Hartvich & Valenta 2013). Variation in inter-electrode spacing dictates both the depth and resolution of imaging by ERT; shorter spacing (i.e. a few metres or less) can usefully resolve features tens of centimetres in size at shallow depth (≤*c.* 5 m), while spacing 500 m spacing may yield deep profiles in the order of several kilometres but only resolve features measuring in the tens of metres (Storz *et al.* 2000; Hartvich & Valenta 2013).

The dipole-dipole ERT array functions as a stepped, progressive system whereby in the first instance the current electrodes (B and A) occupy the first two physical positions in the array while the potential electrodes (M and N) occupy positions 3 and 4 (Samouëlian *et al.* 2005; Advanced Geosciences 2017). After the measuring instrument has recorded the apparent resistivity at the mid-point between the two electrode pairs, the system maintains the locations of electrodes B and A but allocates the potential electrodes one position along (i.e. M moves to position 4 and N to position 5). Another measurement is taken and the process is repeated until the distance between the pairs is such that the current is too weak to be received by electrodes M and N; at this point electrodes B and A are stepped along one position in the array and the complete process is repeated (Advanced Geosciences 2017). Figure 2.1 illustrates electrode position progression.

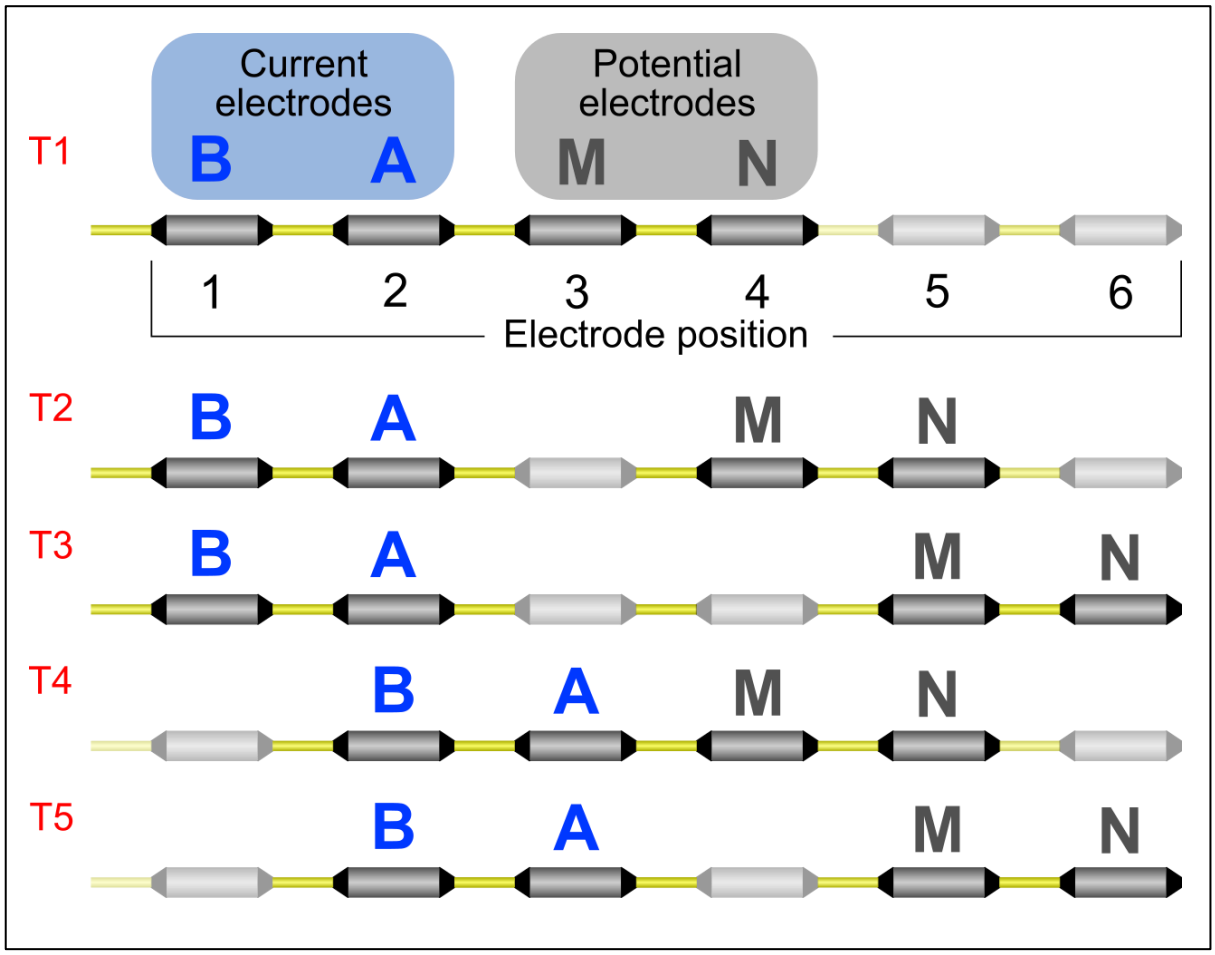

Figure 2.1. Schematic of dipole-dipole current (B, A) and potential (M, N) electrode pair progression in a simplified six electrode ERT array over five time stages. Partly adapted from Advanced Geosciences (2017).

Target sites (Figure 2.2) for ERT arrays were selected based on desktop analysis and field survey results, where these highlighted apparent geomorphic offset or abnormalities such as paleochannel constriction and/or meander barriers - excepting array RUA09, which required the absence of any such features in order to provide a reference profile. Carried out using the university's Advanced Geosciences, Inc. SuperSting™ R8 ER/IP/SP meter with a 28 electrode switch box, each array comprised 28 electrodes in a dipole-dipole with gradient array and all meter settings were unmodified from factory default (Figure 2.3). Where possible, electric fences adjoining the survey area were disconnected to minimise potential interference. Once set up, a measurement cycle for a full array of 28 electrodes took approximately 22 minutes.

Arrays RUA01–RUA04 were conducted using 5 m electrode spacing with 25% roll-along, giving an initial line length of 135 m and a total array of 170 m. Spacing of 10 m between each of these arrays was used as they were intended for quasi-3D modelling; these were also the only surveys conducted using the roll-along technique. RUA05–RUA07 and RUA09–RUA10 also utilised 5 m electrode spacing, for an array of 135 m, whereas RUA08 was a shallow, high resolution re-survey over a portion of RUA04, with 1 m electrode spacing for a 27 m array length. TGH01 was a deeper semi-'wildcat' survey with 8 m electrode spacing for an array of 216 m. Electrode spacing for RUA11–RUA14 was 3 m, giving 81 m array lengths. The geospatial position of each electrode in each array was logged to decimetre accuracy using a Leica GNSS GS16 RTK Rover to incorporate topographic profiles in interpreted plots.

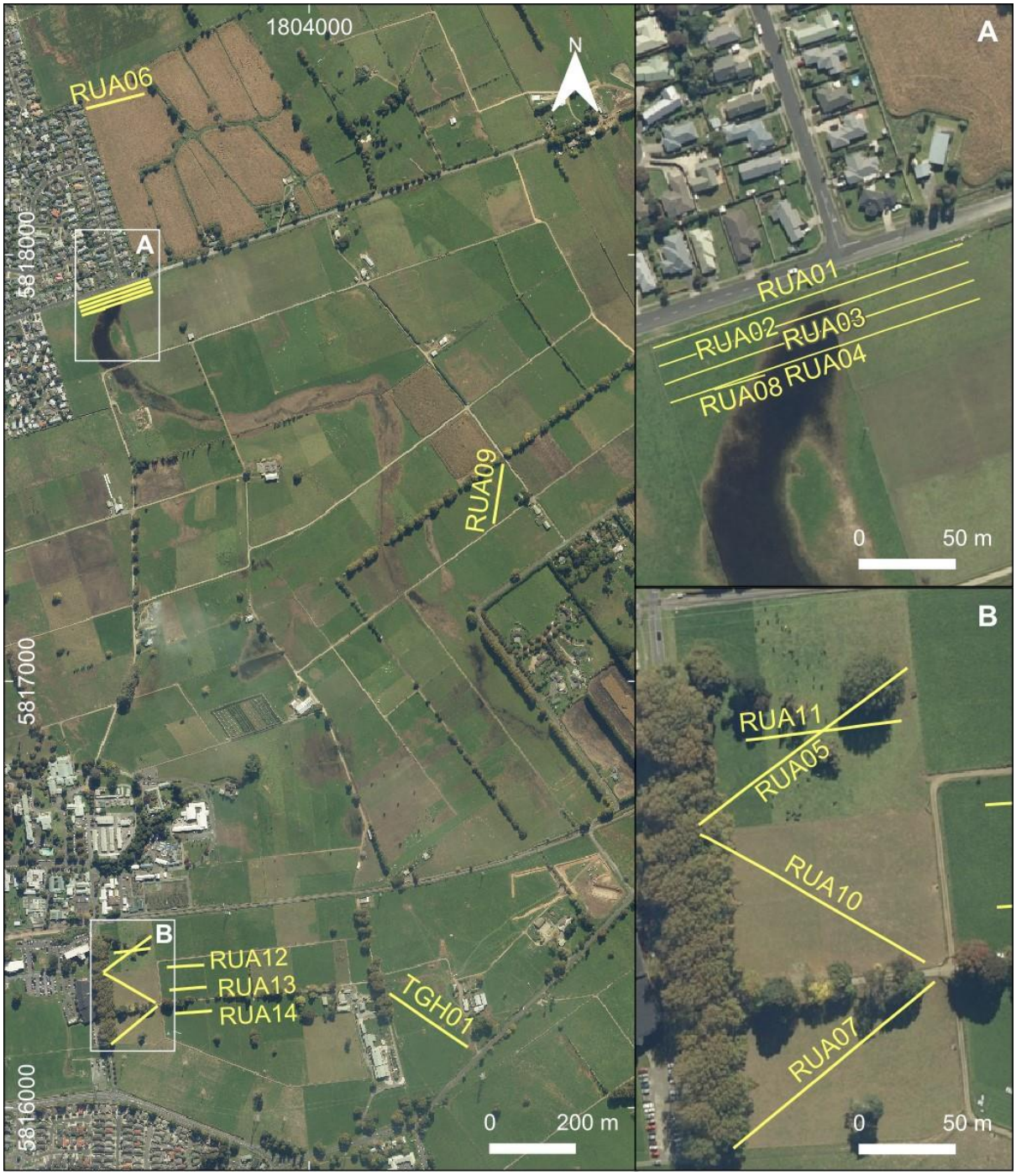

Figure 2.2. Map of electrical resistivity tomography array placements across the AgResearch Ruakura farm (labelled RUAXX) and Tainui Group Holdings Ruakura farm (TGHXX). Insets A and B provide detail where arrays were very closely spaced. Waikato 0.3m Rural Aerial Photos (2016-2019) sourced from the LINZ Data Service and licenced for reuse under CC BY 4.0.

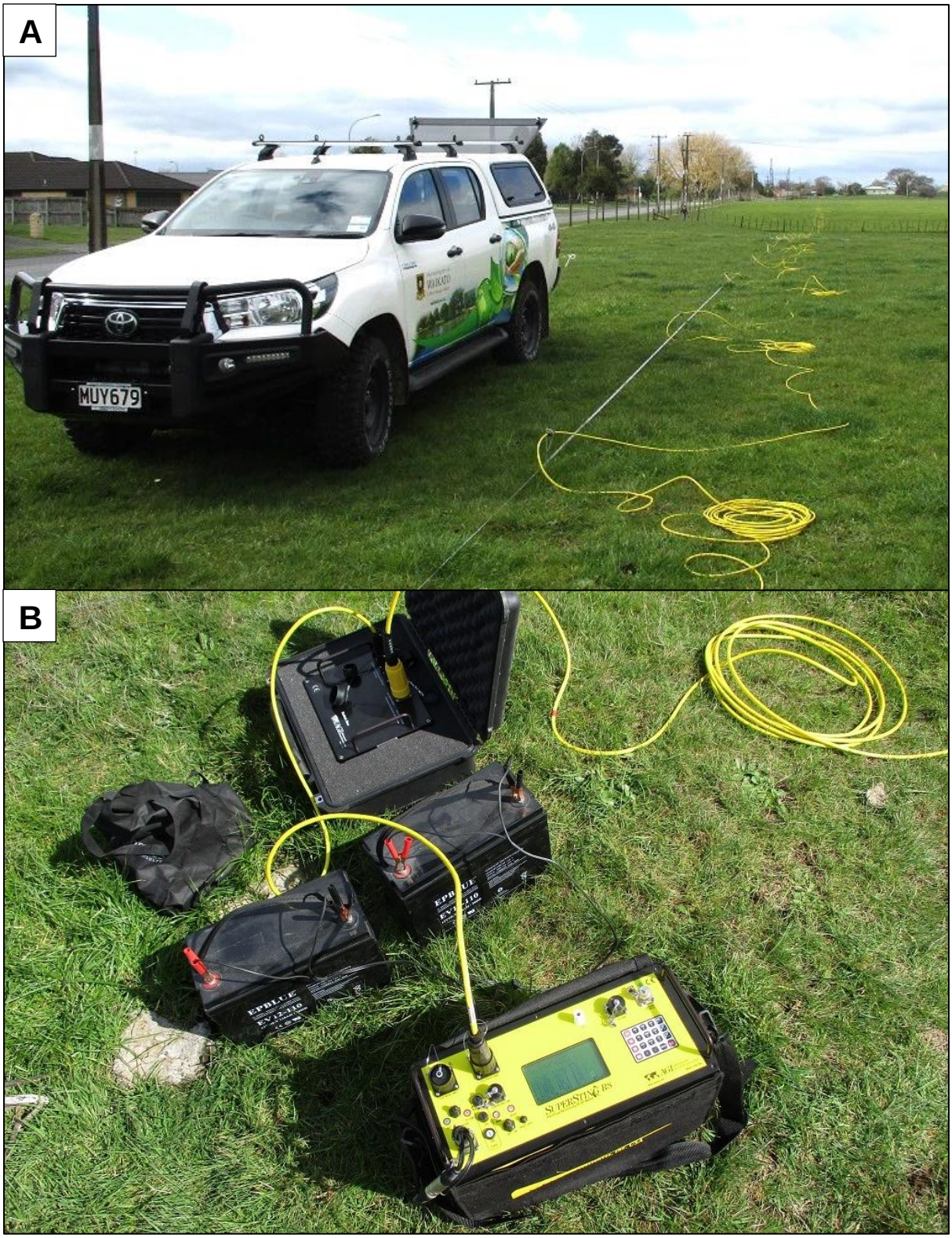

Figure 2.3. Setting up ERT array RUA02. **(A)** Electrodes spaced at 5 m, with current being supplied by the yellow cable to the right of each electrode (excess cable coiled). The straight white line to the right of the vehicle is a tape measure used for electrode peg placement. **(B)** AGI SuperSting R8 ER/IP/SP meter (yellow box, bottom centre) with battery power supply (middle) and switch box (top).

As raw ERT measurements are quantitative, simply measuring a theoretical difference in resistance through the material body, post-survey data inversion must be undertaken in order to provide qualitative values of "true" resistivity in ohm-metres (Storz *et al.* 2000; Caputo *et al.* 2007; Advanced Geosciences 2017). Proprietary post-collection data processing software utilises iterative, non-linear, least squares numerical modelling to minimise the difference between the model-calculated and in situ apparent resistivity values. As part of this process, the programme also derives a root-mean-square (RMS) error, providing an indication as to how reliable the final iteration may be considered (Caputo *et al.* 2007). Post-survey pseudo-section inversion for all arrays was conducted using AGI EarthImager™ 2D and aimed to achieve a ≤5% RMS (i.e. ≥95% fit between apparent and true resistivity). AGI EarthImager™ 3D was used for quasi-3D modelling.

To complement resistivity results, a total of 19 hand augers were undertaken in the vicinity of, or directly along, arrays RUA01-RUA05 and RUA11 to investigate general shallow structure and compare with the inversion profiles (Figure 2.4). A 50 mm Dutch-type clay/sand auger head was used and auger log descriptions were recorded according to standard New Zealand Geotechnical Society guidelines. As the purpose of auger logging was for general stratigraphic correlation rather than geotechnical classification, penetrometer tests were not undertaken and shear vane tests were only completed in augers HA04–08, HA10, HA12–17, and HA19.

Figure 2.4. Locations of hand augers (green diamonds) in relation to ERT arrays (yellow lines). See Figure 2.2 for spatial relationship between areas **(A)** and **(B)**. Waikato 0.3m Rural Aerial Photos (2016-2019) sourced from the LINZ Data Service and licenced for reuse under CC BY 4.0.

2.4. Paleoseismic Trenching

Selection of a site for excavating a paleoseismic trench was based upon consideration of all aspects of the desktop study, field survey, ERT results, site access, hazard management and land holder considerations. A suitable paddock was selected on the AgResearch Ruakura Research Farm that was perpendicular to the hypothesised strike of the fault and where ERT profiles produced anomalies considered consistent with those reported in similar studies (e.g. Hartvich & Valenta 2013; Seminsky *et al.* 2016). It was initially planned to undertake additional geophysical survey (ground penetrating radar) before committing to excavation, however, this became unavailable in the very last stages of planning and as plans were so advanced a decision was taken to proceed anyway. As the site was known to have previously had shallow-piled timber buildings erected on it, Retrolens images which clearly showed the structures were manually georeferenced in ArcMap and the trench orientation planned so as to be between the old footings as much as practicable. Prior to excavation, regional council advice was sought and determined that no resource consent or permits were necessary.

Comprehensive efforts were taken to eliminate risk of service strike, with *BeforeUDig* utilities plans and the farm services map being sourced, and a qualified commercial subsurface utility locator being engaged. Appendix B shows utilities mapped in the immediate vicinity of the trench site. No areas of concern were located within the trench area, however, the utility locator identified some shallow (*c.* 300 mm deep) non-conductive features which were subsequently exposed as abandoned clay drain pipes, galvanised steel water pipes and a wire cable – presumably once connected to the removed buildings. Advice was sought from several contractors familiar with trenching best practice and reference was made to Worksafe New Zealand's *Excavation Safety Guidelines*, which determined the trench profile as shown in Figure 2.5.

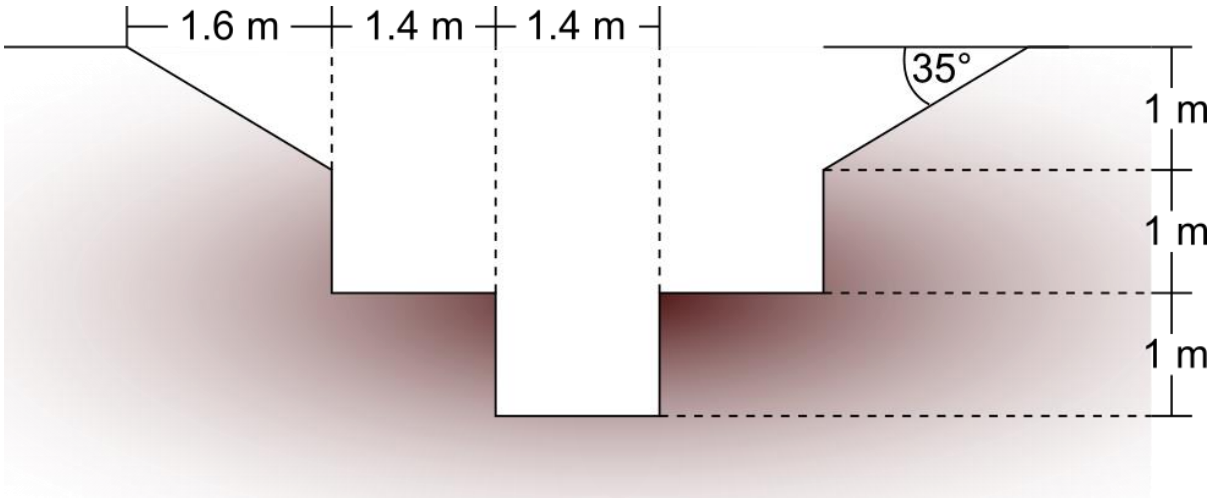

Figure 2.5. Schematic cross-section of the trench profile with key measurements (not to scale).

To comply with health and safety regulations and avoid the necessity of shoring, the trench was battered and benched, with a batter angle of 35° and no vertical wall having a depth >1 m. Depth from trench top to batter edge was 1 m, batter edge to bench 1 m, and bench to trench bottom 1 m, giving a total depth along the central aisle of 3 m. Following topsoil stripping, the excavator operator completed edge-to-edge profiles in approximately 6 m long sections starting from the eastern end, so as to avoid disturbing or damaging stratigraphy by repeat passes. Excavation commenced and was completed on 11 January 2021, with the trench being open for 11 days prior to back-filling on 22 January 2021. Final trench length was 32.8 m and width 7.4 m, with an effective logging length along the north wall of 29.6 m discounting access ramp cuts (Figure 2.6).

Figure 2.6. Photographs of trench excavation showing; **(A)** first section being excavated, illustrating the method of cutting a complete profile in increments rather than progressively deepening the complete trench length; **(B)** view along the completed trench towards the east, showing the full as-cut profile. The north wall to the left of image was comprehensively logged while the south wall was considered less suitable due to the level of human disturbance.

Once excavation was complete, cut edges were cleaned using hand tools such as Niwashi and spades, before fifty-seven *c.* 50 mm numbered plastic discs were pinned along the trench top, base, and at irregular heights across the walls to function as photogrammetry control points (Figure 2.7). A 1 m high x 2 m wide grid was strung across the main portion of the north wall using polypropylene twine, with a 0.5 m x 0.5 m grid across a zone of particular interest slightly east of centre. To mark key bed contacts, small flags of various colours were made using nails punched through doubled-over electrical tape (Figure 2.7). Key point locations were recorded using a Leica GNSS GS16 RTK Rover while trench surface point clouds were gathered via a Trimble VX Total Station with TSC3 Data Collector, and modelled using both ArcScene and Leapfrog Geo. Photographs were taken with a Nikon D5600 24.2 megapixel Digital SLR camera and Hasselblad L1D-20C 20 megapixel digital aerial camera mounted on a DJI Mavic 2 Pro drone, while sketches of varying scale and stratigraphic columns at intervals were drawn by hand. Photo mosaics were assembled in Inkscape 1.0.2 and the same software was used to digitise key sketches.

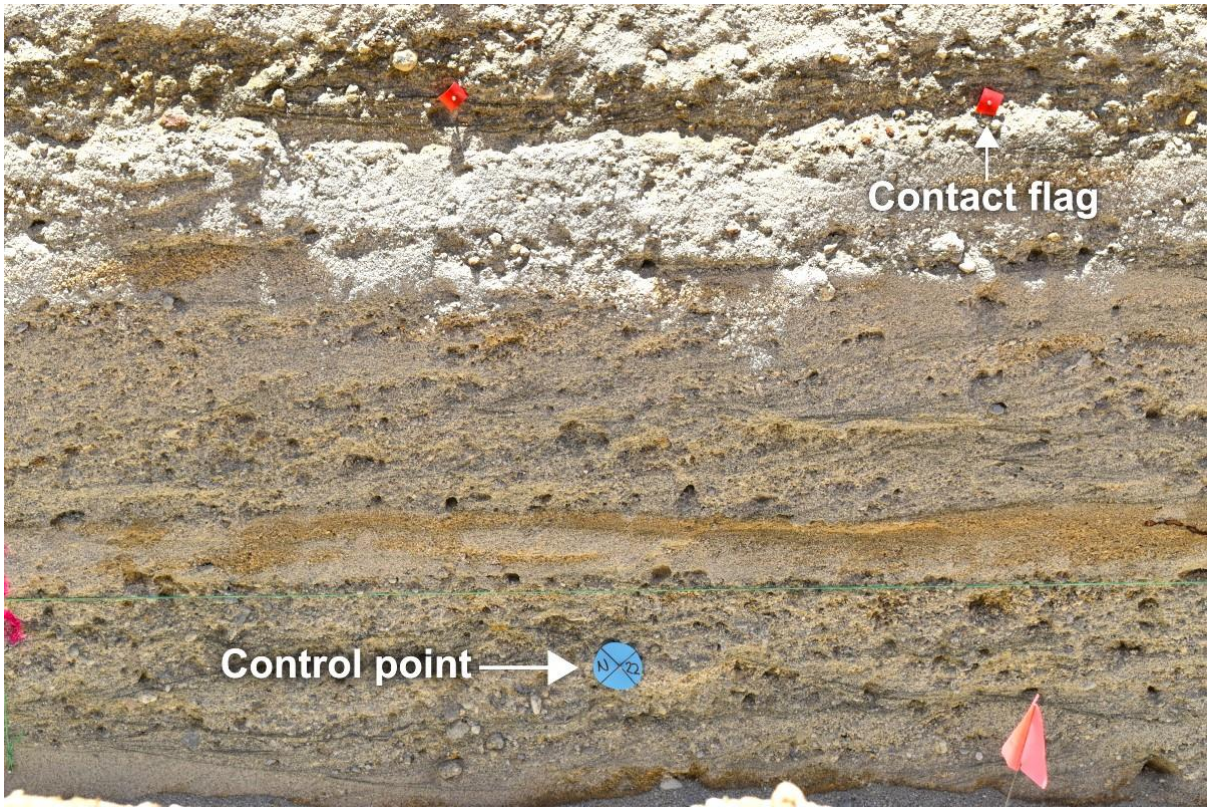

Figure 2.7. Example of bed contact flags and photogrammetry control point on the trench north wall.

2.5. Summary

A desktop study was completed by way of GIS modelling and reviewing geotechnical investigation logs, stereopair images, aerial photographs and historic maps. The results of the desktop study defined an initial broad area of interest for site walkover and field survey. Subsequent field surveying produced a range of observations, sketches and notes that not only helped refine digital modelling but also identified target locations for more intensive investigation. ERT surveys were then completed in the target areas to produce 2D pseudo-sections of subsurface resistivity to identify potential anomalies; a number of hand auger logs were completed to attempt correlations between these anomalies and shallow subsurface stratigraphy. Additional geophysical survey using ground penetrating radar was planned to follow ERT but became unattainable at a late stage. Final investigation consisted of excavating a *c.* 33 m long x 3 m deep x 7.5 m wide paleoseismic trench investigation, which was digitally surveyed and manually stratigraphically logged.

3. Geomorphology of the Hinuera Surface in northern Te Tātua o Wairere Fault Zone

3.1. Introduction

The first research stages comprised remote and non-intrusive investigations, exploring potential relationships between fault zone and regional geomorphology, wider basin geophysical patterns, and high resolution mapping within northern Te Tātua o Wairere Fault Zone. Chapter 3 thus presents models and maps produced from desktop analyses, including interrogation of gravity anomaly, earthquake focus and LiDAR datasets by way of GIS, supported by observations from field survey and reference to historic imagery (including stereopairs).

3.2. GIS Models

3.2.1. 3D Models and Surface Profiles

Three-dimensional modelling of almost the entire Hamilton Basin was possible using the 2017 DEM (the dataset not extending completely to the basin's southern limits) but extremely high vertical exaggeration (60x) was required to identify pertinent features. Figures 3.1–3.4 show that the basin comprises two distinct geomorphic profiles; predominantly hills and ridgelines in the west, interspersed with small plains of negligible to nil slope, and mostly open plains of exceedingly low slope in the east, with no ridgelines and rare low hills. Te Tātua o Wairere Fault Zone straddles the boundary between these two areas. To aid visualisation in the following models, the fault zone has been extended by geomorphic inference to include the line of hills extending southward toward Te Awamutu.

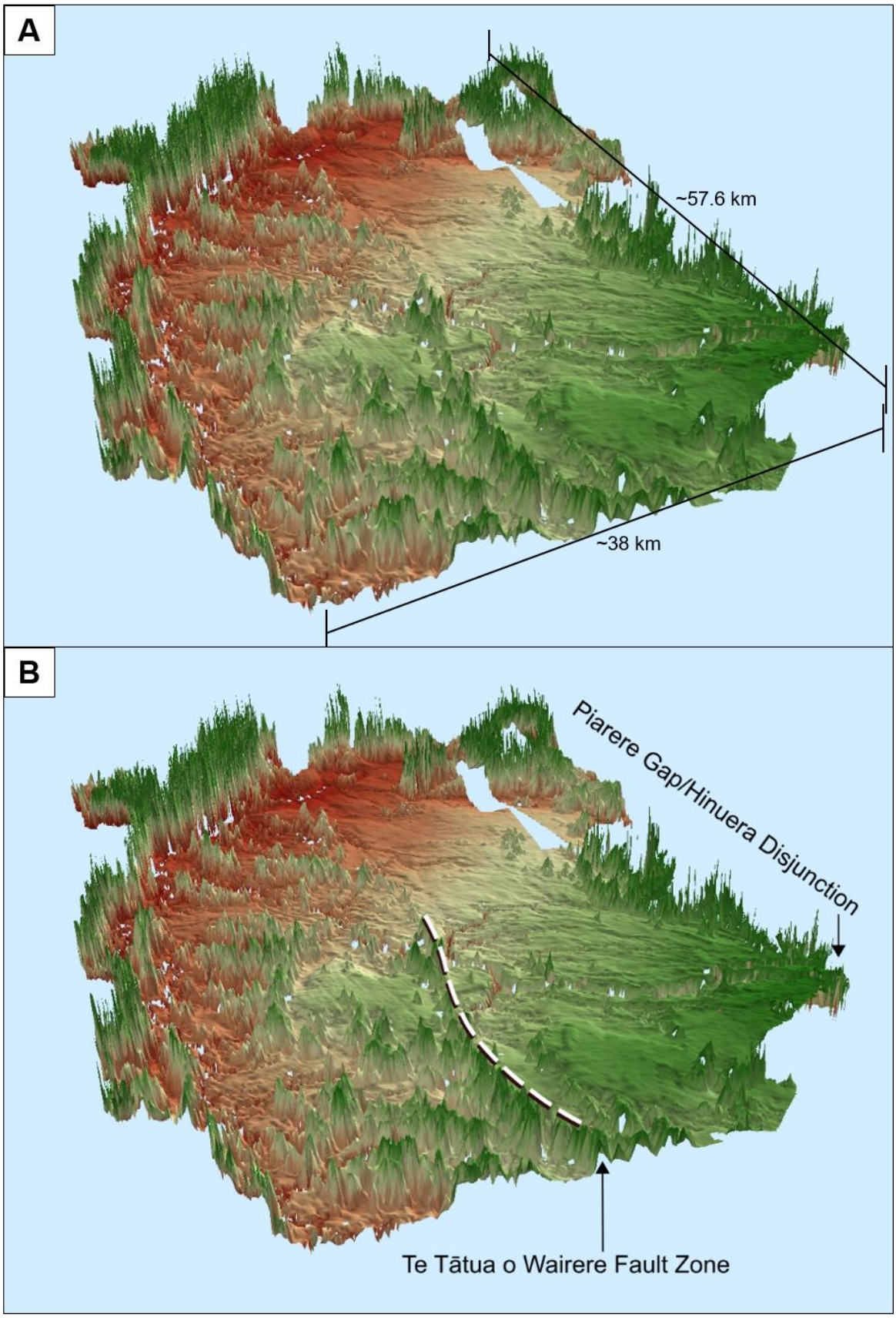

Figure 3.1. High angle oblique view SW–NE across the Hamilton Basin 3D model with green (high) to red (low) stretched colour ramp showing relative elevation. VE=60x. **(A)** Model with approximate scale; **(B)** model with Te Tātua o Wairere Fault Zone and Piarere Gap/Hinuera Disjunction annotated.

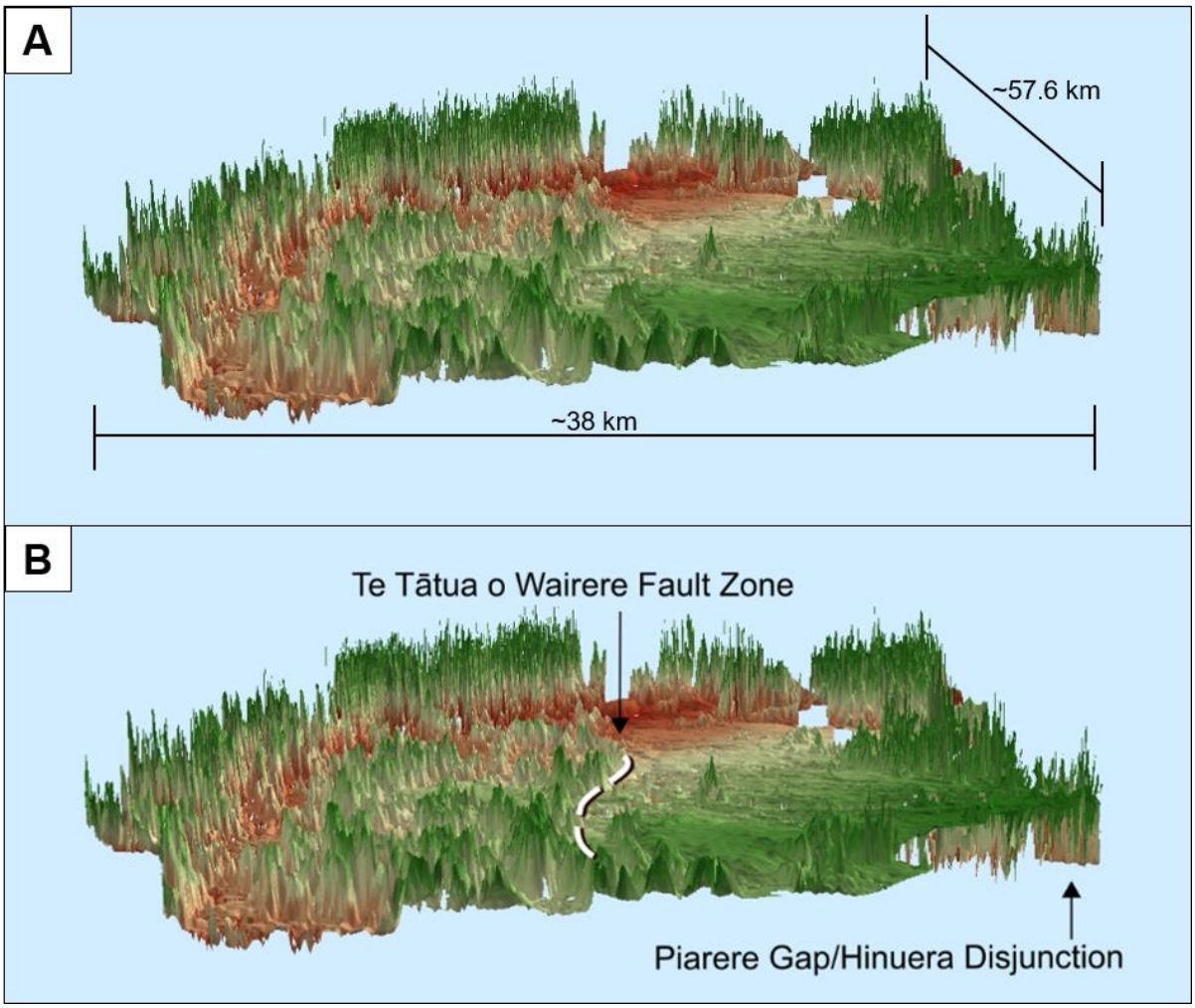

Figure 3.2. Low angle oblique view SSW–NNE across the Hamilton Basin 3D model with green (high) to red (low) stretched colour ramp showing relative elevation. VE=60x **(A)** Model with approximate scale; **(B)** model with Te Tātua o Wairere Fault Zone and Piarere Gap/Hinuera Disjunction annotated.

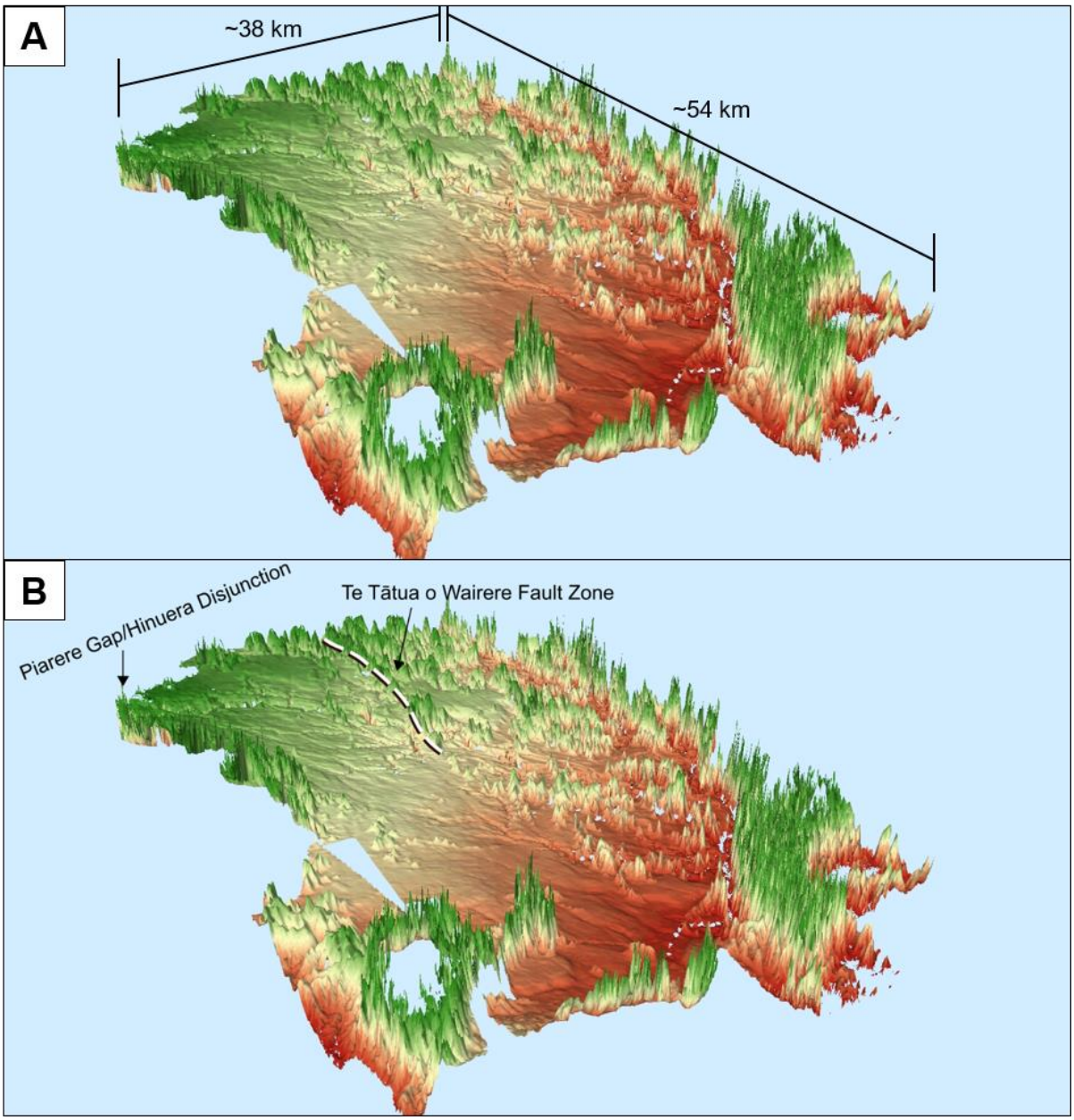

Figure 3.3. High angle oblique view NE–SW across the Hamilton Basin 3D model with green (high) to red (low) stretched colour ramp showing relative elevation. VE=60x. **(A)** Model with approximate scale; **(B)** model with Te Tātua o Wairere Fault Zone and Piarere Gap/Hinuera Disjunction annotated.

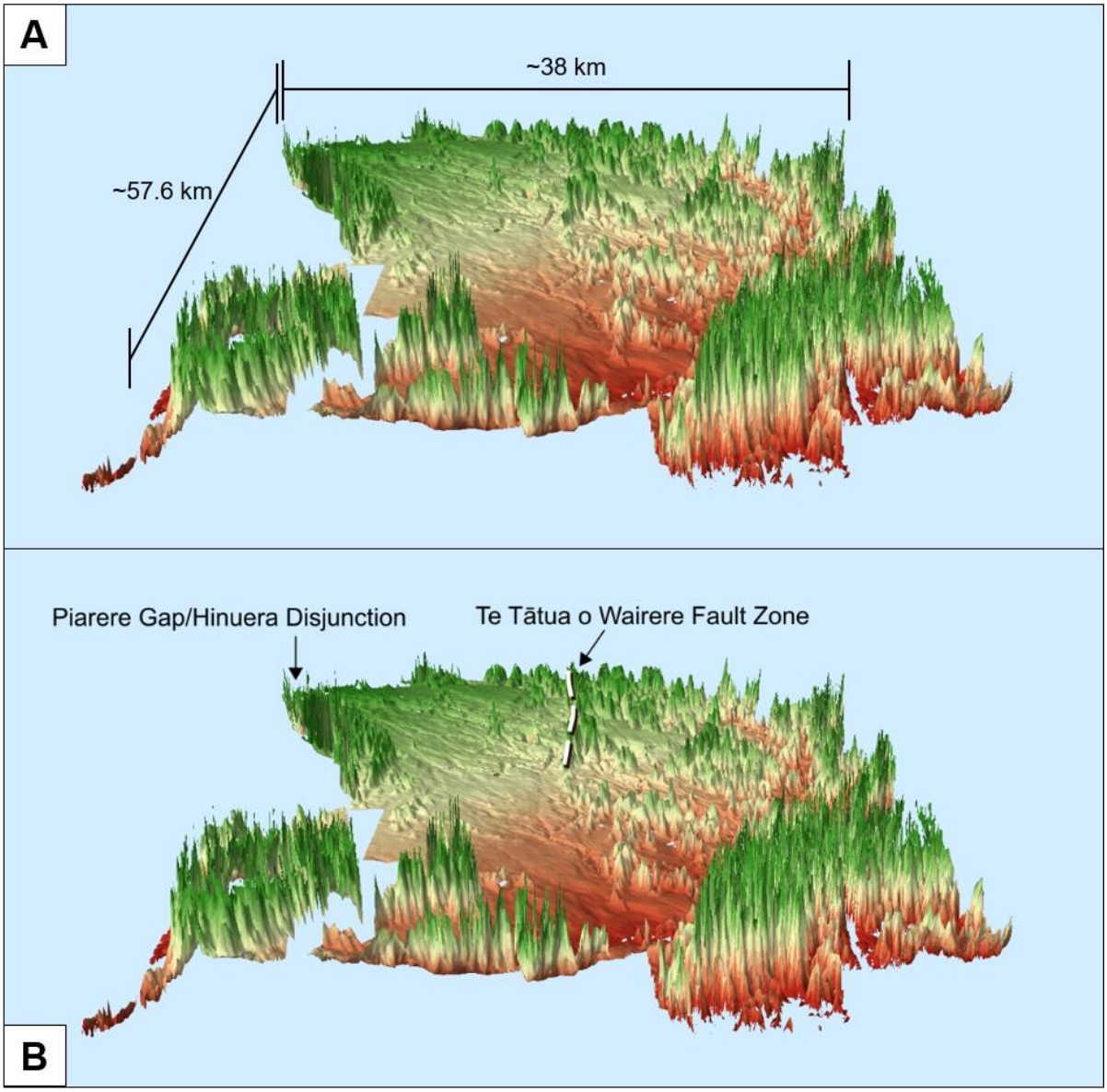

Figure 3.4. High angle oblique view N–S across the Hamilton Basin 3D model with green (high) to red (low) stretched colour ramp showing relative elevation. VE=60x. **(A)** Model with approximate scale; **(B)** model with Te Tātua o Wairere Fault Zone and Piarere Gap/Hinuera Disjunction annotated.

Profile views presented in Figures 3.5–3.6 show that the plains (Hinuera Surface) slope in all directions away from the Piarere Gap/Hinuera Disjunction but the form of this slope is not equal or even in all directions. Viewed from the north-east (Figure 3.5), the surface exhibits a convex dip away from the gap, before transitioning to a shallow concave slope *c.* 22.5 km to the north-west. The slope becomes effectively nil *c.* 35 km from the gap but the surface drops down toward the basin's north-western limit in a pair of very slight, terrace-like steps. By comparison, when viewed from the south-east (Figure 3.6), the surface appears to slope relatively evenly and uninterruptedly to the north of the gap. To the west, however, there is a convex break in the surface *c.* 18.8 km from the Piarere Gap which coincides with Te Tātua o Wairere Fault Zone (Figure 3.7). This convex break imparts a slightly greater gradient for *c.* 4 km prior to a concave break marking the point at which the surface becomes horizontal until it meets the bounding western hills.

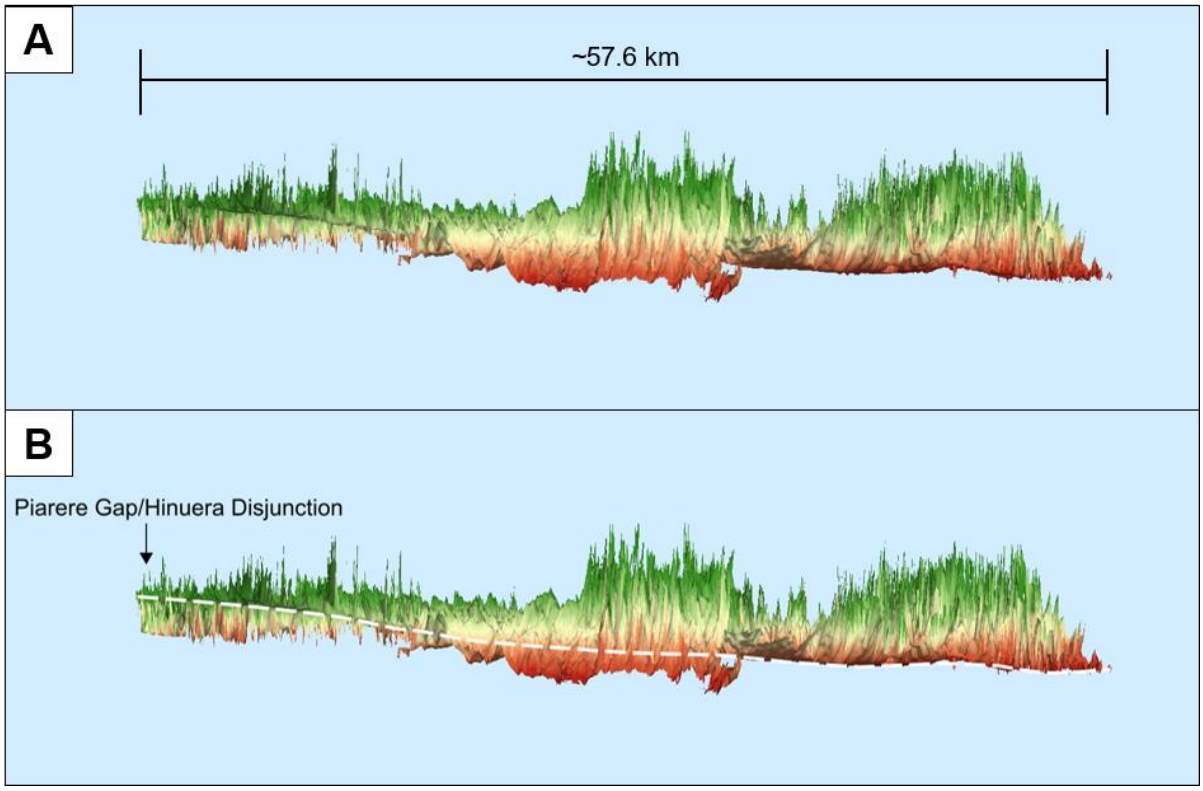

Figure 3.5. Profile of the Hamilton Basin 3D model looking NE–SW, with green (high) to red (low) stretched colour ramp showing relative elevation. VE=60x. **(A)** Model with approximate scale; **(B)** model with apparent surface of plains (dashed white line) and Piarere Gap/Hinuera Disjunction annotated.

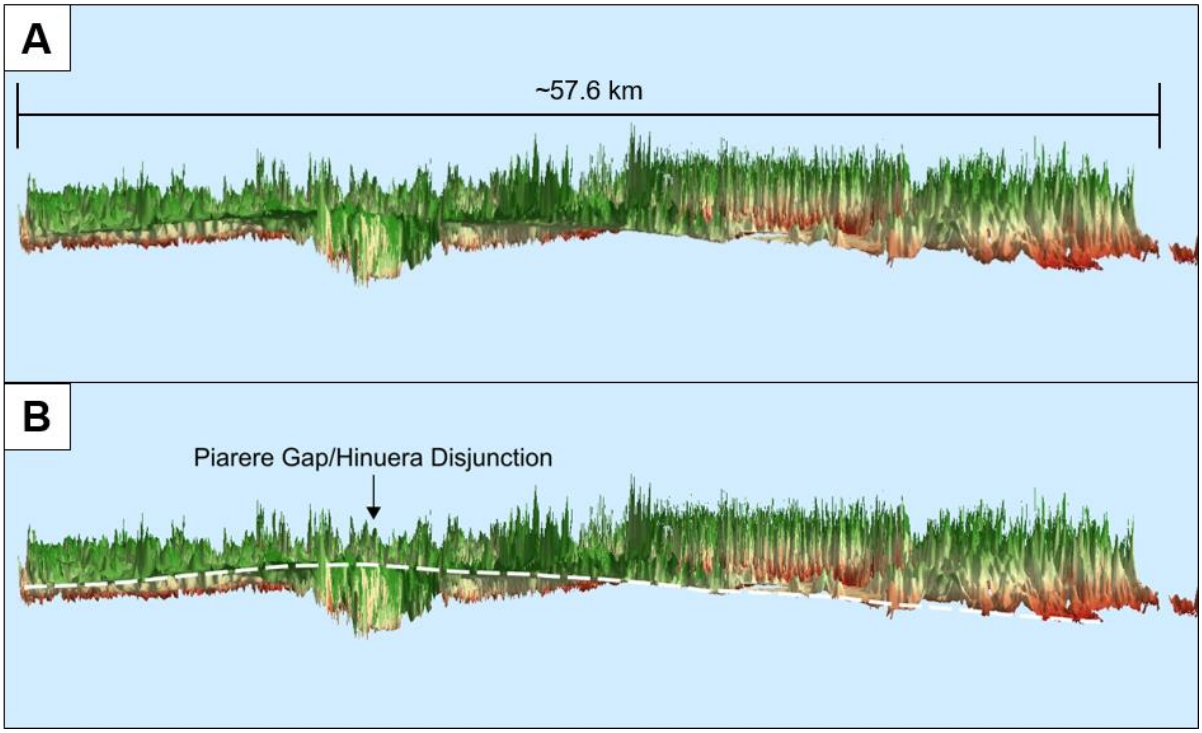

Figure 3.6. Profile of the Hamilton Basin 3D model looking NW from SE, with green (high) to red (low) stretched colour ramp showing relative elevation. VE=60x. **(A)** Model with approximate scale; **(B)** model with apparent surface of plains (dashed white line) and Piarere Gap/Hinuera Disjunction annotated.

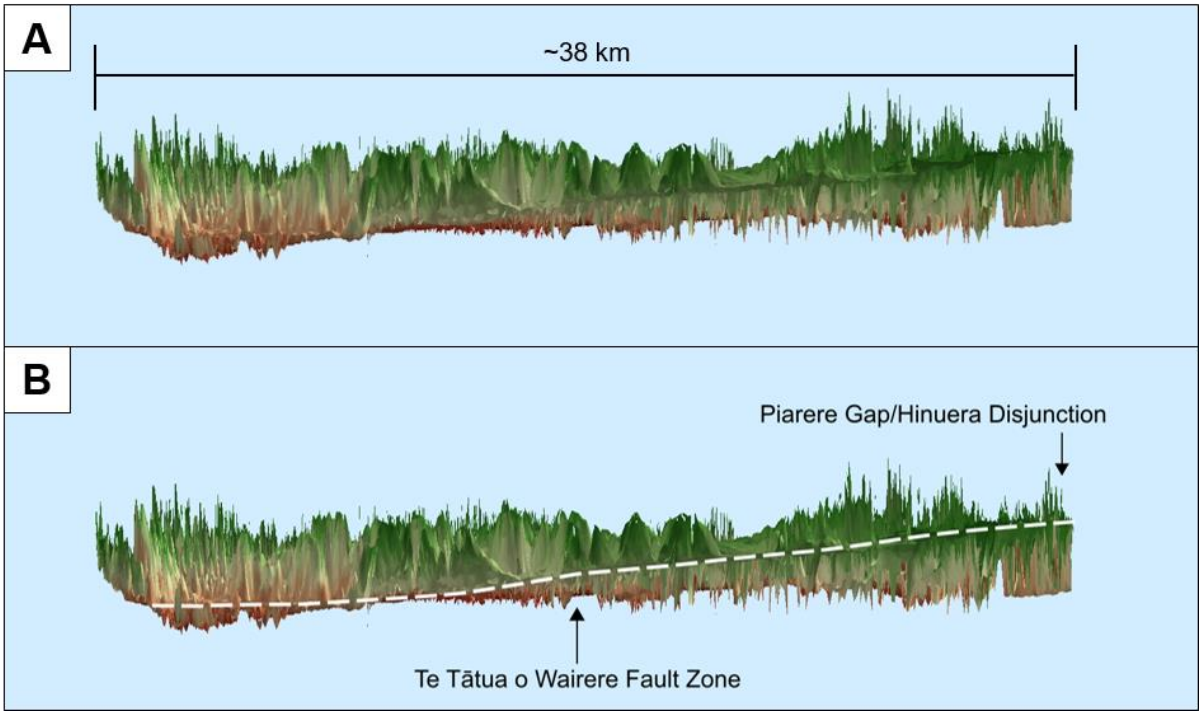

Figure 3.7. Profile of the Hamilton Basin 3D model looking N from S, with green (high) to red (low) stretched colour ramp showing relative elevation. VE=60x. **(A)** Model with approximate scale; **(B)** model with apparent surface of plains (dashed white line), Te Tātua o Wairere Fault Zone and Piarere Gap/Hinuera Disjunction annotated.

Three cross-basin slope profiles were created to visualise the general form of the basin surface with less noise than in the 3D models and to calculate general surface slope from linear trends. Orientation of the sections for each profile are given in Figure 3.8. As with the 3D models, very high vertical exaggeration was necessary (40x), as application of an equal-axis produced essentially flat plots. Slope was near-equal across the three profiles, reflected in minimal variation of slope angles (shallowest slope being 0.0644° and steepest 0.0757°). Figure 3.9 presents each of the exaggerated profiles with associated linear trendlines, calculated slope values and slope values converted to angle in degrees while Figure 3.10 gives sub-profiles of sub-sections identified in Slope Profile 1.

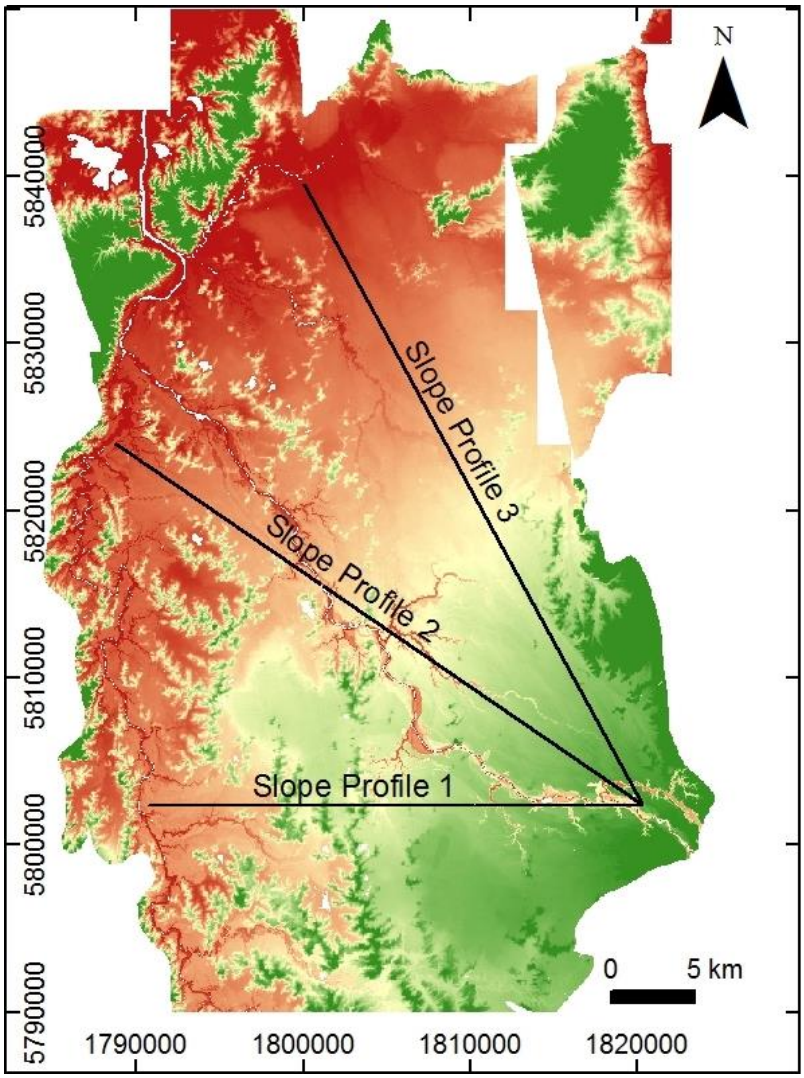

Figure 3.8. Lines of Hamilton Basin slope profiles presented in Figure 3.9, based on the 2017 DEM. Stretched colour ramp indicates relative elevation; green = high, red = low. This is the same DEM and colour ramp as used in the preceding 3D models.

Basin-scale 3D modelling and slope profile analysis confirmed that a key area of interest exists in the vicinity of Te Tātua o Wairere Fault Zone – this is where a subtle, yet notable, break in the Hinuera Surface occurs. This break in slope, from *c.* 0.08° east of the fault zone to *c.* 0.02° west of it, coincides with the change from predominantly plains in the east to hillier terrain in the west. As a result, the analyses which follow progress from modelling of basin-scale features to focusing on the Ruakura area in the northern sector of Te Tātua o Wairere Fault Zone, where the plains meet the hills – in particular, geomorphology adjoining the Hillcrest Road ridge.

This page intentionally left blank

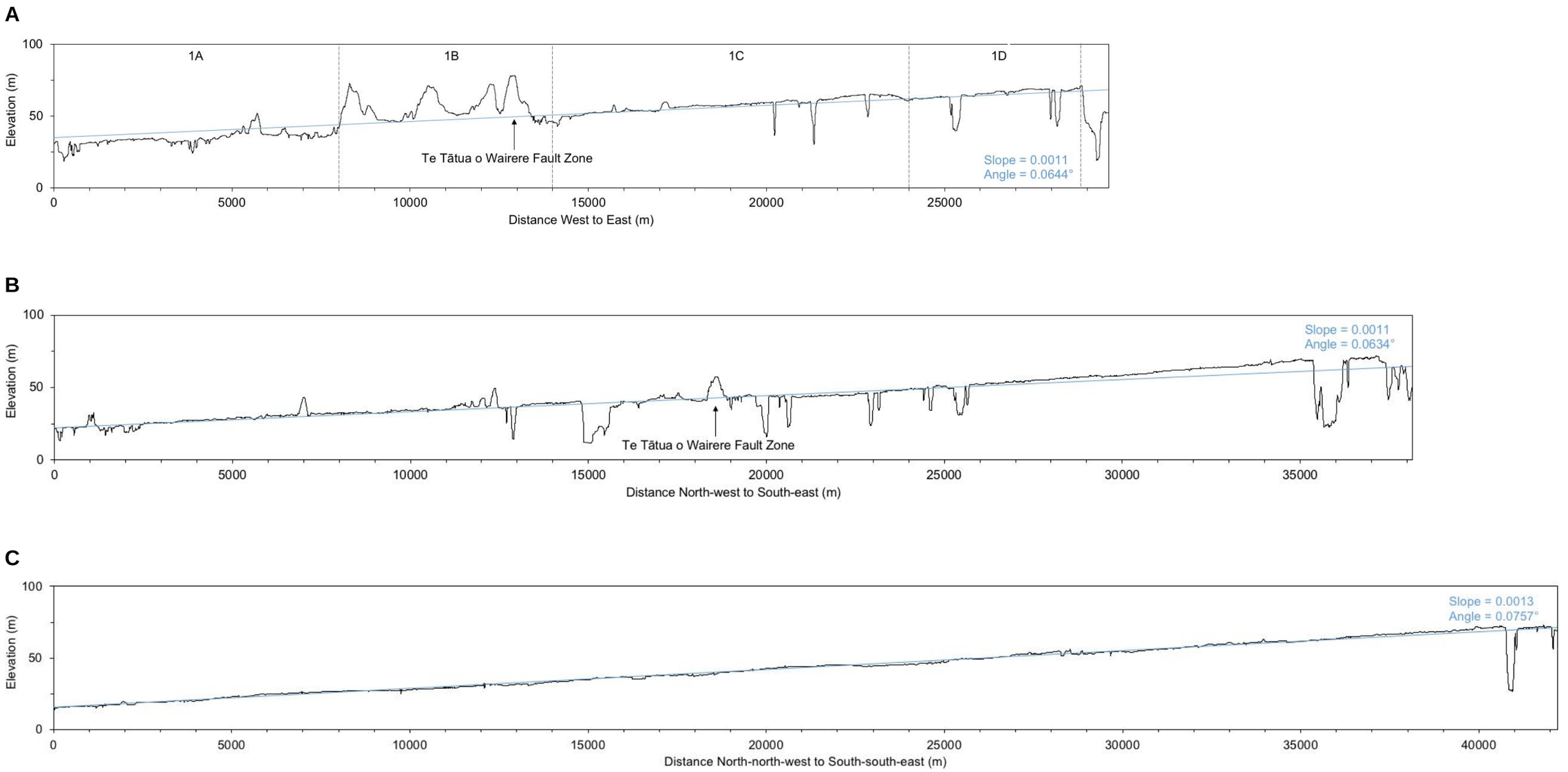

Figure 3.9. Slope Profiles 1 **(A)**, 2 **(B)**, and 3 **(C)**. All profiles plotted to the same X- and Y-scales with global VE=40x. The significant depressions at the head of each profile are the modern Waikato River channel (incorporating an arm of Lake Karapiro). Profiles 1 and 2 intersect Te Tātua o Wairere Fault Zone (annotated), with low hills breaking the planar surface on the toe sides of the fault zone whereas no hills occur in Profile 3. Profile 1 displays the greatest apparent deviation from a linear trendline and can be segmented into four major corresponding sub-profiles. In sub-profile 1A, between 0 m and 8,000 m, the surface is approximately parallel to but below the trendline while 1B, from 8,000 m to 14,000 m, includes the central-basin hills and thus rises above the trendline. Sub-profiles 1C and 1D appear to have a slight steepening of slope headward but are separated by an apparent stepping down of 1D at 24,000 m. All four sub-sections identified in Profile 1 are shown with reduced VE in Figure 3.10.

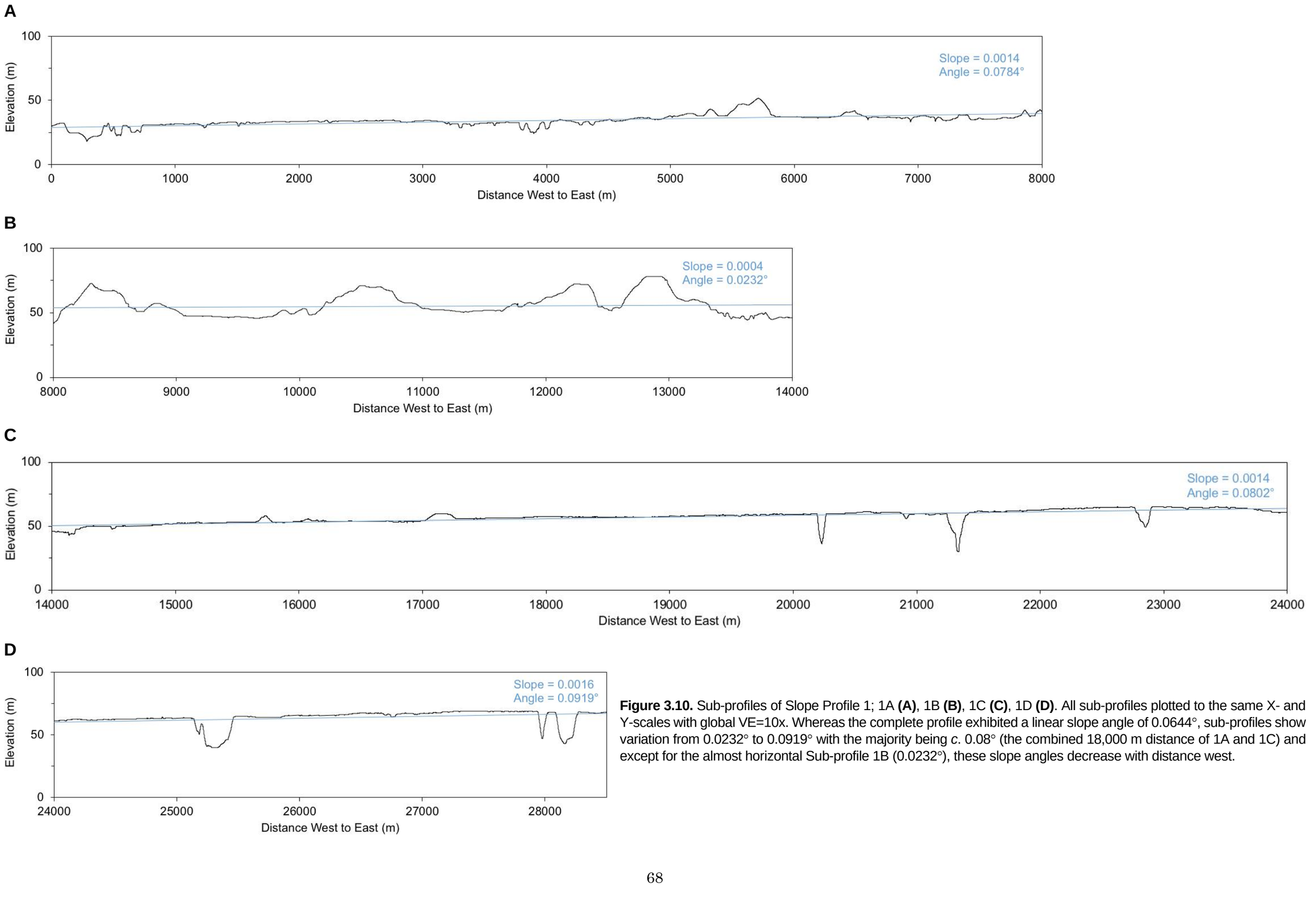

Figure 3.10. Sub-profiles of Slope Profile 1; 1A **(A)**, 1B **(B)**, 1C **(C)**, 1D **(D)**. All sub-profiles plotted to the same X- and Y-scales with global VE=10x. Whereas the complete profile exhibited a linear slope angle of 0.0644°, sub-profiles show variation from 0.0232° to 0.0919° with the majority being *c*. 0.08° (the combined 18,000 m distance of 1A and 1C) and except for the almost horizontal Sub-profile 1B (0.0232°), these slope angles decrease with distance west.

3.2.2. Gravity Anomalies

Topographically corrected Bouguer gravity anomalies show that gravity values are not homogenous throughout and adjoining the Hamilton Basin. The lowest gravity anomaly occurs as an ellipsoidal zone of 20–25 mGal across the basin's north-west, with a long axis trending SW-NE (sub-parallel to the Hakarimata and Taupiri Ranges) and perpendicular to the general flow of the Waikato River (Figure 3.11). Classified in 5 mGal increments, the central area of the gravity low is approximately 5.5 km in width, crossing beneath northern Hamilton City, north-west of, and approximately parallel, to the northern section of Kukutaruhe Fault Zone (refer Figure 1.2). The centre of the low extends to approximately half way between Hamilton City and Ngāruawāhia.

Within the Hamilton Basin, the gravity anomaly ranges over 40 mGal. North, east and south-east of the central low, the anomaly steadily increases in strength from 20 mGal to 60 mGal. Across the central mass of the extra-basin Central Hills (Hapuakohe Range and Tahuroa Ranges (Kiwitahi volcanics)) and in the extreme northern part of the gap between the Hakarimata and Taupiri Ranges, the gravity anomaly reaches highs between 55 mGal and 65 mGal. Most of the Central Hills and Taupiri Range are 50–55 mGal however, including the prominent gap between the Hangawera Hills and Pakaroa Range, west of Morrinsville. Figure 3.11 shows that west and south of the low, gravity does not increase to the same degree – across the West Waikato Hills and Ranges, the maximum anomaly measures 35–40 mGal, with a slight reduction to 30–35 mGal across the south-eastern flank of Mt. Pirongia.

Much of the southern basin is 35–45 mGal but an area of 45–50 mGal projects west from the Pakaroa and Tahuroa Ranges, into the central basin, *c.* 13 km east of Cambridge, delineating the southern edge of the basin low to the north-west. This area of relatively high intra-basin gravity terminates to the west against the lineament of unnamed low hills that extend nearly due N-S between Te Awamutu and Hamilton City; hills that align with the Hillcrest ridge and Te Tātua o Wairere Fault Zone. The north-western Waipa Basin, from the area around the volcanic cones of Kakepuku and Te Kawa, south of Pirongia township, is also 45–50 mGal.

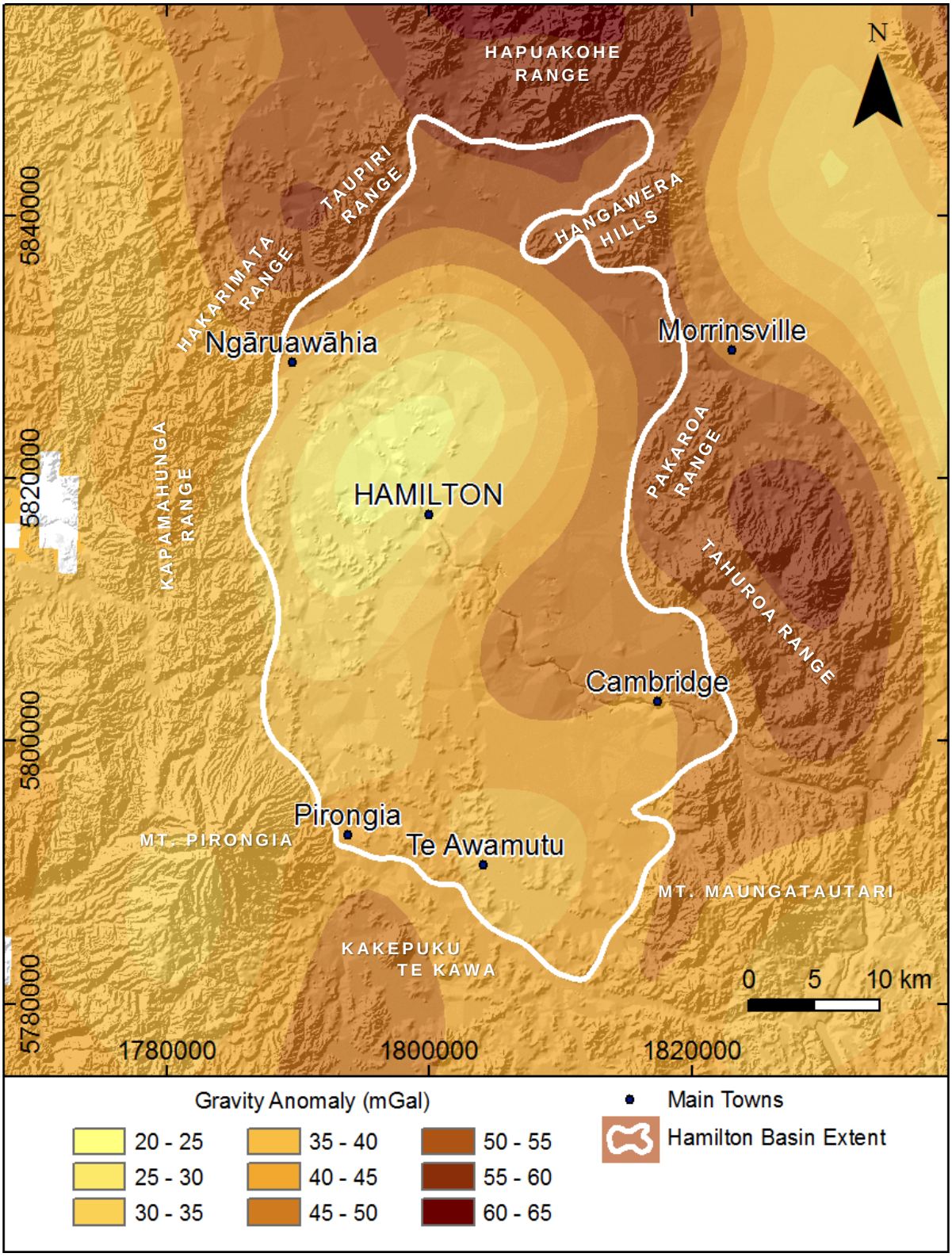

Figure 3.11. Topographically corrected Bouguer gravity anomalies in the Hamilton Basin area with a transparent hillshade relief, main towns and hills noted for geographic context. The lowest anomaly (light yellow) occurs in the north-western area of the basin while the highest anomalies (dark brown) are associated with extra-basin hills to the north and east. Gravity anomaly grids from McCubbine *et al.* (2017), downloaded from http://shop.gns.cri.nz/nzrgg/.

3.2.3. Earthquake Focal Points

All recorded earthquakes ≥M_L 2.0 and shallower than 40 km in the Hamilton Basin (and adjoining area) are shown with relation to topographically corrected Bouguer gravity anomalies in Figure 3.12. Relatively few earthquakes have occurred within the basin compared to areas outside it (28 intra- *cf.* >360 extra-basin within the map frame). Earthquakes were mapped across all intra-basin gravity ranges except for the lowest zone of 20–25 mGal. Twelve earthquakes were spread relatively evenly across the southern third of the basin, in areas from 30–45 mGal. Nine earthquakes were closely clustered north-east of Hamilton City, between the north-eastern tip of the gravity low and the Pakaroa Range, with two being in the 25–30 mGal zone, six in 30–35 mGal and one in 35–40 mGal. The remaining seven intra-basin earthquakes occurred ungrouped but close to or across the basin's northern edges in areas of 45–60 mGal.

Numerical interpolation between earthquake focal points produced depth and pseudo-contour models as shown in Figure 3.13. Comparison between models using ordinary kriging and natural neighbour methods shows similar results, varying only slightly from one another. Figures 3.13A and 3.13C show most earthquakes at >20 km depth are more widely spaced than those <20 km deep and clusters are more apparent at <20 km depth, although the small cluster north of Hamilton City is an exception, being deeper. Figures 3.13B and 3.13D provide depth pseudo-contours by classifying earthquakes in unequal intervals (Jenks natural breaks), showing that 15 of 28 intra-basin earthquakes were deeper than 29.9 km while 13 were shallower than 17.3 km – none occurred between 29.9 km and 17.3 km. Eleven of the <17.3 km deep earthquakes occurred along or very close to the perimeters of the Hamilton Basin but two were further toward the centre – one in the Puketaha area, *c.* 7 km NNE of the Hillcrest ridge and the other in the Kaipaki area, *c.* 13 km SSE of the ridge. Three earthquakes had focal points <6.8 km deep, all in the extreme east near Mt. Maungatautari and the foot of the Pakaroa Range. Figures 3.14 and 3.15 show the spatial relationship between Te Tātua o Wairere Fault Zone and the pseudo-contours for these two events.

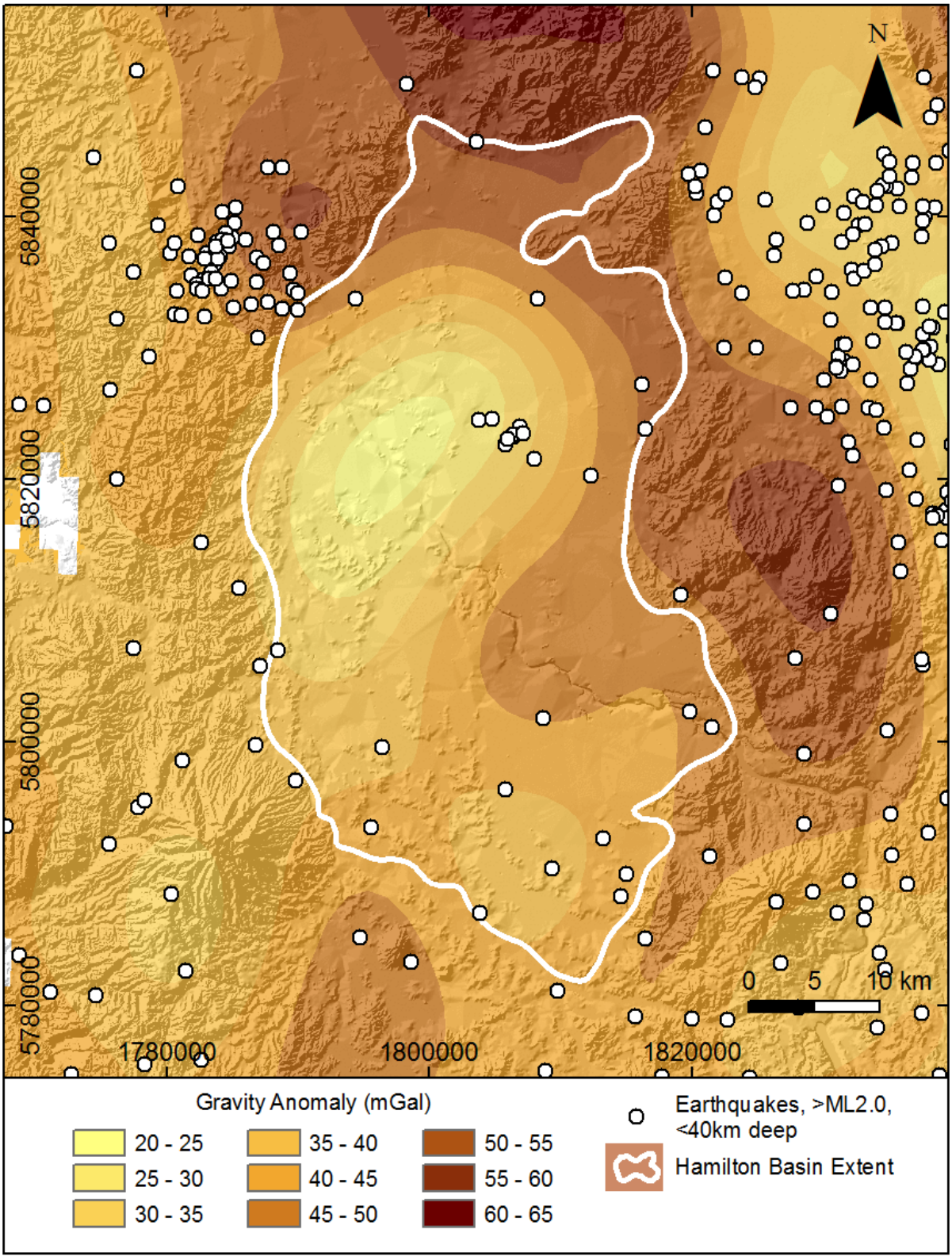

Figure 3.12. All recorded earthquakes ≥M_L 2.0, shallower than 40 km depth in the Hamilton Basin area (as at 24 April 2020), overlaid on topographically corrected Bouguer gravity anomalies and a transparent hillshade relief. Refer to Figure 3.11 for spatial reference annotations. The largest clusters of earthquakes occur to the east (Hauraki Basin) and north-west (Hakarimata Range) of the basin, with a small intra-basin cluster across the eastern edge of the central low gravity anomaly. Gravity anomaly grids from McCubbine *et al.* (2017), downloaded from http://shop.gns.cri.nz/nzrgg/.

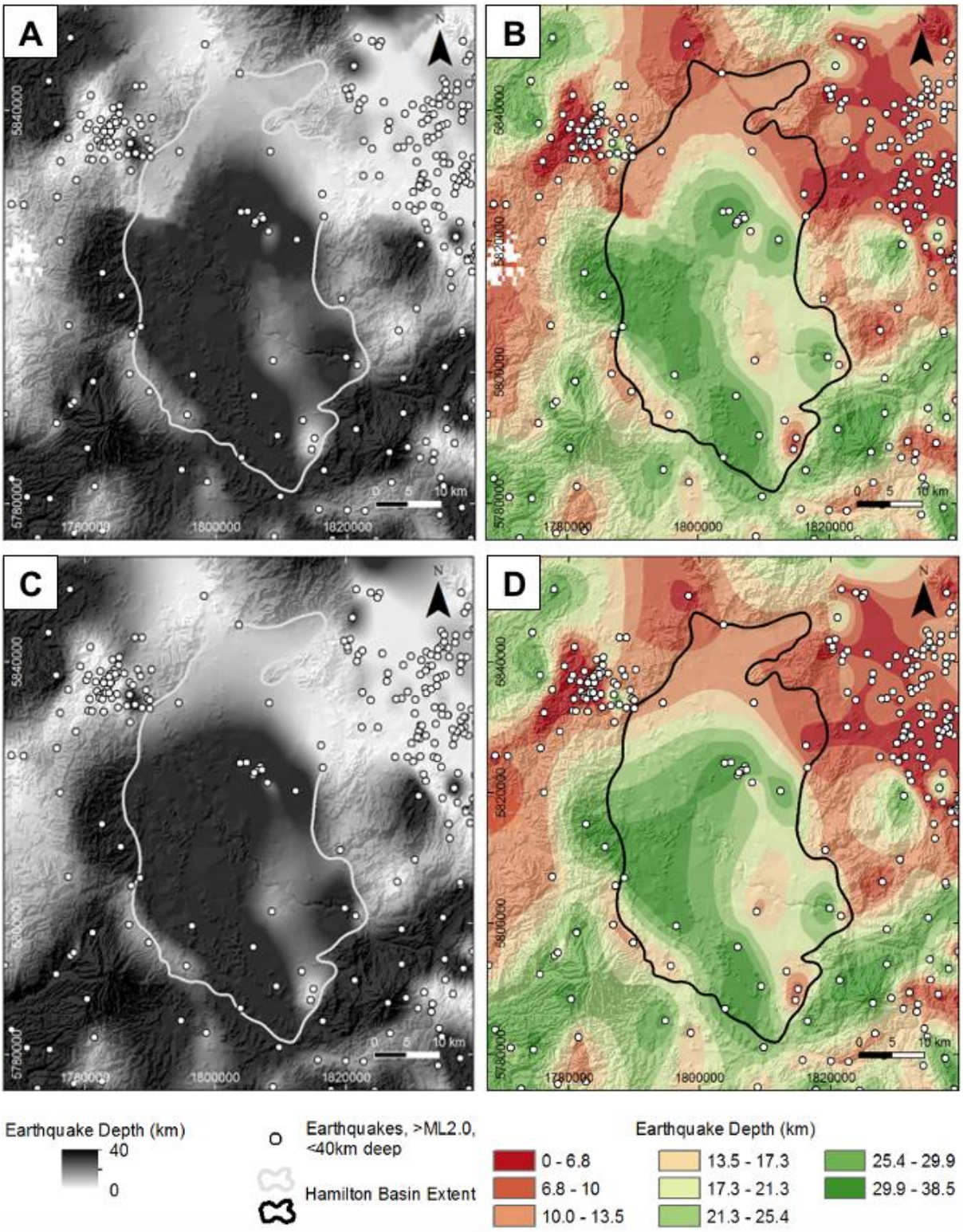

Figure 3.13. Interpolation models of similar focal depths for all recorded earthquakes ≥M_L 2.0, <40 km deep, in the Hamilton Basin area (as at 24 April 2020), created using: **(A)** The ordinary kriging method classified to 1σ using a stretched monochrome ramp; **(B)** ordinary kriging and classified using the Jenks natural breaks method; **(C)** the natural neighbour method classified to 1σ using a stretched monochrome ramp; **(D)** natural neighbour and classified using the Jenks natural breaks method. Both methods result in models approximating each other and show that most historic earthquakes outside the basin have occurred at <6.8 km depth while those within the basin have generally been >29.9 km deep.

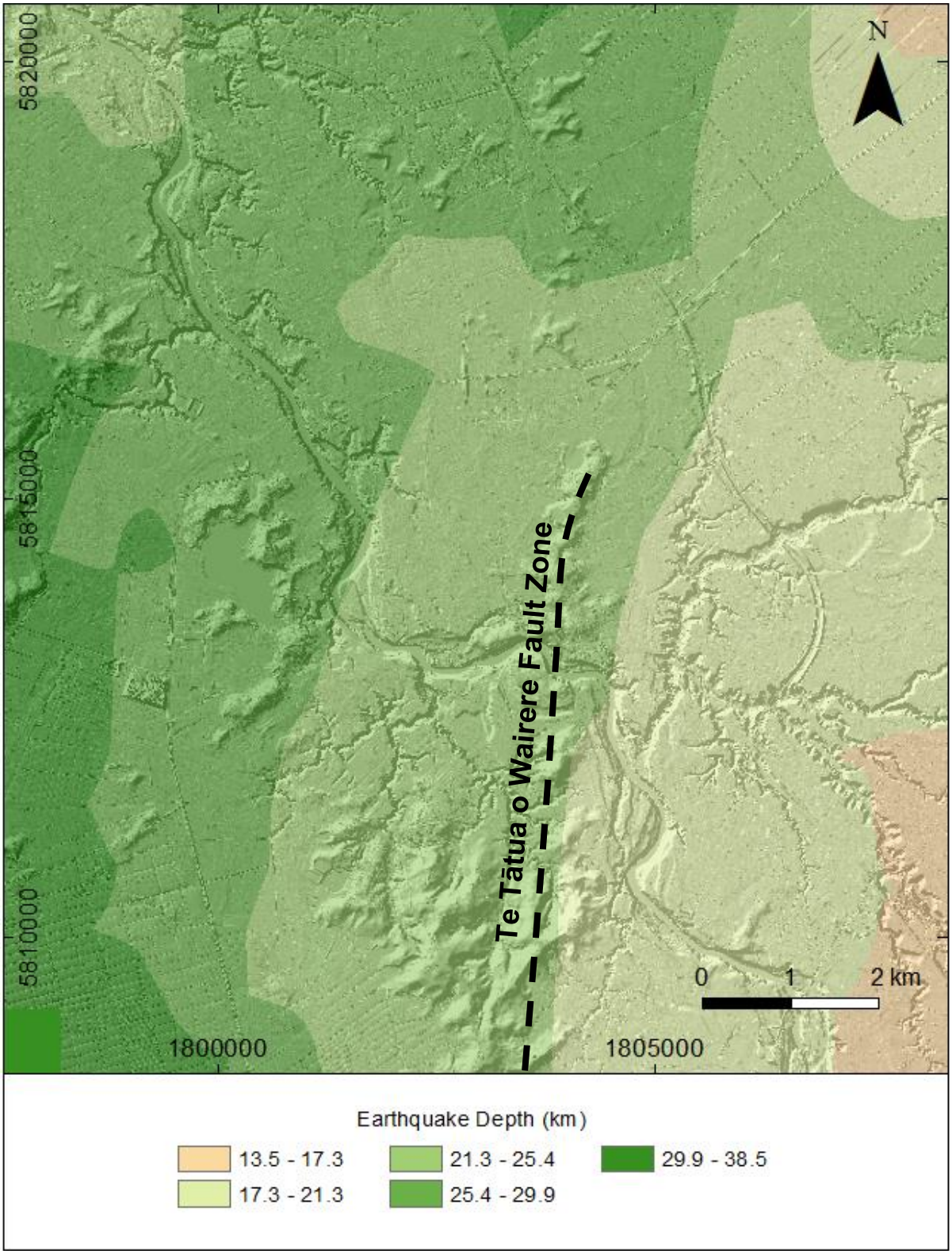

Figure 3.14. Enhanced and cropped ordinary kriging interpolation model from Figure 3.13B, showing earthquake depth pseudo-contour relationships to Te Tātua o Wairere Fault Zone. No earthquakes have been recorded within the frame thus breaks do not represent actual earthquake depths but indicate inferred relationships between the most proximal hypocentres. Closest recorded earthquakes are just out of view; one to the NE, being M_L 2.9 at a nominal depth of 12 km on 9 June 1966 (GNS Public ID 1549124), and the other approximately 12 km SSE from map centre, M_L 2.5 at 12 km nominal depth on 14 November 2008 (GNS Public ID 2999267).

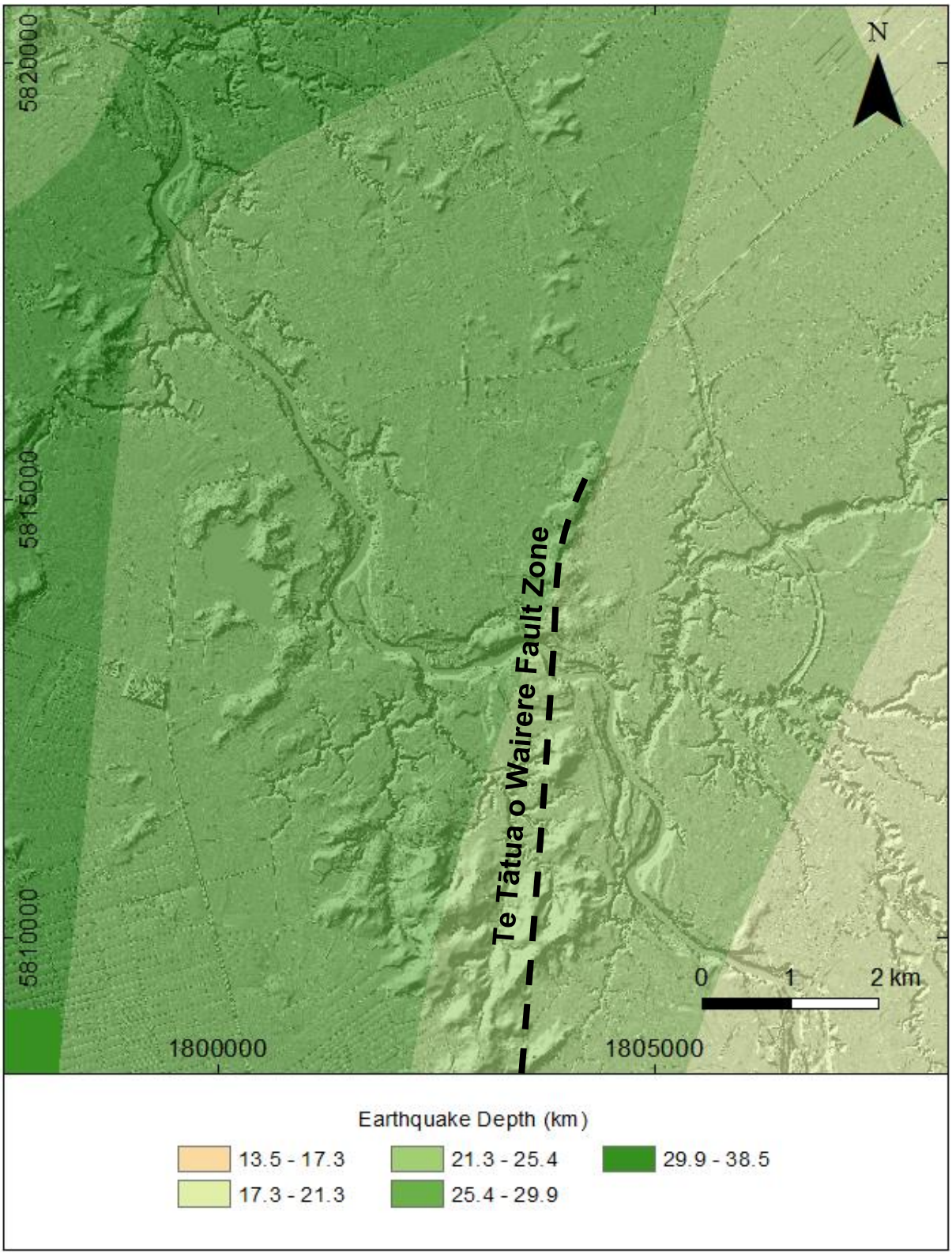

Figure 3.15. Enhanced and cropped natural neighbour interpolation model from Figure 3.13D, showing relationship of earthquake depth pseudo-contours to Te Tātua o Wairere Fault Zone per Figure 3.14.

The closest recorded earthquakes to Te Tātua o Wairere Fault Zone have all occurred within a small area in the vicinity of Puketaha, *c.* 7 km north-north-east of Ruakura and adjoining a basement high given by Liles (1971), <3.5 km east of the central west-southeast fault (Figures 3.16 and 3.17). A total of nine low-magnitude earthquakes have occurred in the area, being noticeable both by their proximity to each other and isolation from other, more distal, events. Maximum distance between epicentres is 5 km but although the whole group may be considered a cluster, eight of the nine Puketaha earthquakes occurred between March and July 1993, within a maximum distance from one another of 3.5 km, and are thus considered a distinct cluster in their own right. Table 3.1 provides details for all nine Puketaha earthquakes. True focal depth for all nine earthquakes is unknown as, prior to 2011, unless recording stations were located within a certain distance of the epicentre, GNS' evaluation results were placed against somewhat arbitrary depth boundaries depending on the degree of error in calculation (GNS Science n.d.).

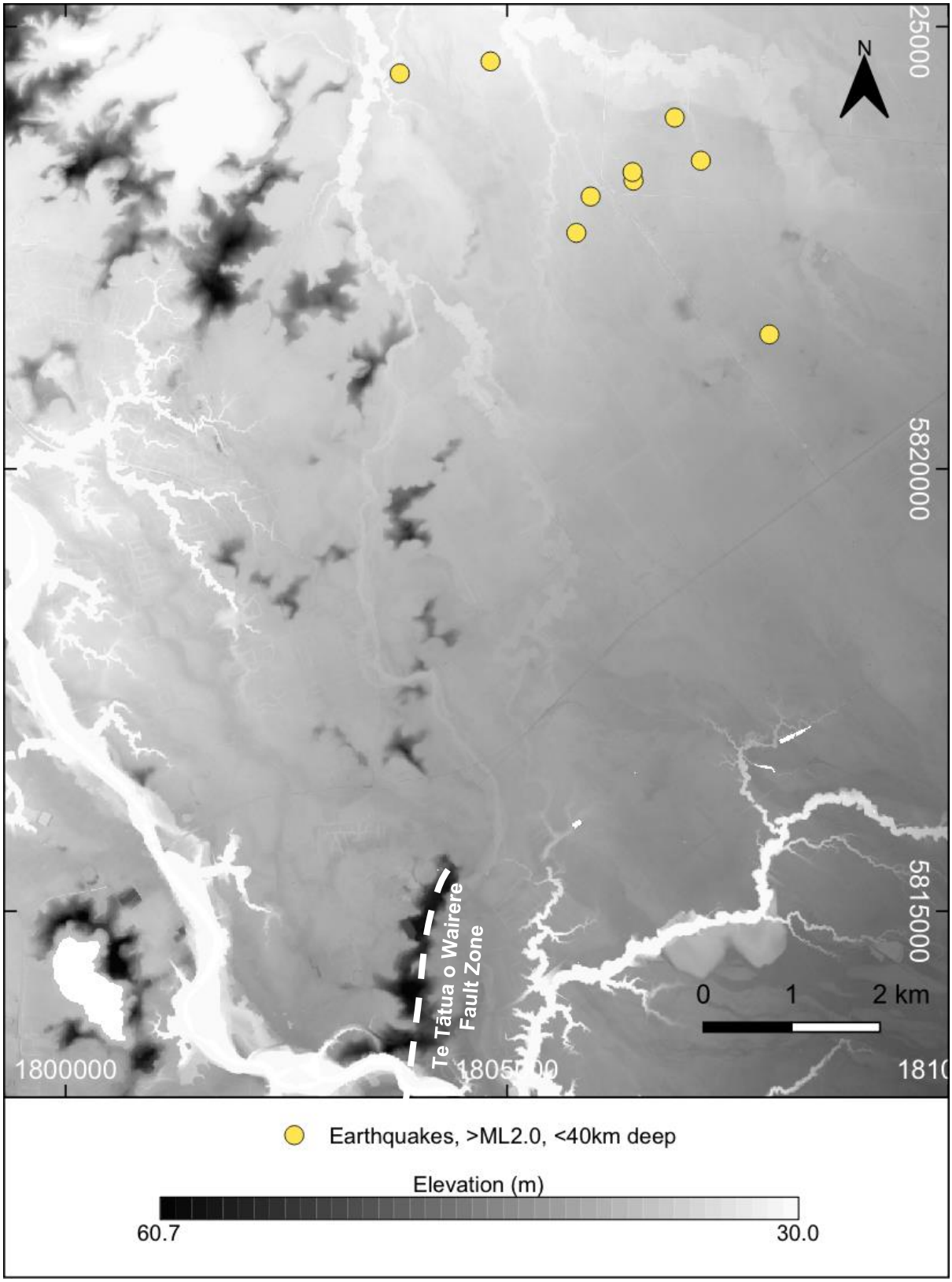

Figure 3.16. DEM showing proximity of the 1993 earthquake cluster and 1966 earthquake to Te Tātua o Wairere Fault Zone. A total of eight earthquakes (eight points at centre top) ranging from M_L 2.1–2.6 were recorded between March and July 1993 just north of Ruakura, in the Puketaha area, nominally placed at 33 km depth. Alongside the M_L 2.9 of 1966 (lowermost point), also nominally 33 km deep, these are the only recorded shallow earthquakes to have been generated near the city of Hamilton.

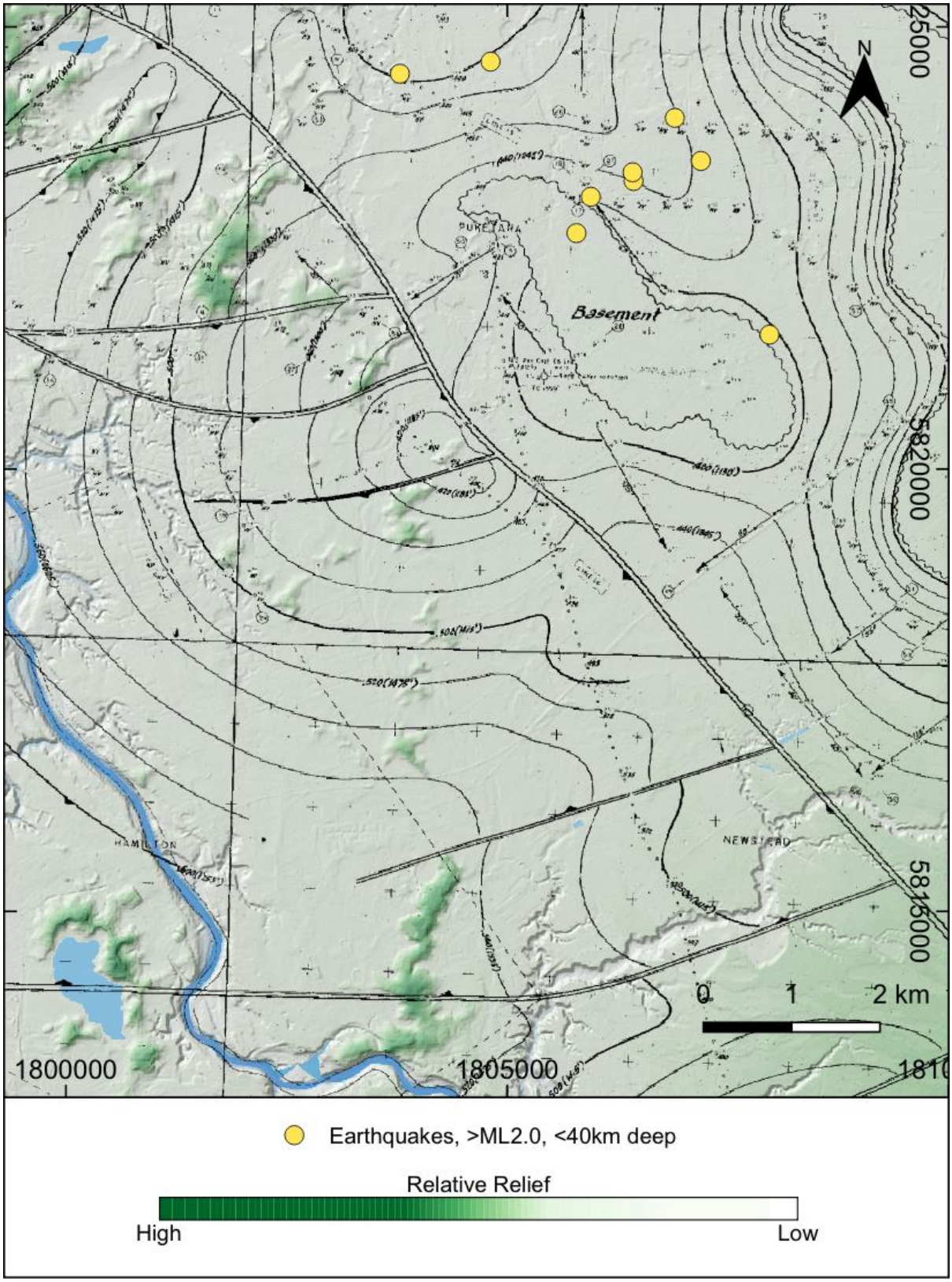

Figure 3.17. 1993 and 1966 earthquake epicentres per Figure 3.16, overlaid on the Miocene-Pliocene horizon map of Liles (1971), in turn overlaid on a false-colour hillshade relief (darker green = greater elevation). The epicentres were in the vicinity of a basement high, <3.5 km east of Liles' central west-southeast fault.

Table 3.1. Details for the closest recorded earthquakes ≥M_L 2.0 and <40 km deep, having occurred near Te Tātua o Wairere Fault Zone. Note that true depth is unknown, with nominal depths representing only a maximum depth boundary. Data from GNS Science, licenced for reuse in accordance with CC BY 3.0 NZ.

GNS Public ID	Date	Magnitude (M_L)	Nominal Depth	Easting (NZTM2000)	Northing (NZTM2000)
1549124	1966-06-08	2.900	12	1807973.886	5821518.607
418374	1993-03-10	2.282	33	1803785.382	5824470.172
429988	1993-03-18	2.397	33	1804813.020	5824606.853
423847	1993-03-30	2.357	33	1805948.249	5823078.469
457420	1993-07-01	2.076	33	1807196.869	5823483.596
458946	1993-07-02	2.188	33	1805786.274	5822667.224
458949	1993-07-03	2.265	33	1806422.678	5823355.316

3.3. Historic Images

A range of historic black and white stereopair images covering Te Tātua o Wairere Fault Zone and the wider Hamilton City area were examined (dating from the 1930s to the 1970s), along with a collection of oblique aerial photographs from the late 1950s. Geomorphology of interest was noted on the north-western side of the Hillcrest ridge and north of the AgResearch Ruakura campus. Figure 3.18 shows an apparent paleochannel at the foot of the Hillcrest ridge that is no longer identifiable either in the field or in DEM – the area having been extensively modified in later development of the University of Waikato campus. Also seen in Figure 3.18 is a small, scarp-like feature, seemingly striking NNE, along the north-eastern face of a low rise on which the building known as the cowshed is sited. While the cowshed is one of the only original structures that still remain on the university campus, the immediate surrounds have been entirely redeveloped and any trace of a vertical slope break has been removed since the image was taken; it is unknown whether the feature was natural or anthropogenic in origin.

Figure 3.18. Oblique aerial photograph *Ruakura, Waikato Region* dated 19 May 1958. View is NW, across the Hillcrest ridge (Hillcrest Road annotated), with the white compound just left of centre being the cowshed, still part of the University of Waikato campus to this day. The light toned sinuous feature (outlined with dotted white lines) that appears to enter frame from SE and run NNE in a shallow depression is interpreted as being a paleochannel that has since been removed in campus development. Inset shows a smaller scale crop of the cowshed, highlighting its position atop a low rise. The NE flank of the hill appears to be steepest, with a low, near-vertical bluff but as all sides of the hill have subsequently been modified during campus development it is difficult to determine if this was a natural feature. Image ref: WA-46232, courtesy Whites Aviation Collection, Alexander Turnbull Library, downloaded from https://natlib.govt.nz/records/32054541 and licenced for reuse in accordance with CC BY 4.0.

A photograph from the opposite (north-eastern) side of the Hillcrest ridge is partially reproduced as Figure 3.19; taken at a lower angle and from greater distance, the paleochannel of Figure 3.18 is not as prominent but is possibly still visible to the left of image, as a subtle tonal difference at the ridge's base. The small bluff adjacent to the cowshed is also barely visible but, more prominently, to the south-west and forming the edge of an apparent plateau atop the Hillcrest ridge, is a sharp break in slope not apparent in any stereoscopic imagery. This break appears to have some degree of scarp-like form and a perpendicular treeline reflects this, highlighting a degree of concavity immediately east. As with aforementioned features, this area has been heavily modified since the early 1960s and the form is no longer identifiable in field or DEM – it is difficult to determine whether it was in the area now occupied by the University of Waikato or neighbouring St John's College.

Figure 3.19. Crop of oblique aerial photograph *Ruakura, Waikato Region* dated 12 November 1959. View is SSW, toward the Hillcrest ridge, with the cowshed and key roads annotated. An abnormally sharp slope break is visible at the edge of a small ridge-top plateau. Image ref: WA-46232, courtesy Whites Aviation Collection, Alexander Turnbull Library, downloaded from https://natlib.govt.nz/records/32054541 and licenced for reuse in accordance with CC BY 4.0.

Figure 3.20 is a stereoscopic image of the Hillcrest/Ruakura area from 1943, before either the cowshed or the university had been constructed. The low rise the cowshed was later built on – and associated scarp-like feature – is obscured by trees but approximately 200 m NNE east of the trees is a dark linear feature that appears to have a similar orientation. Apparently removed or heavily modified in subsequent land development – not being seen in any more recent images – this line is visible in all other photographs from the run so the possibility of being a mark or scratch on the image is considered low. Given its proximity and orientation with regard to other features of interest in the area, it may be that this line had some relationship to them but there is no other evidence to conclude it is a seismogenic form.

Extending the photographed area of Figure 3.20 further north, Figure 3.21 highlights a significant paleochannel that breaches low hills within the Ruakura campus (herein the 'Ruakura hills') from east to west in a very unusual manner. Initially marking a northward flow direction, on the eastern side of the Ruakura hills, the paleochannel kinks abruptly (<90°) to the west, between two hills, before immediately bending sharply again (≈90°) upon emerging on the western side and returning to a northward flow. Shortly thereafter, immediately north of Powells Road, this paleochannel appears to rapidly pinch out against the eastern bank, before re-emerging a short distance north but slightly further west. This combination of extreme directional change and pinching of channels was not observed in any other area of either historic images or modern DEMs.

Figure 3.20. Stereoscopic aerial photograph 830/41 of Hillcrest/Ruakura dated 14 June 1943. North to top of frame. The original homestead on the future AgResearch campus is just north of the area marked 'ERT anomalies' (refer Figure 4.26). The dark linear feature of unknown origin seems to align with both the cowshed hill (obscured by trees, pre-shed construction) and paddocks with ERT anomalies. Image courtesy LINZ, downloaded from http://retrolens.nz and licenced for reuse in accordance with CC BY 3.0.

Figure 3.21. Stereoscopic aerial photograph 632/40 of Ruakura/Fairview Downs dated 13 March 1943. North to top of frame and frame partially overlaps Figure 3.20. The circled area highlights apparent offset and pinching against the eastern bank of a major paleochannel (outlined with white dotted lines) following breaching of the Ruakura Hills (outlined with white dashed lines). Image courtesy LINZ, downloaded from http://retrolens.nz and licenced for reuse in accordance with CC BY 3.0.

3.4. Geomorphic Maps

As well as being less intensively developed and easier to access than adjoining urban areas, potential evidence for fault-related features in desktop models and historic images warranted open farmland around Ruakura being the focus for field survey and geomorphic mapping. Whilst much in the way of geomorphology could be determined via DEM – especially macro-scale features such as hills and significant paleochannels – site walkover and field reconnaissance was necessary to understand and ground-truth several micro-scale features. Microtopographic artefacts confirmed or added in this manner included shallow depressions where treelines or shelter belts had been removed, and where subtle offsets or breaks cut across continuous features, such as levees or terraces. Such otherwise cryptic features were often noticeable as a change in vegetation (e.g. dark green broadleaf flora growing within shallow depressions *cf*. lighter green grasses elsewhere) or where brief shadows were observed when the sun was low against the horizon.

Figure 3.22 is a geomorphic map of the Ruakura area containing much detail but this deliberately serves to illustrate areas of considerable complexity that called for particular exploratory emphasis during field work. These areas included:

- a discrete, oxbow-like section of an eastern paleochannel, with a crevasse splay of breakout channels but no clear inflow (Figure 3.23A);
- abrupt paleochannel axis switching of a western paleochannel (Figure 3.23B);
- offset and interrupted longitudinal bar adjoining a minor paleochannel (Figure 3.23C), and;
- pinching/constriction of the western paleochannel following an abrupt breach of the Ruakura hills as noted in Figure 3.21 (Figure 3.23D).

A series of abrupt (≈45°) paleochannel switchbacks in the north-east of Figure 3.22, connected to the oxbow-like section, were an additional area of interest. Unfortunately, this and significant portions of the areas highlighted in Figure 3.23A, B, and D, were unable to be ground-truthed due to the impact of recent construction projects and/or lack of access. Figure 3.24 shows how the field area had been affected by development since the initial DEM was assembled.

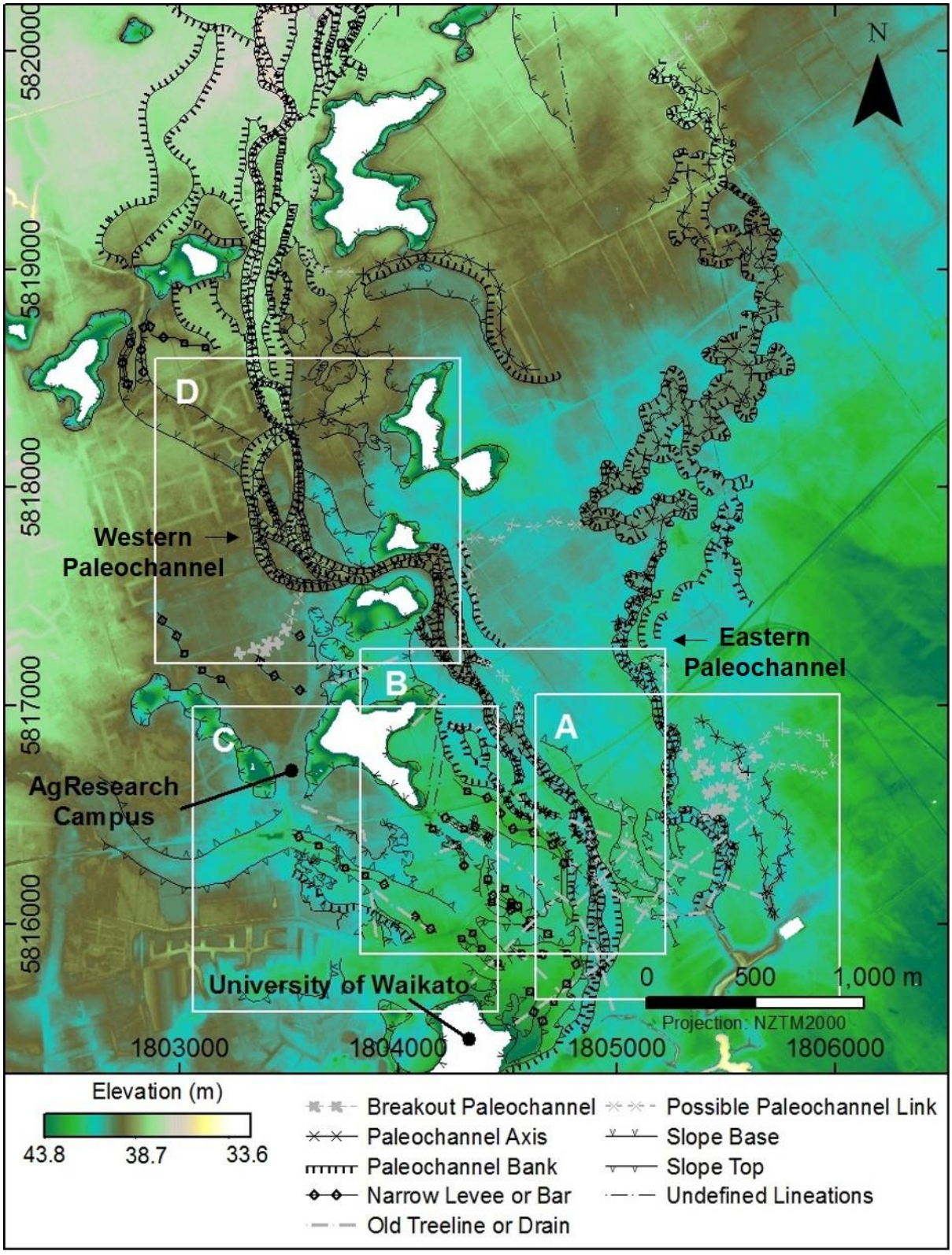

Figure 3.22. Geomorphic map of the Ruakura area in which field survey and microtopographic reconnaissance was undertaken. As the focus was on plains of the Hinuera Surface, elevations >43.8 m have been excluded from the DEM colour ramp to allow more detail thus the hills appear as plain white areas. A western paleochannel extending from the Hillcrest ridge, north through Ruakura and beyond, and a shorter, eastern paleochannel with no clear inflow and dying out in the north-east of the map frame are the predominant macrogeomorphic features. Boxes A–D highlight key sub-areas shown in Figure 3.23.

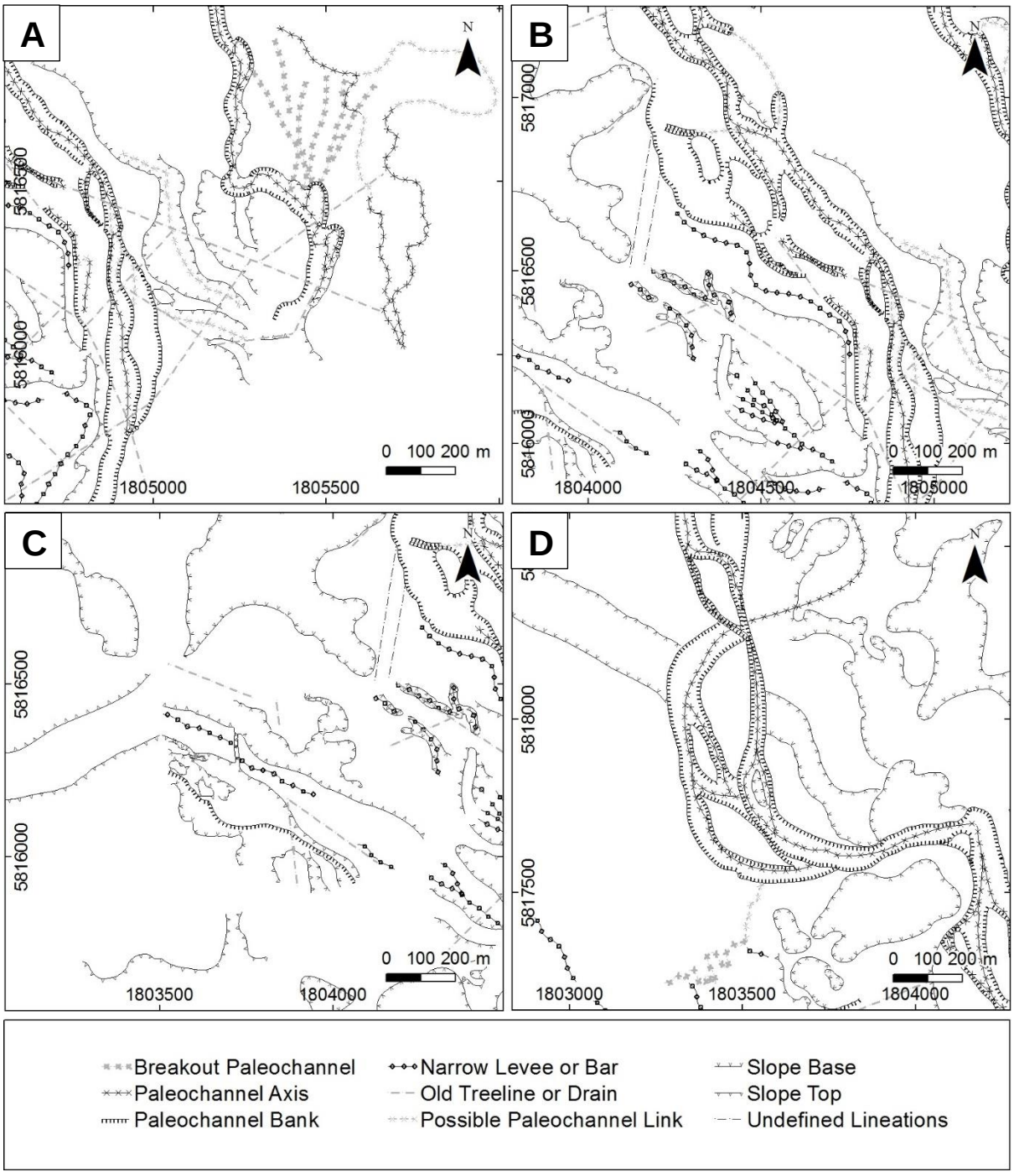

Figure 3.23. Target areas for field survey of complex geomorphology from Figure 3.22. **(A)** Unusual oxbow-shaped paleochannel with no clear inflow but breakout channels forming a crevasse splay; **(B)** abrupt switching of paleochannel axis coinciding with cutting off of an eastern terrace and linearity of the eastern bank; **(C)** offset and interrupted longitudinal bar and paleochannel banks; **(D)** pinched/constricted paleochannel downcutting an older channel.

Figure 3.24. Annotated Google Earth screenshot of the area mapped in Figure 3.22, illustrating post-DEM landscape modification and areas obscured by construction projects. Of particular note are the expressway and interchange east of Silverdale Road, the container park preload/sediment ponds east of the AgResearch campus, and the Greenhill Park subdivision; these precluded intensive survey of much of the areas identified in Figure 3.23A, B, and D. Satellite image dated 12 December 2020 © 2021 Maxar Technologies.

3.4.1. Western Paleochannel

Field survey confirmed the form of the western paleochannel system as mapped in Figure 3.22 and shown in Figure 3.25. Near the tip of the Hillcrest ridge, the western paleochannel is flanked by terraces atop both western and eastern banks and the apparent channel axis is approximately central, though veering gently to parallel the western bank north from *c.* 1804915 E, 5815713 N (Figure 3.26, point A). Figure 3.26 shows that around 200 m south-east of the Ruakura Road/Percival Road intersection, at *c.* 1804881 E, 5816345 N, the axis shifts abruptly eastward to cut the eastern terrace and flow against the eastern bank, leaving only a wide terrace to the west (point B). Numerous disconnected small levees and narrow longitudinal bars, generally trending SE-NW, feature upon the plain west of the western terrace while the terrace itself is crossed by smaller, discontinuous and seemingly offset channels (Figure 3.26, point C); both the terrace and the main channel also incorporate longitudinal bars 50–100 m wide (Figures 3.26 and 3.27).

Figure 3.25. Photograph looking south along the western paleochannel toward the abrupt change in channel axis (not visible, far side of fenceline). The NE tip of the Hillcrest ridge is out of frame to the right. Darker green pasture within the channel highlights channel form. Note the subtly steeper eastern bank (left of image) – the shallower western bank forms the edge of a low terrace.

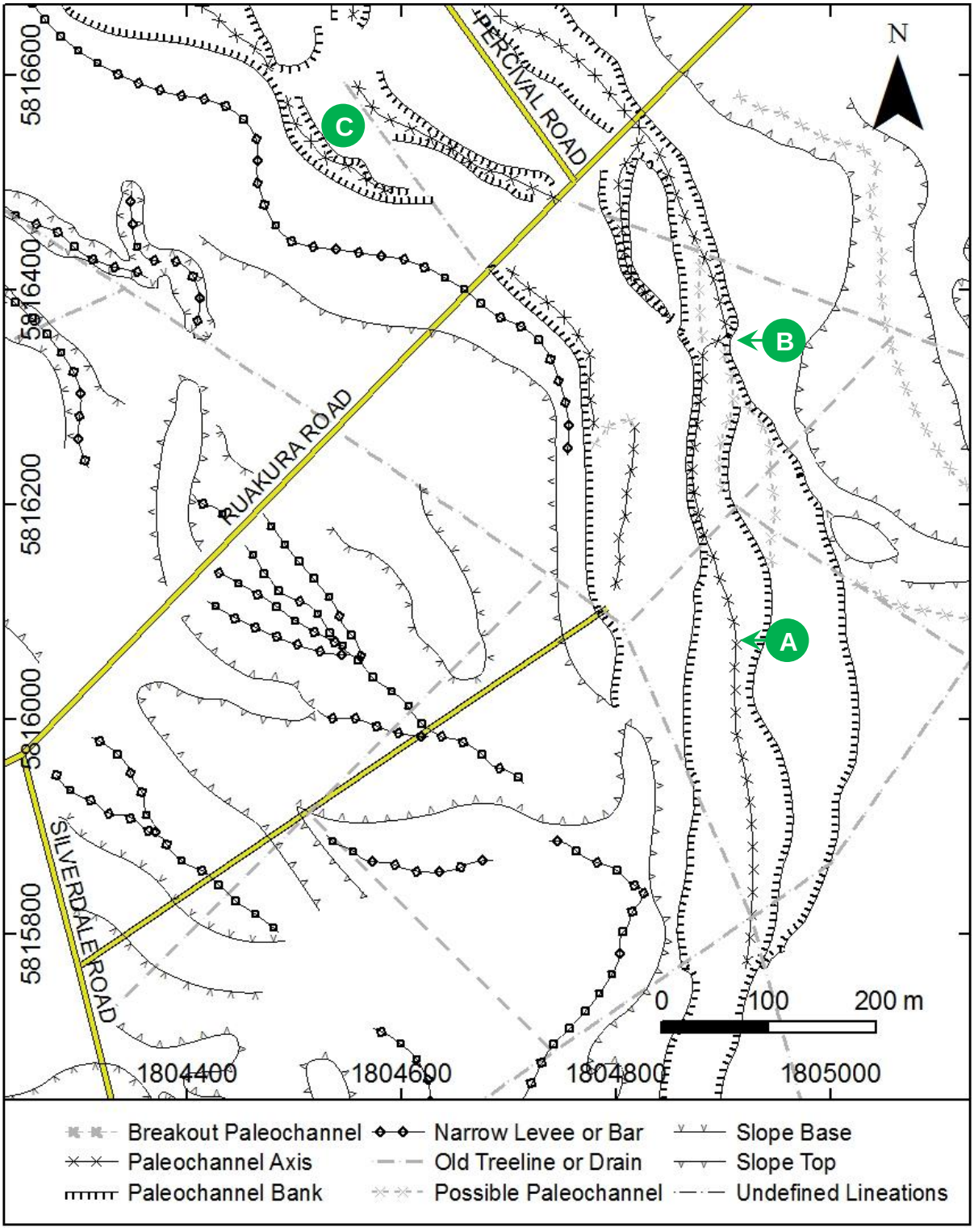

Figure 3.26. Geomorphic map of the western paleochannel between Ruakura Road and Silverdale Road. Key features include the paleochannel axis veering west around [A] before shifting sharply eastward and cutting off an eastern terrace at [B]. Small, discontinuous channels, which seem to be offset, cross the western terrace in the vicinity of [C].

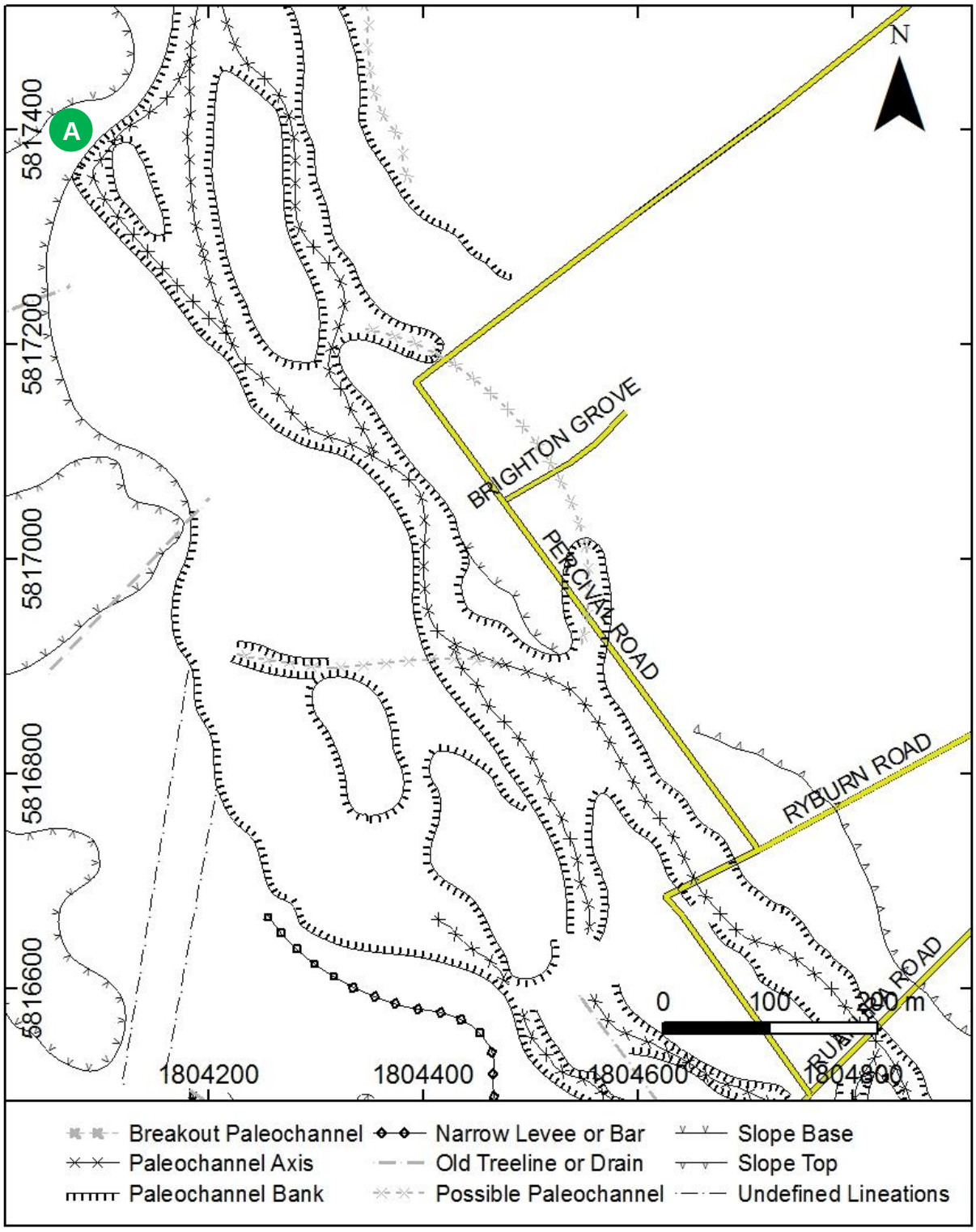

Figure 3.27. Geomorphic map of the western paleochannel adjoining Percival Road, north of Ruakura Road. Note the abrupt directional change of a minor paleochannel branch where the foot of the SE flank of a central Ruakura hill appears to form a barrier around [A]. The paleochannel's eastern bank is relatively linear parallel to Percival Road, although this may not represent the true form as a small westward looping channel may have existed in the vicinity of Brighton Grove.

The northern termination of the western terrace coincides with a sharp change in direction (≈90° to the NE) of a minor paleochannel branch, which appears to run hard against the foot of a central Ruakura hill (point A, Figures 3.27 and 3.28). Approximately 200 m north of this point, the paleochannel hooks sharply WSW from around 1804178 E, 5817698 N, to breach the Ruakura hills (Figure 3.28, point B). Coincident with a veering north of the paleochannel upon exiting the western side of the hills, the channel appears to have either avulsed itself, or cut through a section of an even older channel that formed a wide loop (Figure 3.28, point C, and Figure 3.29, point A). The western paleochannel then becomes increasingly constricted over a short distance (<350 m), effectively pinching out against the eastern bank at *c.* 1803520 E, 5818236 N (Figure 3.29, point B). In DEM the main channel seems to r eappear *c.* 100 m north and a much narrower avulsion channel bypasses the pinch point; in the field, however, these are indistinguishable and the paleochannel axis gives way completely to hummocky, semi-drained swamp (Figures 3.30 and 3.31).

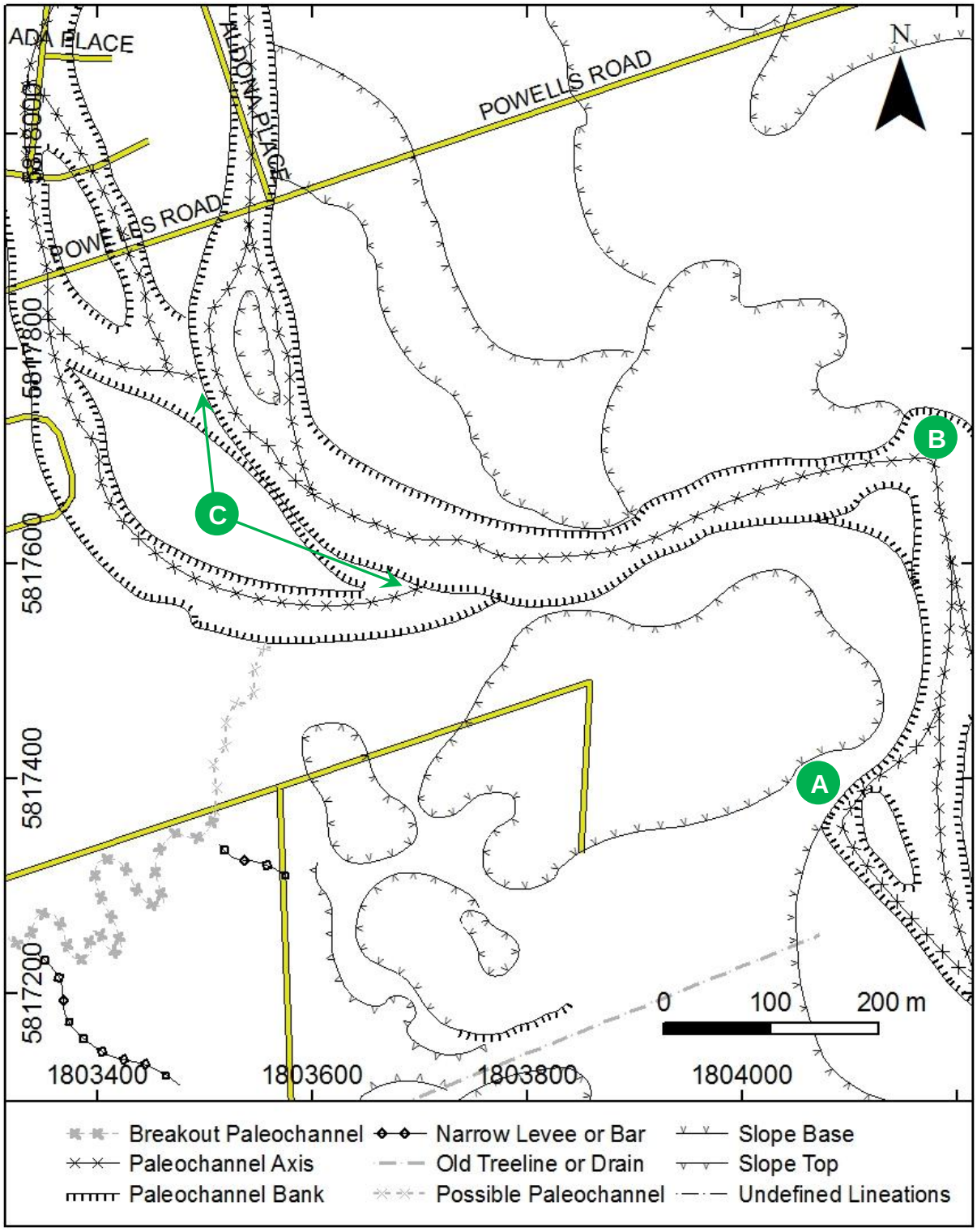

Figure 3.28. Geomorphic map of the central AgResearch Ruakura Farm area, south of Powells Road. Key features include the abrupt directional change of a minor paleochannel branch where the foot of the SE flank of a central Ruakura hill appears to form a barrier around [A]; the western paleochannel turning sharply WSW to breach the low hills from [B], before resuming a northerly course on the western side. The paleochannel appears to have undergone avulsion or cut through an even older channel which looped more widely to the west, around [C].

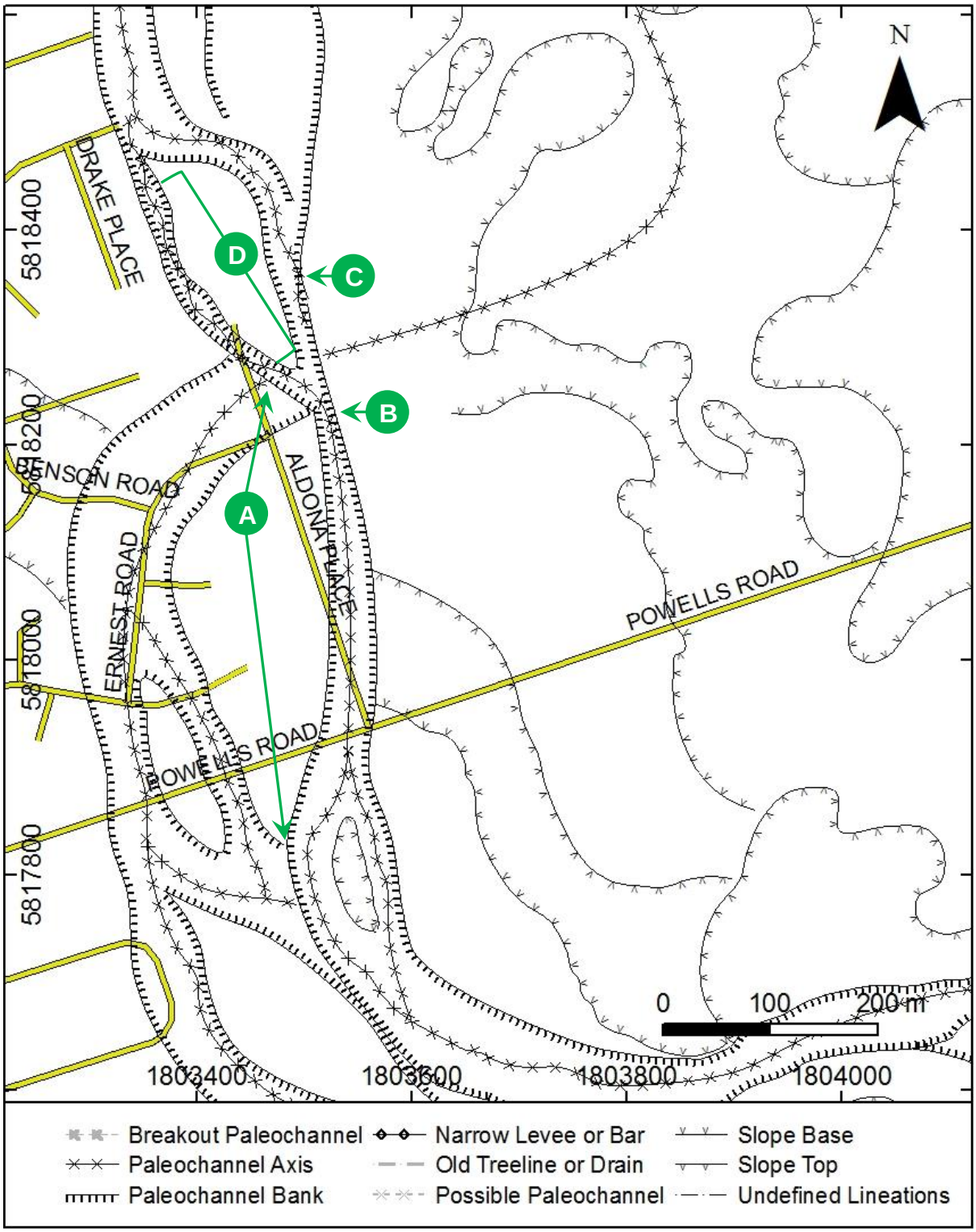

Figure 3.29. Geomorphic map of the Ruakura/Fairview Downs area adjoining Powells Road. The paleochannel appears to have undergone avulsion or cut through an even older channel at [A] and the main paleochannel axis appears to pinch against the eastern bank at [B], reappearing around [C] but with a small avulsion channel appearing to maintain a flow bypass [D]. While constriction of the main channel is visible in-field, the area to the north is swamp; the northern reappearance and the avulsion channel were only seen in DEM.

Figure 3.30. Annotated photograph of the western paleochannel and its eastern bank, north-west of the Ruakura hills, looking south, just shy of where the axis pinches and is lost amongst scrubby swamp vegetation to the north.

Figure 3.31. Photograph of the western paleochannel, north-west of the Ruakura Hills, looking north from the point where the channel axis is lost amongst swamp.

3.4.2. Eastern Paleochannel

Having largely been altered by Waikato Expressway and Ruakura Interchange development, the main observations regarding the eastern paleochannel were of adjoining former swamp areas. Unlike the generally smooth, gently rolling surfaces across most other areas, terrain around the point of the oxbow-like section where the outflow channel hooks north is uneven and hummocky for a distance of 150–180 m in all directions (though up to 300 m toward the south) (Figure 3.32, point A). This difference in terrain is not only noticeable underfoot but also visually highlighted during the late summer, as larger, darker, stalky plant species form a distributed patchwork of pseudo-islands amongst shorter, yellowed pasture grasses at slightly lower (<0.5 m) elevation. As with the area north of the major western paleochannel constriction, this appears to have been a swamp, though has been more extensively drained and lacks dense scrub. Similar swampy terrain occurred on the north-eastern side of the expressway which – while their exact forms could not be ground-truthed – suggested the DEM-inferred crevasse splay and tight, horseshoe-shaped meanders were correct. The remnant swamp is thus inferred as evidence for breakout flooding north-east of the main channel (Figure 3.32, point B).

3.4.2.1. Additional Note Relating to the Eastern Paleochannel

Although not directly geomorphic and thus not mapped, an expressway cutting below an excavated drain (pre-expressway) that links to the eastern paleochannel showed an apparent unconformity and lateral discontinuity (Figure 3.33). Viewed at a distance of some 60 m from farmland on the western side (1805612 E, 5815737 N), unconsolidated sediments in the north-west of this cutting appeared to be massive, light brown silt, with an overlying unconformity *c.* 4 m below the modern surface where weedy vegetation has established. This observation was *c.* 480 m south-east of the southern end of the oxbow-like paleochannel section and the unconformity coincides with a perched water table noted in Beca Ltd (2016). A lateral contact was obscured by spoil but in the south-east of the cutting, the brown silt appears to be replaced by horizontally bedded, fine to coarse, light grey and orange silts and sands.

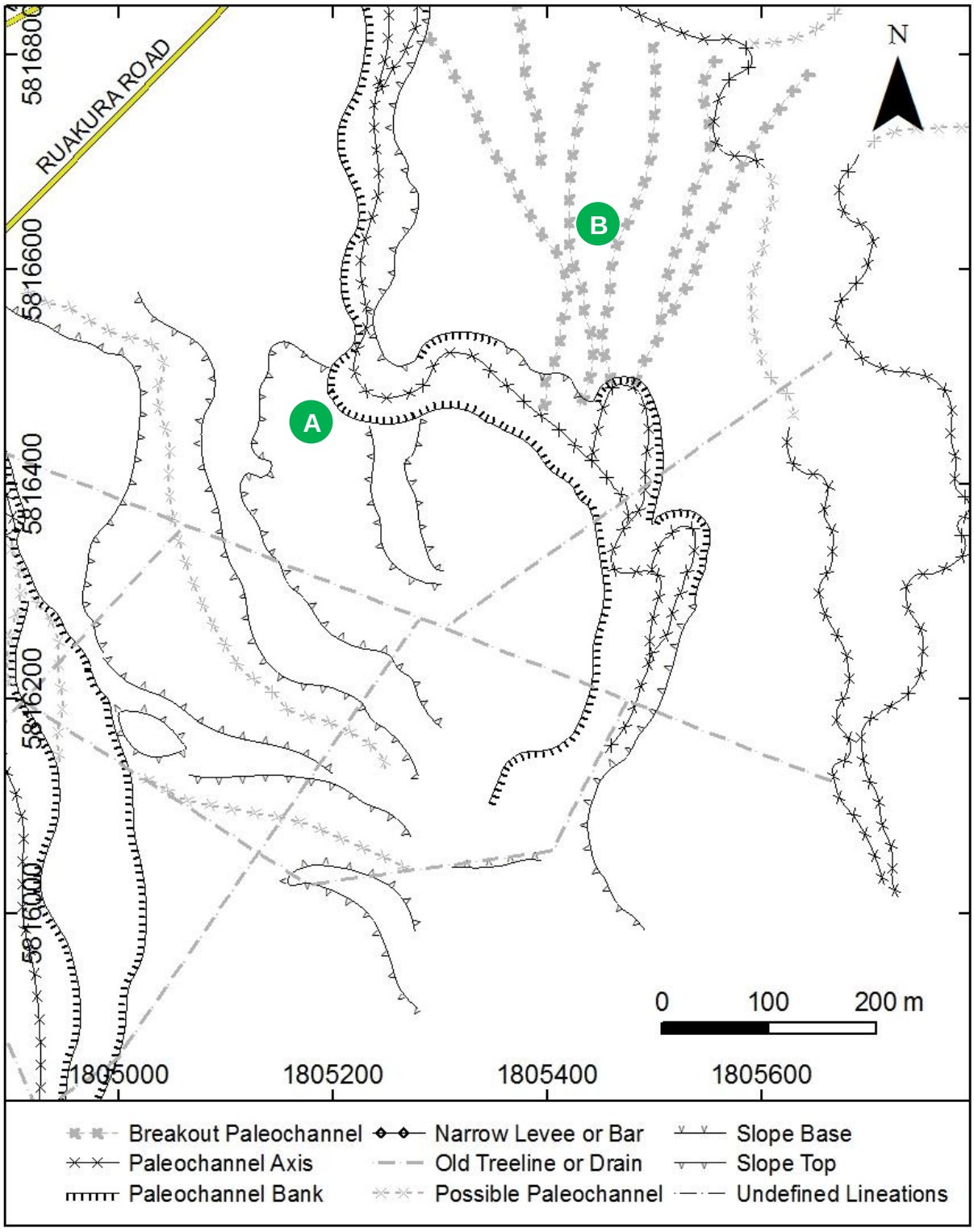

Figure 3.32. Geomorphic map of the eastern paleochannel's oxbow-like feature, SW of Ruakura Road (predominantly mapped from DEM, pre-expressway construction). Former swamp was noted in the areas around [A] and [B] – note the breakout channels and tight, horseshoe-shaped meanders that lead toward [B], indicative of paleoflow having preferentially sought a path to the NE. The channel axes noted in the east of the map frame are very slight, without well-defined banks and are interpreted as very modern, surficial drainages.

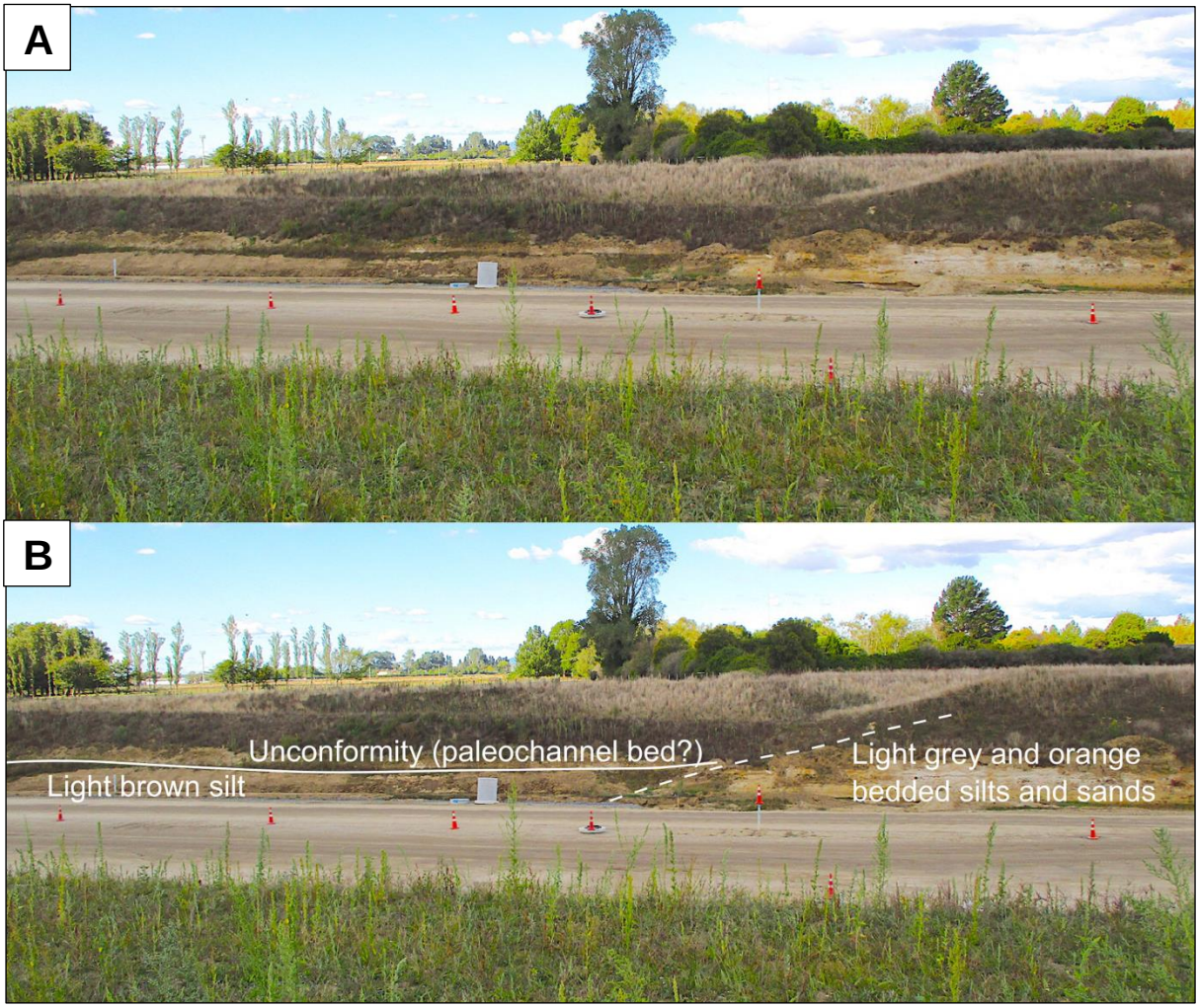

Figure 3.33. Waikato Expressway cutting approximately 500 m south of the Ruakura Interchange. **(A)** Photograph of the eastern wall; **(B)** same photograph annotated, showing what appear to be a lateral discontinuity and unconformity – possibly a paleochannel bed – the latter coinciding with perched groundwater given in Beca Ltd (2016).

3.4.3. Southern AgResearch Farm

Although the area given in Figure 3.34 was geomorphically simpler to map than the western and eastern paleochannels, lacking a major paleochannel complex, it exhibited several noteworthy features. Foremost of these was a wide longitudinal bar with a lower terrace adjoining its southern edge (Figure 3.34, point A). The bar is orientated ESE-WNW, measuring *c.* 180 m across at the ESE extremity and *c.* 80 m at the WNW. Rather than progressively diminishing in width along its length, this bar narrowed significantly at a point along its southern flank which aligns with the eastern flank of a small raised plateau *c.* 25 m to the south (Figure 3.34, points B and C). This plateau area appears to have formed the southern bank of a paleochannel that flowed between it and the longitudinal bar. However, unlike the other mapped paleochannels, this is not an uninterrupted channel with a constant profile – a *c.* 0.6 m high transverse bar interrupts the channel and connects the raised plateau to the terrace (Figure 3.34, point D). Historic aerial images for this area of the AgResearch farm show a treeline <16 m W of this area that was removed some time in the 1940s so it is possible the transverse bar may be a related remnant. If not, this bar, together with the apparent alignment and similar flank orientations of the narrowed portion of the longitudinal bar and the raised plateau, suggests *c.* 135 m of sinistral offset NNE-SSW.

Some 290 m north-west of the point where the transverse bar links the terrace to the raised plateau, the longitudinal bar is cut across its width and appears offset by a shallow, semi-linear depression ≤0.2 m deep (Figure 3.34, point E). This cross-cutting depression is mid-paddock (i.e. not a fence or treeline) and does not appear to be anthropogenic from any historic images or maps. Apparent offset is dextral, NNE-SSW, in the order of 50 m. Approximately 245 m further north-west, the longitudinal bar becomes indistinguishable against Ruakura Lane; given the degree of development immediately west of this position it was impossible to determine whether this is the natural terminus of the bar or if a continuation to the north-west has been obscured. Within the *c.* 150 m east of Ruakura Lane, a number of shallow depressions and hummocks appear on the surface of the terrace and the paleochannel is lost (Figure 3.34, point F).

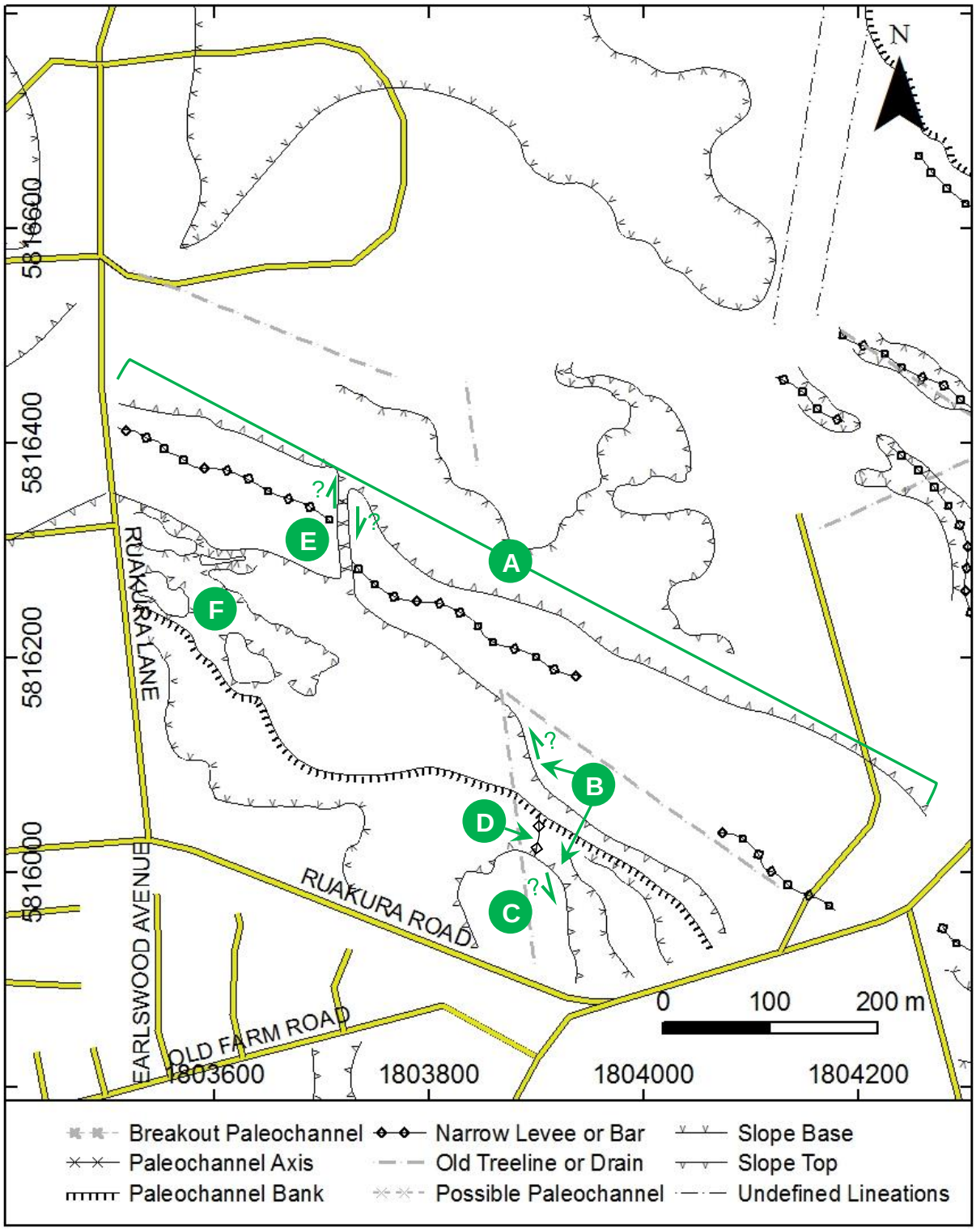

Figure 3.34. Geomorphic map of the southern AgResearch Ruakura Farm area, between Ruakura Lane and Ruakura Road. Key features include a longitudinal bar [A] that narrows in width from *c*. 180 m to *c*. 80 m at [B]. The narrowing of [A] at [B] aligns with, and appears sinistrally offset from, the eastern flank of a small plateau to the south [C] and is connected to it by a small transverse bar [D] that cuts across a subtle paleochannel which lacks a clear axis. [A] also appears to be cut by a shallow depression and dextrally offset around [E] while the subtle paleochannel is lost west of [D] and the low terrace adjoining the longitudinal bar incorporates several small depressions and hummocks [F].

3.5. DEMs of the Ruakura/Fairview Downs Area

The 2020 LiDAR dataset enabled production of the elevation and contour maps covering the Ruakura/Fairview Downs area, centred on the AgResearch farm, given as Figures 3.35–3.37. The high resolution of these maps reflects geomorphology mapped in-field and particularly emphasises features such as the offset longitudinal bar near Ruakura Road, the bar's offset relationship to the small raised plateau, and a subtle difference in elevation along the western side of the Ruakura hills that aligns both with the pinched western paleochannel and a sharp N-S edge to the south-western spur of the southernmost hill. Based on these features and by inferring a relationship to the fault observations made at Cobham Drive, a main line of faulting, with two related splinters or strands, was hypothesised per Figures 3.37 and 3.38.

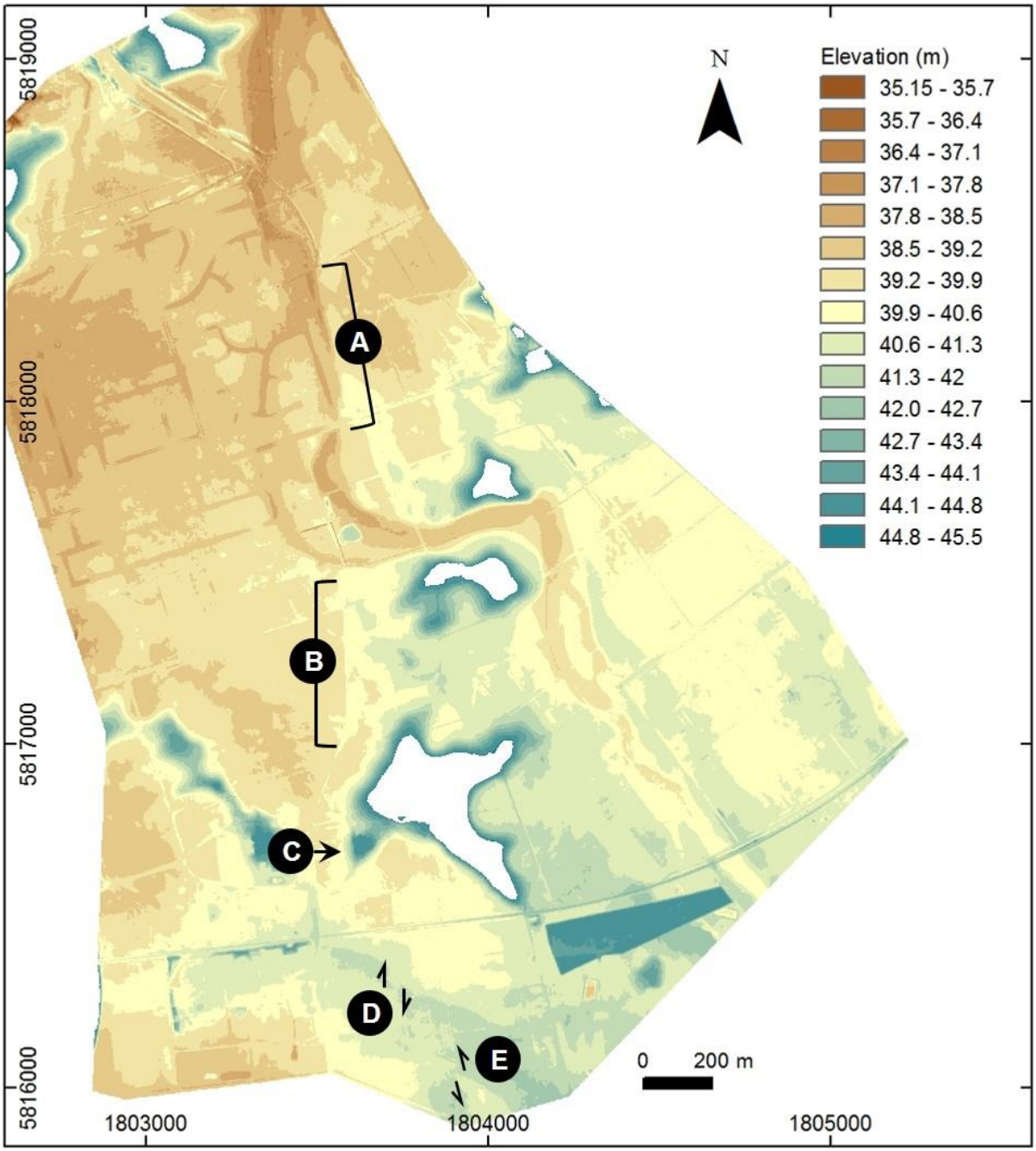

Figure 3.35. DEM of Ruakura/Fairview Downs classified to 0.7 m breaks. Notable features reflecting observations from field survey and/or historic image analysis include: [A] Constriction and pinching of the western paleochannel; [B] linear elevation difference aligned with a sharp termination of the SW spur of the southernmost Ruakura hill [C]; apparent offset of a longitudinal bar [D], and; offset plateau aligned with where the longitudinal bar narrows abruptly [E].

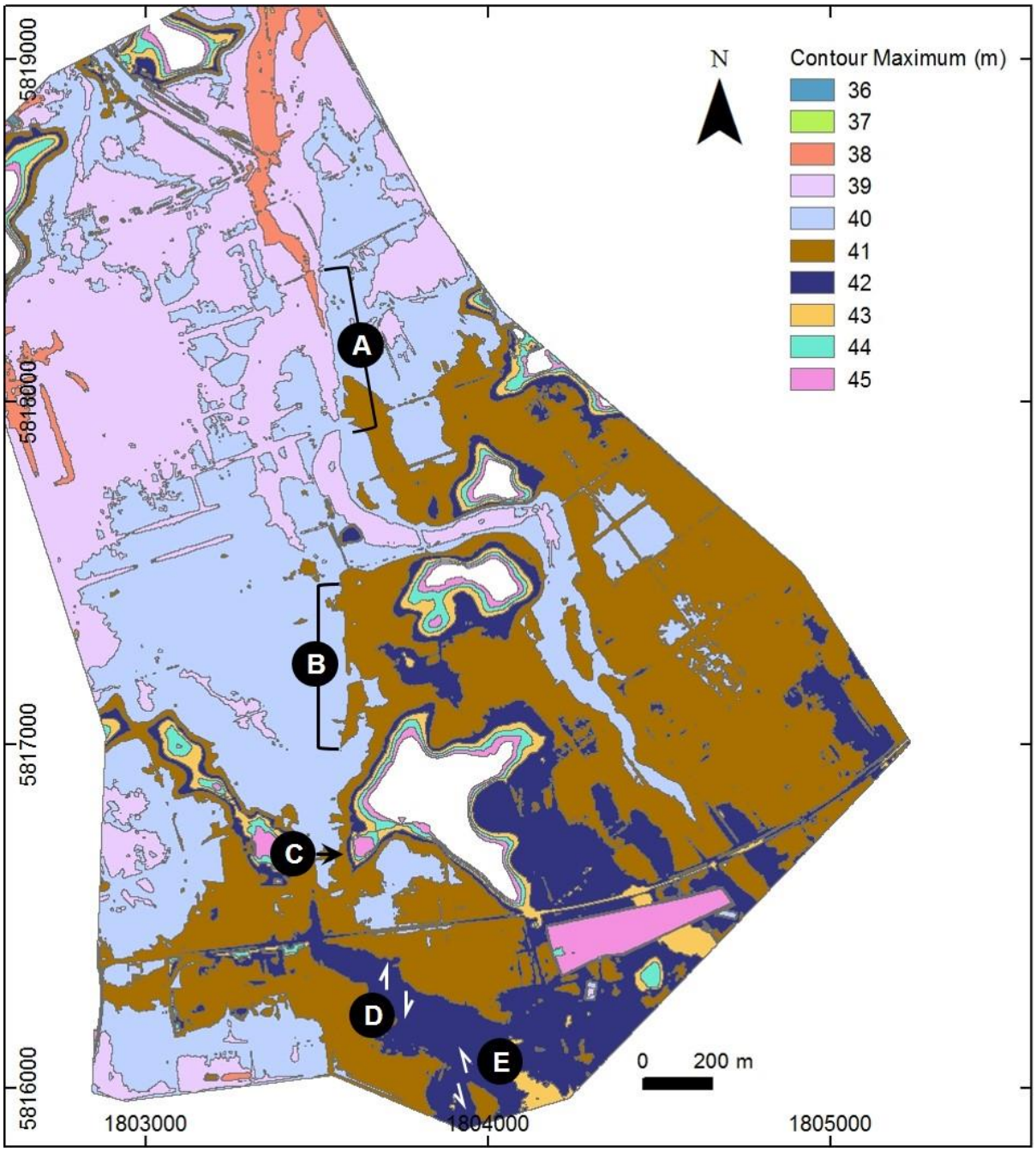

Figure 3.36. Polygon contour map of Ruakura/Fairview Downs classified to 1 m breaks. Notable features reflecting observations from field survey and/or historic image analysis include: [A] Constriction and pinching of the western paleochannel; [B] linear elevation difference aligned with a sharp termination of the SW spur of the southernmost Ruakura hill [C]; apparent offset of a longitudinal bar [D], and; offset plateau aligned with where the longitudinal bar narrows abruptly [E].

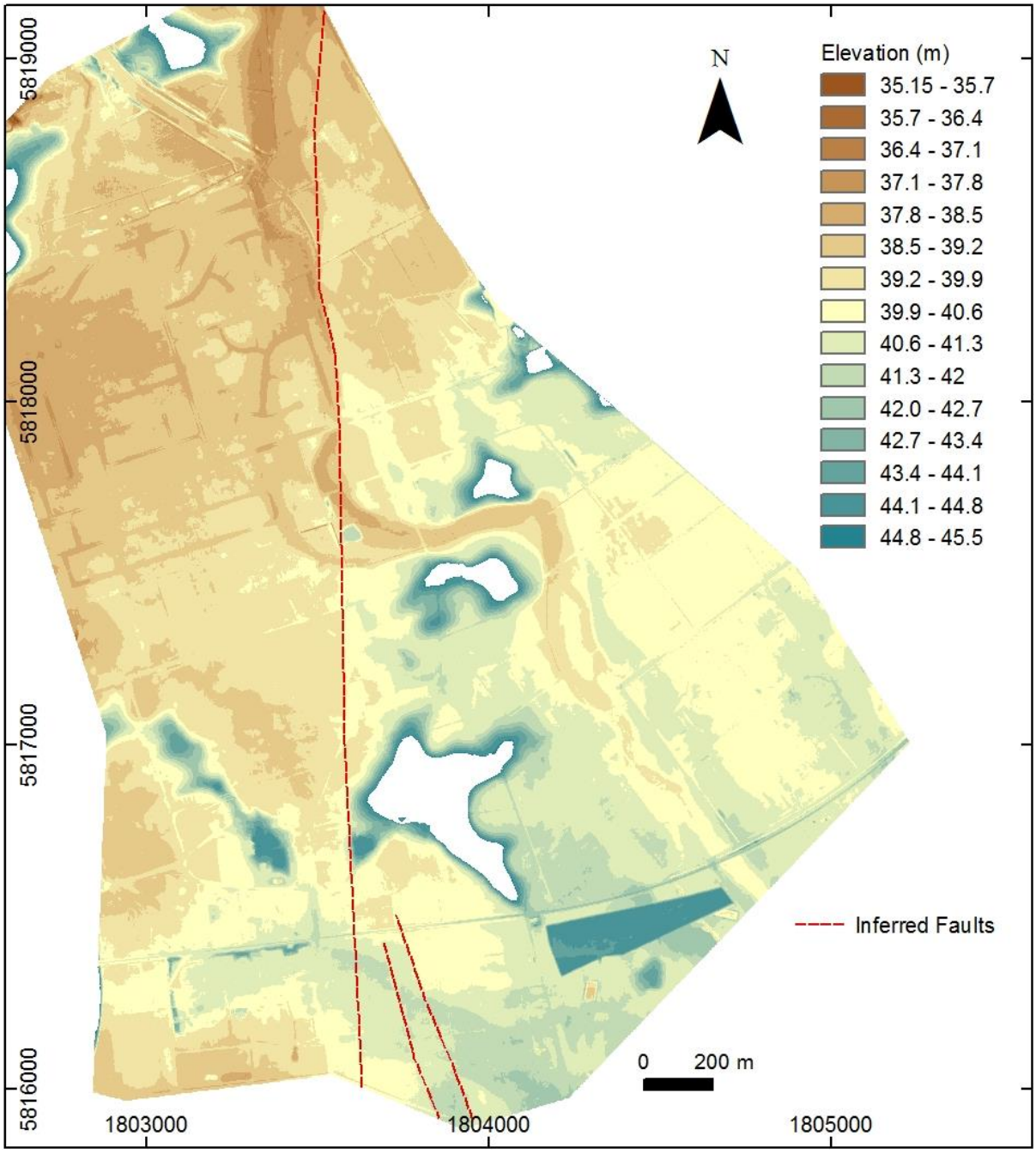

Figure 3.37. DEM of Ruakura/Fairview Downs classified to 0.7 m breaks with hypothesised faults based on geomorphological and microtopographical signatures.

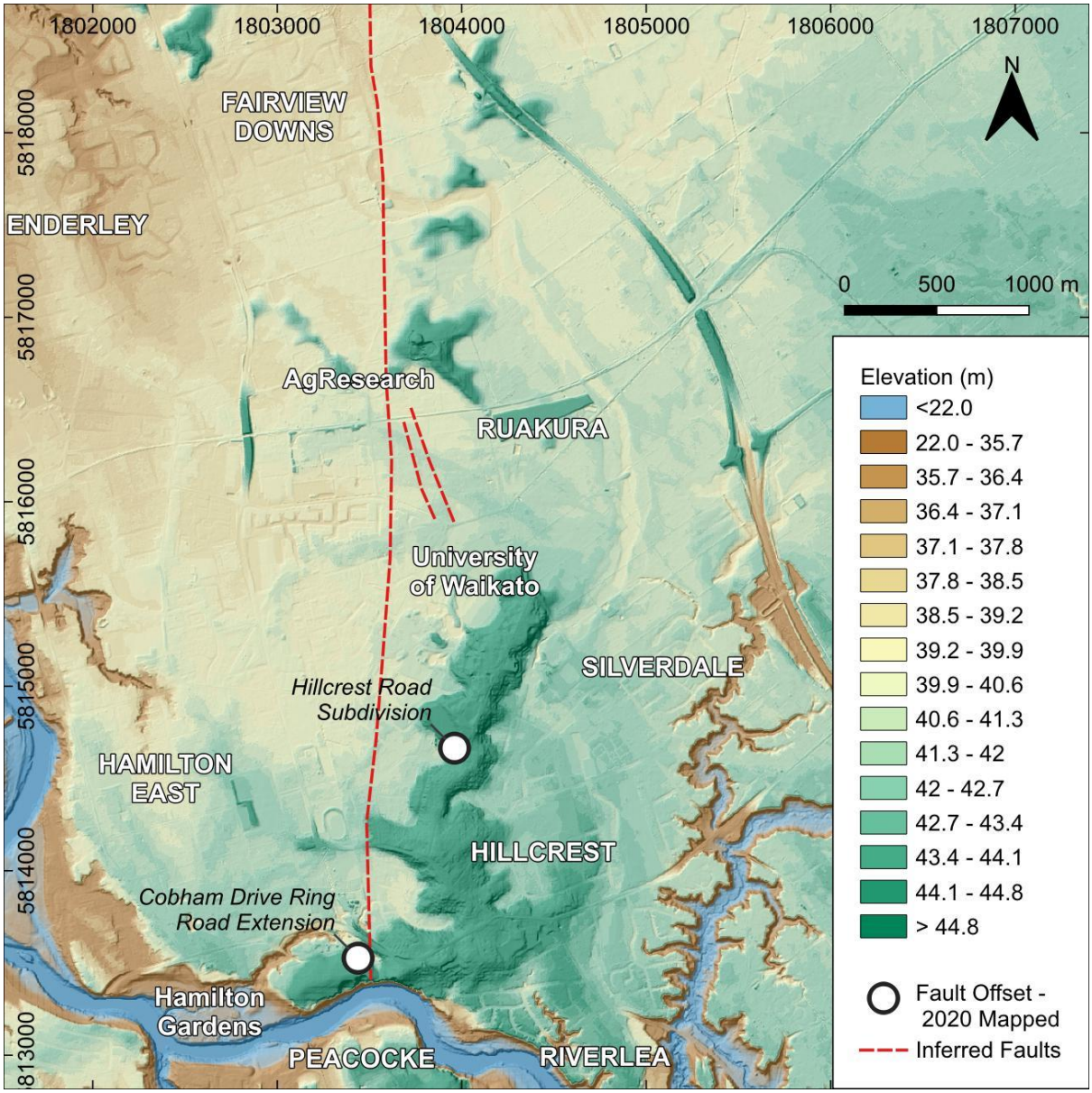

Figure 3.38. DEM of the eastern Hamilton area classified to 0.7 m breaks, overlaid with a hillshade relief, showing hypothesised relationship between inferred faulting at Ruakura and faults mapped in 2020 (particularly Cobham Drive).

3.6. Summary

Three-dimensional modelling of the Hamilton Basin provided useful information not only as confirmation for Te Tātua o Wairere Fault Zone being relevant for further study but also the general form of the Hinuera Surface. The fault zone occurs at, and effectively forms, the boundary between a hilly western half of the basin and the flatter alluvial plains in the eastern half in which hills are rare. Often alluded to as a ≤1° alluvial fan, the Hinuera Surface is more than an order of magnitude less than 1°, with 0.09° being the steepest slope profile found, nearest the Piarere Gap/Hinuera Disjunction. Taken from the eastern foot of the Hillcrest ridge and for some 6 km distance west of Te Tātua o Wairere Fault Zone, the planar surface is only 0.02° – the fault zone thus marking an extremely slight down-fan slope break.

Gravity anomaly and earthquake focal point data did not yield any readily identifiable patterns relating to the fault zone but did identify some general patterns within the Hamilton Basin. The lowest basin gravity anomaly (20–25 mGal) is ellipsoidal in shape, with the southern extent being parallel to the Kukutaruhe Fault Zone but no apparent relationship to either Te Tātua o Wairere Fault Zone or intra-basin earthquakes. Few earthquakes (28) have been recorded within the basin and the majority have been assigned nominal depths only, in accordance with methodology in place at the time they occurred. Notably, most earthquakes within the southern basin have been widely distributed whereas those in the north have mostly been clustered around the Puketaha area, c. 7 km NNE of the Hillcrest ridge.

Geomorphic mapping determined that the eastern paleochannel incorporated a number of features of interest which could be fault-influenced. Abrupt changes in paleochannel direction in conjunction with evidence for breakout flooding and attempts to find new flow paths, together with possible lateral stratigraphic discontinuities, may reflect seismic perturbation. The western paleochannel also exhibited discrete geomorphic abnormalities which may reflect seismogenesis. Of particular note is the constriction and ultimate pinching out of this channel north of the Ruakura hills, against a steep, semi-linear eastern bank. To the south, in close alignment with this section, was a slight (<0.5 m) semi-linear elevation difference

along the western side of the hills and a sharp, N-S aligned edge to the south-western spur of the southernmost hill. South of this area is a longitudinal bar that narrows in a seemingly disrupted manner and appears to have a degree of dextral offset. Inferring a line of faulting between these features aligns with the faults observed at Hillcrest Road and Cobham Drive and could also align with apparent features seen in historic imagery. On this basis – as well as site accessibility – the hypothesised lineament was selected as the target zone for ERT survey and scoping of paleoseismic trench placement, the results of which are presented in Chapter 4.

4. Stratigraphy of the Hinuera Surface at Ruakura

4.1. Introduction

Electrical resistivity surveys, hand auger investigations and trench stratigraphic analyses were completed within a narrow zone around the AgResearch and Tainui Group Holdings Ruakura farms (see Figure 2.2). Chapter 4 presents the resulting 2D inverted resistivity sections (and a single quasi-3D model), auger logs, trench sketches and stratigraphic logs.

4.2. Geophysical Inference via Electrical Resistivity Tomography

Without proximal intrusive insights such as along-array drill holes, direct correlation of inverted resistivity with stratigraphy was not possible; some hand augers were undertaken on the farm (see Section 4.3) but they were of limited depth and detail was at a scale too small to be correlated with inverted resistivity sections. Nevertheless, a broad assumption could be made, based on existing geological descriptions (e.g. Edbrooke 2005), that three-four relatively planar main sediment packages should be interpretable in an inverted resistivity section of as-deposited, non-fault disturbed stratigraphy:

- A soil-forming package with recent peat and/or tephra parent material;
- A sub-soil package or packages of alluvium (Hinuera Formation), and;
- A deep package of weathered clay (Hamilton and/or Kauroa Ash Formation) and/or ignimbrite (Walton Sub-Group).

Table 4.1 provides some guidelines as to what resistivity contours may represent. Although the inherent variability in earth materials and environments dictates that this table not be regarded as a strict diagnostic tool, local geology is

known to comprise deposits which could be expected to approximate the given ranges, thus comparison is considered appropriate. Low resistivity (<*c.* 100 Ω-m) is often representative of fresh water, silt/clay and weathered volcanics (such as rhyolitic tephra), high resistivity (>*c.* 200 Ω-m) tends to indicate coarse sediments (e.g. sand, gravel), while very high resistivity (>*c.* 1,000 Ω-m) is typical of indurated rocks and gravels.

Table 4.1. Typical reported resistivity values for selected earth materials. Values should be viewed as very general guides only, as true values can be influenced by many factors, such as weathering, saturation, temperature, acidity, and salinity (White 1985; Palacky 1988).

Material	**Resistivity Ω-m**
New Zealand fresh water[1]	50–100
Canterbury gravels (saturated)[1]	5,000–20,000 (500–1,000)
Glacial sand and gravel[2]	600–10,000
Silt/Clay[2,6] (saturated[1])	5–100 (2–20)
Hamilton Ash Formation[5]	27–60
Hinuera Formation gravels[5]	225–460
Saturated ignimbrite[1]	100–800
Weathered felsic volcanics[2]	60–120
Limestone and unweathered igneous rocks[2]	1,000–100,000
Peat[3,4]	22–200

[1] White (1985)
[2] Palacky (1988)
[3] Comas *et al.* (2015)
[4] Kowalczyk *et al.* (2017)
[5] Moon and de Lange (2017)
[6] Verstraeten *et al.* (2017)

The inverted resistivity sections that follow are presented in order of relevance and spatial relationship, rather than strict numerical sequence. A logarithmic ($\log_{10}$) scale is applied to inverted section resistivity contours; contour ranges for some sections were modified to allow direct comparison to one another but the raw sections (and cross-plots of measured *vs*. predicted apparent resistivity) are provided in Appendix C.

4.2.1. ERT Array RUA09

The first section presented is RUA09 as this was undertaken to provide an off-inferred fault reference against which other sections could be compared (Figures 2.2, 4.1 and 4.2). When compared against Table 4.1, the resistivity values and contours of Figure 4.2 lie within the range and stratigraphic sequence of anticipated lithological packages, also being relatively horizontal and uniform, so RUA09 is considered an appropriate reference section. It is probable that Figure 4.2 indicates a *c.* 1 m deep soil-forming layer (topmost green contours) of late Quaternary tephra (possibly peaty), underlain by *c.* 8 m of Hinuera Formation silts, sands and gravels (yellow to red contours). Some 3.5 m of possibly silt/clay, peat, or weathered volcanics (green contours) separates the base of the Hinuera Formation from the top of either Hamilton (or Kauroa) Ash Formation, or deeper, sub-water table Hinuera Formation (blue contours) which forms the remaining depth of the profile. Given the proximity of the other arrays, this starting assumption is maintained throughout analysis of the other arrays.

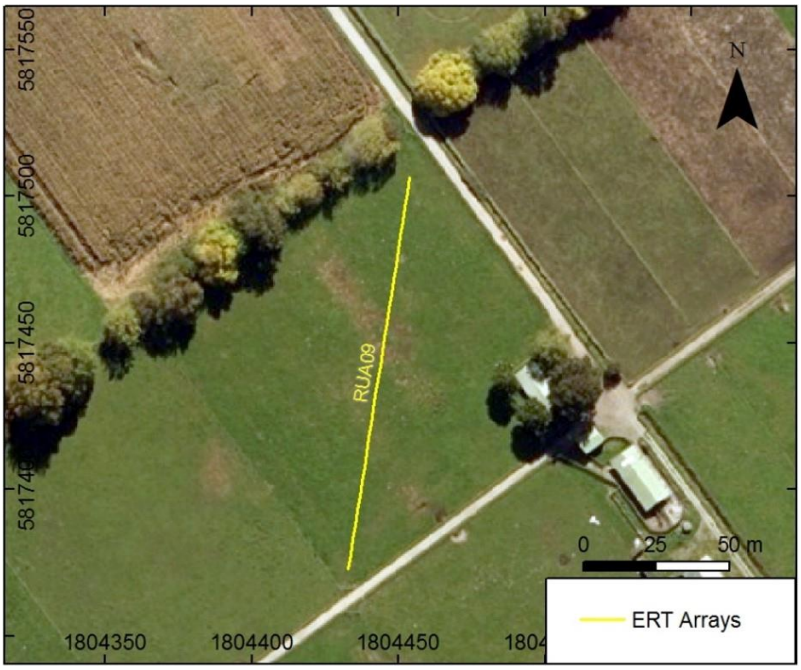

Figure 4.1. Aerial photograph overlaid with position of ERT array RUA09. Waikato 0.3m Rural Aerial Photos (2016-2019) sourced from the LINZ Data Service and licenced for reuse under CC BY 4.0.

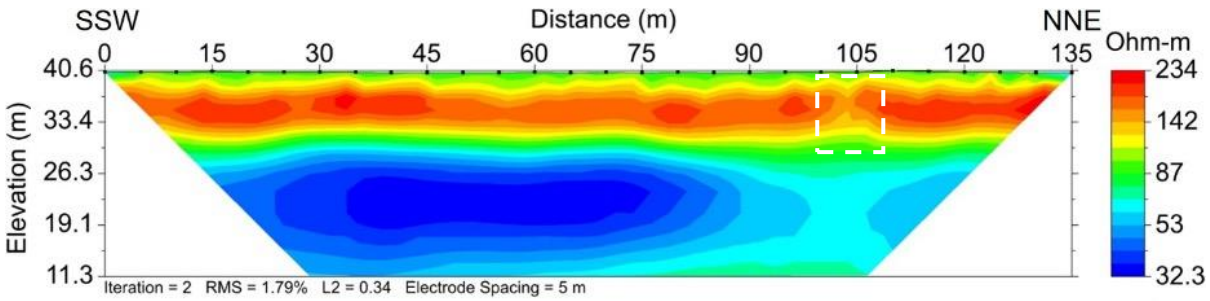

Figure 4.2. Inverted resistivity section for reference array RUA09. Against a mid-range of 68–112 Ω-m (green), there exists a lateral high resistivity anomaly close to the surface (yellow to red, *c.* 39.5–31.5 m ASL (elevation above sea level)), with a small area of relative intra-anomaly weakness (yet still >142 Ω-m) around 105 m (dashed white box). Approximately 3.5 m deeper than the base of the high resistivity anomaly a near-parallel low resistivity anomaly occurs (blue, *c.* 26.3–11.3 m ASL), with an intra-anomaly area of relatively higher resistivity (but still <68 Ω-m) beneath the subtly weaker zone of the high resistivity anomaly.

4.2.2. ERT Arrays RUA01 to RUA04, and RUA08

An unknown error resulted in unrecoverable data corruption for the first on-fault array so there is no inversion section for RUA01. RUA02–04, however, were parallel to and commenced only 10 m south of RUA01 (Figure 4.3), producing similar plots to one another so it is considered unlikely RUA01 would have been substantially different. Figures 4.4–4.6 show that the western paleochannel is distinguishable across RUA02–04 not only by topographic depression but also by a slight decrease in resistance across a shallow zone of high resistivity (134–325 Ω-m). The top of this lateral, approximately 3.8–6.8 m thick, anomaly is *c.* 2 m below the surface either side of the paleochannel banks while within the paleochannel itself it is thinner (*c.* 2.3–3.8 m) and occurs *c.* 3.8 m below the channel surface. A maximum surface high of 500 Ω-m is seen in the extreme WSW but with abnormal vertical zones of minimal resistivity (15 Ω-m) directly adjoining individual electrodes. This extreme anomaly is most pronounced in RUA04, which also shows a secondary high resistivity anomaly at depth, separated from the surface high by a large zone of minimal resistivity (Figure 4.6). Neither of these deeper major anomalies are seen in RUA02 or RUA03 but the vertical, electrode-adjacent minimal resistivity anomalies, surrounded by zones of maximum resistivity are seen in all three sections which suggest some form of localised interference or error.

Figure 4.3. Aerial photograph with inferred fault, overlaid with positions of ERT arrays RUA01–04 and RUA08. Waikato 0.3m Rural Aerial Photos (2016-2019) sourced from the LINZ Data Service and licenced for reuse under CC BY 4.0.

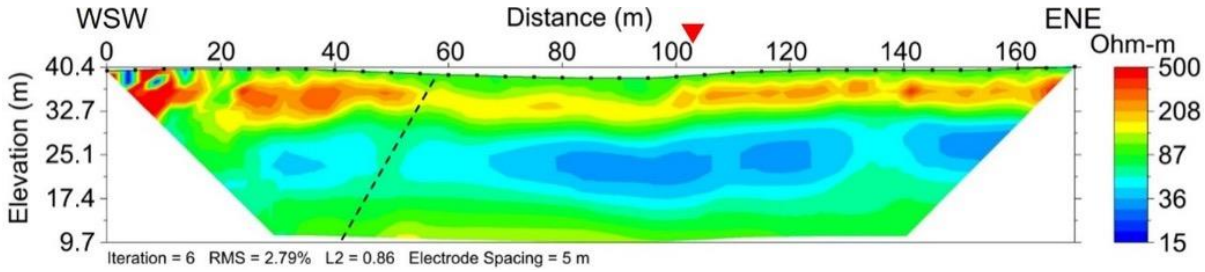

Figure 4.4. Inverted resistivity section RUA02, with the western paleochannel visible as a topographic depression between *c*. 35–120 m and red triangle marking position of geomorphically inferred fault. Against a 56–134 Ω-m mid-range (green), a shallow zone of high resistivity (yellow to orange) thins and weakens beneath the paleochannel, and is replaced in the extreme WSW by a zone of maximum resistivity (red). From *c*. 29–17.4 m ASL is a semi-contiguous zone of low resistivity (blue) which wanes in intensity and breaks up toward the WSW. Hypothesising a normal fault plane (dashed black line) between the high resistivity anomalies in the paleochannel's left bank and the break in the deeper low resistivity anomaly suggests an apparent *c*. 60° dip to the west.

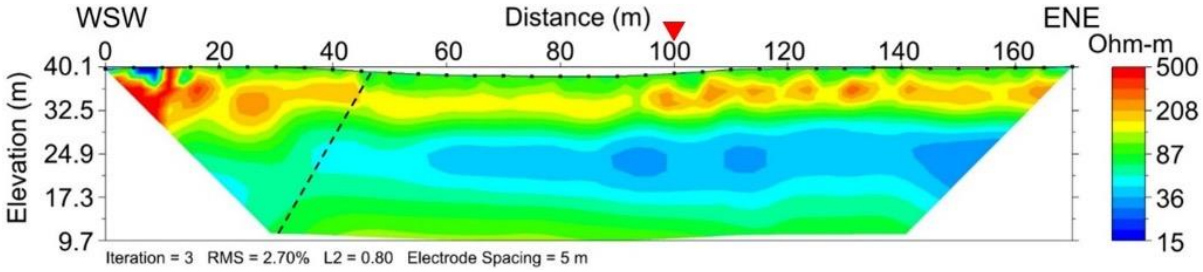

Figure 4.5. Inverted resistivity section RUA03, with the western paleochannel visible as a topographic depression between *c*. 40–110 m and red triangle marking position of geomorphically inferred fault. Against a 56–134 Ω-m mid-range (green), a shallow zone of high resistivity(yellow to orange) thins and weakens beneath the paleochannel, and is replaced in the extreme WSW by a zone of maximum resistivity (red). A lateral low resistivity anomaly (blue) wanes in intensity and appears to be offset to the WSW – the top being *c*. 24.9 m ASL in the WSW but stepping up to *c*. 29 m around the 30 m mark. Hypothesising a normal fault plane (dashed black line) between the high resistivity anomalies in the paleochannel's left bank and the low resistivity offset suggests an apparent *c*. 60° dip to the west.

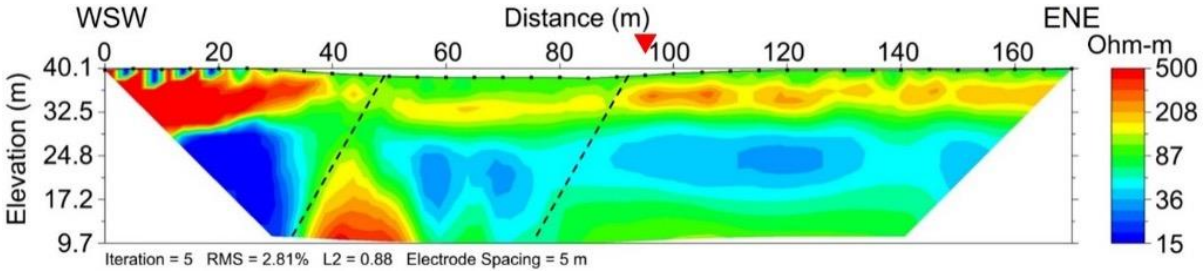

Figure 4.6. Inverted resistivity section RUA04, with the western paleochannel visible as a topographic depression between *c*. 25–115 m and red triangle marking position of geomorphically inferred fault. Against a 56–134 Ω-m mid-range (green), a shallow zone of high resistivity (yellow to orange) thins and weakens beneath the paleochannel, and is replaced in the WSW by a zone of maximum resistivity (red). A second zone of high resistivity occurs below *c*. 24.8 m ASL, between 35 m and 55 m distance, separated from the WSW surface high by a large block of low resistivity (dark blue). Two sub-vertical lobes of low resistivity (blue) between 50 m and 80 m, below c. 28.7 m ASL, connect to a horizontal low resistivity zone which continues ENE. Two normal fault planes of apparent *c*. 60° dip to the west are hypothesised; one between the major high anomalies, in a similar position to that shown in Figures 4.4 and 4.5, and the other between the eastern edge of the sub-vertical low resistivity lobes and a gap in shallow high resistivity along the paleochannel's right bank.

Although a fault was geomorphically inferred along the paleochannel's right bank, resistivity contours did not – except in RUA04 – provide any obvious evidence to support this, but potential fault planes were identified in all sections through the left bank. Figures 4.4–4.6 show a *c*. 60° apparent dip to the west when a plane is hypothesised from the edge of the shallow high anomaly within the left bank and

through the underlying breaks in low resistivity. Figure 4.6 incorporates an additional, parallel plane, from the approximate base of the eastern bank and following the eastern edge of the sub-channel sub-vertical lobes of low resistivity.

RUA08 was a short, high resolution survey, conducted across a portion of the same transect as RUA04 in an attempt to better resolve the observed anomalies in the WSW but with little success – RUA08 returned an highly abnormal range of resistivity from 1–100,000 Ω-m and the lowest RMS possible without discarding >20% of the data was 48.64% (Figure 4.7). Data discrepancy within such a discrete section could be explained by the presence of electrical interference, such as an electric fence shorting to earth but nearby electric fences were turned off. The nearest known underground utilities (water, storm water, fibre, and gas) were >30 m distant; the nearest utilities were also parallel to the arrays so the entirety of RUA04 (as well as RUA02 and RUA03) should have been affected if these were the cause. It is possible an unmapped or abandoned utility is present although there are no historic indications to suggest the likelihood. Cause notwithstanding, RUA08 indicates that there exists a physical reason, rather than processing error, for the major WSW anomalies of RUA04 (and likely RUA02–03).

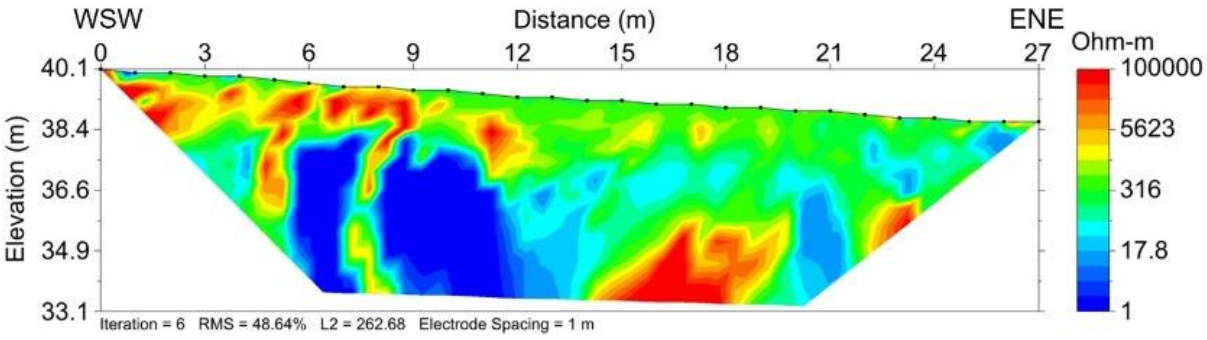

Figure 4.7. Inverted resistivity section RUA08, a high-resolution re-survey along the 20–47 m section of RUA04. Note the high RMS of 48.64% and L2-norm of 262.28; the section confirms an unknown source of data chaos within the paleochannel's left bank.

Arrays RUA02–04 were combined to produce the quasi-3D model of Figure 4.8. As the programme attempts to fit data across 10 m spaces between sections, twice the 5 m spacing between electrodes in the X-axes, detail is lost and greater error is introduced, highlighted by Figure 4.9 (hence the higher maximum resistivity of the 3D model *vs.* 2D sections). Figure 4.8 can be seen to generally reflect the presence of a deep, horizontal, low resistivity anomaly and a shallow high resistivity anomaly within the paleochannel left bank but offers little other detail. Detail loss is particularly a result of a calculated 1,779 Ω-m maximum resistivity (*cf.* 500 Ω-m in RUA02–04); the larger resistivity range effectively differentiates areas <*c.* 78 Ω-m as a homogenous low resistivity anomaly and all areas >c. 628 Ω-m as high anomalies.

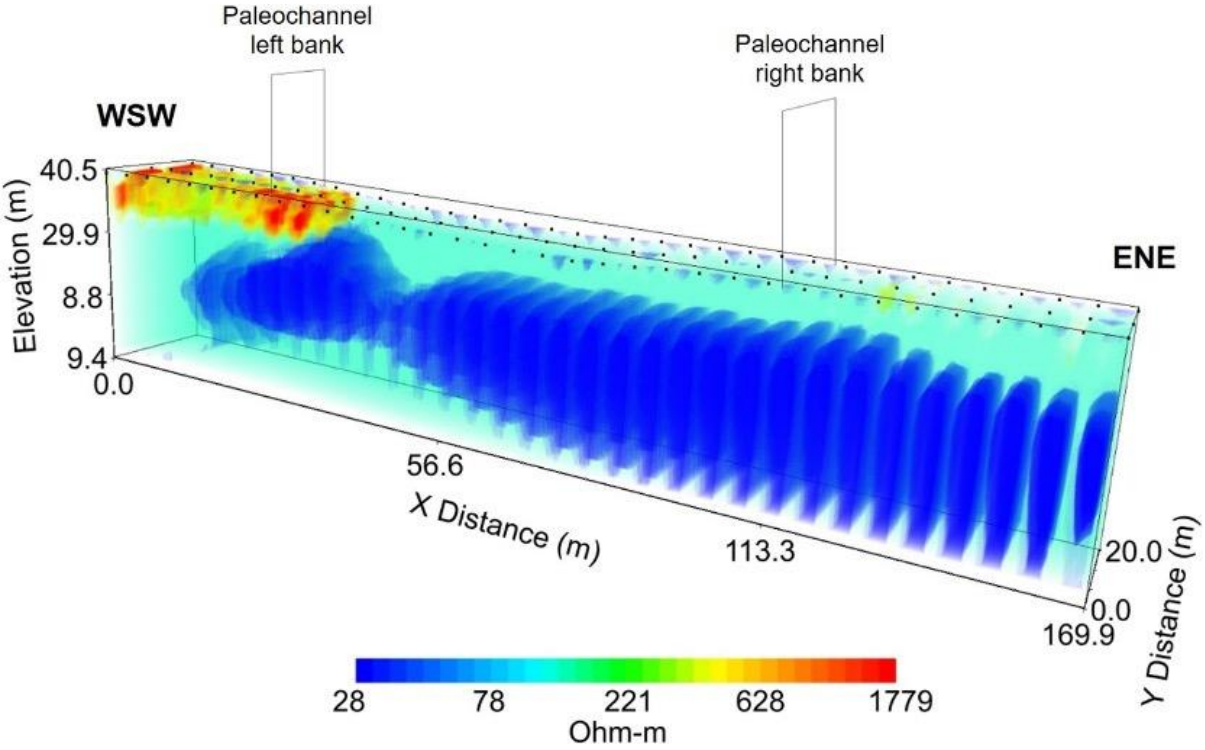

Figure 4.8. Quasi-3D model of 2D inverted resistivity sections RUA02–RUA04. An unresolved issue caused data to appear rather like silos. RMS of 16.2% and loss of detail over the 2D sections indicates that the model be regarded useful only for general visualisation of the low resistivity body and surficial highest resistivity anomalies atop the paleochannel's left bank.

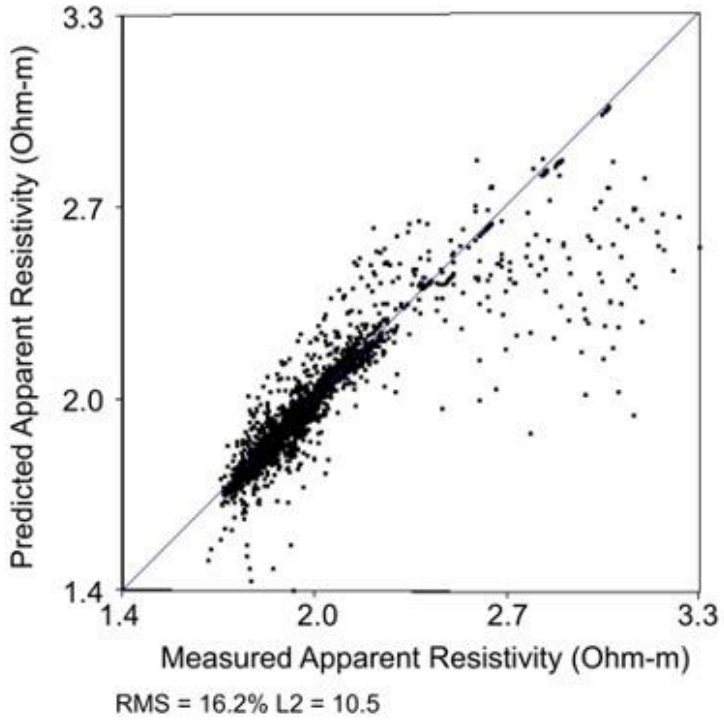

Figure 4.9. Cross-plot of measured vs. predicted apparent resistivity data for the quasi-3D combination of arrays RUA02–04 (third iteration). RMS (16.2%) and L2-norm (10.5) are much higher than all 2D inversion sections, highlighting the error introduced by attempting to fit data across space larger than the distance between electrodes.

Discounting the extreme anomalies in the WSW of RUA02–04, being twice as high as the maximum observed in RUA09, the range of resistivity values in each section are not dissimilar from those seen in the reference section. The general relationship between high, low and mid-range resistivity values also suggest that RUA02–04 are stratigraphically akin to RUA09 but with some difference at surface and possible deformation to the WSW. Shallow high anomalies are slightly depressed in both height and value beneath the paleochannel, which it is reasonable to presume relates to natural channel erosion through upper Hinuera Formation sands and gravels. The nature of apparent offset to the WSW in the deep, lateral low resistivity anomaly (particularly in RUA02 and RUA03) suggests the anomaly reflects a lithological change rather than groundwater body; the anomaly is possibly either deeper, weathered rhyolitic Hinuera Formation or one of the ash formations.

4.2.3. ERT Array RUA06

RUA06 crossed the same line of inferred fault as RUA02–04, *c.* 430 m to the north, but returned a narrower resistivity range with a maximum 143 Ω-m (*cf.* 500 Ω-m) and minimum 80 Ω-m (*cf.* 15 Ω-m) (Figures Figure 4.10 and 4.11). By direct

comparison, the entirety of RUA06 falls within the mid-range of the earlier sections and would seem non-anomalous. In relative context, however, Figure 4.11 shows a semi-lenticular, concave zone of high resistivity within the right bank of the paleochannel, disconnected from a second high beneath the paleochannel. The shallowest portions of this high resistivity anomaly are <2 m below surface while the core is *c.* 21 m deep, at *c.* 18.5 m ASL. The slight gap between high anomalies coincides with the geomorphically inferred line of fault (Figures Figure 4.10 and 4.11). A low resistivity anomaly is seen at the ENE edge of the section at the same elevation as the lenticular high and there is also an undulating zone of slightly lowered resistivity across the base, though lowest resistivity occurs within the upper *c.* 5 m of the paleochannel (Figure 4.11). The lack of lateral continuity in conjunction with lower overall resistivity values suggests a lithostratigraphic change between RUA06 and the earlier sections. High resistivity values in the section are within the upper range for peat while the low resistivity values are consistent with fine sediments; given the proximity to modern swampland it may be that the section represents an older backswamp, with peat overlying silt and/or clay.

Figure 4.10. Aerial photograph with inferred fault, overlaid with position of ERT array RUA06. Waikato 0.3m Rural Aerial Photos (2016-2019) sourced from the LINZ Data Service and licenced for reuse under CC BY 4.0.

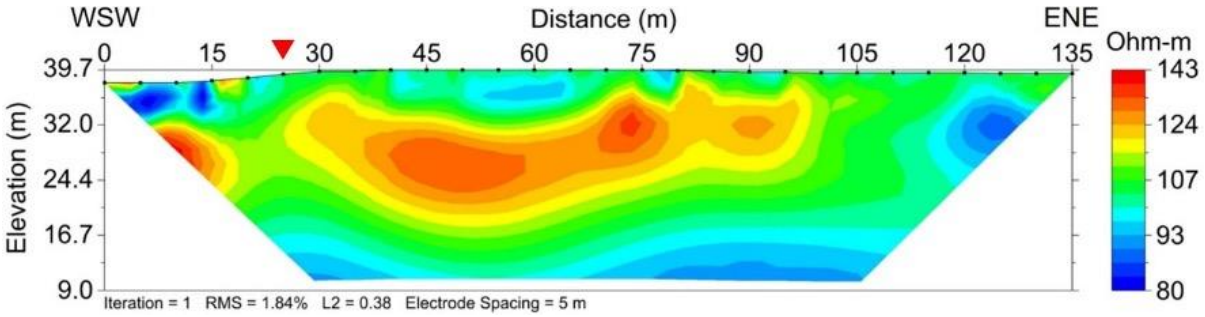

Figure 4.11. Inverted resistivity section RUA06, with the western paleochannel visible as the topographic low at the WSW edge and red triangle marking position of geomorphically inferred fault. The range of resistivity is small and the entire section would be considered relatively non-anomalous using the same contour ranges as RUA02–04 but against a 100–116 Ω-m mid-range (green), a semi-lenticular, concave high resistivity zone (yellow to orange) is the predominant feature, potentially related to a high in the extreme WSW but displaced by a low anomaly (blue) in the ENE.

4.2.4. ERT Arrays RUA05, RUA07, RUA10 and RUA11

Arrays RUA05, RUA10 and RUA07 were along (but oblique to) the N-S line of inferred fault, *c.* 350 m south of RUA01–04 (Figure 4.12). All three displayed notable anomalies but RUA05 was particularly unusual (Figure 4.13). A large block of low resistivity, *c.* 25 m wide, is seen in the SW half of RUA05, below *c.* 34.2 m ASL, and sub-vertical low anomalies occur across the NE half, from *c.* 38 m ASL to base; the most prominent, central low being within 10 m of the inferred fault. Notably, the SW block of low resistivity in Figure 4.13 was initially thought to be interference from a buried water pipe, mapped at the 30 m mark (see Appendix B). However, the top of the anomaly is >7.5 m deep which would be an unusual depth for such a pipe to have been laid; subsequent hand augers (refer Section 4.3) also found the subsoil to comprise apparently natural material whereas fill – more likely to be associated with a buried utility – was recorded at the 15 m mark. The water pipe is potentially the cause of this large anomaly, particularly if it is leaking and water is exploiting a zone around it, but it may also be un-related and its' location has simply been inaccurately mapped.

A shallow high resistivity zone in RUA05 is non-contiguous, absent altogether between *c.* 65 m and 80 m, and becomes particularly patchy and sub-horizontal across the SW (Figure 4.13). Coinciding with this disruption of the shallow high anomaly is a slight surface slope break and decrease in elevation; the top of the high appears to be *c.* 1.2 m lower in the SW than in the NE. Two significant high resistivity anomalies also occur at depth. The first is at *c.* 27 m ASL, between 50 m and 65 m, and is the zone of highest resistivity (64,543 Ω-m) while the second, at *c.* 28.5 m ASL, between 95 m and 100 m, is weaker (1,845–6,036 Ω-m) and coincides with the inferred fault.

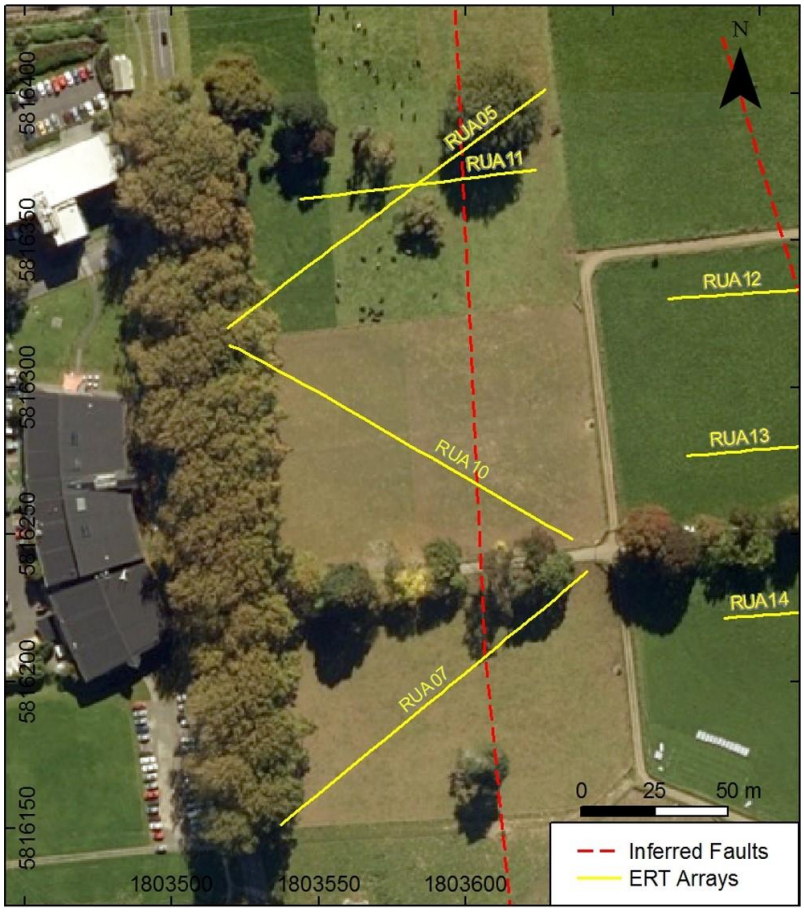

Figure 4.12. Aerial photograph with inferred fault, overlaid with positions of ERT arrays RUA05, RUA07, RUA10 and RUA11. Waikato 0.3m Rural Aerial Photos (2016-2019) sourced from the LINZ Data Service and licenced for reuse under CC BY 4.0.

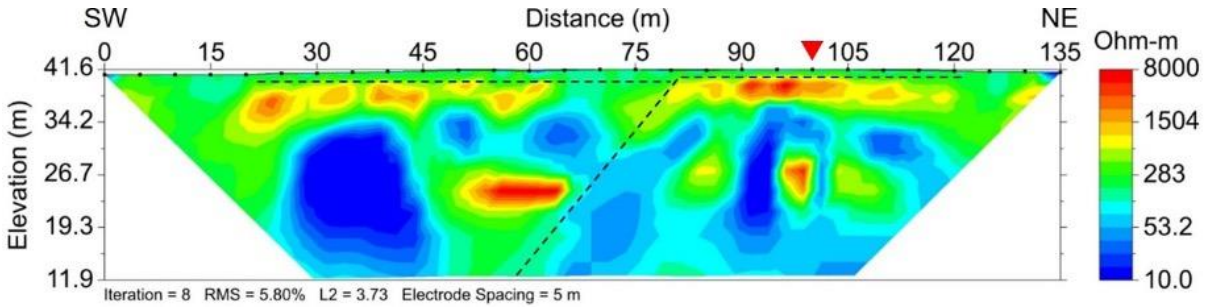

Figure 4.13. Inverted resistivity section RUA05 with red triangle marking position of geomorphically inferred fault. Maximum resistivity is 64,543 Ω-m but the contour range has been clipped for consistency with RUA07 and RUA10–14, and to preserve detail. Original, un-clipped section is included in Appendix C. Against a *c*. 120–650 Ω-m mid-range (green), a shallow but non-contiguous high resistivity anomaly (yellow to red) appears to be significantly disrupted towards the SW and slightly deeper than in the NE (*c*. 39.1 m *cf*. 40.3 m, horizontal dashed black lines for emphasis). Discrete high resistivity anomalies also occur at depth and appear slightly offset; a central ellipsoidal anomaly occurs below 26.7 m ASL with a smaller semi-triangular anomaly between *c*. 90 m and 100 m, below *c*. 28.5 m ASL. Major low resistivity anomalies (blue) occur across the section – a single large block in the SW half and multiple sub-vertical zones across the NE half. Hypothesising a plane through the central gap in the surface high anomaly, along the edge of the central sub-vertical low and the deep central high, produces an apparent c. 51° dip to the SW (oblique dashed black line).

RUA10 is the section in this series most similar to the reference RUA09, in having a lateral, relatively planar, low resistivity layer between *c*. 33.7–19.4 m ASL but that is as far as the similarity extends. Where it reaches lowest resistivity, near the NW edge of the section and in a similar position to the major SW low of RUA05, the lateral low anomaly of RUA10 appears to deepen to the base of the section (Figure 4.14). A dike-like downward extension of the low resistivity anomaly between the 80 m and 90 m electrodes is also at a similar along-section distance to the strongest NE sub-vertical low in RUA05. This vertical extension is *c*. 7.5 m off the inferred fault and a lobe of similar width and value can be seen at the base of the section to the immediate SE, with the inferred fault midway between them. High resistivity occurs at shallow depth across the central and SE side of the section but is absent between *c*. 7.5 m and 46 m; this otherwise horizontal high is strongest in the extreme NW, being a maximum 12,000 Ω-m. A second, weaker high resistivity anomaly (*c*. 1,020–3,500 Ω-m) occurs at the base of the section (<c. 16 m ASL) between 45 m and 75 m.

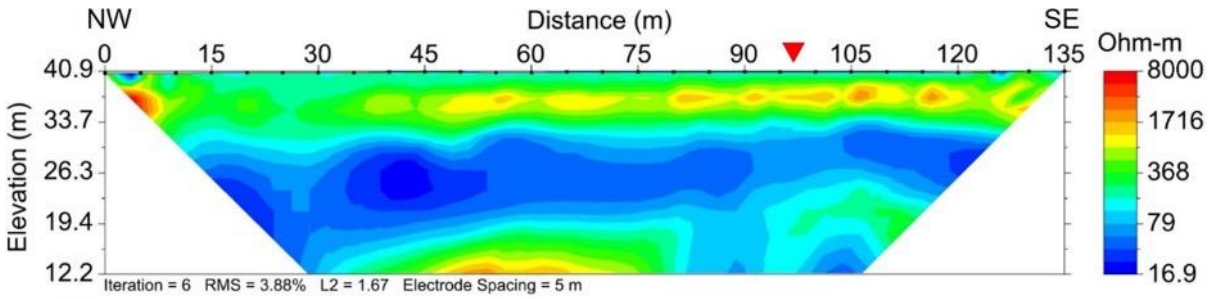

Figure 4.14. Inverted resistivity section RUA10 with red triangle marking position of geomorphically inferred fault. Maximum resistivity is 12,000 Ω-m but the contour range has been clipped for consistency with RUA05, RUA07 and RUA11–14, and to preserve detail. Original, un-clipped section is included in Appendix C. Against a *c*. 170–795 Ω-m mid-range (green), a shallow, non-continuous high resistivity zone (yellow to red) is strongest in the NW but absent between *c*. 7.5–46 m. Beneath the break in this high anomaly is a pronounced portion of a deeper, semi-horizontal low resistivity anomaly (blue); a downward vertical extension of this low occurs between the 80 m and 90 m electrodes.

Similar to RUA10, the most prominent feature of RUA07 is a lateral low resistivity anomaly <*c*. 33.7 m ASL (Figure 4.15). However, this anomaly is less planar, with a gently undulating upper contour and lower contours dipping to the base of the section between *c*. 0–40 m and *c*. 60–105 m, with the latter coinciding with the line of inferred fault. Little shallow high resistivity exists, only a few small patches (*c*. 640–1,200 Ω-m); a discrete area of very high resistivity (4729 Ω-m) at <1 m depth in the NE is close to a known buried telephone cable so is presumed to be interference. A *c*. 5 m wide lobe of high resistivity (maximum 1851 Ω-m) is seen *c*. 22.5 m ASL, below a small hump in the low resistivity layer between 45–50 m.

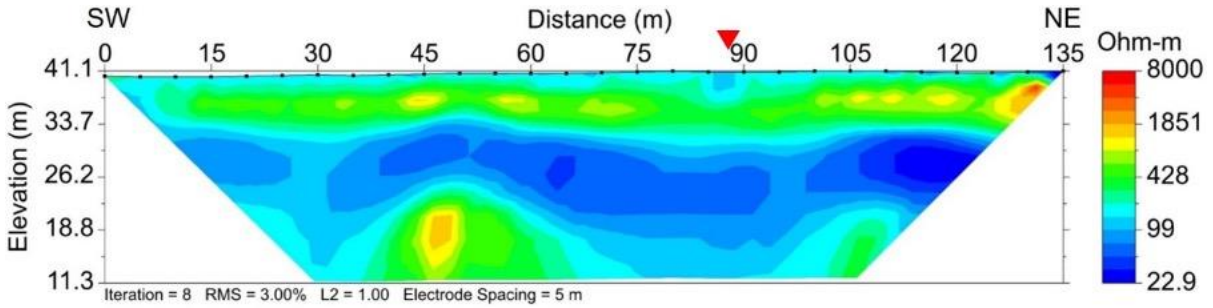

Figure 4.15. Inverted resistivity section RUA07 with red triangle marking position of geomorphically inferred fault. Maximum resistivity is 4,725 Ω-m but the contour range has been extended for consistency with RUA05 and RUA10–14. Original, un-clipped section is included in Appendix C. Against a *c*. 205–890 mid-range (green), a lateral low resistivity anomaly (blue) undulates, deepening toward the base and rising above a small high resistivity anomaly in the SW. The small zone of maximum resistivity in the NE(yellow to red) is presumed to be interference from a buried telephone cable in the vicinity.

RUA11 crossed RUA05 at a 30° angle, using reduced electrode spacing to try and image the central anomalies of the latter with slightly greater resolution. The arrays crossed at the 80 m point of RUA05 and 40 m point of RUA11. An otherwise lateral shallow high resistivity anomaly, similar to the reference section RUA09, is broken between 36 m and 39 m and the western zone appears to dip toward centre. As can be seen in Figure 4.16, the maximum resistivity anomaly of RUA05 does not occur in RUA11 but a substantial high exists below *c.* 32 m ASL, between 42–52 m, which may correlate with the smaller, semi-triangular high anomaly of RUA05. Low anomaly zones either side of this deep high anomaly – appearing to be sub-vertical to the east – appear to match similar areas of RUA05. The line of inferred fault is between the deep high and adjoining eastern sub-vertical low (Figure 4.16).

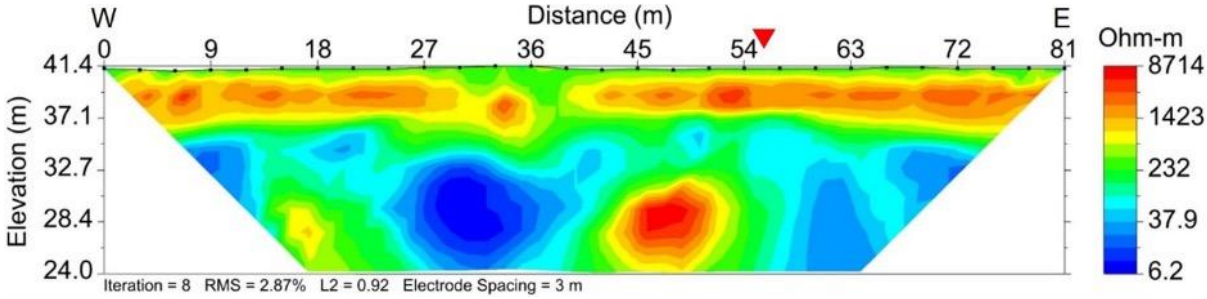

Figure 4.16. Inverted resistivity section RUA11 with red triangle marking position of geomorphically inferred fault. A shallow lateral high resistivity anomaly (yellow to red) is broken near the centre, with the western portion appearing to dip toward centre. Deeper high (yellow to red) and low (blue) resistivity anomalies appear to be of similar form and at similar elevations to those seen in RUA05.

The pattern of anomalies in RUA05, RUA07, RUA10, and RUA11 suggested this area warranted particular scrutiny and that 3D-visualisation would be useful. Although conducted in close proximity, the arrays were not in parallel so quasi-3D modelling was not possible and earlier attempts with RUA02–04 had in any case proved this method to be unsatisfactory. Instead, 2D sections were georeferenced and placed into a Leapfrog Geo 3D mesh with a polyline of the geomorphically inferred fault. As well as providing visual context, the mesh confirmed that sub-vertical low resistivity anomalies of RUA05, RUA10, and RUA11 aligned along-fault with one another, as well as the area of RUA07 in which the lateral low resistivity anomaly rises above a deep high resistivity anomaly (Figures 4.17 and 4.18).

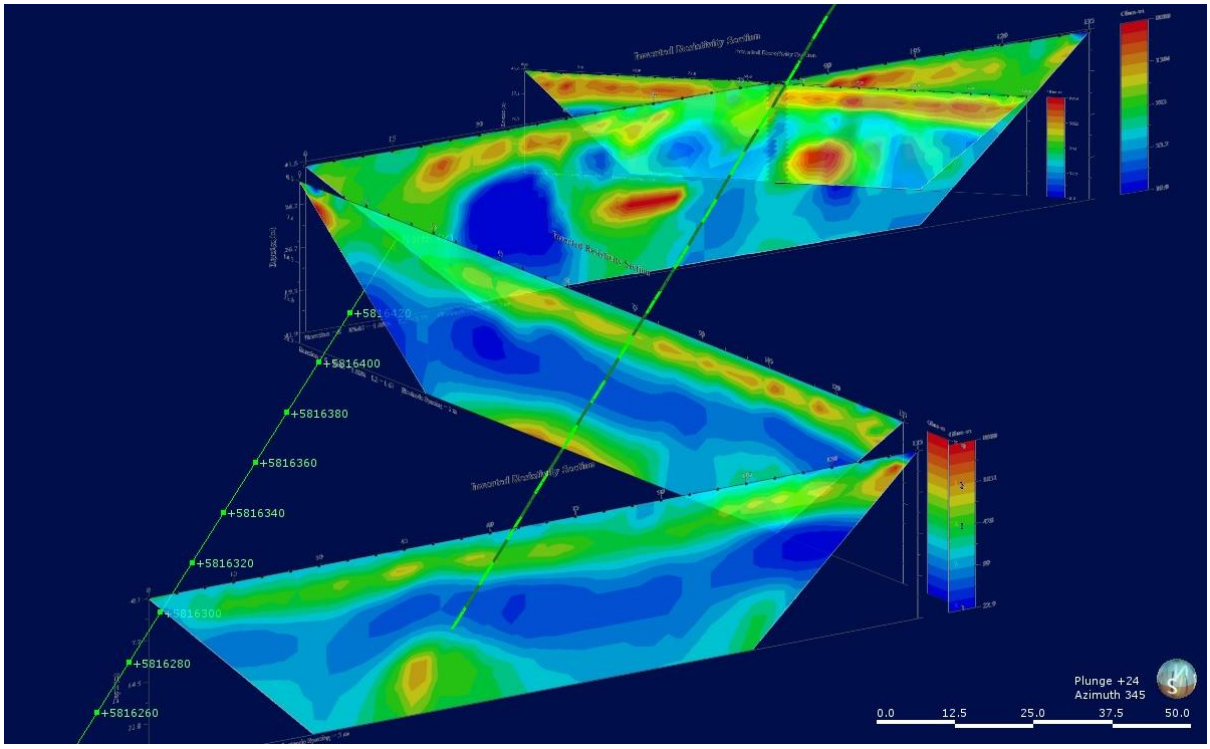

Figure 4.17. Oblique 3D rendering looking NNE across ERT arrays RUA07, RUA10, RUA05, and RUA11 (nearest to farthest). Dashed line is hypothesised fault trace.

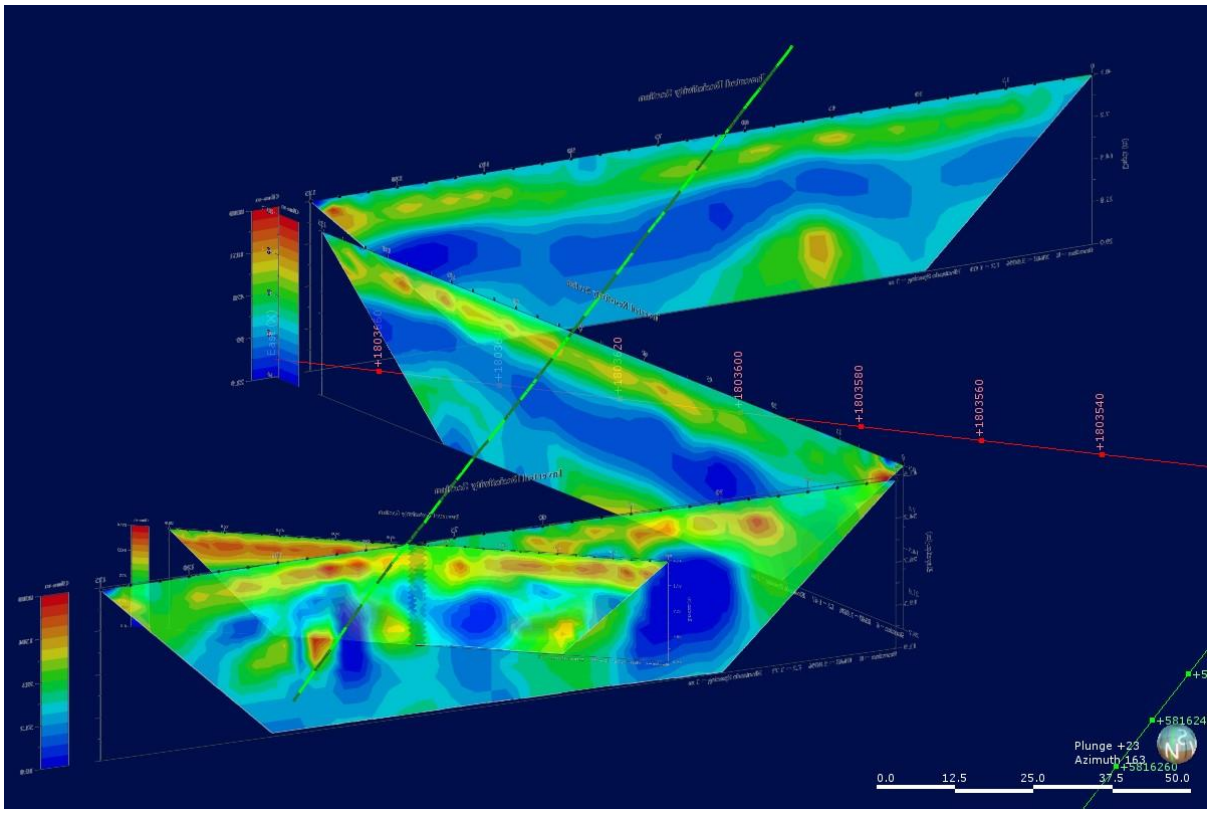

Figure 4.18. Oblique 3D rendering looking SSW across ERT arrays RUA11, RUA05, RUA10, and RUA07 (nearest to farthest). Dashed line is hypothesised fault trace.

While RUA07 and RUA10 bore some relationship to the reference section RUA09, this was essentially only by having a lateral low resistivity anomaly at depth. These low anomalies displayed greater variation than the reference, being semi-horizontal but with undulating contours and varying thicknesses. Low resistivity anomalies generally occurred at similar depth in RUA05 and RUA11 but were chaotic in form and distribution, lacking any lateral continuity (Figures Figure 4.13 and 4.16). True resistivity values for low anomalies in RUA07 and RUA10 were a little higher than in RUA09 (but still <100 Ω-m) while those for RUA05 and RUA11 were similar to RUA09, thus lithology is likely to still be dominated by silt or clay. Deep high resistivity anomalies >800 Ω-m in RUA07 and RUA10, beneath the low resistivity layers, approximate the range for saturated ignimbrites so the sections may show deeply buried Puketoka Formation (Figures Figure 4.14 and 4.15). The immediate sub-surface in all four sections is much higher in resistivity value than RUA09 (>570 Ω-m *cf.* >112 Ω-m) with anomalous high resistivity areas being non-planar and non-contiguous but, given the similar elevations and assumed depositional environments, it is likely that the four sections reflect lenses of greater gravel content. Beyond suggesting that much deeper, discrete lenses of high resistivity amongst the chaotic low resistivity anomalies of RUA05 and RUA11 may be fault-displaced units, their lithology is undecipherable – particularly as their resistivity values are vastly greater than any other expected units.

4.2.5. ERT Arrays RUA12 to RUA14

To the east of the main geomorphically inferred fault, arrays RUA12–14 were placed parallel to one another, across a hypothesised minor strand or splinter fault (Figure 4.19). RUA12 appears similar to RUA05 and RUA11, in showing rather chaotic, non-contiguous low resistivity anomalies at depth, whereas deep anomalies in RUA13 and RUA14 are like those of RUA07 and RUA10 – lateral and contiguous but undulating (Figures Figure 4.20–4.22). In all three sections, there is either a gap between low resistivity anomalies (Figure 4.20) or a slight relative increase in resistivity (Figures Figure 4.21 and 4.22) in the vicinity of the inferred fault. There are no deep high resistivity anomalies but all sections have shallow, semi-horizontal anomalies, although their values vary greatly.

Maximum resistivity in RUA12 is *c.* 60,000 Ω-m and the anomaly extends from the western edge of the section to *c.* 63 m distance – dipping slightly to the east as it thins (Figure 4.20). There is a noticeable jump in elevation at 27 m distance, where the base of the high resistivity anomaly pinches upward, coinciding with an upward tapering of the tops of two underlying low resistivity zones. A much lower maximum resistivity of *c.* 9,600 Ω-m occurs in RUA13 and the anomaly appears to be the reverse of RUA12, extending from the eastern edge of the section to thin out by *c.* 21 m distance (Figure 4.21). The anomaly may, however, just be discontinuous and actually continue westward, albeit with lesser resistivity value; a gap of 3–4 m separates the main anomaly from a weaker (but still >1,100 Ω-m) anomaly of similar elevation and thickness. There appears to be a very subtle convex form to the main high anomaly of RUA12 directly at the point coinciding with the inferred fault. RUA14 incorporates the lowest maximum resistivity of the three sections, *c.* 3,300 Ω-m, and by comparison to RUA12 and RUA13, shallow high resistivity anomalies are patchy with no significant features (Figure 4.22). Lithological inference for the three sections is as for RUA05, RUA07, RUA10, and RUA11.

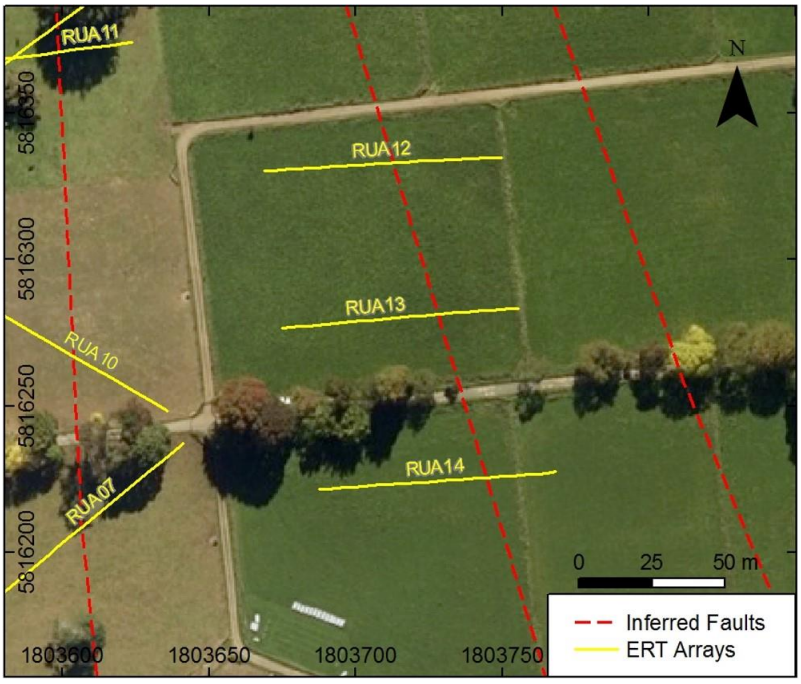

Figure 4.19. Aerial photograph with inferred faults, overlaid with positions of ERT arrays RUA12–14. Waikato 0.3m Rural Aerial Photos (2016-2019) sourced from the LINZ Data Service and licenced for reuse under CC BY 4.0.

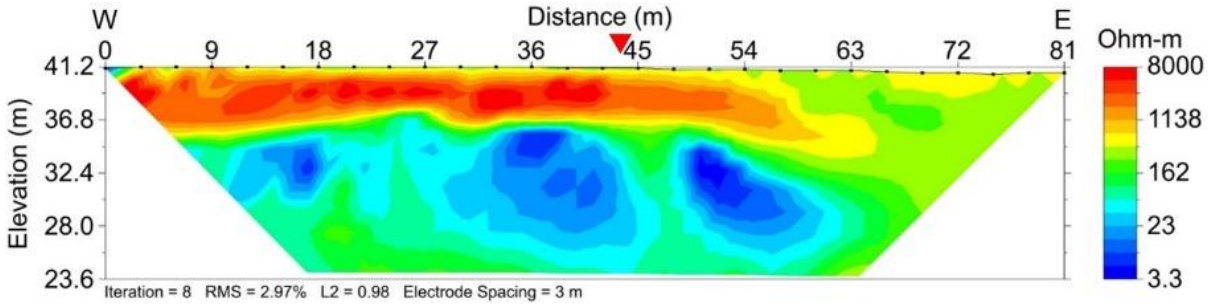

Figure 4.20. Inverted resistivity section RUA12. Maximum resistivity is 59,577 Ω-m but the contour range has been clipped for consistency with RUA05, RUA07, RUA10–11 and RUA13–14, and to preserve detail. Original, un-clipped section is included in Appendix C. Against a *c*. 60–430 Ω-m mid-range (green), discrete, semi-ellipsoidal low resistivity anomalies (blue) occur at depth while a shallow, relatively planar high resistivity anomaly (yellow to red) stretches from the western edge to *c*. 63 m, with a small pinch upward around 27 m.

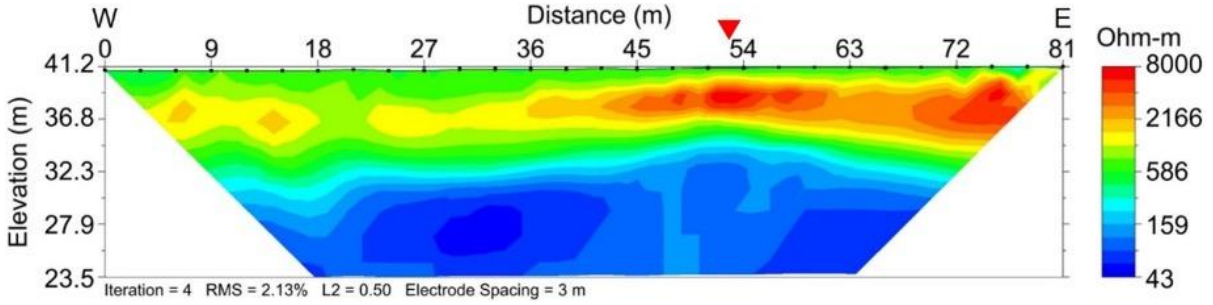

Figure 4.21. Inverted resistivity section RUA13. Maximum resistivity is 9,629 Ω-m but the contour range has been clipped for consistency with RUA05, RUA07, RUA10–12 and RUA14, and to preserve detail. Original, un-clipped section is included in Appendix C. Against a *c*. 305 – 1,100 Ω-m mid-range (green), a lateral, undulating low resistivity anomaly (blue) occurs at depth which exhibits a subtle increase in resistivity in the vicinity of the inferred fault. A similar shallow high resistivity anomaly to RUA12 exists but in the reverse orientation, being strongest toward the eastern edge.

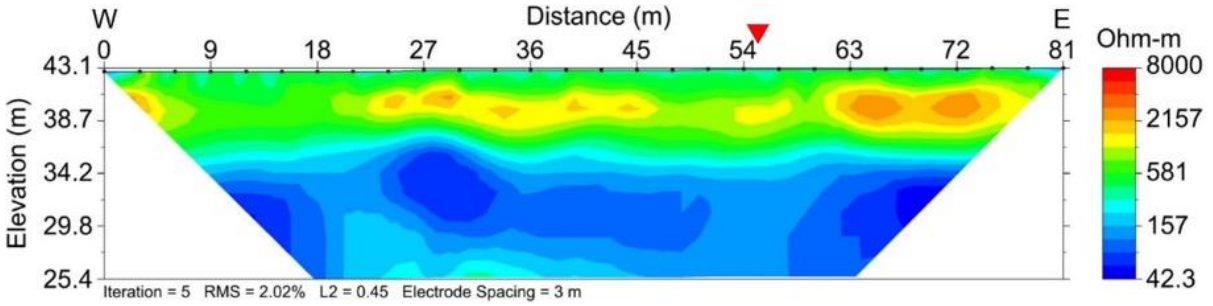

Figure 4.22. Inverted resistivity section RUA14. Maximum resistivity is 3,332 Ω-m but the contour range has been extended for consistency with RUA05, RUA07 and RUA10–13. Original section is included in Appendix C. Against a 300–1,100 Ω-m mid-range (green), a lateral, undulating low resistivity anomaly (blue) occurs at depth which exhibits a subtle increase in resistivity in the vicinity of the inferred fault and around the 18 m mark. Shallow high resistivity anomalies (yellow to orange) are patchy but relatively planar.

4.2.6. ERT Array TGH01

TGH01 was the longest array attempted, being a semi-wildcat, off-inferred fault survey (Figure 4.23). Resistivity values were most akin to RUA07 and RUA14, and TGH01 appears to support the general premise of a major lateral (but variable) <100 Ω-m low resistivity anomaly across the field area between *c.* 33 m and 15.5 m ASL. There is a large, 50–60 m wide, downward extension of the low anomaly, between *c.* 48–100 m distance. As with RUA07 and RUA14, shallow high resistivity anomalies are approximately surface-parallel but non-contiguous and variable in intensity (750–5,636 Ω-m). Lithological inference for the section is as for RUA05, RUA07, RUA10, and RUA11.

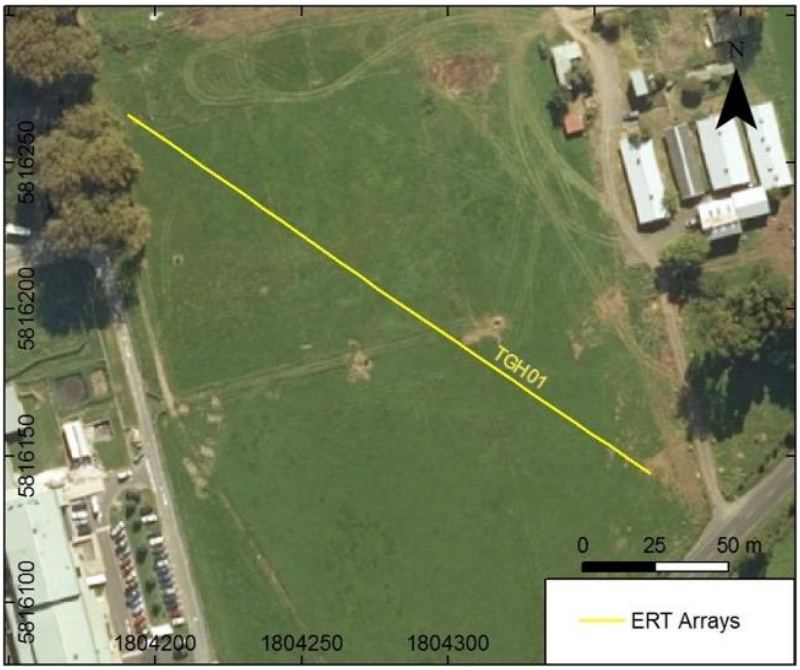

Figure 4.23. Aerial photograph overlaid with position of ERT array TGH01. Waikato 0.3m Rural Aerial Photos (2016-2019) sourced from the LINZ Data Service and licenced for reuse under CC BY 4.0.

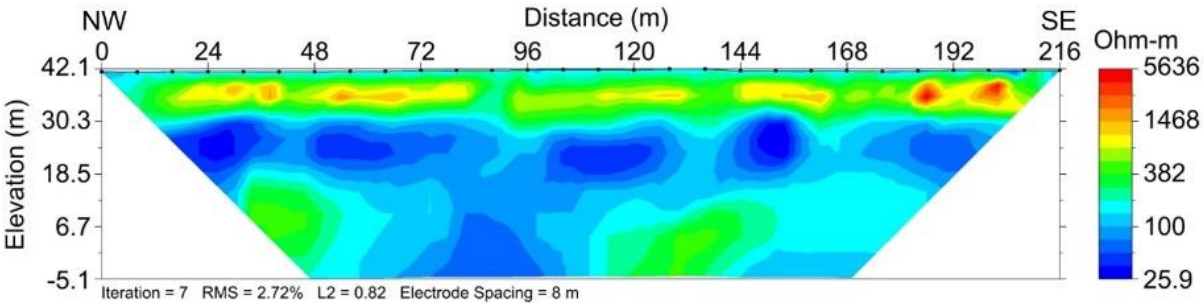

Figure 4.24. Inverted resistivity section TGH01. Against a 195–750 Ω-m mid-range, a lateral, undulating low resistivity anomaly occurs between *c.* 33 – 15.5 m ASL, but extending all the way to the section base between *c.* 48–100 m distance. Shallow high resistivity anomalies are patchy but relatively planar.

4.3. Hand Augers

Hand augers proved unsatisfactory at correlating ERT results with shallow stratigraphy, as the deepest auger hole achieved was 2 m (HA04) but the majority were terminated <1.5 m due to hole collapse or inability to penetrate gravel beds. For the most part, auger logging was limited to validating that the shallowest Hinuera Surface consisted of *c.* 10–30 cm of topsoil formed atop 25–80 cm of silts or sandy silts which overlie silty sands, sands, and gravelly sands/sandy gravels. Figure 4.25 summarises this relationship in the form of a long-section across ERT array RUA05 while all field logs are included in Appendix D. Only one auger encountered groundwater, HA03, at 1.3 m (see Figure 2.4 for location).

Of note, a water pipe was shown in supplied service plans to be below the 30 m point of RUA05 but material at this location (in HA06) appeared to be natural. Atypical material interpreted as fill was, however, encountered in HA05, which was unable to be progressed beyond 0.9 m and Figure 4.25 shows coinciding with a slight vertical reduction in resistivity. This leads to an inference that the water pipe has been inaccurately mapped and is 15 m WSW of the marked location (Appendix B).

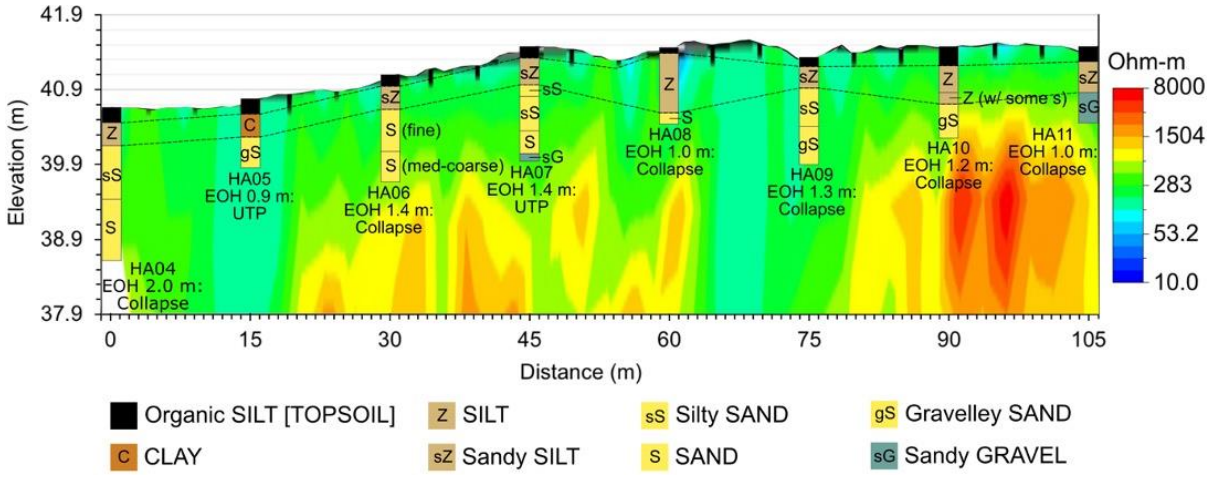

Figure 4.25. Simplified graphic long-section of hand auger logs overlaid on a cropped portion of inverted resistivity section RUA05; VE=8x and resistivity contours have been clipped per Figure 4.13. Dashed black lines are an interpolation of silt-dominated horizons – incorporating the clay component of HA05, which is assumed to be fill above a water pipe. The graphic highlights the inability to auger beyond 1–2 m depth and a lack of substantial correlation with inverted resistivity sections, although HA06–08 and HA10–11 either collapsed or were unable to be progressed (UTP) directly above the upper bounds of high resistivity anomalies which were interpreted as being gravel-rich.

4.4. Paleoseismic Trench

Whilst all of the ERT arrays produced sections of interest, those in the southern area of the AgResearch farm were deemed to show a range of anomalies most dissimilar to the reference section RUA09 and share some consistency with observations from comparative studies (e.g. Caputo *et al.* 2007; Kuebler *et al.* 2016). Particularly intriguing was the chaotic nature of anomalies and sub-vertical low resistivity zones of RUA05 and RUA11, with their apparent along-strike relationship to RUA10 and RUA07. The more northerly sections RUA02–04 and RUA12–14 were of equally strong interest but operational farm considerations (including agricultural field trials in progress) precluded trenching in their location, thus the paddock in which RUA05 and RUA11 had been completed was the preferred trench site.

4.4.1. Pre-trenching and Anthropic Complications

A cause for concern regarding trenching the selected paddock was that buildings had previously been sited there (removed during the 1970s) so it was possible their footprint may have interfered with ERT results. Subsequent archival research identified that the buildings had been single storey, shallow-piled (<1 m), timber-framed accommodation blocks, serviced by an unsealed driveway (Figures 4.26 and 4.27). No experimental or industrial use for the buildings was known to have taken place, nor the presence of any structures such as sheep dips, which may otherwise have given cause for concern regarding chemical contamination.

Hand clearance of topsoil through the driveway area (centre of RUA11) revealed remnants of the driveway within the upper *c.* 30 cm, with limestone gravel forming a thin (<20 cm), patchy, compacted layer with occasional concrete gravel (Figure 4.28). Given the smallest electrode spacing used here was 3 m (RUA11), features <1.5 m in size would not have been resolved during ERT inversion and neither RUA11 or RUA05 showed anomalies at such shallow depth, thus the impact of these remnants was deemed nil to minimal. All noteworthy anomalies were >1 m in depth and due to the nature and construction of the buildings it was not anticipated they should have had any deep impacts that may still remain to interfere with data.

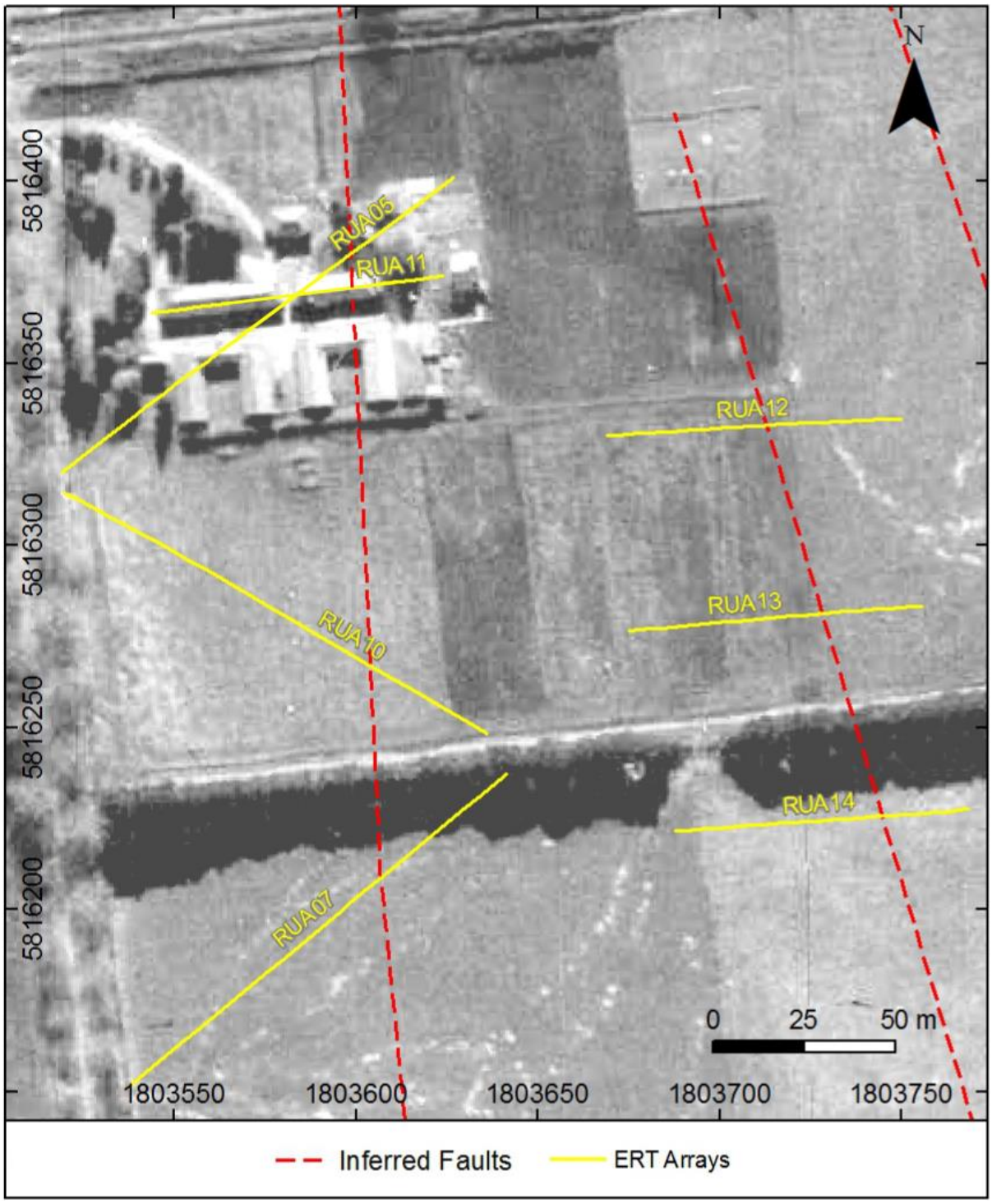

Figure 4.26. Portion of stereoscopic aerial photograph 830/42 of Hillcrest/Ruakura dated 14 June 1943, showing paddocks on south side of the AgResearch farm with significant ERT anomalies (arrays and inferred faults overlaid) and the shallow-piled buildings present in the trenched paddock until the early 1970s. Image courtesy LINZ, downloaded from http://retrolens.nz and licenced for reuse in accordance with CC BY 3.0.

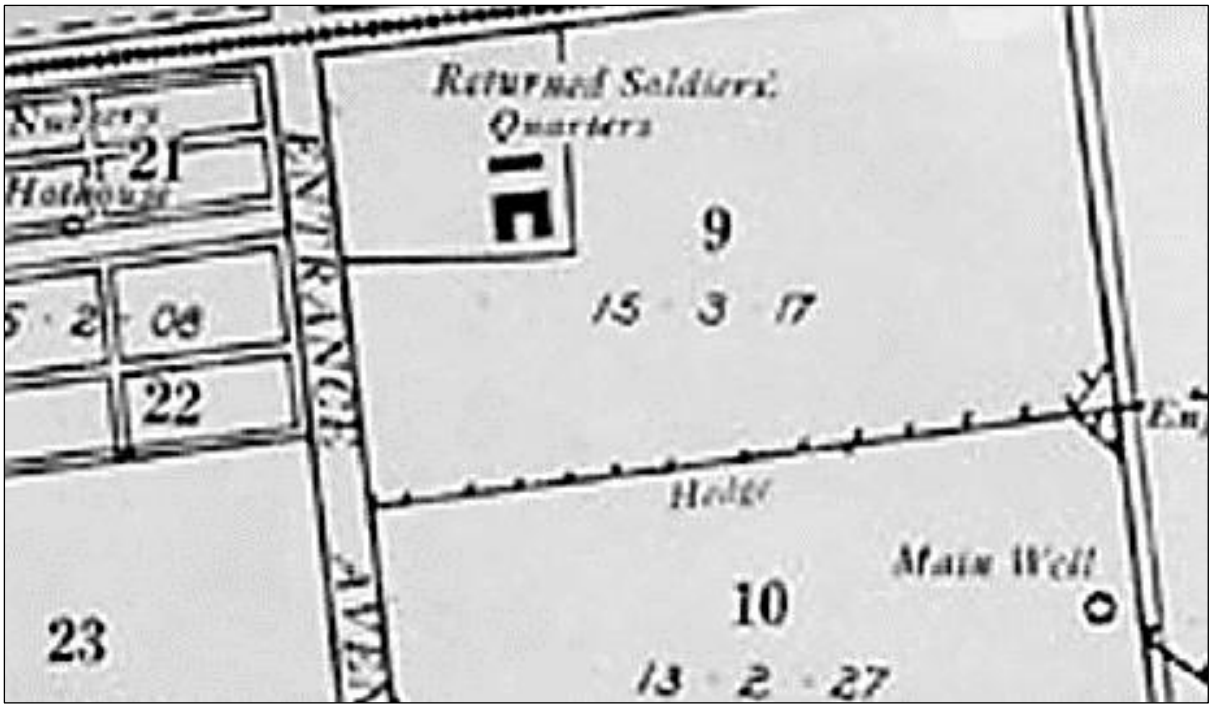

Figure 4.27. Extract from *Plan of Ruakura Experimental Farm*, *c*. 1920, showing the buildings in Figure 4.26 to be returned soldiers' quarters. Note also the main well, since abandoned with no obvious surface trace. Map record group AG40, series 2122, courtesy Archives New Zealand, reproduced from Kellaway *et al.* (2015, p. 3).

Figure 4.28. Photograph of hand cleared section of topsoil, confirming presence of limestone and concrete chips from old driveway.

Following selection of the target paddock it was decided to trench perpendicular to the inferred fault, directly between the two former rows of buildings, avoiding footings as much as possible (Figure 4.29). Unfortunately, an error when georeferencing the 1943 aerial image, and having to avoid a large tree, meant the final trench was slightly oblique to the planned long axis and the western end was *c.* 5 m further north than anticipated. This resulted in much of the trench's northern wall being directly beneath portions of old buildings, although no foundations were encountered. Additionally, the trench was *c.* 6 m shorter than planned, as an unexpected, centrally-placed well was struck when excavations commenced at the eastern end (Figure 4.30). The strike resulted in a precautionary approach, avoiding the area and recommencing excavation further west. A second well was struck *c.* 13 m further east and a rubbish pit another *c.* 11 m on but both were within the trench's southern wall, rather than central, so excavation continued around both.

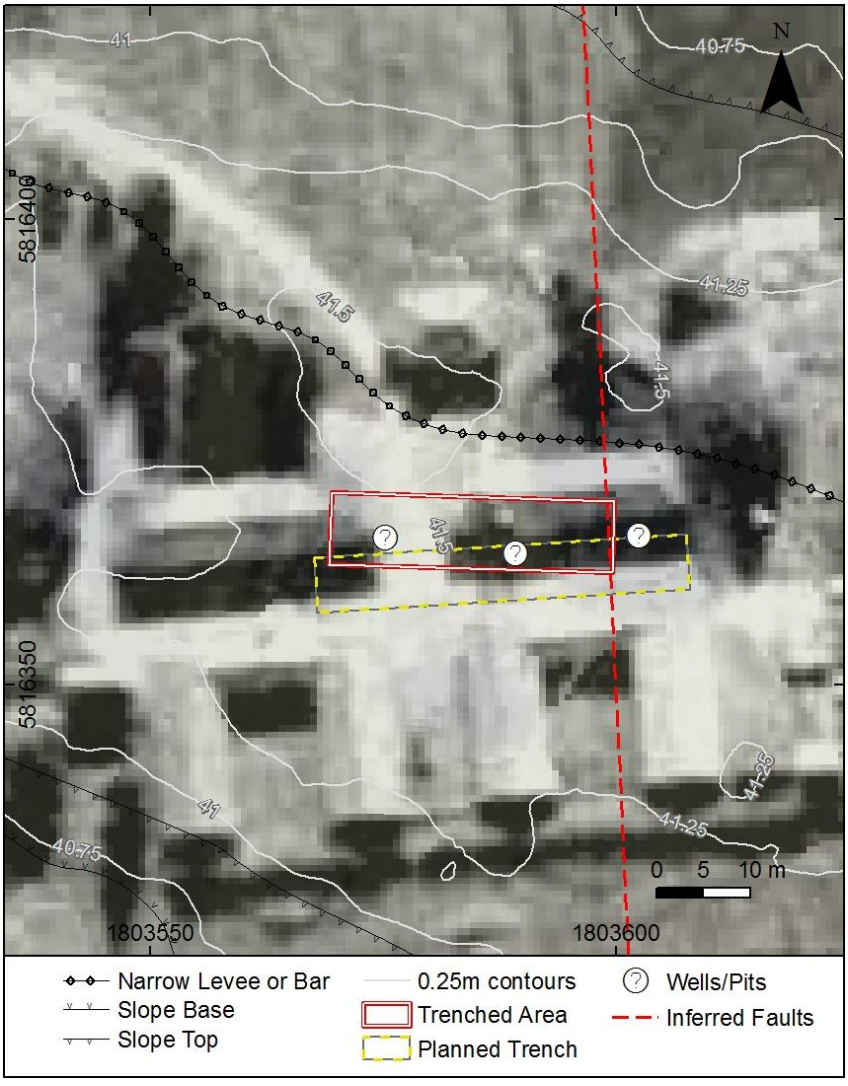

Figure 4.29. Map showing planned and actual trench area, with stereoscopic aerial photograph 830/42 of Hillcrest/Ruakura dated 14 June 1943 as background and incorporating geomorphology and 0.25 m contours. Image courtesy LINZ, downloaded from http://retrolens.nz and licenced for reuse in accordance with CC BY 3.0.

Figure 4.30. Photograph of the first well struck during trench excavation. This and an identical second structure appeared to have been hand-dug, brick-lined, were partially filled and capped with concrete lids prior to abandonment. No records were found as to their location or purpose but farm staff suggested the style and condition indicates water wells.

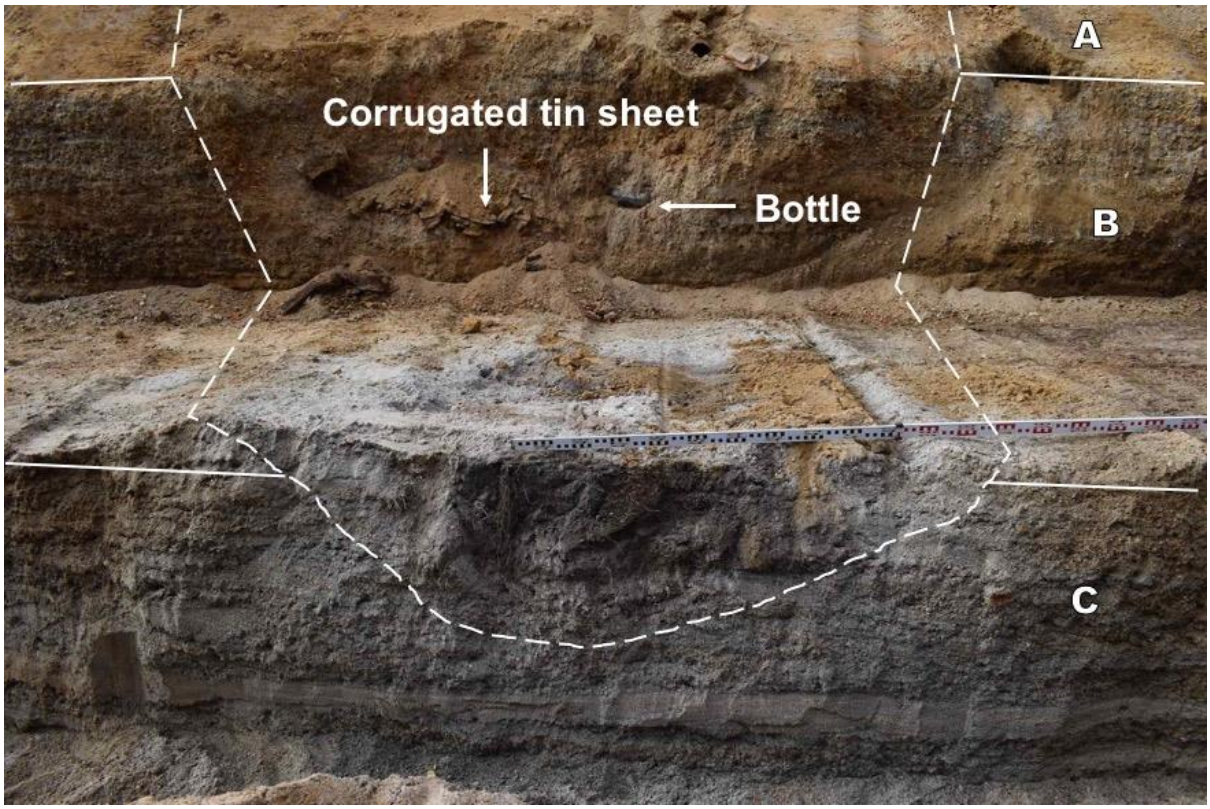

Figure 4.31. Westernmost pit discovered during trench excavation, being an infilled rubbish dump (dashed white line shows approximate extent). Stratigraphic packages A, B, and C annotated – see Section 4.4.2.

4.4.2. Trench Logging

Whereas the northern wall of the trench was fully logged, the southern wall was unable to be fully excavated due to the presence of the abandoned wells or pits. Trench stratigraphy was subdivided into three main packages (excluding topsoil), as shown in Table 4.2 and Figure 4.32. Package contacts were relatively easy to follow as they coincided with as-cut slope breaks in the trench; although wavy and varying in height, the contact between Package I and II was generally a few decimetres above the batter edge while the contact between Package II and III was *c*. 10–20 cm below the edge of the bench (Figure 4.32). In addition to stratigraphic packages, 19 primary geological units were identified (including differentiations of topsoil), shown in Figure 4.34 and described in Table 4.3. Figures 4.35–4.38 provide stratigraphic columns logged at 8 m, 14 m, and 24 m grid distances, illustrating the nature of primary units from which the overarching descriptions of Table 4.3 were drawn.

Table 4.2. Main stratigraphic packages of the Ruakura trench.

Package	Description	Notes
I	Silty tephric soils:	Brownish orange clayey silt, massive, some roots. Occasional clay pipes buried at *c*. 0.5 m. Diffuse, wavy lower contact with Package B.
II	Coarse rhyolitic gravels & sands:	Light grey coarse gravels with abundant fine sand, rhyolitic, with dark reddish grey beds 10–20 cm thick, separated by iron-stained orange gravelly sands. Prominent pale zones and white pumiceous patches. Distinct, gently undulating lower contact with Package C.
III	Fine pumiceous gravels & sands:	Light grey gravelly fine sands, pumiceous, 10–20 cm thick with prominent cross-bedding, separated by pale pinkish-grey sands up to 10 cm thick. Heavy mineral lag between beds. Lower contact not seen.

This page intentionally left blank

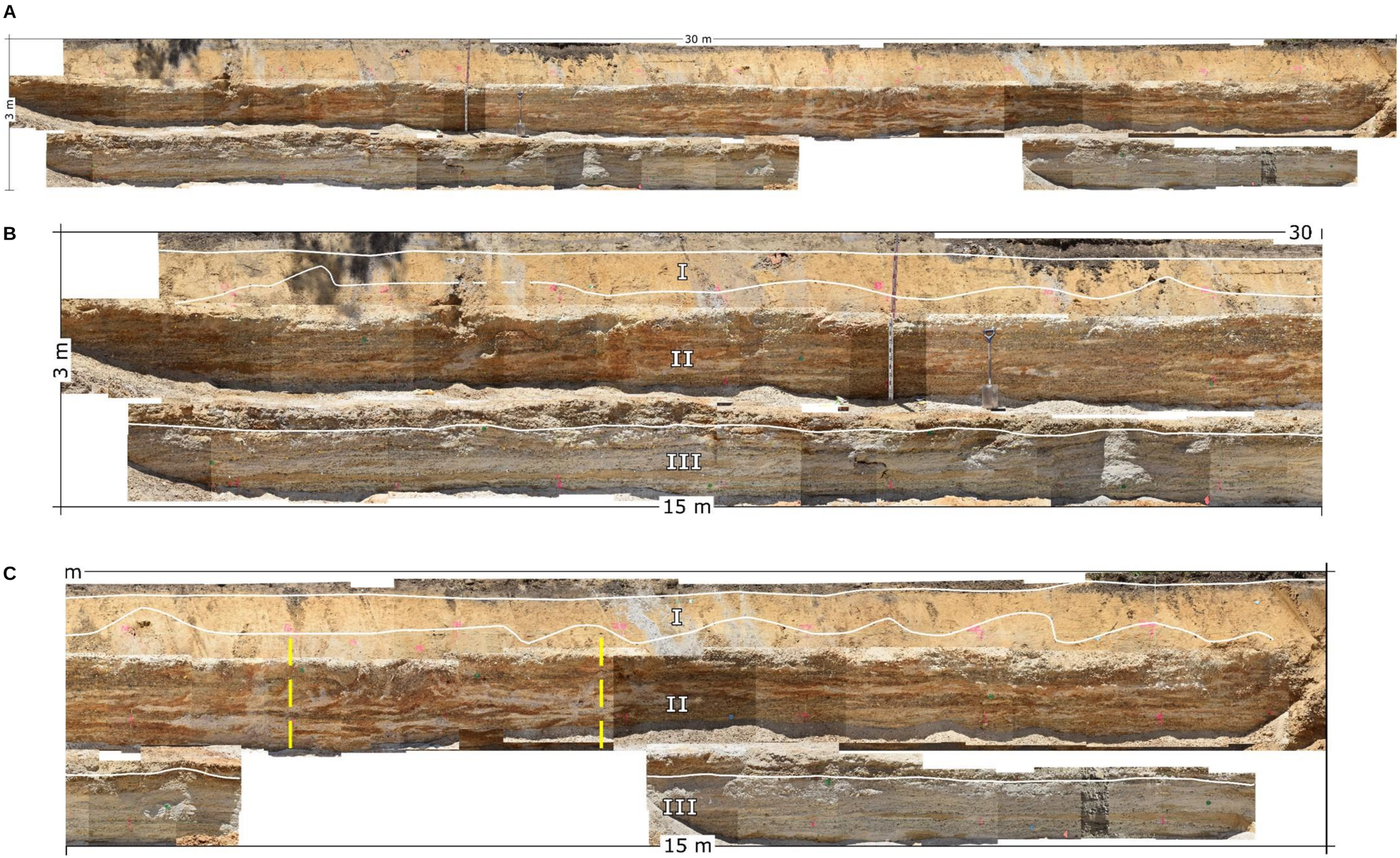

Figure 4.32. Overview of the trench north wall and subdivision into three main packages; **(A)** photo-mosaic of full wall, **(B)** photo-mosaic of the westernmost 15 m with packages annotated, **(C)** photo-mosaic of the easternmost 15 m with packages annotated and vertical dashed yellow lines indicating extent of the deformed zone of section 4 (see Figure 4.34). Refer to Table 4.2 for package descriptions.

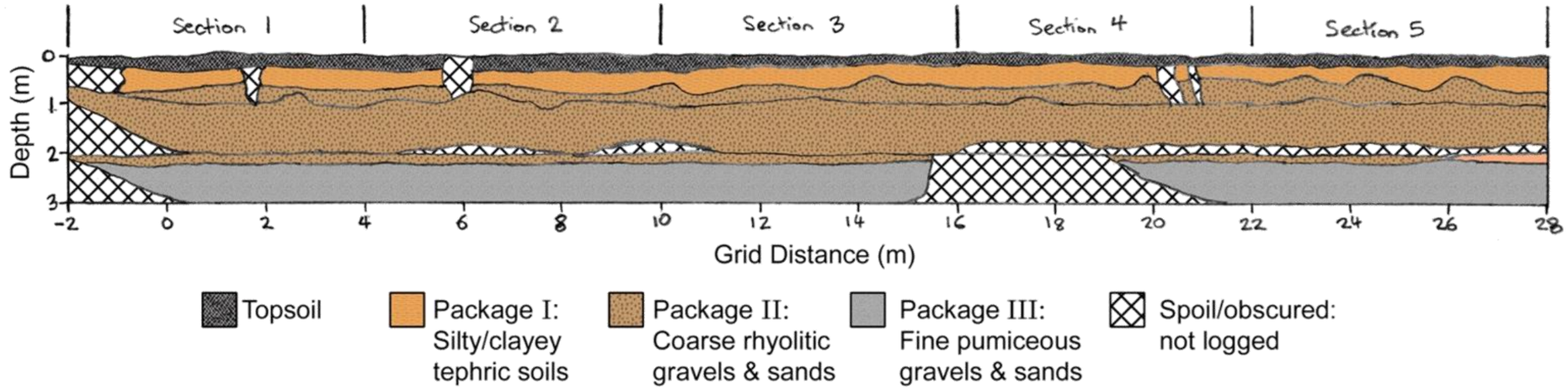

Figure 4.33. Sketch of trench north wall showing subdivision into stratigraphic packages and 6 m mapping sections.

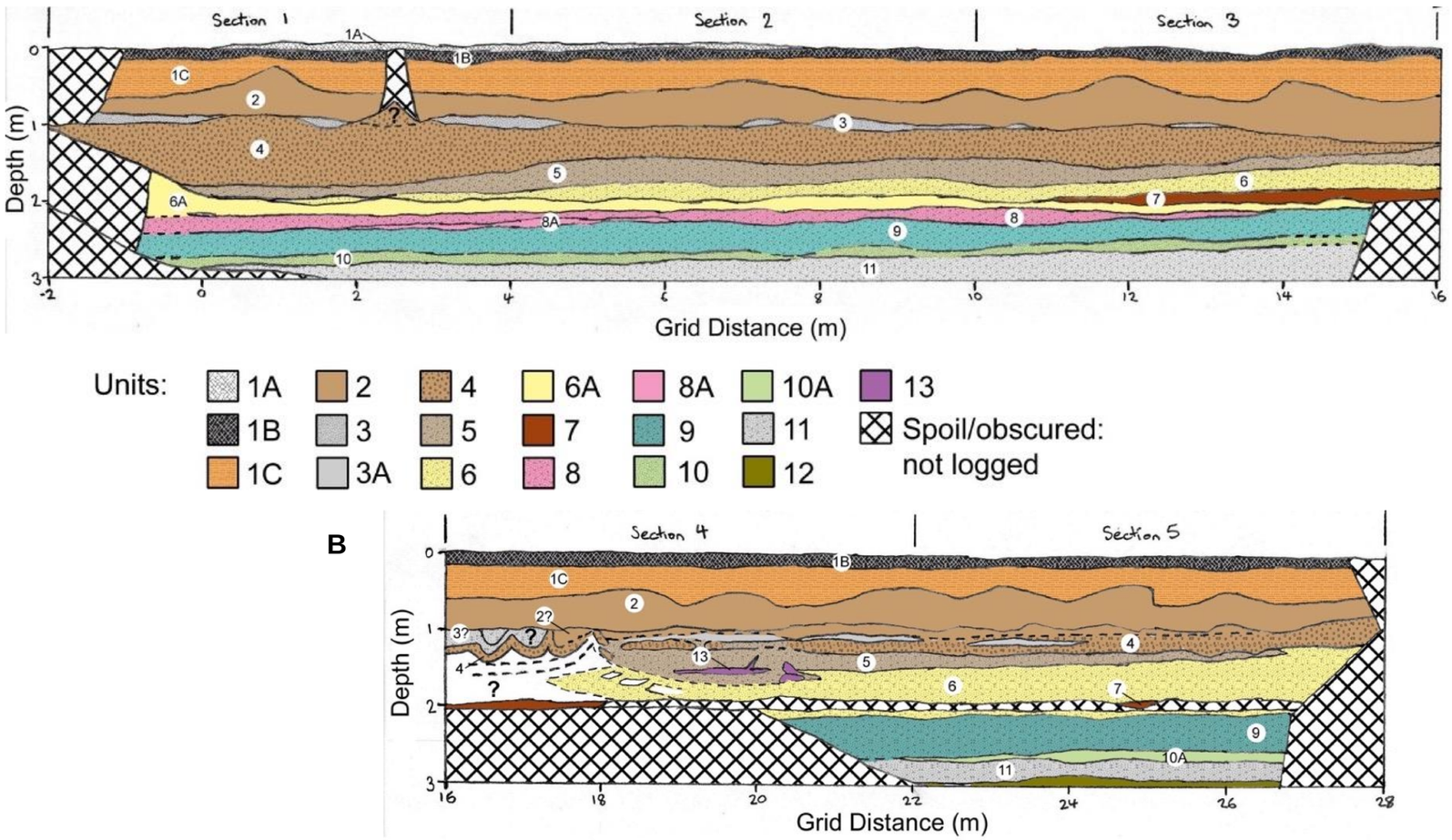

Figure 4.34. Sketches of trench north wall identifying primary stratigraphic units in sections 1–3 **(A)** and sections 5 **(B)**. Refer to Table 4.3 for unit descriptions.

Table 4.3. Primary geological units of the Ruakura trench.

Pkg.	Unit	Description
I	1A	Dark brown gravelly silt with organics. Gravel is angular to subangular, equant, limestone and concrete. Organics are roots. Remnant driveway mixed with underlying Unit 1B. Sharp lower contact.
	1B	Dark brownish black silt with organics and minor fine sand. Organics are roots. Anthropically altered topsoil. Distinct, undulating lower contact.
	1C	Light brownish orange clayey silt with trace of fine sand, non-indurated, non-cemented, massive. Highly weather tephra, pedogenically altered. Gradational, wavy lower contact.
II	2	Light brownish grey sandy gravel grading up to sandy silt, non-indurated, non-cemented, massive, strong normal grading. Sand is fine. Gravel is fine to medium, equant, subangular to subrounded, rhyolite, lithics. Weathered tephric soil. Indistinct, wavy lower contact.
	3	Light brownish grey fine to coarse sand with some gravel, non-indurated, non-cemented, moderately cross-bedded, moderately sorted. Beds alternate sand with gravel/gravel with sand. Sand is subangular to subrounded, quartz, feldspar, lithics, heavy minerals. Gravel is fine to medium, equant to tabular, subangular to subrounded, rhyolite, pumice. Heavy mineral lag at base and occurs as lenses. Indistinct, undulating lower contact.
	3A	*Per Unit 3 but light yellowish grey and finer sand/less gravel.*
	4	Dark grey sandy medium to coarse gravel, stained dark reddish orange, non-indurated, non-cemented, massive, weakly reverse graded, poorly sorted. Gravel is subangular to subrounded, equant, rare tabular, rhyolite, lithics, rare pumice. Sand is fine to coarse, angular to subrounded, quartz, feldspar and heavy minerals. Sharp, undulating lower contact.
	5	Light yellowish grey gravelly fine to coarse sand, stained brownish orange, non-indurated, non-cemented, patchy weak cross-bedding, weak reverse grading (coarsest gravel in 3 cm bed near top), poorly sorted. Sand is angular to subrounded, pumice, quartz, feldspar, rhyolite, lithics. Gravel is fine to medium (rare coarse), equant, subangular to subrounded, rhyolite, pumice, lithics. Pumice lenses up to 8 cm thick. Gradational lower contact.
	6	Grey to light grey medium to coarse gravel with some sand, stained orange towards top, non-indurated, weakly cemented (especially where stained), weakly bedded, weakly reverse graded, poorly sorted. Gravel is subangular, equant, rhyolite, lithics. Sand is subangular to subrounded, fine to coarse, quartz, feldspar, heavy minerals. Pumice lens 5 cm thick, fine sand to medium gravel, highly vesicular, with intragranular fine gravel lithics. Distinct, undulating lower contact.
	6A	*Per Unit 6 but darker grey and trace sand.*
	7	Light purplish grey silty fine to medium sand with some gravel, non-indurated, non-cemented, weakly cross-bedded towards base, moderately sorted. Sand is angular to subrounded, quartz, rhyolite, lithics, heavy minerals. Gravel is fine to medium, subangular to subrounded, pumice, rhyolite, lithics. Prominent yellowish lenses where pumice concentrated. Sharp, irregular lower contact.
III	8	Light grey coarse sand with some gravel thinly bedded within weak cross-beds, non-indurated, non-cemented, well sorted. Sand is subangular to subrounded, quartz, feldspar, lithics, heavy minerals. Gravel is medium to coarse, subrounded, equant, pumice, rhyolite, lithics. Unit 8A interbeds as lenses. Sharp lower contact.

9	Light grey gravelly coarse sand, non-indurated, non-cemented, dark heavy mineral lag at top and base, grading up to fine sand then to sandy coarse gravel in top 5 cm, very weakly cross-bedded. Sand is angular to subrounded, feldspar, pumice, lithics, heavy minerals. Gravel is medium to coarse, subangular to rounded, equant, some tabular, pumice (very soft, weathering to clay), rhyolite, lithics. Sharp, undulating lower contact.
10	Light yellowish grey fine to medium sand, non-indurated, non-cemented, weakly cross-bedded, moderately well sorted. Sand is dominantly pumice with lesser quartz, biotite, opaques. Sharp lower contact forms moderate overhang.
10A	*Per Unit 10 but predominantly fine sand. Coarsens westward.*
11	Light grey gravelly fine to coarse sand grading up to sandy gravel, non-indurated, non-cemented, cross-bedded, poorly sorted. Sand is angular to subrounded, quartz, feldspar, heavy minerals (prominent). Gravel is fine to coarse, subangular to subrounded, equant, rhyolite, lithics. Lower contact not seen.
12	Light yellowish grey gravelly coarse sand, non-indurated, non-cemented, weakly cross-bedded, well sorted. Sand is subangular to subrounded, quartz, feldspar, lithics, heavy minerals. Gravel is medium to coarse, subrounded, equant, pumice, rhyolite, lithics.
13	Greyish brown sandy gravelly silt, mottled purplish grey, non-indurated, non-cemented, massive, poorly sorted. Sand is fine. Gravel is fine, subangular to subrounded, pumice, rhyolite.

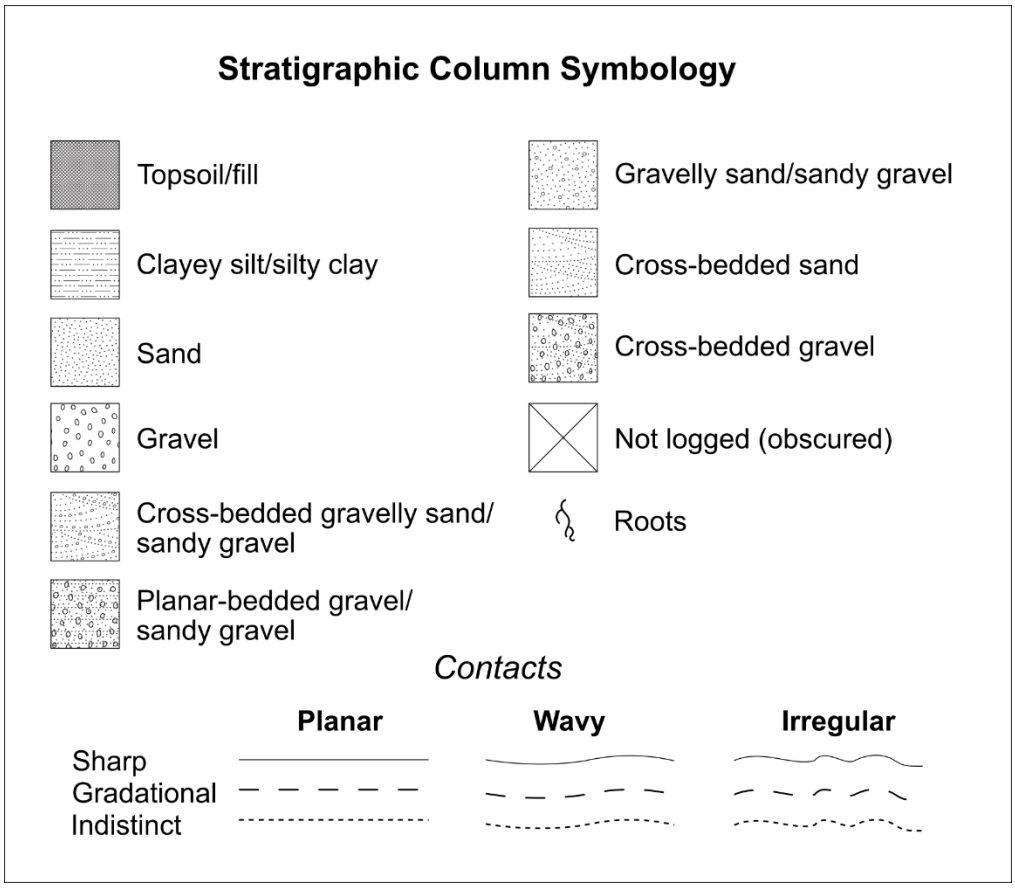

Figure 4.35. Symbology for stratigraphic columns in Figures 4.36–4.38.

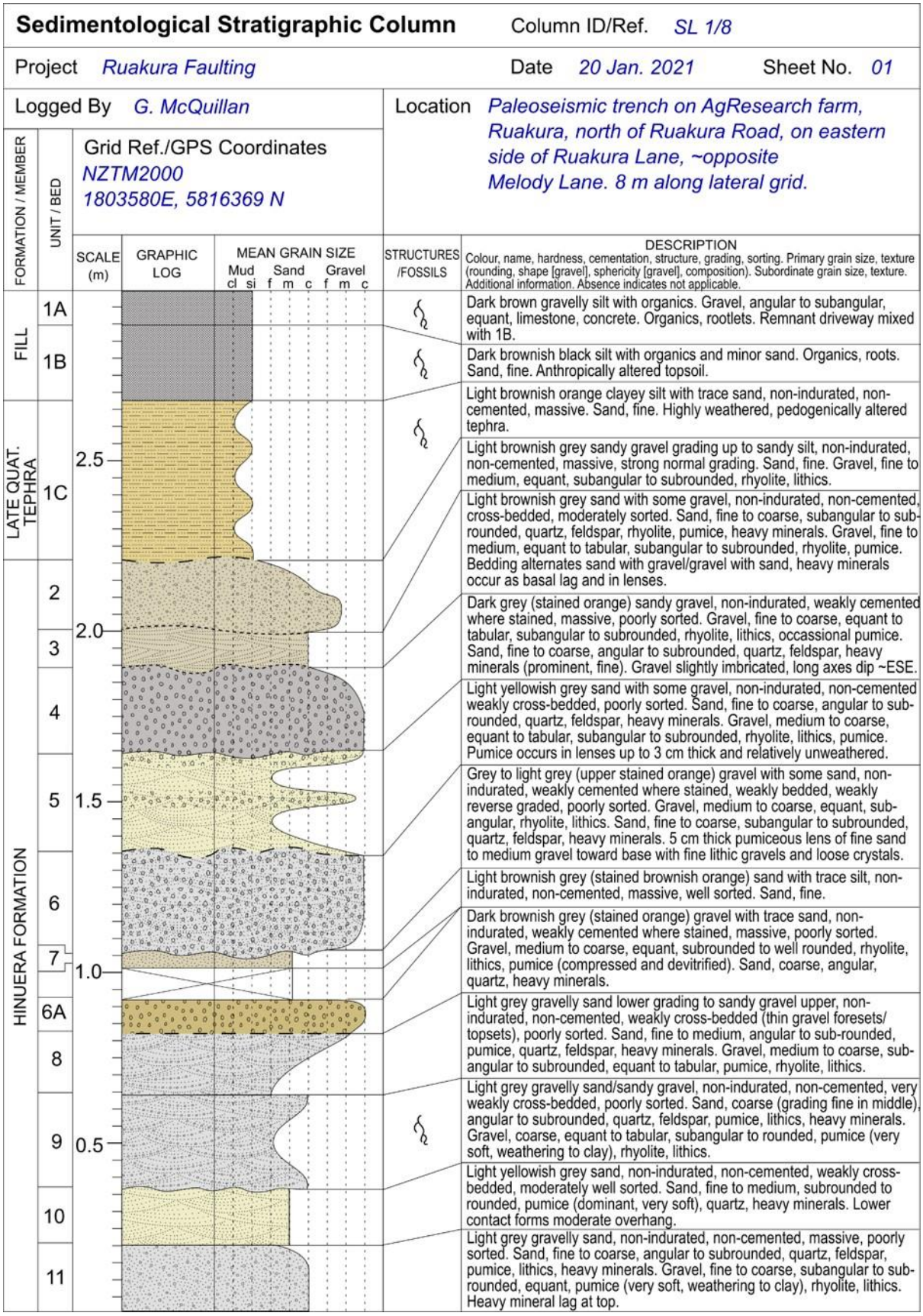

Figure 4.36. Ruakura trench stratigraphic column SL1/8.

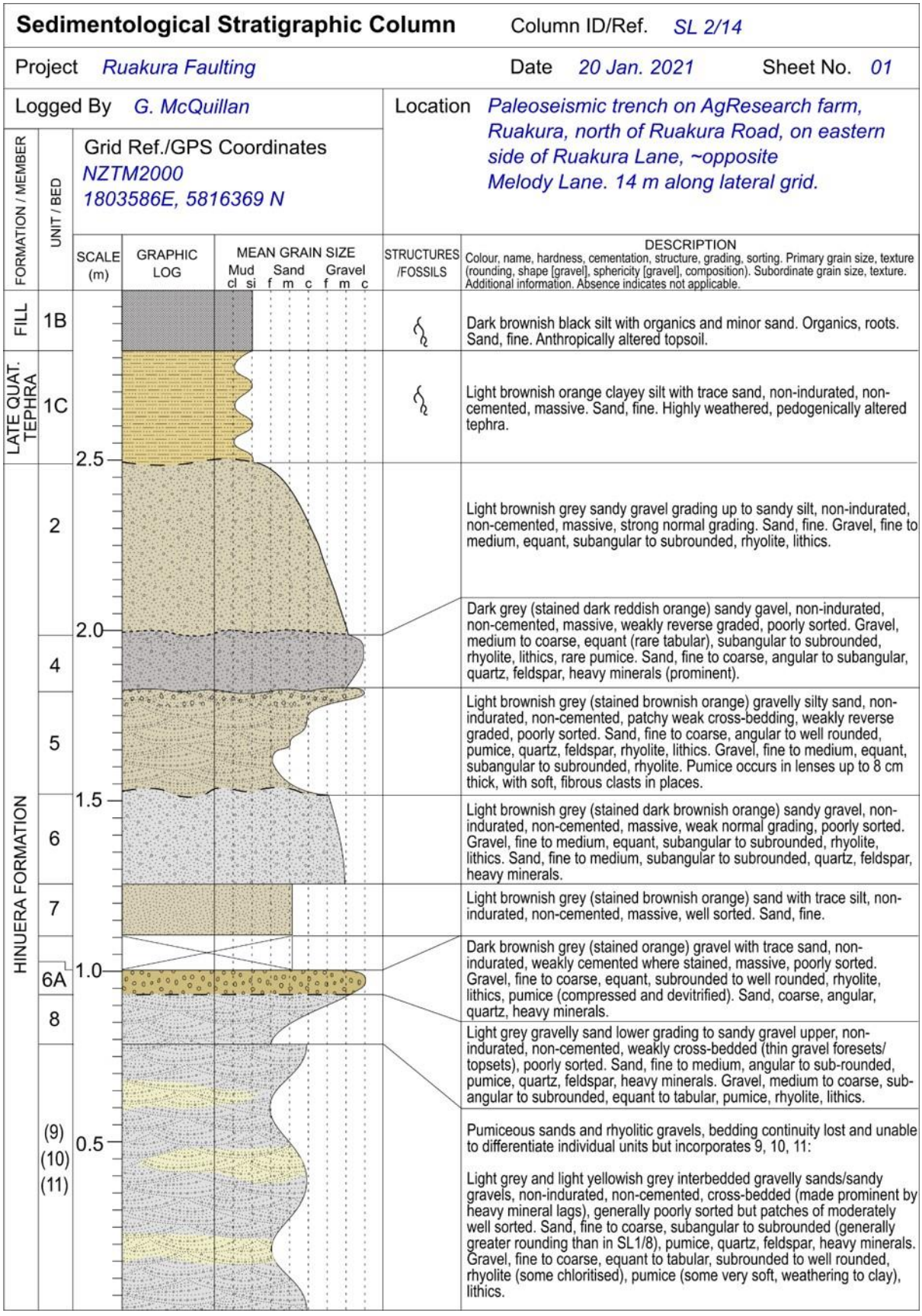

Figure 4.37. Ruakura trench stratigraphic column SL2/14.

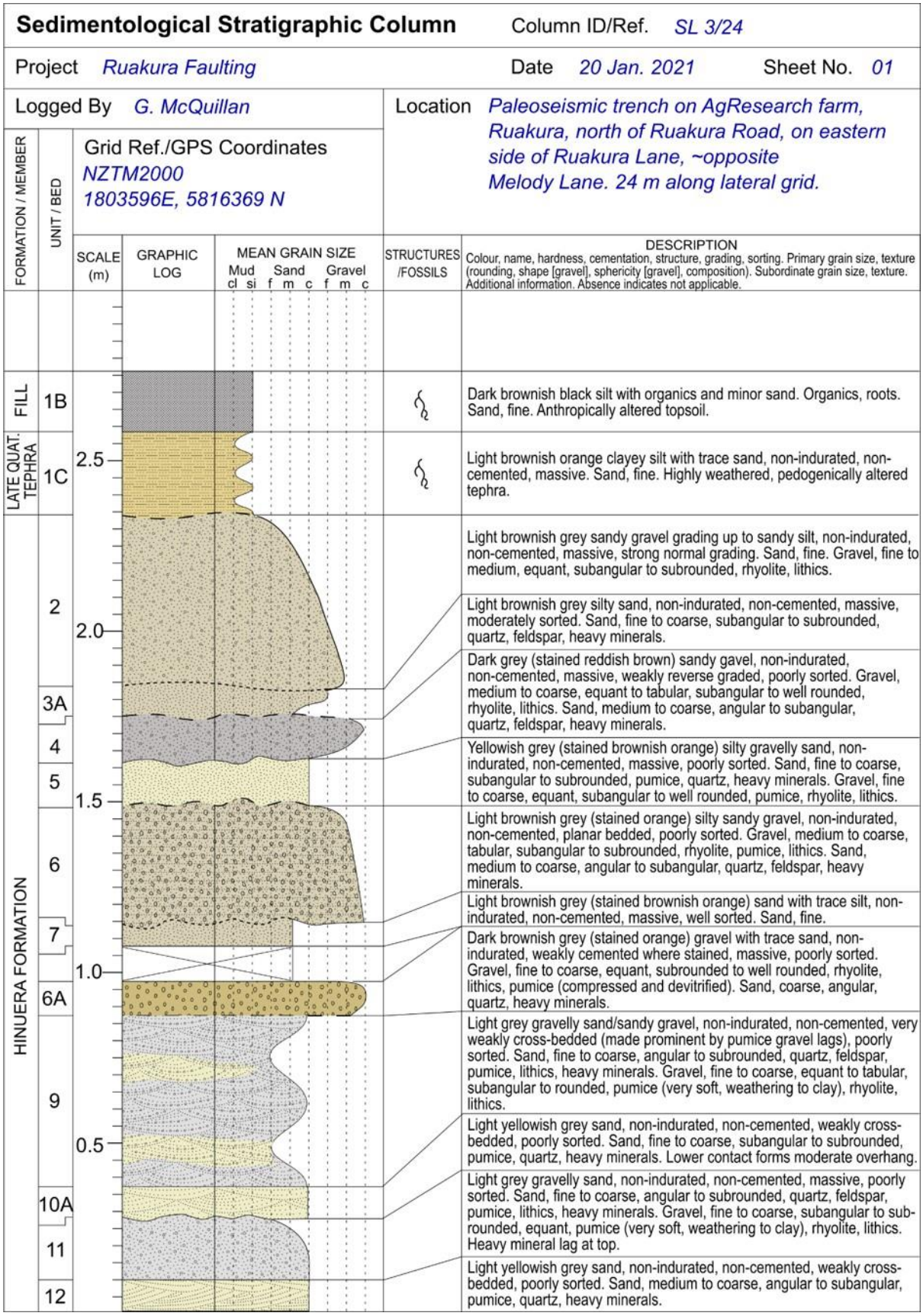

Figure 4.38. Ruakura trench stratigraphic column SL3/24.

Limited time and resource constraints combined with the presence of anthropically modified portions of the southern wall resulted in only the northern wall being comprehensively logged and the southern wall was sketched only at a low level of detail (though comprehensively photographed) (Figure 4.39). Nevertheless, the southern wall generally reflected stratigraphy identified in the northern wall, with only detail remaining unexamined.

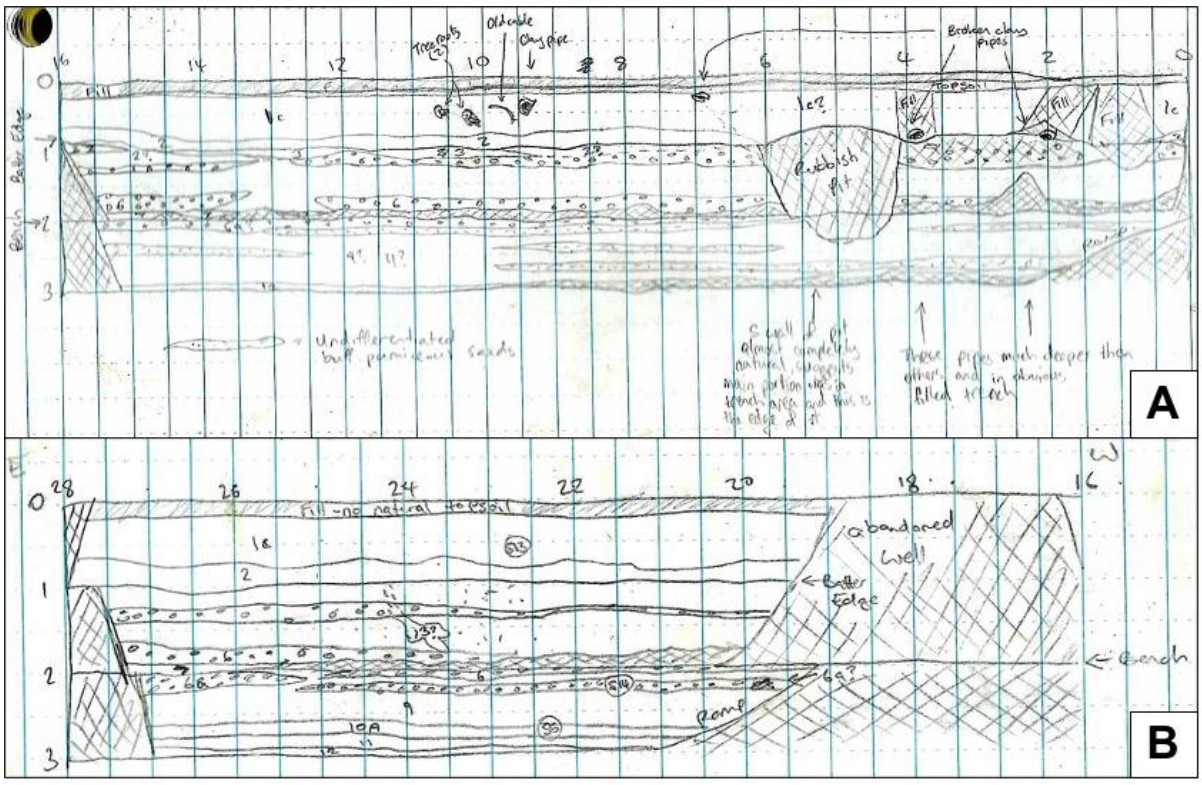

Figure 4.39. Field sketches of the trench south wall. (A) Western section from 0–16 m, (B) eastern section from 16–28 m. Sketch illustrates a general correlation with stratigraphy of the north wall. All distance and depth measurements in metres – note the horizontal grid does not start at -2 m (as does the northern wall) due to no access ramp having been cut.

Figures 4.40–4.44 provide sketches of sequences within the 6 m trench sections showing general stratigraphic relationships between primary units. Package I incorporated Units 1A–1C but Units 1A and 1B were heavily modified topsoil, including remnant driveway fill, so were not logged in detail. Unit 1C was in situ tephra, essentially homogenous in composition but variable in thickness (*c.* 25–45 cm), mantling and forming a gradational but wavy contact with units belonging to Package II. The wavy nature of contact between Packages I and II was at times unusually vertical, appearing to be cut-off (e.g. *c.* 25 m in Figure 4.44) but offset or deformation was not observed within Package I and as this package was the most highly impacted by human activity, with several clay pipes *c.* 0.5 m deep (maximum 1 m), observations are not regarded as conclusive.

Although variable in relative thickness, lateral extent, grainsize and bedding structures, primary units within Packages II and III appeared for the most planar and contiguous (Figures 4.40–4.44). However, within section 4, lateral continuity of Package II was lost, being replaced by a zone of deformation in which beds dipped, warped and, in some cases, became indistinguishable (Figure 4.43). No clear plane of offset was distinguished but the aligned long axes of larger gravel clasts, pumice lenses, or heavy mineral strands highlighted disturbed orientations. Primary deformation was traceable through Unit 4, which appeared to thin from *c.* 30 cm through section 3 to <10 cm in section 4 before warping downwards in a series of three scallops (Figure 4.43). Boudin-like lenses of disrupted gravels emphasised this warping along the extreme eastern edge of the deformation zone. A number of tension cracks with apertures <10 mm and dipping near-vertical back into the face were prominent associations with the deformation zone, which was also generally lighter in colour than adjoining units (Figure 4.45).

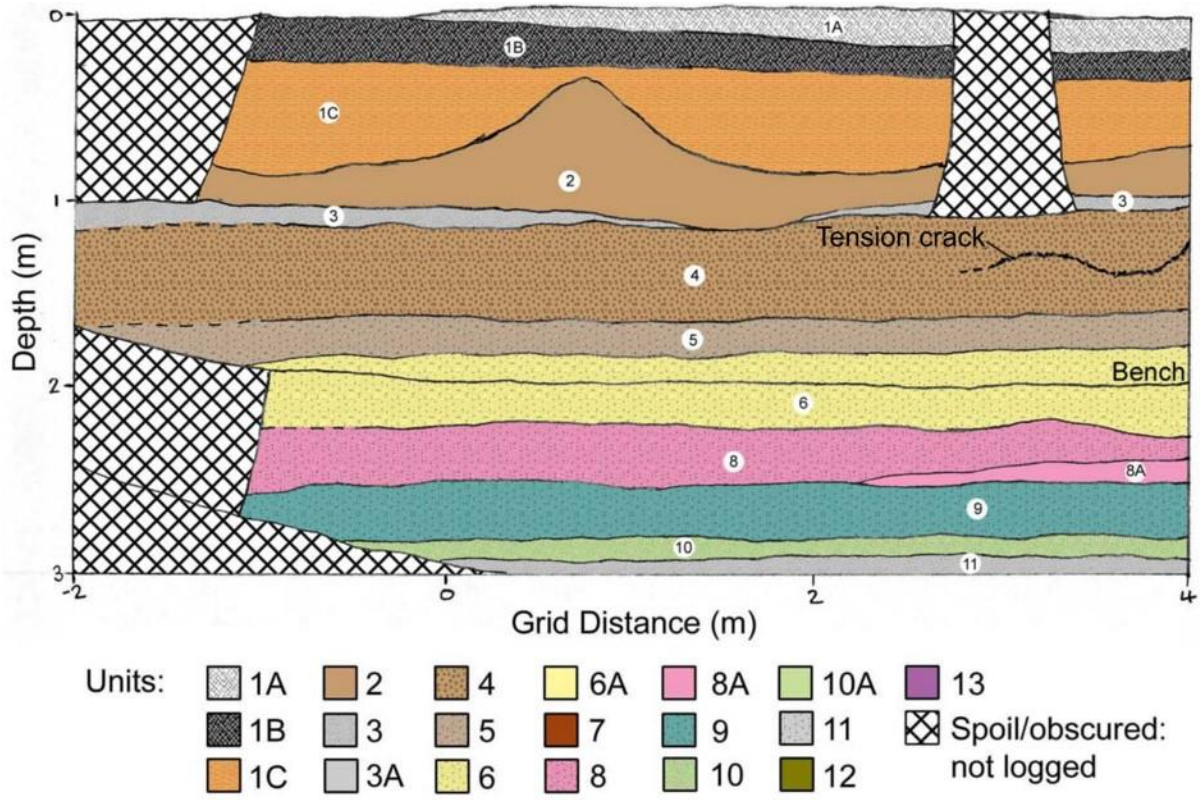

Figure 4.40. Sketch of trench northern wall section 1.

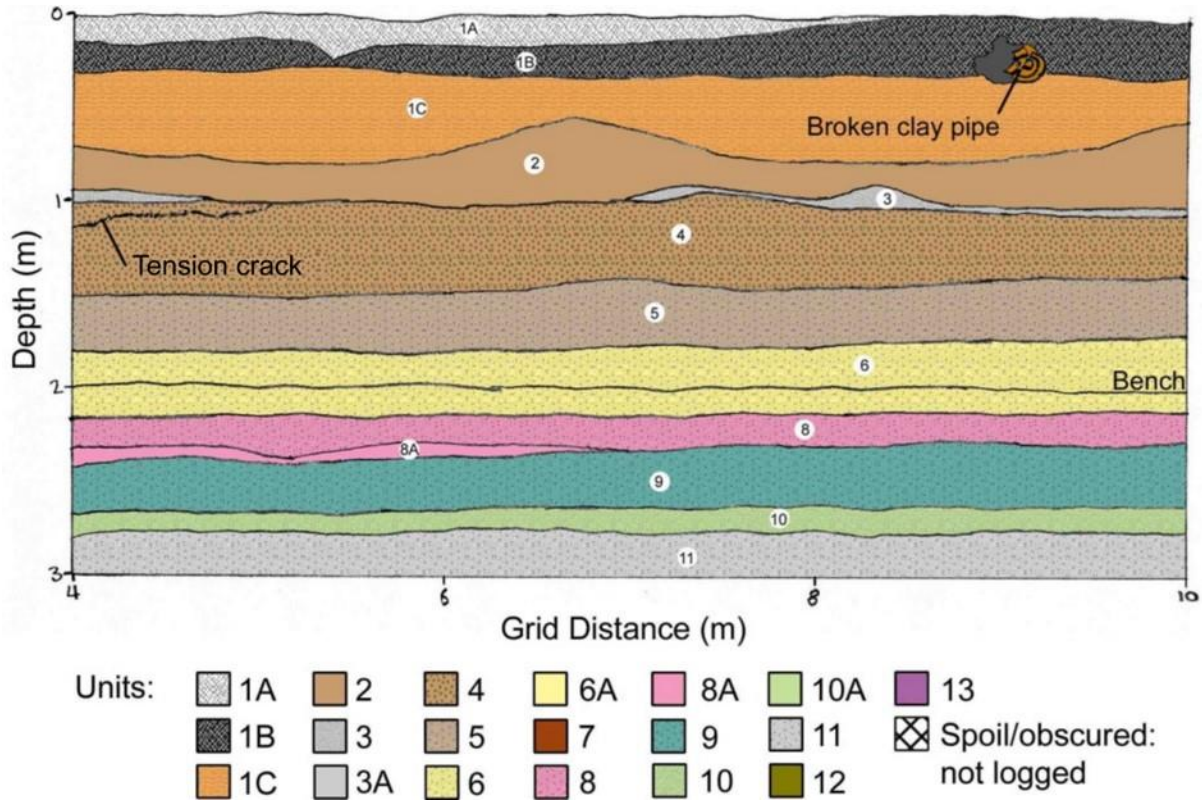

Figure 4.41. Sketch of trench northern wall section 2.

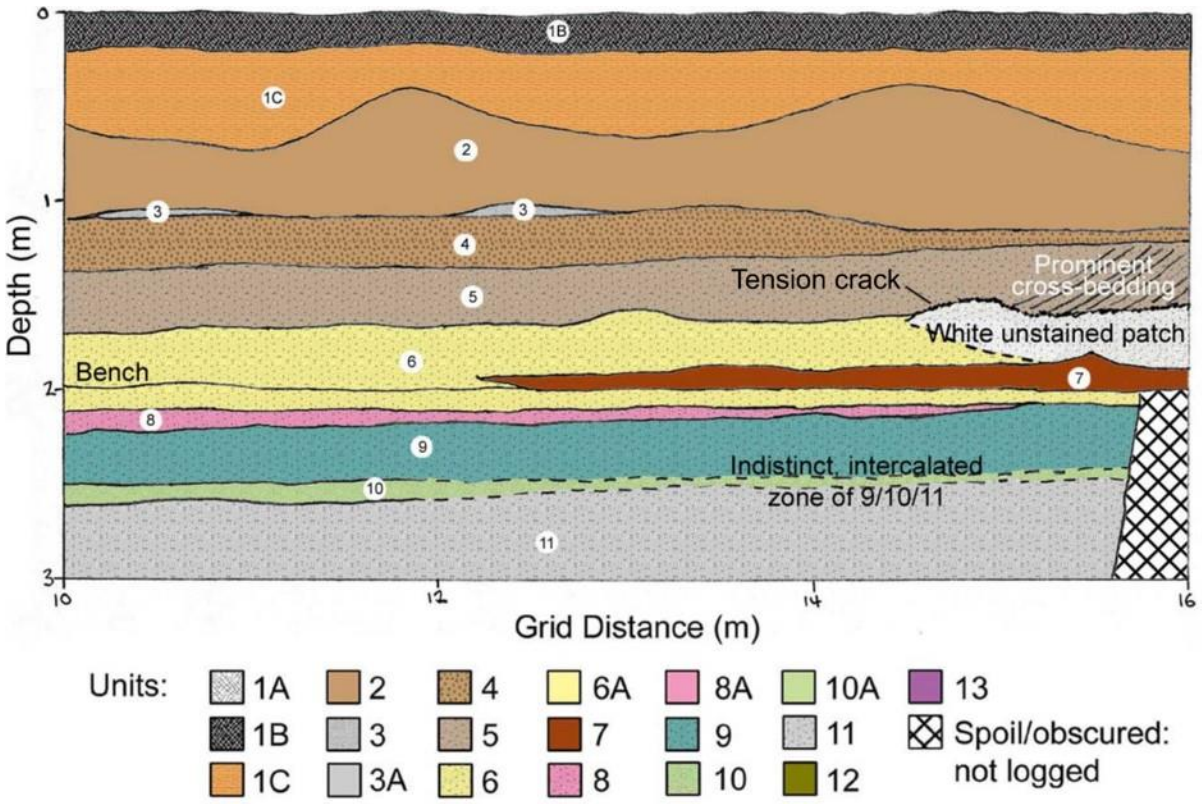

Figure 4.42. Sketch of trench northern wall section 3.

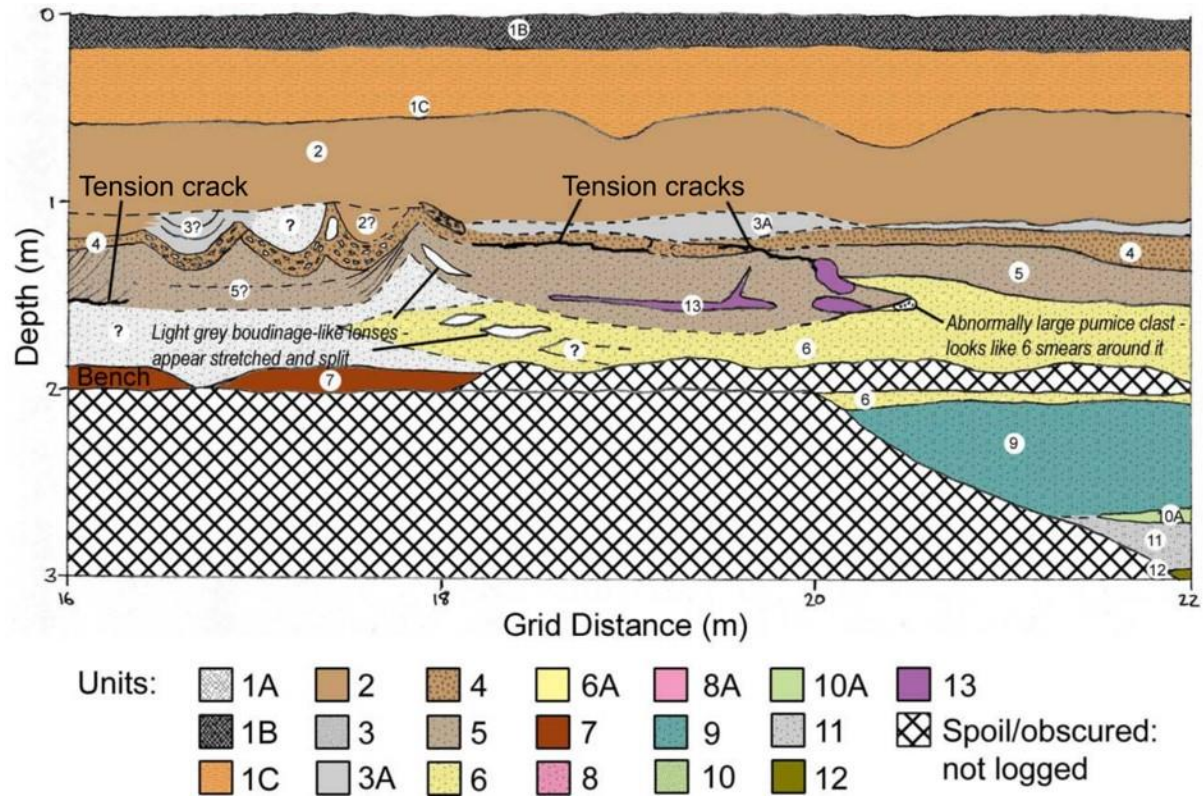

Figure 4.43. Sketch of trench northern wall section 4.

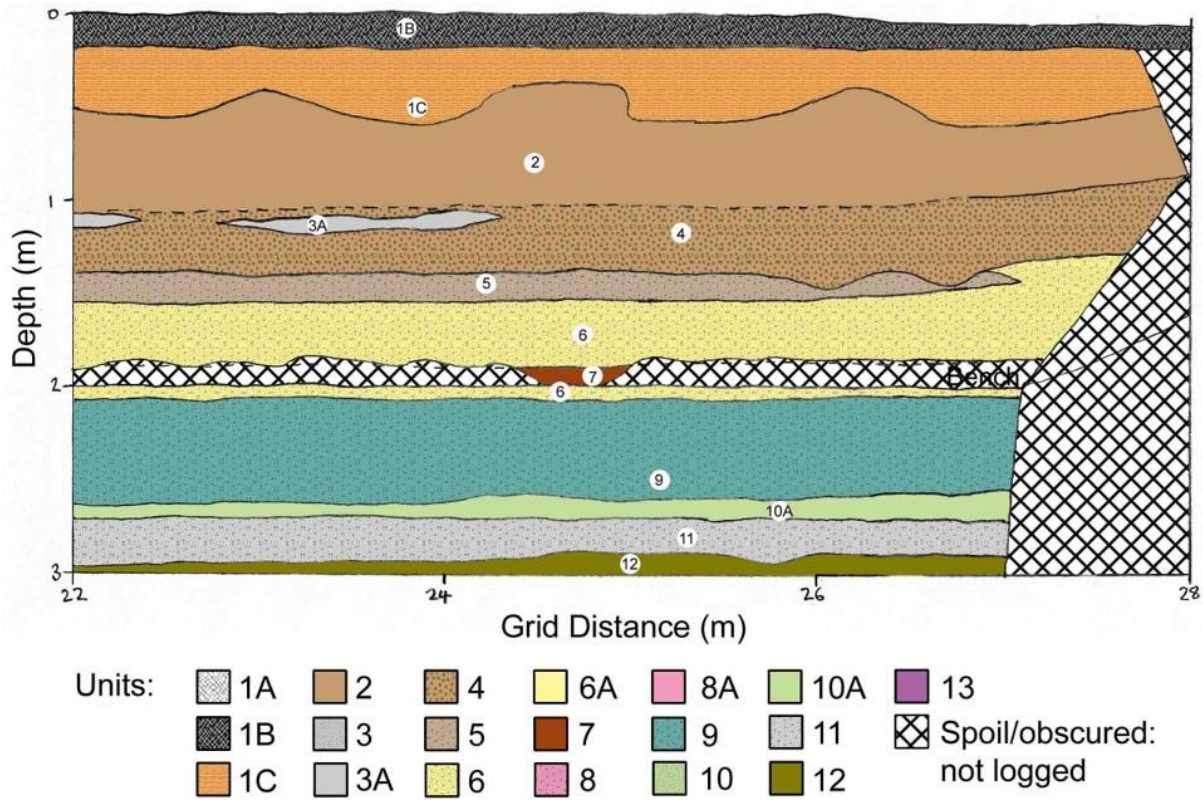

Figure 4.44. Sketch of trench northern wall section 5.

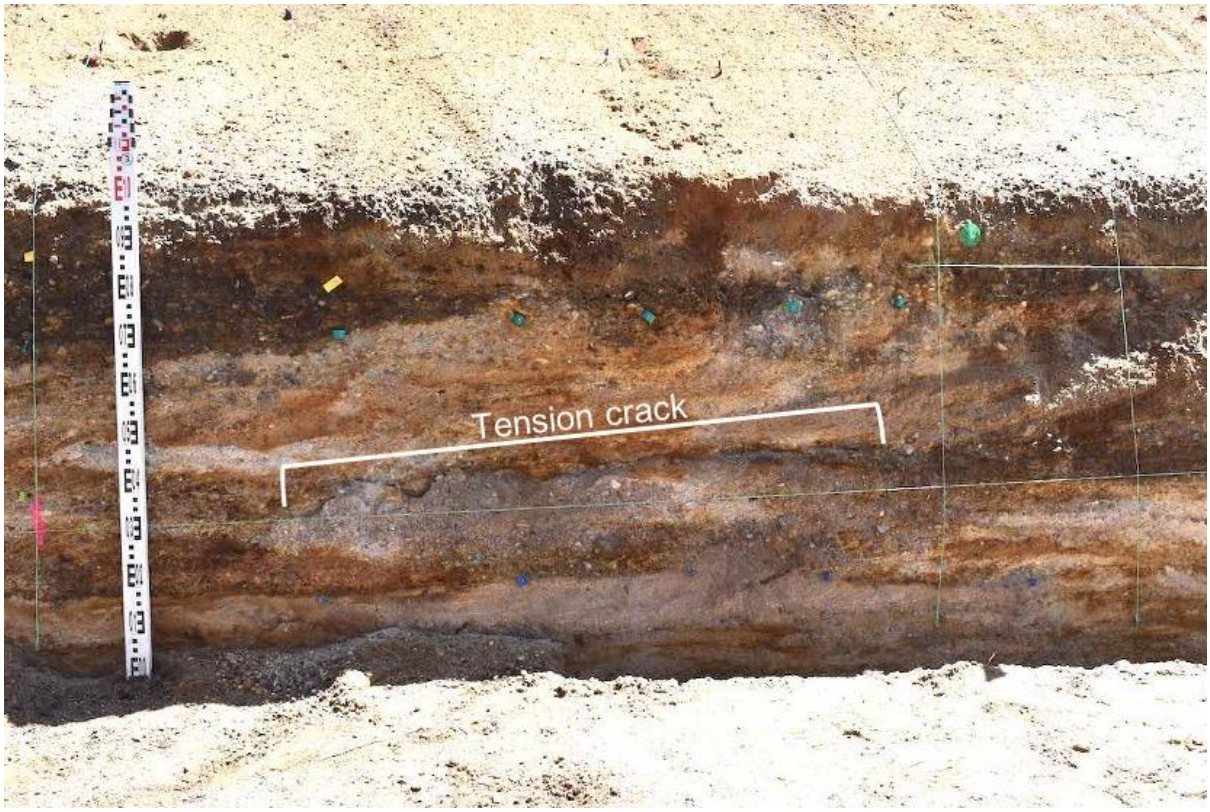

Figure 4.45. Photograph of the 14–16 m portion of section 3 highlighting nature of tension cracks and light colouration near/within the deformation zone of section 4.

Figures 4.46–4.51 provide greater detail of the deformation zone within section 4, sketched using the 0.5 m x 0.5 m grid. As a result of the higher level of examination, 18 secondary geological units were identified within the half-metre grids and these are summarised in Table 4.4. All secondary units belonged to Package II but classification within primary units (aside from those which were obvious) is not attempted, due to the lack of similar detail at whole-of-trench scale. Of note, primary Unit 13 was in fact found to constitute a small, normally graded lens of otherwise non-graded secondary unit *j*, with basal gravels appearing to in-fill pockets of underlying secondary unit *o* (Figure 4.47). Additional trench photographs and sketches, including of this deformed zone, are given as Appendix E.

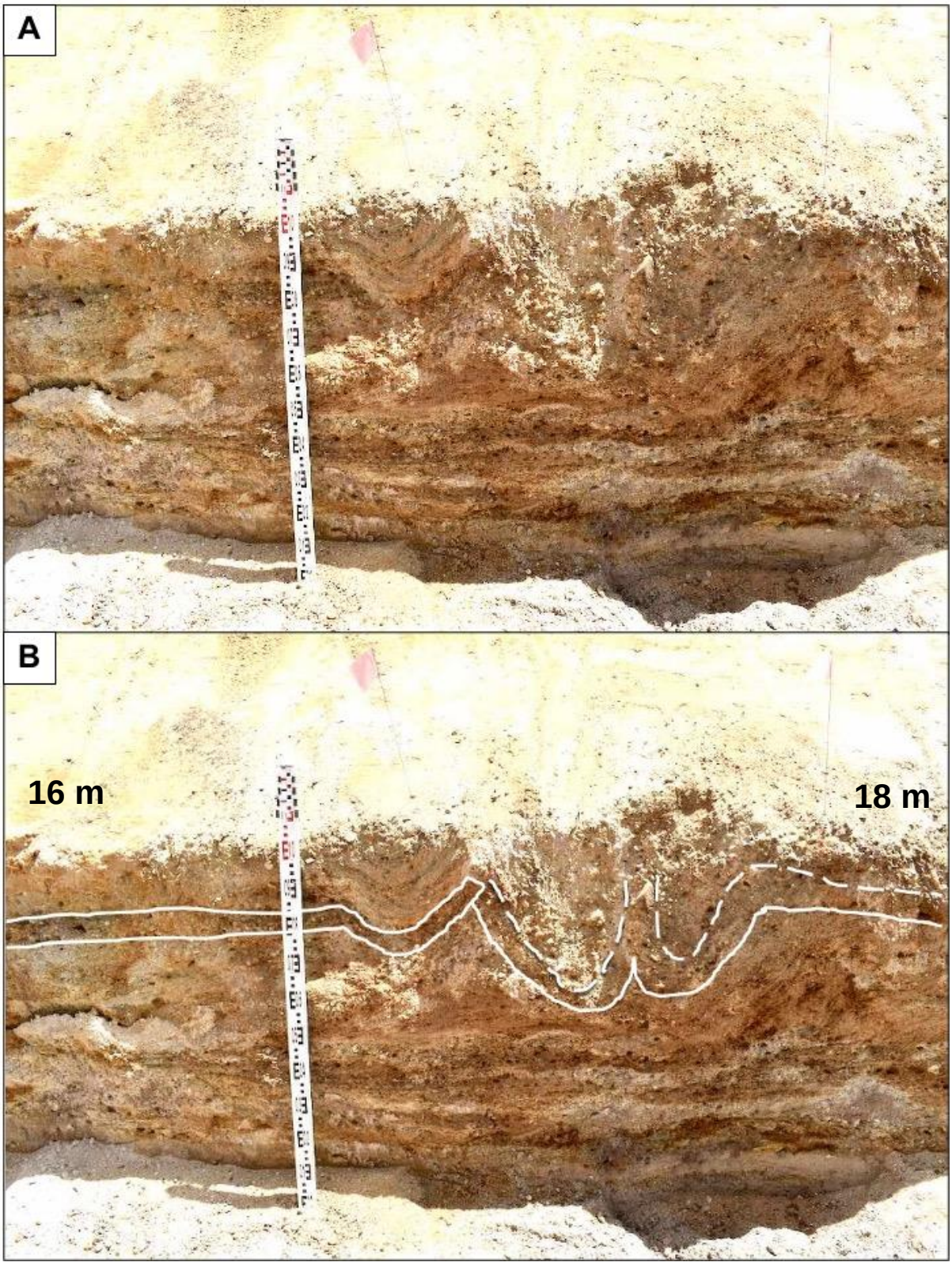

Figure 4.46. Photograph of deformation zone within section 4 of the Ruakura trench; **(A)** unannotated image (pre-gridding), **(B)** Unit 4 outlined in white as a marker bed, highlighting scallops formed by downwarping.

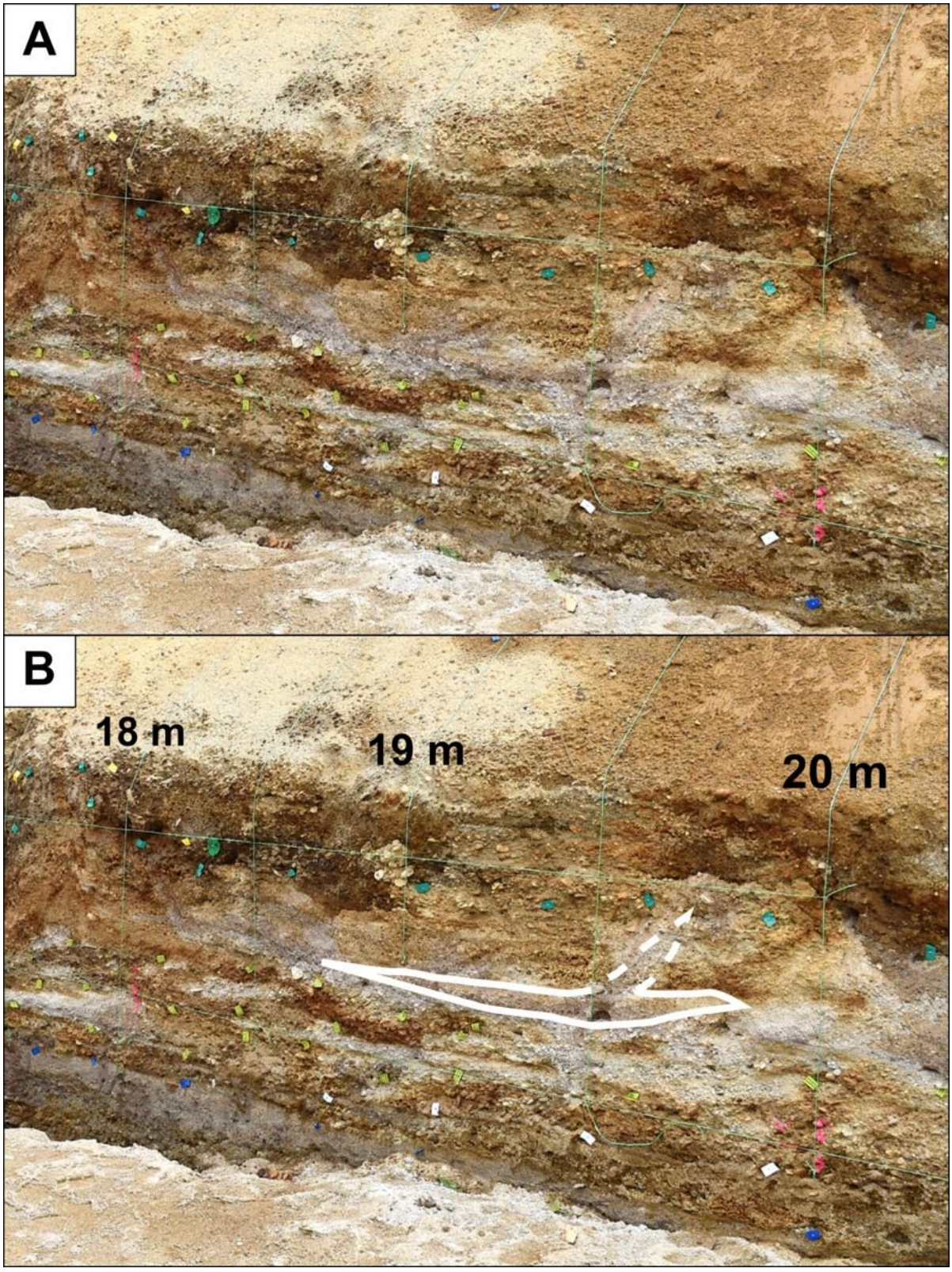

Figure 4.47. Photograph of Unit 13 within section 4 of the Ruakura trench; **(A)** unannotated image, **(B)** Unit 13 outlined in white; this unit is in fact a subtle, semi-lenticular, normally graded zone within secondary unit *j*.

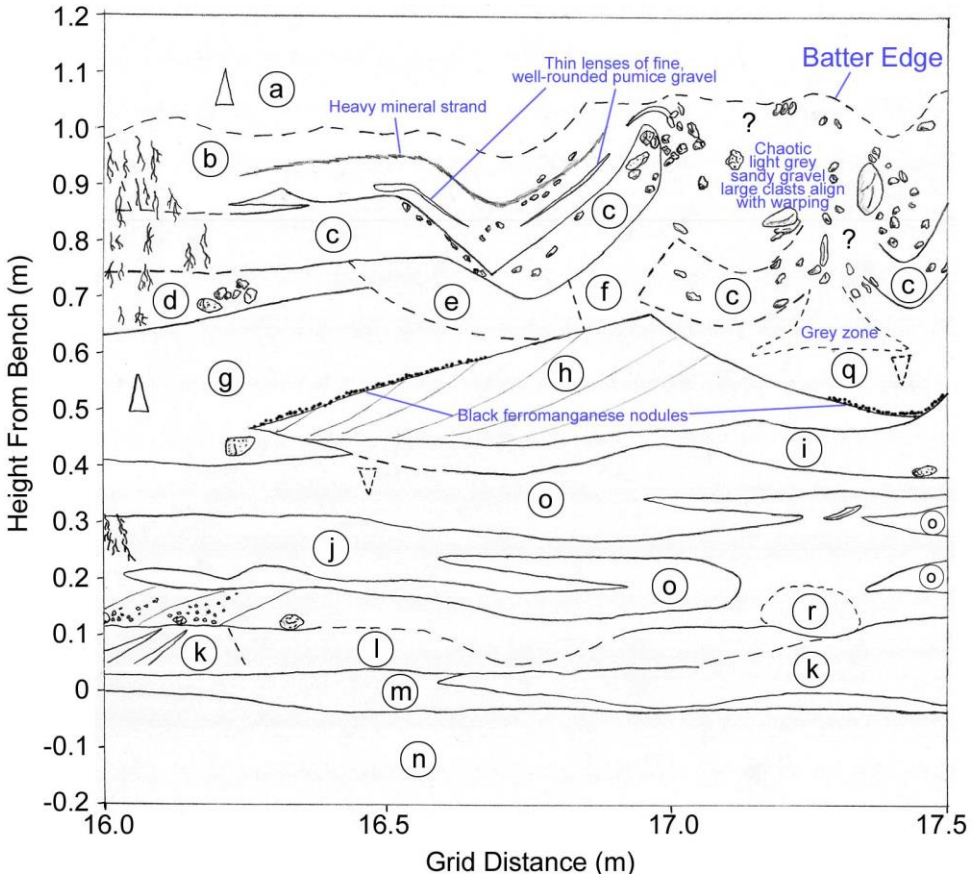

Figure 4.48. Sketch of the trench northern wall deformation zone between 16.0–17.5 m. Note that a very small window was hand-excavated to extend the profile below bench height. Refer to Table 4.4 for unit descriptions.

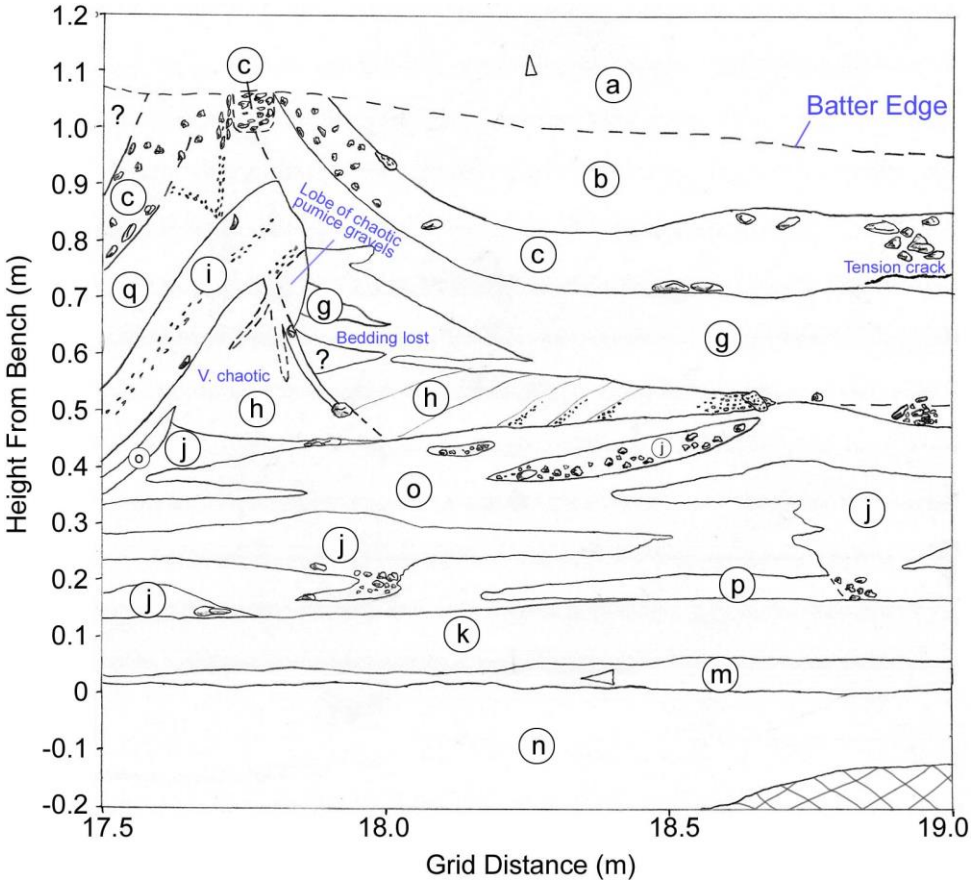

Figure 4.49. Sketch of the trench northern wall deformation zone between 17.5–19.0 m. Note that a very small window was hand-excavated to extend the profile below bench height. Refer to Table 4.4 for unit descriptions.

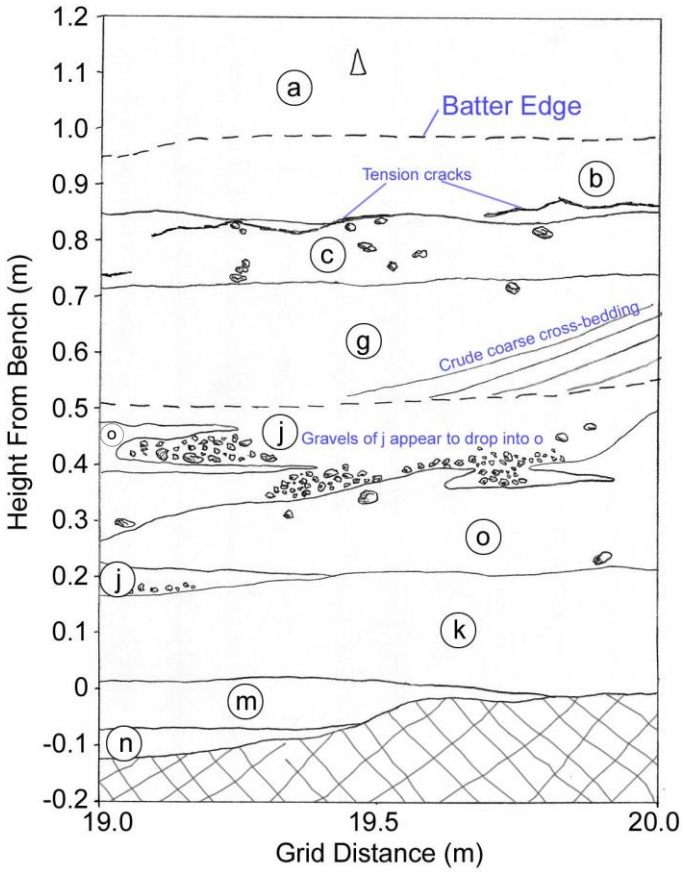

Figure 4.50. Sketch of the trench northern wall deformation zone between 19.0–20.0 m. Refer to Table 4.4 for unit descriptions.

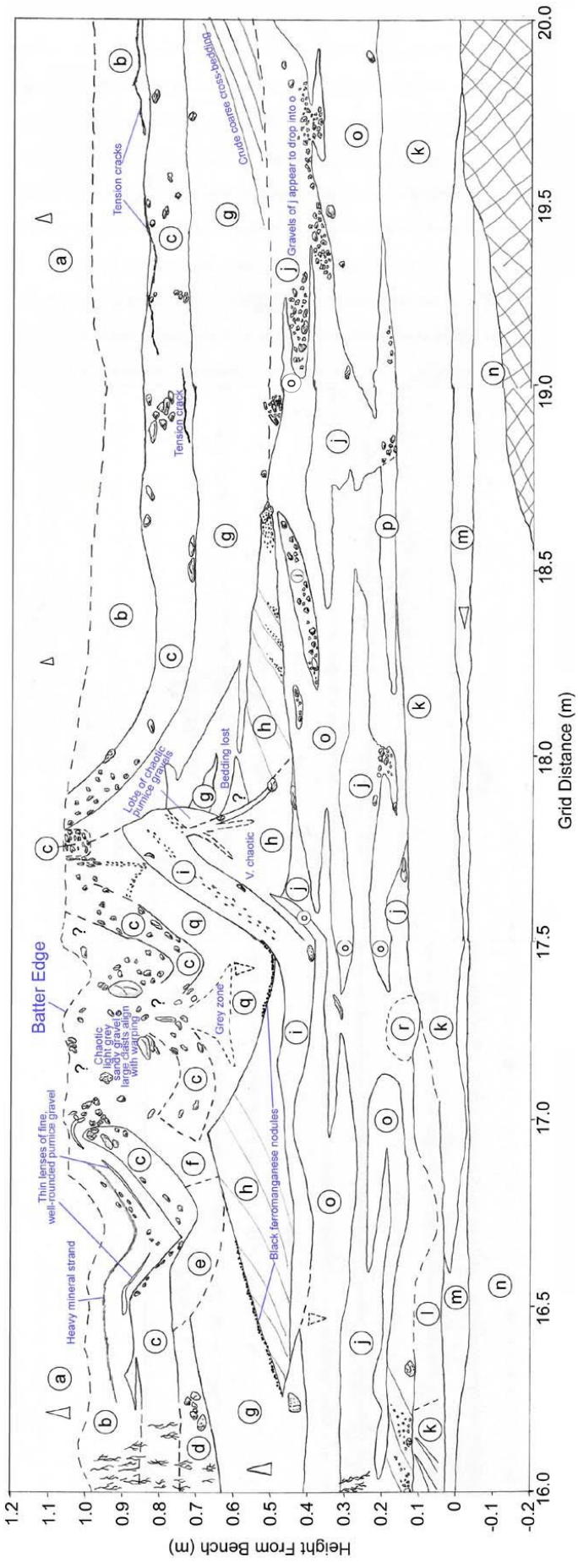

Figure 4.51. Composite sketch combining Figures 4.48–4.50. Note the area between *c*. 18.5–19 m where, beneath a horizontal but graded contact with *g*, gravels of *j* in-fill pockets of *o* – at primary unit scale, this zone forms Unit 13. Refer to Table 4.4 for unit descriptions.

Table 4.4. Secondary geological units of Package II within the half-metre grid of Ruakura trench section 4. Secondary units relate to sketches given in Figures 4.48–4.51.

Sub-Unit	Description
a	*Per Unit 2:* Light brownish grey sandy gravel grading up to sandy silt, non-indurated, non-cemented, massive, strong normal grading. Sand is fine. Gravel is fine to medium, equant, subangular to subrounded, rhyolite, lithics. Weathered tephric soil. Indistinct, wavy lower contact.
b	Light yellowish brown fine to medium sand with some gravel, non-indurated, non-cemented, planar bedded, moderately sorted. Sand is angular to subrounded, high sphericity, quartz, feldspar, rhyolite, lithics, heavy minerals. Gravel is fine to coarse (mostly medium), subangular to rounded, low sphericity, equant to tabular, quartz, rhyolite, pumice, lithics. Heavy mineral strand forms prominent central marker and there are lenses of pumice. Possibly variation of Unit 3A. Sharp, irregular lower contact.
c	*Per Unit 4:* Dark grey sandy medium to coarse gravel, stained dark reddish orange, non-indurated, non-cemented, massive, weakly reverse graded, poorly sorted. Gravel is subangular to subrounded, equant, rare tabular, rhyolite, lithics, rare pumice. Sand is fine to coarse, angular to subrounded, quartz, feldspar and heavy minerals. Sharp, undulating lower contact.
d	Light yellowish grey fine sand with some gravel, non-indurated, non-cemented, moderately sorted. Sand is angular to subrounded, high sphericity, quartz, feldspar, rhyolite, lithics, heavy minerals. Gravel is coarse, subangular to subrounded, low sphericity, equant to tabular, rhyolite, lithics. Gradational, irregular lower contact.
e	Dark reddish brown medium to coarse sand with some gravel, non-indurated, weakly cemented, poorly sorted. Sand is subangular to subrounded, high sphericity, equant, quartz, feldspar, rhyolite, lithics, heavy minerals. Gravel is medium to coarse, subangular to subrounded, high sphericity, equant, rhyolite, lithics. Sharp, irregular lower contact.
f	Dark yellowish brown sandy medium to coarse gravel, non-indurated, non-cemented, poorly sorted. Gravel is subangular to subrounded, low sphericity, equant to tabular, rhyolite, lithics. Sand is fine to coarse, angular to subrounded, low sphericity, equant to tabular, quartz, feldspar, rhyolite, lithics, heavy minerals. Sharp, irregular lower contact.
g	Light yellowish grey silty fine to medium gravel with some sand, non-indurated, weakly cemented, poorly sorted, strong normal grading. Gravel is subangular to subrounded, high sphericity, equant, rhyolite, pumice, volcanic glass (angular), lithics. Sand is fine. Sharp to gradational, irregular lower contact, defined in places by fine to medium ferromanganese nodules.
h	Light yellowish grey fine to medium sand with some gravel, stained dark reddish orange in places, non-indurated, non-cemented, cross-bedded, moderately sorted. Sand is subangular to subrounded, high sphericity, equant, quartz, feldspar, rhyolite, lithics, heavy minerals. Gravel is subangular to subrounded, high sphericity, equant, rhyolite, lithics. Sharp to gradational, irregular lower contact.
i	Light grey sandy fine to medium gravel, non-indurated, non-cemented, poorly sorted. Gravel is subangular, high sphericity, equant, rhyolite, quartz, lithics, volcanic glass. Sand is fine to coarse, angular to subrounded, high sphericity, equant, quartz, feldspar, rhyolite, lithics, heavy minerals. Sharp to gradational, irregular lower contact.

j Greyish white silty sandy fine to medium gravel, non-indurated, weakly cemented, weakly cross-bedded towards base in places, poorly sorted. Gravel is subangular to rounded, low to high sphericity, equant to tabular, pumice, lithics. Sand is fine to coarse, low sphericity, equant to tabular, pumice (fine), quartz, heavy minerals (coarse). Sharp to gradational, irregular lower contact. Greyish brown, silt-dominated, semi-lenticular zone between *c*. 18.5–20 m appears to have been normally graded and forms primary Unit 13.[1]

k Light purplish grey silty fine to medium sand with some gravel, non-indurated, non-cemented, weakly cross-bedded toward base, moderately sorted. Sand is angular to subrounded, low sphericity, equant to tabular, quartz, rhyolite, lithics, heavy minerals. Gravel is subangular to subrounded, low sphericity, equant, pumice, rhyolite, lithics. Prominent yellowish lenses where pumice is concentrated. Sharp, irregular lower contact.

l Light yellowish grey medium sand grading horizontally to sandy gravel in the east, stained light brownish orange, non-indurated, non-cemented, moderately well sorted. Sand is subangular to subrounded, low sphericity, equant, quartz, rhyolite, volcanic glass, feldspar. Gravel is fine to medium, subrounded to rounded, high sphericity, equant, rhyolite, lithics. Gradational, irregular lower contact.

m Light brownish grey gravelly fine to medium sand grading horizontally to sandy gravel in the east, stained dark brownish orange, non-indurated, weakly cemented where iron staining is strong, moderately sorted. Sand is subangular to subrounded, high sphericity, equant, quartz, feldspar, rhyolite, lithics. Gravel in west is fine to coarse, rounded, high sphericity, equant, rhyolite, lithics; in east is coarse, subrounded to rounded, low sphericity, tabular, rhyolite, lithics. Sharp, irregular lower contact.

n Dark brownish grey fine to coarse sand with some gravel, non-indurated, non-cemented, asymmetric hummocky and swaley cross-bedding, poorly sorted. Sand is subrounded to rounded, high sphericity, spherical, quartz, feldspar, rhyolite, lithics, heavy minerals. Gravel is subangular to rounded, high sphericity, equant, rhyolite, lithics. Cross-bedding marked by prominent concentrations of heavy minerals. Lower contact obscured.

o Dark reddish brown sandy medium to coarse gravel, non-indurated, weakly cemented (due to iron staining), massive, poorly sorted. Gravel is subangular to rounded, high sphericity, equant to tabular, rhyolite, dense poor-vesicularity pumice. Sand is fine to coarse, angular to rounded, high sphericity, equant, quartz, rhyolite, lithics, heavy minerals. Sharp, irregular lower contact.

p Light grey silty fine sand with some gravel, non-indurated, non-cemented, poorly sorted. Sand and silt is pumice. Gravel is fine, subangular to rounded, high sphericity, equant, quartz, rhyolite, lithics. Sharp, irregular lower contact.

q Dark yellowish brown sandy fine to medium gravel, stained dark brownish orange, non-indurated, non-cemented, poorly sorted. Gravel is subangular to subrounded, low sphericity, equant to tabular, rhyolite, pumice, lithics. Sand is fine to coarse, subangular to subrounded, low sphericity, equant to tabular, quartz, feldspar, rhyolite, lithics. Medium ferromanganese nodules in places. Gradational, irregular lower contact.

r Purplish grey silty fine sand with trace of gravel, non-indurated, non-cemented, massive, poorly sorted. Sand is pumice, quartz, lithics. Gravel is fine to medium, subangular to subrounded, low to high sphericity, equant, pumice, lithics. Occurs as pockets, possibly sub unit j modified by plant roots. Gradational, lenticular contact

[1] Sub-unit *j* appears to be a pyroclastic flow deposit.

No offset or deformation was observable within Package III due to obscuration resulting from non-excavation of the area around the central well, so description to secondary unit level for that package was not undertaken (Figure 4.52). For the same reason, the southern wall (directly opposite) could not be logged but a rapid visual observation of this portion was made and photographs were taken on the day the trench was back-filled, when the area was cut back for a short period. While no detailed investigation was possible, an observation is tentatively made for possible minor offset (*c.* 7 cm) within a bed of Package II, with an overlying liquefaction structure (Figure 4.53).

Figure 4.52. Photograph looking west along the trench just prior to full completion, highlighting position of wells and rubbish pit in relation to deformation zone.

Figure 4.53. Photograph of possible deformation within Package II in the southern wall, opposite the northern wall deformation zone and exposed for a short time prior to trench back-filling. Solid white line indicates possible offset of a silty-sandy bed, dashed white line is a possible liquefaction structure. Hand tool for scale is *c*. 30 cm in length.

4.5. Correlation of Geophysics with Stratigraphy

Laser scanning of the trench enabled a georeferenced 3D model to be placed into a mesh with inverted resistivity sections RUA05 and RUA11. Figures 4.54–4.58 show that the upper contours of shallow high resistivity anomalies are a little higher in elevation than the edge of the trench batter and are therefore correlated with the top of Package II. The lower contour for these lateral anomalies is just below the maximum depth of the trench and could correlate with the base of Package III. A slightly deeper (but still shallow), semi-detached high resistivity lobe within the centre of RUA11 appears to be in the area of the rubbish pit and possibly reflects a small zone of leachate. Of additional note, the eastern end of the trench-proper just misses the eastern vertical low of RUA11 (although it is deeper than the trench), which is directly beneath the position of the first well unearthed (Figure 4.54).

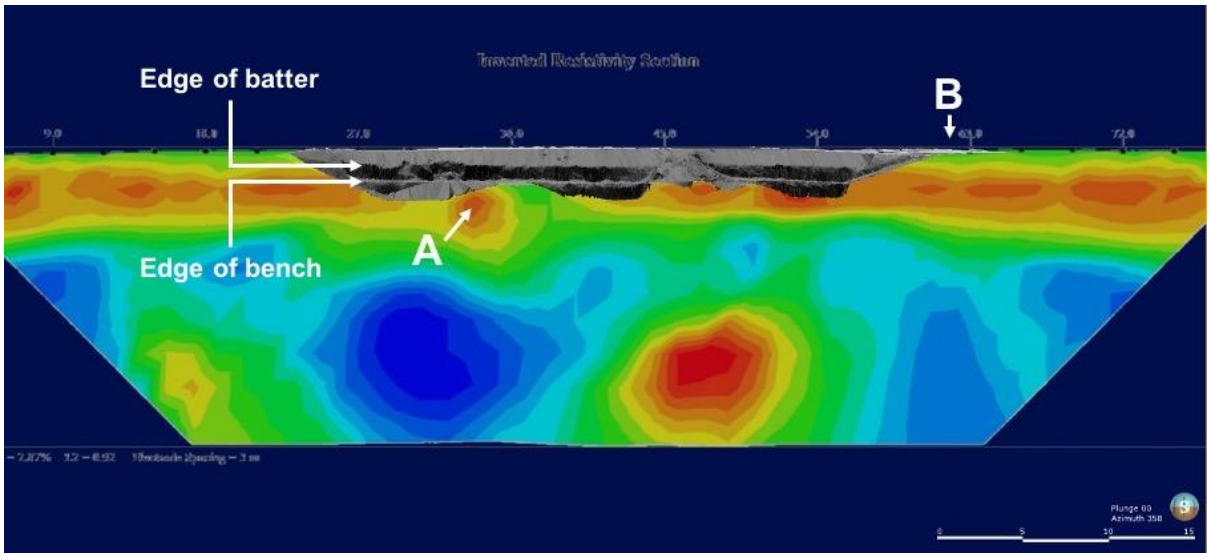

Figure 4.54. Profile view looking due north from 3D rendering of the trench superimposed over ERT inverted resistivity section RUA11. Note the portion of the shallow high resistivity anomaly seemingly dipping toward the centre of the section [A], approximately beneath the rubbish pit, and the vertical low resistivity anomaly directly beneath the easternmost well [B].

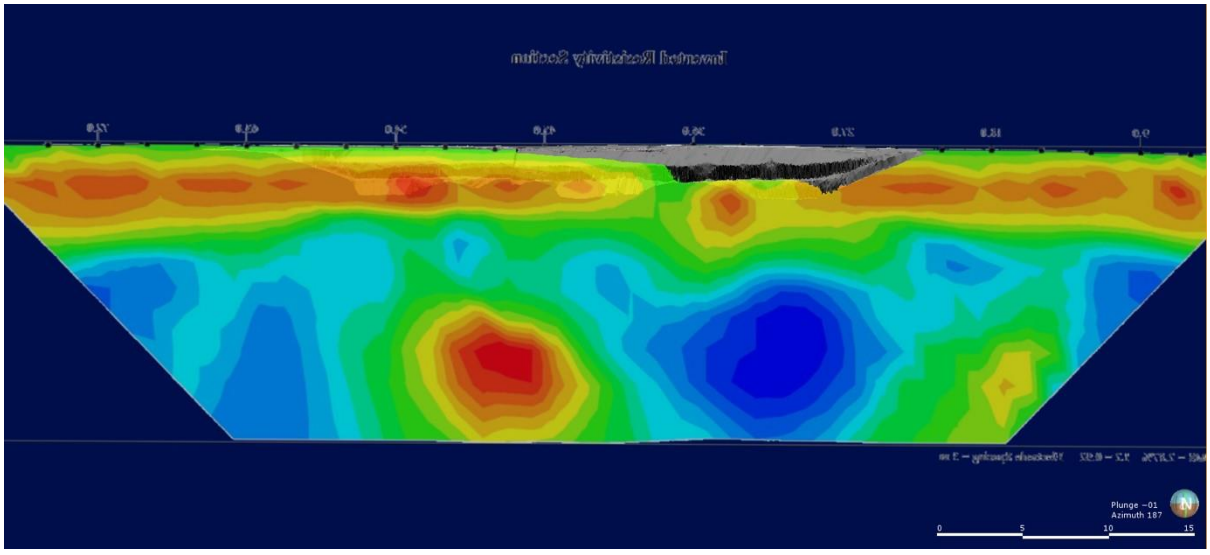

Figure 4.55. Profile view looking due south from 3D rendering of the trench superimposed over ERT inverted resistivity section RUA11. Note the eastern end of the trench being partially obscured by the ERT plot as they were not completely parallel.

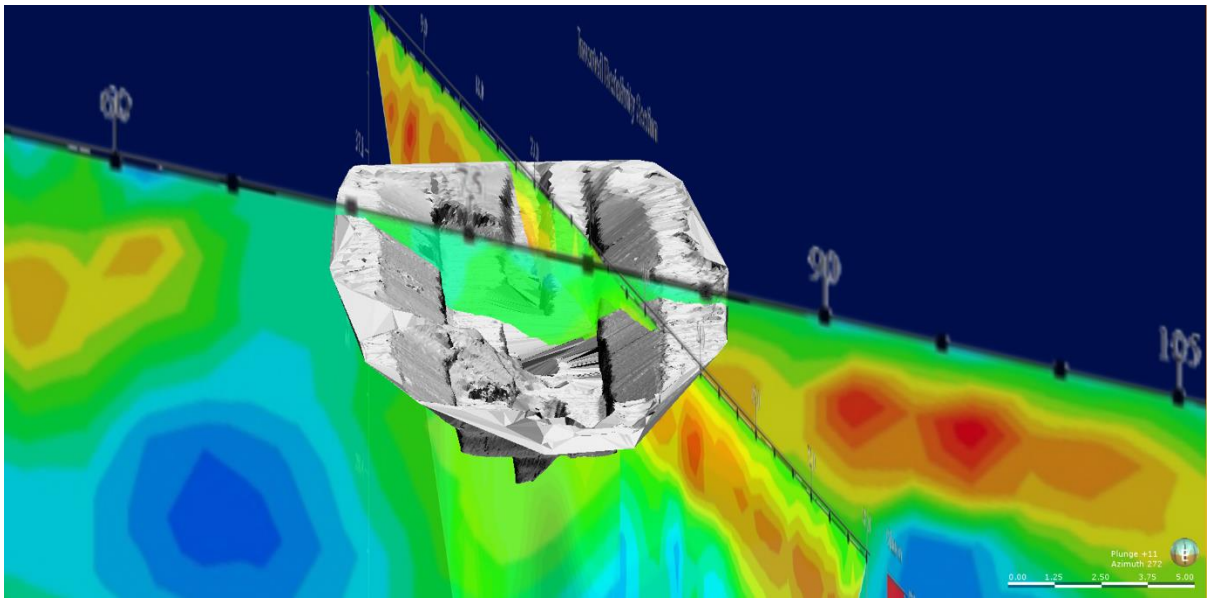

Figure 4.56. Oblique view looking WNW from 3D rendering of the trench superimposed over ERT inverted resistivity sections RUA05 (upper left to lower right of image) and RUA11 (subparallel lengthwise to trench).

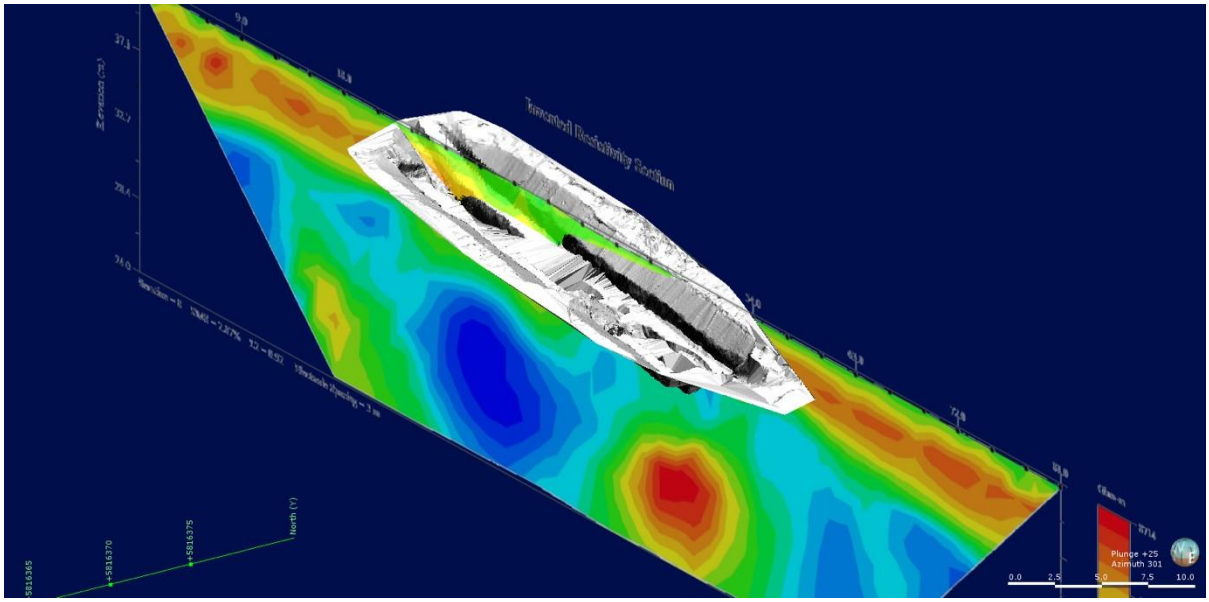

Figure 4.57. Oblique view looking WNW from 3D rendering of the trench superimposed over ERT inverted resistivity section RUA11.

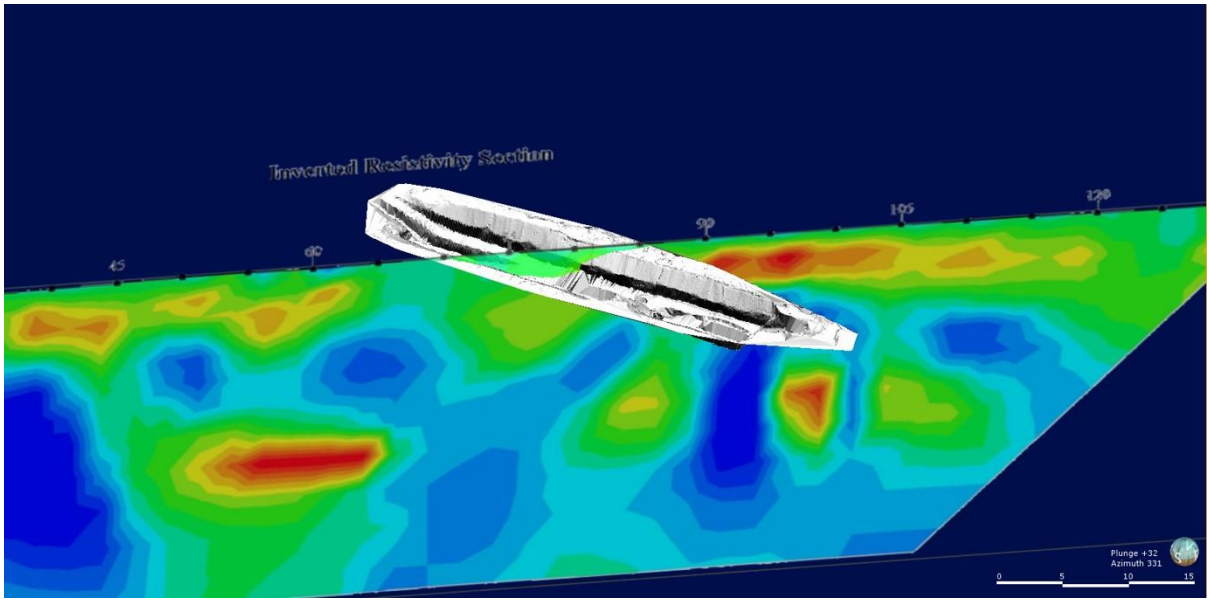

Figure 4.58. Oblique view looking NW from 3D rendering of the trench superimposed over ERT inverted resistivity section RUA05.

4.6. Summary

A reference ERT section established that, in general, the Ruakura area comprises a surface-forming *c.* 1 m layer of moderate electrical resistivity, overlying a *c.* 8 m thick, approximately horizontal, high resistivity anomaly. Moderate resistivity separates this shallow high resistivity zone from a deep low resistivity anomaly, which is also relatively horizontal. All inferred on-fault inverted resistivity sections displayed anomalies that reflected this general arrangement but with varying degrees of apparent abnormality. Sections from the south of the AgResearch farm in particular displayed apparent disruption, with high anomalies broken laterally and occurring at significant depth, while a range of vertical to subvertical features were seen in low resistivity anomalies.

Hand auger investigations were of limited value for significant ERT correlation but established that in most areas, shallow stratigraphy is consistent with that expected for Hinuera Formation. Hole collapse or the inability to penetrate beyond *c.* 1–2 m indicated significant gravel-rich beds at this depth. Notably, hand auger results strongly suggested that a buried water pipe in the trenched paddock is

15 m SW of its supposed position so probably did not interfere with ERT results and is not the cause of a large low resistivity anomaly. Groundwater was only encountered in one auger hole, adjacent to the western paleochannel, and groundwater was not encountered in a 3 m deep trench over the fortnight it was open, even following prolonged rain, so much of the local water table must be >> 3 m below surface.

An inference made from ERT results was proved by stratigraphic logging, being that, in the field area, the top *c.* 1 m of the Hinuera Surface is predominantly formed of late Quaternary tephra, with Hinuera Formation silts, sands and gravels comprising a deeper package at least 8 m in thickness. Trench logs and 3D modelling provided a correlation between upper high resistivity anomaly contours and the contact between a tephric, soil-forming upper package and underlying gravel-rich packages. However, a lower contact between this gravel-rich package and hypothesised silt/clay, peat, or weathered volcanic layers at even greater depth was unable to be observed.

Trenching provided direct lithostratigraphic insight to a depth of 3 m, revealing three distinct sedimentological packages: a topmost, clayey silt, soil-forming package (tephra); an underlying package of coarse gravels and sands (rhyolitic alluvium), and; a lower package of fine sands and gravels (pumiceous alluvium). These packages were essentially laterally contiguous through the trench and often cross-bedded, indicative of an earlier dynamic fluvial depositional environment capped by more recent volcanic ash, but a discrete zone of deformation was present through the middle package in the northern wall.

Deformation across an area some 4 m in width caused upper sand and gravel beds of Package II to be displaced, rotated and down-warped. The most distinctive displacement features were three convex fold-like structures that lacked intervening concave folds from which a fold train might otherwise have been deduced. Normal offset with downthrow to the east was observed within the westernmost of these structures, producing displacement of a faulting nature rather than folding. Offset was not obvious within the down-warped central and eastern structures themselves

but chaotic gravels had in-filled small fractures between these two pseudo-folds. Beneath and slightly offset from the easternmost pseudo-fold, otherwise horizontal beds become chaotic, with a lower unit (*i*) prominently intruding upward through a scour-like gap within an overlying unit (*h*) and reflecting the back-tilted nature of the westernmost pseudo-fold.

Lower still, deformation continued to the base of Package II but was more subtle, visible by way of thinning, lateral discontinuity, and overlapping of beds rather than by down-warping or offset. Secondary unit *o* thinned significantly toward the centre of the main deformation zone, becoming subtly but definitively discontinuous toward the top of a sub-vertical structure formed by *j*. Either side of this dike-like feature, *j* intercalated horizontally with *o* to form thin, vertically alternating, sill-like sequences. Approximately 1 m east of the core deformation zone, a sub-horizontal lens within *j* (with possibly a small, sub-vertical upward extension) displayed atypical normal grading, with basal gravels appearing to in-fill pockets atop *o*. Neither of these forms were seen elsewhere and illustrate that *j* was – at least in part – injected through *o* and become kinetically sorted. Whilst detailed logging of the southern wall directly opposite these features was not possible, rapid visual assessment undertaken immediately prior to trench in-filling did highlight possible offset and injection structures within the same package.

5. Discussion

5.1. Introduction

The results presented in Chapters 3 and 4 provide a suite of information showing that surficial and underlying features of the Hinuera Surface exhibit geomorphic and stratigraphic phenomena of some complexity in the Ruakura area. Chapter 5 discusses and offers interpretations of the key findings, including any assumptions made and limitations to the methodologies. A variety of alternative explanations for deformation observed in the paleoseismic trench and the relative likelihood of their validity is also considered.

5.2. Nature of the Hamilton Basin and Hinuera Surface

It has traditionally been accepted theory that the Hamilton Hills are features of an eroded Pleistocene landscape, more prominent in the west of the Hamilton Basin because towards the east they lie beneath the Hinuera Surface, buried by thickest Hinuera Formation deposits towards the apex of an alluvial fan (e.g. Selby & Lowe 1992; McCraw 2011). Modelling of the basin using high resolution LiDAR shows neither the buried hills nor alluvial fan concepts to be entirely accurate. While a few low hills do exist in the east, the Hinuera Surface is clearly the dominant landscape east of Te Tātua o Wairere Fault Zone; Figures 3.1–3.5 show that, except closest to the feet of the Central Hills in the extreme east, the surface is lower than the peaks of the hills to the west so cannot be covering similar hills across the eastern basin. This relationship is very subtle and perhaps not immediately apparent when viewed without vertical exaggeration (VE) but becomes obvious when exaggeration is applied. Caution must be taken when examining any features at high VE, as false interpretations are possible; for example, at small-scale, a shallow ditch can appear to be a much more significant feature such as a steep embankment. However, VE was applied over a very large (basin-scale) area, the entire basin landscape was

exaggerated at a consistent scale, and individual slope profiles provide additional evidence to give confidence in a revised interpretation.

The profiles of Figures 3.9–3.10 illustrate that Hinuera Surface slope is exceedingly low, never more than *c.* 0.09º and, for a distance of some 6 km immediately west of Te Tātua o Wairere Fault Zone, reduces to a mere *c.* 0.02º. Not only do these profiles show that the concept of an alluvial fan is a little misleading – given these are usually associated with slope angles >1º (Bowman 2019) – but also that the fault zone marks a very slight yet contextually significant change in both surface angle and landscape elevation. Exiting the Piarere Gap, the Hinuera Surface slopes from a maximum *c.* 70 m ASL at a very low angle of *c.* 0.08º across a landscape effectively devoid of hills and at lower elevation than those which occur across the basin's west (which are *c.* 80 m ASL). Coincident with Te Tātua o Wairere Fault Zone, the slope of the Hinuera Surface becomes effectively nil (*c.* 0.02º) through a zone dominated by hills but 6 km further west, the hills end and slope returns to almost the same as on the eastern side (*c.* 0.07º).

Fault zones have been inferred *c.* 4–8 km west of Te Tātua o Wairere Fault Zone, including Te Kourahi and Kukutaruhe Fault Zones, so it is possible one (or more) of these form a western boundary to an uplifted central-basin fault block – essentially a horst and graben complex (uplift being relative, graben subsidence may have occurred rather than the horst being directly uplifted). The concept is illustrated in Figure 5.1 but is based only on general geomorphology along the transect of Slope Profile 1 (Figure 3.9A); a transect further to the north or south would almost certainly incorporate additional hills to the west (see Figure 3.8) and the hypothesised horst may extend almost as far as, or to, the Western Waikato Hills and Ranges.

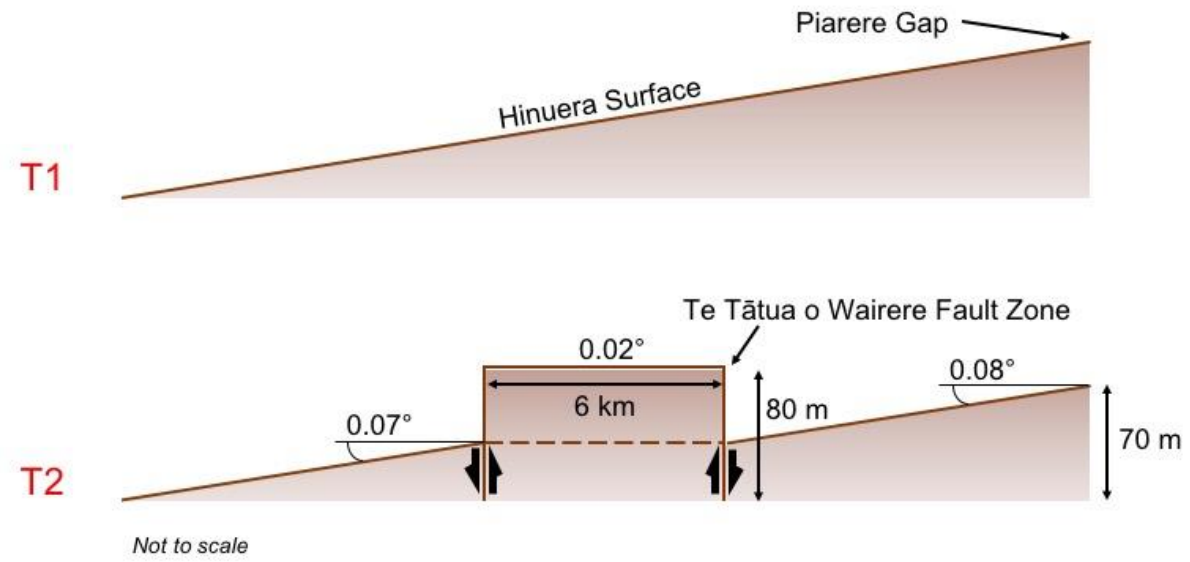

Figure 5.1. Cartoon of hypothesised relationship between slope and elevation of the Hinuera Surface, and slope and elevation of the zone of hills commencing immediately east from Te Tātua o Wairere Fault Zone. T1 represents the basin surface pre-faulting, T2 represents the fault zone forming the eastern boundary of an uplifted central fault block (horst). Cartoon is not to scale and slope is exaggerated.

If the horst of Figure 5.1 was uplifted following deposition of the Hinuera Formation, then the elevation difference between the horst hills and graben plains indicates a minimum uplift of *c.* 28 m (exclusive of elevation loss due to erosion) (refer Figure 3.9A). No evidence of Hinuera Formation materials atop the Hamilton Hills has previously been recorded to support this scenario and ≥28 m within 20 ka would appear to be significant uplift to have occurred without producing greater physical expression. However, such a scenario cannot be entirely discounted; the Hinuera Formation is almost entirely loose sands and gravels, which would be expected to erode very quickly, especially if seismically perturbed beyond their natural static friction angle of *c.* 30° (Opus International Consultants Ltd 2013; Gill & Orense 2019) and small fault scarps may once have existed along and in the vicinity of the Hillcrest ridge (Figures 3.18 and 3.19). In addition, Gibbons (2020) has demonstrated that materials in the Hamilton Hills can accommodate seismic deformation in a ductile manner – dampening the potential for widespread or obvious surface fault traces as evidence of seismicity.

In the absence of definitive evidence to support the hypothesis of horst uplift through the Hinuera Surface, it must be presumed that the postulated fault block was partly or wholly uplifted >*c.* 20 ka, thus any subsequent (post-Hinuera Surface) uplift must be <*c.* 28 m. Tectonomorphological relationships of this scale were not the prime focus of the study, thus further analysis in this regard has not been undertaken but the observations are made as they do lend support to the initial premise that geomorphology in the plains of Te Tātua o Wairere Fault Zone could reflect faulting. The observations also highlight intimately related areas of research which deserve future attention.

With regard to the fundamental nature of the Hinuera Surface itself, to avoid potential misrepresentation it would be pertinent for future studies to be mindful that the surface angle should not simply be regarded as <1° but in fact an order of magnitude lower, <0.1°. Consideration should also be given to using a term such as braided fluvial fan, or braid-plain, as postulated for comparable depositional systems elsewhere (e.g. McPherson *et al.* 1987). Indeed, Selby and Lowe (1992) touched upon this by considering the "fan" more akin to an extensive floodplain of many braided channels, which this study finds a more appropriate concept than that of a conical, valley-disgorged form, which tends to be implied by the term 'alluvial fan'.

5.3. Gravity Anomalies

Gravity anomalies are not interpreted as offering any significant insight with direct regard to Te Tātua o Wairere Fault Zone, beyond showing that anomalies are lower to the northwest of the zone than to the southeast (Figure 3.11). This relationship is not unexpected as the deepest part of the Hamilton Basin is northwest of the fault zone and thicker sedimentary sequences overlying basement are known to reflect weaker gravity anomalies (Edbrooke *et al.* 2009). Somewhat outside the scope of this thesis however, it is noted that the zone of lowest gravity anomaly appears not only parallel to the Hakarimata and Taupiri Ranges but also Kukutaruhe Fault Zone (compare Figure 3.11 with Figure 1.2). With the interpretation offered above, regarding a potentially Kukutaruhe Fault Zone-bounded horst, the low gravity anomaly and associated depth to basement could

support the notion of a deeper graben to the northwest of a fault block than to the southeast. A possible issue in this assessment of gravity anomalies is the very large scale of the dataset, as it comes from a regional dataset, aggregated from numerous surveys and recording flights covering not only the New Zealand landmass but the adjoining oceanic area. It may well be that a basin-specific, high resolution gravity anomaly survey could identify fine detail otherwise missed, or lost in the processes of regional data aggregation, normalisation and correction.

5.4. Earthquakes

As with gravity anomalies, earthquake epicentres did not appear to have any measurable relationship to Te Tātua o Wairere Fault Zone but some spatial association is not entirely discounted. Relatively few earthquakes have been recorded within the Hamilton Basin and of those that were, it is clear the only cluster – both spatially and temporally – occurred in relatively close proximity to the fault zone, around Puketaha, *c.* 5–7 km to the north (Figure 3.16). Liles (1971) had mapped a significant NW-SE striking fault in the Miocene-Pliocene horizon between Puketaha and Ruakura, a little over 2 km southeast of the Puketaha earthquake cluster, with a basement unconformity at the same level, almost directly beneath the epicentres. Estimates of depth to basement in this area are <500 m, it is between the 200 m and 500 m contours of Edbrooke *et al.* (2009), and around 350 m in Liles (1971); if faults occur at the same depth as basement then they must share a similar maximum depth and the fault trace may well extend through younger, shallower horizons.

Presuming Liles' faults are correct, then at Puketaha/Ruakura their traces must be no deeper than *c.* 350 m below the Hinuera Surface and are potentially even shallower. No evidence was found in this study to indicate surface fault rupture from any of the recorded earthquakes but, as records only extend as far back as *c.* 150 years, that does not preclude rupture either having occurred in the *c.* 20–15 ka prior, or the faults being blind and terminating within the Hinuera Formation. The Puketaha earthquakes have only maximum focal depths assigned (a consequence of the recording methodology at their times of occurrence), with one being assigned a 12 km depth and the remainder 33 km, so it is almost a certainty that true focal depth

was shallower. A leap in true focal depth from tens/several tens of kilometres to a few hundred metres may be overly ambitious but it is possible that shallow cryptic fault traces could be associated with deeper fault planes, dispersing seismic energy generated at depth. Section 5.6.1 discusses this in more detail, particularly how shallow faults may occur that do not share a common plane with the fault on which the focus is located.

5.5. Paleochannel Geomorphology

Early in the field survey period it became clear that despite the high resolution of the original Waikato LiDAR dataset, the topographic features of smallest relief (<*c.* 25 cm) were often too subtle to be distinguished. This was partially rectified during re-modelling using the newer Hamilton City LiDAR dataset but many gains were often nullified as the features themselves no longer existed – much of the area of interest had been obscured or extensively modified by development during the intervening period. Two major paleochannels were identified – western and eastern – both with particularly intriguing geomorphic stretches that could be seismogenic but unfortunately the largest physical developments happened to coincide with them. In the western paleochannel, an area of apparently disconnected and potentially offset minor levees, bars, and channels had since been covered by a *c.* 52,000 m^2 soil densification preload for the inland port container terminal. Areas of the eastern paleochannel with abnormal switchback meanders within a disconnected oxbow-like section now lie beneath the Waikato Expressway/Ruakura Interchange. While other channel stretches outside of these two sites were surveyed on foot and did exhibit geomorphology interpreted as seismically influenced, the inability to physically investigate these areas resulted in knowledge gaps which may otherwise have significantly altered the findings of this study.

With no clear connection to the western paleochannel (which skirts the Hillcrest ridge *c.* 500 m to the west) or any other obvious feeder channel, the eastern paleochannel describes a smooth, wide, eastward arc. In the northern portion of this arc, the channel turns back toward the west, before abruptly switching almost due north, effectively completing the full arc of a semi-circle (Figure 3.32). The western

extremes of this eastern paleochannel – its origination point and the northern *c.* 90º hook – were visible during field survey, with the channel's eastern bank being steeper than the western which suggests greater erosion and an eastward migration of the channel. Within the central part of this oxbow-like arc, DEM and aerial photograph analysis highlighted an overlying series of small, high-tortuosity meanders that all break away from the main channel and flow east/north-east before turning sharply west/south-west back onto themselves. The northern end of the section was bounded by swamp and, in conjunction with overlying small meanders, this leads to a supposition that the wider main paleochannel was significantly in-filled prior to being overlaid by a later, much smaller channel. The cause of the channel becoming blocked and filling with sediment could have been the result of avulsion, although there is no clear evidence for this and it is also possible that faulting could introduce an obstruction.

Of exceptional note, rather than exhibiting sinusoidal meanders, the tortuous secondary channel meanders of the eastern paleochannel all pushed out east and north from, and hooked sharply back to, the main axis; the channel appears to have been attempting to migrate east, as per the earlier, wider channel. No directly comparative stream pattern was found in literature but Burbank and Anderson (2001) suggest that channel migration occurs in the direction of down-displacement where alluvial plains are tilted. If the migration pattern of both the primary and secondary eastern paleochannels reflects a channel response to subtle tilting towards the east, this would suggest normal faulting with upward displacement to the west/north-west. This hypothesis is certainly supported, at least topologically, by the presence of a confirmed-faulted ridge to the south-west (the Hillcrest Ridge).

By comparison, the most notable features of the western paleochannel were observed to the north-west, where it breaches the Ruakura hills then appears to encounter a barrier that leads to severe constriction, if not complete blockage. That barrier is the paleochannel's own eastern bank (Figures 3.28 and 3.29). The nature of the channel's relationship to the hills is not easily resolved, as it would seem that the hills create an obstacle that caused the paleochannel to turn abruptly westward but there is little evidence to suggest where the channel may have flowed in the absence of the hills. The lack of abandoned channels or terraces on the eastern side suggests that the ancient river always flowed through this low gap, yet the gap does not offer an obvious natural path for river flow and, without being forced, it would seem to have been easier for a river to continue to flow along the eastern side of the hills. Perhaps the answer to the question of river-forcing between the Ruakura hills relates to the channel's subsequent pinching against the eastern bank a little further north.

Just north of the hills, the western paleochannel's eastern bank appears to obliquely cut the channel – not necessarily blocking it entirely, as a small avulsion channel may have maintained at least some degree of flow. It could be that the paleochannel bank is the scarp of a southward-propagating fault (downthrow to the west) along the edge of a block subtly tilted to the south/southwest. Such a tilt may have been sufficient to cause a river flowing northward along the eastern edge of the hills to exploit a gap in the hills then turn north again, along the fault scarp. The apparent lack of evidence for paleoflow atop the footwall block may be masked by the swamp that subsequently developed. This hypothesis is illustrated in Figure 5.2, and subsequent fault re-activation is postulated to explain (at least partial) blockage of the paleochannel. Much more work is required in this area to establish the validity or otherwise of this hypothesis but it served as a plausible theoretical link connecting the geomorphic features in this area with those approximately aligned to the south.

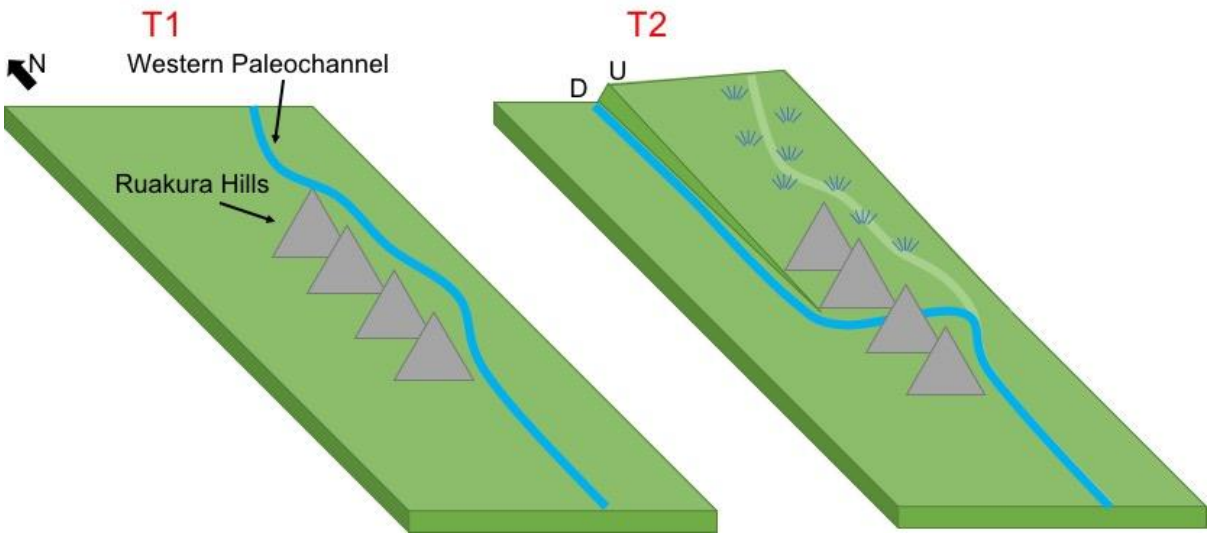

Figure 5.2. Cartoon of hypothesised fault block tilting causing the western paleochannel to seek a new path through the Ruakura hills and along the scarp on the footwall of a normal fault.

Along the western edge of the Ruakura hills, between the paleochannel constriction to the north and the ERT anomalies in the south, there seemed to be a subtle (<0.5 m) difference in elevation, being higher toward the east (feature B of Figures 3.35 and 3.36). It was difficult to ascertain whether this difference was entirely natural or if a farm race has caused/exacerbated an accumulation of sediment on the hillward side but the apparent break also aligned with a spur off the southernmost Ruakura hill which has an abnormally sharp and steep slope break (feature C of Figures 3.35 and 3.36). The slope break appeared in all historic images, including from well before the research farm campus was developed, so it and the <0.5 m elevation break were considered likely to be natural. A semi-linear connection was thus inferred as the most likely evidence for a fault across the farm, from the northern paleochannel constriction, along the elevation break, across the spur and through the southern ERT anomalies (Figure 3.37).

5.6. Paleoseismic Trench

5.6.1. Stratigraphy and Deformation

Although it had been intended to validate ERT via stratigraphic GPR, GPR unavailability at a very late stage of planning dictated the decision to proceed with trenching on the AgResearch farm based on the most promising ERT analysis. Trench logging revealed stratigraphy consistent both with general expectations from existing knowledge of the Hinuera Surface and shallow depth ERT inferences. Package I comprised late Quaternary tephra, rather than Hinuera Formation materials, and these are the true Hinuera Surface-forming beds at this location but afford little insight into possible fault movement (Figure 4.34). A wavy contact with Package II was notable in places for sharp ridge-like forms and seemingly vertical edges but the massive clays and silts of Package I are devoid of structure in which offset or deformation may be preserved. Unfortunately, this package also suffered from the most anthropic impact, having been built upon, then farmed for at least 40 years following building removal. As any apparent irregularities of Package I occurred shallower than *c.* 1 m – the depth within which most piles and utilities had been installed – it cannot be presumed that the unusual Package I-Package II contact represents natural phenomena, thus no interpretation is made.

Packages II and III are Hinuera Formation, their lithology and structure being consistent with numerous other studies (e.g. Schofield 1965; Hume *et al.* 1975; Kleyburg 2015) and while dating of the packages would have been beneficial to give precision regarding emplacement timespans (particularly cessation for the uppermost unit), it is considered appropriate to assume that deposition occurred no more than *c.* 20 ka and ceased no later than *c.* 15 ka. It was clear from the interbedded, semi-contiguous, essentially horizontal nature of units within Packages II and III, that the trench did not exhibit a clear, simple fault trace. However, a narrow zone of deformation within section 4 of the northern wall (and possibly the southern wall) clearly disrupted upper beds of Package II at a depth greater than any anthropic installations (except the rubbish pit which was *c.* 2 m deep but more than 12 m distant) (Figures 4.43 and 4.53).

The top of the deformation zone was defined by a trio of convex, fold-like scallops (pseudo-folds) marked by the long axes of prominent gravel clasts, heavy mineral strands and pumice lenses (predominantly of secondary units *b*, *c*, and *q*) following lines of apparent warping (Figures 4.48–4.51). Secondary unit *b* from the detailed sections is primary Unit 4 of the main sections, having thinned from ≥30 cm either side of the deformation zone to <10 cm within it, and was the key marker for identifying pseudo-folds. The westernmost scallop (between *c.* 16.5–17 m) was notable for upon close examination it comprised a downthrown block, back-tilted to the west, rather than being a down-warped pseudo-fold (Figure 4.48). Conversely, the easternmost scallop (*c.* 17.25–17.5 m) is more of a down-warped feature with an element of forcing to the east which significantly disrupted units *g* and *h* (Figure 4.49). Secondary unit *h* was cut to the west and east by *g*, and appeared to have been scoured through its centre by *c*, *q*, and *i* (Figure 4.51). The relationship between *h* and *i* was particularly noteworthy as *i* was overlain by *h* in the west but *i* cut upward through the scour zone to become thickened and overlie *h* to the east.

Juxtaposition of otherwise horizontal units against one another within the deformation zone is traceable through several semi-parallel, concave pseudo-planes which become essentially horizontal at base, providing evidence for a small listric fault complex reflecting tensional stress. Figure 5.3 illustrates this near-surface fault complex, characterised by anticlockwise rotation of curved segments along a near-horizontal basal shear plane (similar in form to a décollement) at *c.* 1.8 m depth (0.1–0.2 m height from bench). Segment A is downthrown against a main footwall to the west, with A in turn forming the footwall for synthetic segment D. Segment C has also rotated anticlockwise but sheared antithetically atop segment D and been forced against the main hanging wall to the east. Localised compression of segment C has effectively formed a minor reverse fault that has rolled over and appears synthetic with D (Figure 5.3). Segment B is a minor section that has accommodated differential stress between segments A and C. Uppermost, undifferentiated units of Package II have in-filled small voids and fractures between segments A, B, and C.

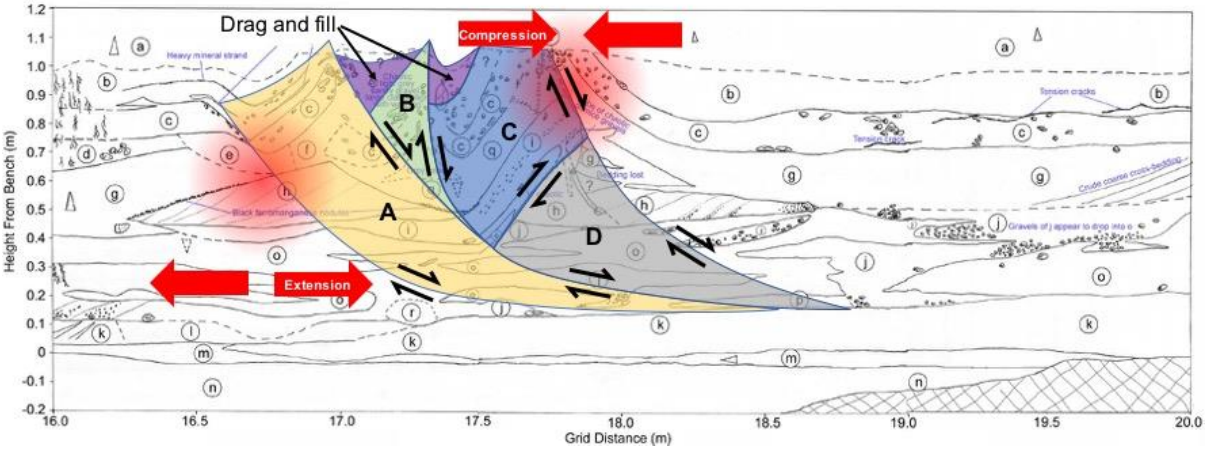

Figure 5.3. Sketch from Figure 4.51 modified to show displacement of four fault segments A–D within the trench. Segments A, B, and D have rotated toward the east (right) along a basal plane, while segment C has sheared atop D and been compressed against the main hanging wall, forming a small rollover reverse fault. It is important to note that planes are inferred from apparent offset and intercalation of secondary stratigraphic units – true planes do not occur due to granular displacement masking failure surfaces (and cross-cutting by liquefaction features, see Figure 5.4).

Whilst a lack of clear displacement beneath segments A–D (particularly in secondary unit *k*) negates identification of a simple through-going fault, secondary unit *m* thinned noticeably from *c.* 7 cm to <2 cm directly beneath the segments and comprised finer particle sizing than elsewhere through that unit. This thinned and fined zone of *m* is considered potential evidence of horizontal shear, as particle breakage during such shearing commonly imparts volumetric reduction and a reduction in particle size (Coop *et al.* 2004). Additionally, distinctive hummocky and swaley-type cross-bedding was seen in *n* but nowhere else. This type of bedform is typically attributed to wave oscillations in shallow marine or lacustrine environments (Eyles & Clark 1986). As no other evidence was found to support such a paleoenvironment (e.g. wave-cut features, calcareous inclusions, organics), it is suggested the patterns result from originally more laminar, fluvially emplaced heavy mineral lags being seismically reworked. In conjunction with the presence of overlying displaced and rotated segments, the thinned, fined, and reworked nature of underlying strata strongly suggests the deformation zone has accommodated lateral extension by way of normal displacement. At least some of this extensional movement must have occurred as cryptic inter-granular displacement, as no deformation or reworking was obvious in secondary unit *k*.

Below the pseudo-folds and displaced segments, between *c.* 16.5–18.5 m, secondary unit *j* intercalated with *o* to form a broad dike-like structure with sills of *j* branching horizontally/sub-horizontally into surrounding *o* – this is interpreted as one of three cross-cutting injections of *j* due to liquefaction (Figure 5.4). Gravelly, asymmetric boudin-like lenses of *j*, surrounded by *o*, slightly overlapped and stacked atop one another immediately east of the pseudo-folds, appearing to have been subjected to lateral compression with a resulting semi-imbricate relationship (Figure 5.4). In the eastern extremity of the deformation zone, between 18.5–20 m, two further liquefaction structures comprised of *j* are interpreted; a second dike-and-sill structure between *c.* 0.20–0.45 m height above bench, and an overlying but offset semi-lenticular zone between *c.* 0.40–0.55 m height above bench (Figure 5.4).

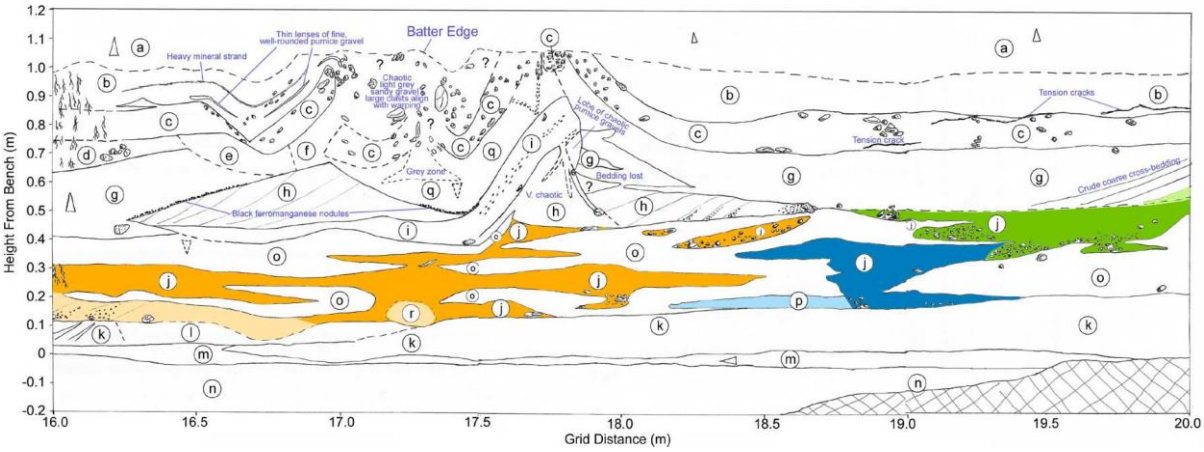

Figure 5.4. Sketch from Figure 4.51 modified to highlight three liquefaction features formed by secondary unit *j*. The first liquefaction feature is coloured orange, the second blue and the third green – lighter shades of each colour represent materials that may be part of these features but are not confirmed. The third (green) feature is interpreted as reliquefaction of the second (blue), comprising the same range of materials but being silt-dominated and normally graded.

Though formed of the same materials as the rest of *j*, the semi-lenticular zone was especially notable as it was much siltier and exhibited strong normal grading, with gravels appearing to have settled to the lens' base and filled pockets within both the top of *o* and underlying *j* (Figure 5.4). A sub-vertical extension of silt from this lens was tentatively inferred through *g* but may have been a foreset within coarse cross-bedding of that unit. Sketched as primary Unit 13 in Figure 4.43, the notable characteristics of the *j* lens suggests a possible subsequent reactivation event (i.e. earthquake aftershock or later main shock) that reliquefied and graded an initial

liquefaction structure (the underlying dike-and-sill structure). As reported by Yasuda and Tohno (1988), liquefaction of sandy sedimentary sequences and reworking of initial structures is not an uncommon phenomenon and probably happens much more often than is reported. Seismogenesis of the liquefaction structures is considered highly likely, given the proximal relationship with fault deformation and earlier work identifying seismically-induced paleoliquefaction in the same materials (i.e. Kleyburg 2015). However, as the structures cross-cut rotated segments and did not appear to have been themselves deformed, these injections must have occurred post-failure, thus liquefaction is suggested as a result of (or at least coincident with) listric displacement rather than being the cause of it.

Being in such close proximity to a number of anthropic installations and underlying previous building foundations, it would be tempting to dismiss the deformed section as simply resulting from these anthropogenic impacts. Despite comprehensive utilities clearance being undertaken, abandoned wells and a rubbish pit near the deformed section were not detected prior to trenching. However, no comparable deformation occurred anywhere else within the trench, the deformation was deeper than the building foundations and majority of utilities, and it is considered that the nearby wells may have unwittingly been installed for reasons relating to the cause of deformation. While their discovery impacted the ability to log the southern wall and imparts some concern regarding validity of stratigraphic interpretation in places, the fact that these structures did not appear in either (non-stratigraphic) GPR or electromagnetic tracing used by the service locator provides confidence they were not responsible for any significant ERT anomalies. While the westernmost structure was an unlined, infilled rubbish pit, and is probably the cause of a slightly deeper (yet still relatively shallow) high resistivity anomaly, the two wells are considered likely to have exploited low resistivity zones rather than be the cause of them (Figure 4.54).

The lack of records for these structures led to a number of suggestions as to their possible purpose, including long-drop toilets and offal pits, but they were remarkably clean to have likely been the former, and too small and well-constructed

to be the latter. Farm staff and experienced contractors suggested the pits were water wells for the old accommodation blocks, as they appeared to have been hand-dug, carefully brick-lined and capped with removable concrete lids. Both wells had been only partially filled prior to (or during) abandonment, with a resulting void of *c.* 1–1.5 m. As an empty, non-conductive space, these would be expected to show as extremely high resistivity anomalies in ERT sections but the voids were smaller than able to be resolved with the electrode spacing used, so are concluded to not have affected results. Most pertinently, it is not unreasonable to consider that wells would have been installed where water was easiest to access, either close to or at the surface. Given that this location is on a bar, higher than terrain to the north and south, and where groundwater was not encountered in hand augers, the fact the easternmost well was sited directly above a vertical zone of low resistivity suggests its placement atop a deep, hydrologically-favourable feature. Indeed, the eastern well is located directly along the strike of inferred fault and its presence was the sole reason the trench commenced *c.* 6 m further west than intended. Groundwater could be closer to the surface along this line of strike due to exploitation of fault-related fissures or zones of increased porosity.

5.6.2. Co-seismic Deformation

The deformation within the northern trench wall is not identified as a direct fault structure, as it was not able to be traced below Package II so cannot have propagated from below, vertically through Package III. Instead, based on the proximity of the inferred fault, the possibility of co-seismic origin deserves consideration. Unlike simple shear mechanisms in homogenous lithologies, discrete-element modelling of fault propagation in disparate lithostratigraphic sequences has shown that surficial layers of unconsolidated granular sedimentary covers can undergo stretching, thinning and fracture at locations dislocated from an underlying basement fault plane (Finch *et al.* 2004; Jackson *et al.* 2006; Hardy 2011).

Basement fault dip and cover sequence inter-granular bond strength are both key influences, but in the early stages of upward fault propagation – while a fault remains blind – no matter the variables, a shallow monocline forms in the footwall

that broadens upward (Figure 5.5A [*D*=1.5] and B [*D*=1.5]). Roll-over also takes place in the hanging-wall to create a low-angle syncline within the same layers as the monocline but as propagation continues, the fault becomes through-going and the monocline is eventually breached (Finch *et al.* 2004). However, more importantly, surface fracture or displacement may not be directly located above the fault plane/s and lateral, bed-parallel slip can be discrete, apparently unconnected to a fault and manifest within the footwall some distance off-fault (Finch *et al.* 2004; Jackson *et al.* 2006) (Figure 5.5).

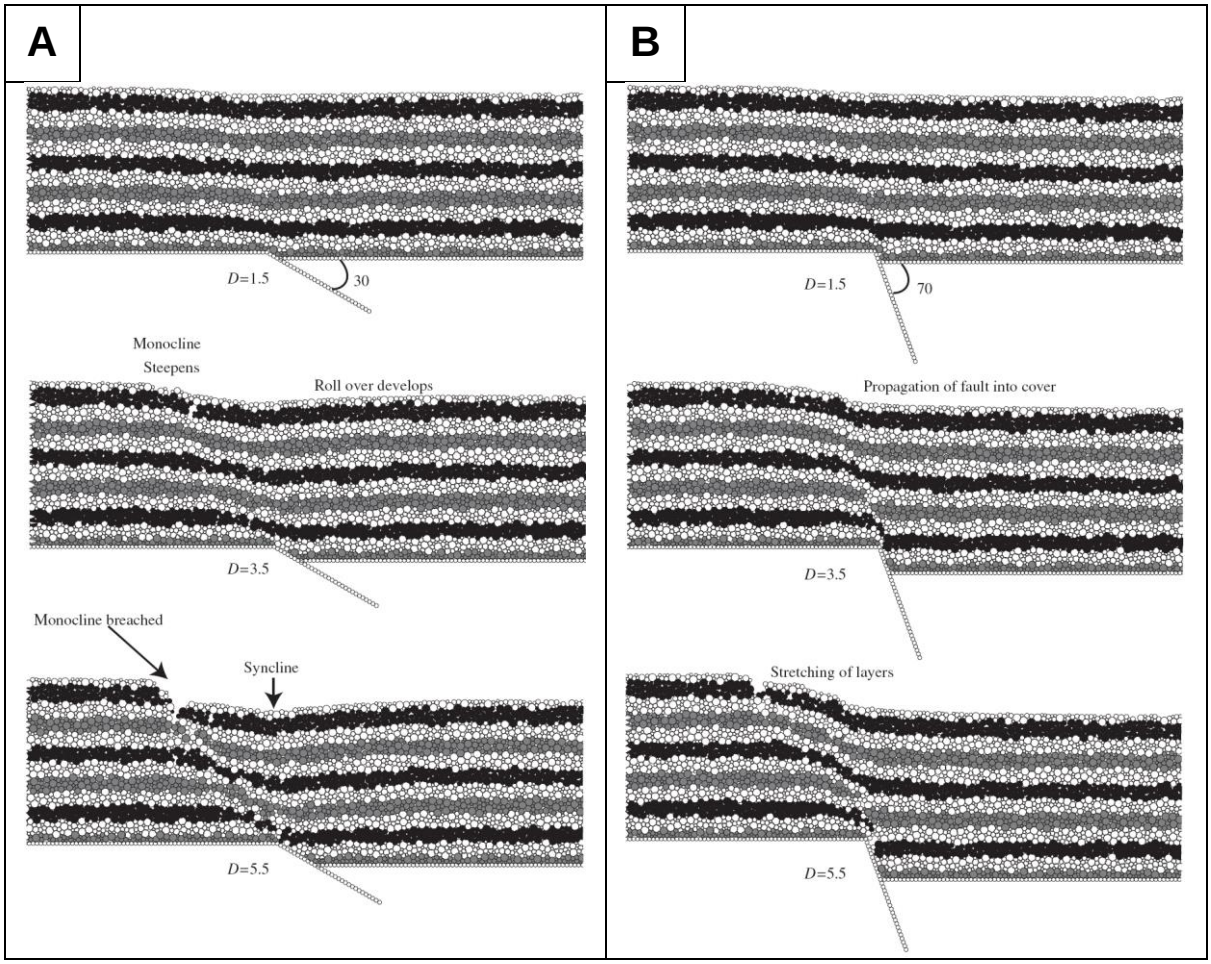

Figure 5.5. Comparative discrete-element fault propagation models through unconsolidated granular cover sequences with fault initiation in basement at angles of (A) 30° and (B) 70°. *D* values represent a relative measure of basement displacement, e.g. *D*=5.5 indicates a heave of 5.5 units. With a 30° basement fault, the final-stage fault plane extends through sediments at an angle of *c*. 40° and breaches the surface along-plane. For a 70° basement fault, the final-stage fault plane continues at 70° through sediments but is only visible at shallower depths as a thinning of those layers – the tip does not breach the surface but discrete plane-parallel fracturing occurs within the footwall. From Finch *et al.* (2004, p. 494, Figure 6 & p. 496, Figure 8).

Affecting both the relative proximity of surface fracture/s and the angle of any fault plane that may develop within overlying sedimentary covers, the angle of basement fault dip plays a critical role. With a basement fault dip of 30° in what Finch *et al.* (2004) classed as "standard" covers (having a particle breaking separation of $0.05R - R$ being the inter-particle equilibrium separation, the point at which attractive and repulsive forces are balanced), a granular cover sequence fault plane develops at *c.* 40° and the plane breaches the surface monocline. By comparison, as basement fault dip increases, faulting structures within the cover sequence become increasingly distributed and cryptic (Figure 5.5). In particular, at 70° basement fault dip a cover sequence fault plane maintains the same angle but only as a narrow zone of pseudo-ductile deformation, traceable through layer thinning and pinching without a direct surface breach; small brittle surface fractures do form within the footwall block but at some distance away from the plane (Finch *et al.* 2004; Hardy 2011) (Figure 5.5).

A reduction in cover sequence strength to $0.01R$ ("ultra-weak") further impedes development of a simple fault plane in granular sediments, dampening shallow and surficial deformation, resulting in the prominent features being distributed surface fractures and sub-surface warping (Finch *et al.* 2004) (Figure 5.6). As Figures 5.5 and 5.6 illustrate, brittle failure or offset is not necessarily seen at depth, directly below surface-breaching fractures (especially during earlier stages of fault development) and off-fault co-seismic deformation may only be seen by way of extremely subtle layer thickening, thinning or dipping. The combination of broadly analogous materials, apparent sub-surface lateral continuity, and no obvious root for shallow depth deformation structures in the Ruakura trench, reflects those theorised in numerical models. In particular, thinning is observed in secondary unit *m*, beneath a surface fracture (listric faulting), and there appears to be a very subtle (<10 cm), monoclinal-like decrease in elevation of the Unit 2-3 contact (Figure 4.43) (secondary units *a-b* in Figure 4.51) to the immediate east of the deformation zone.

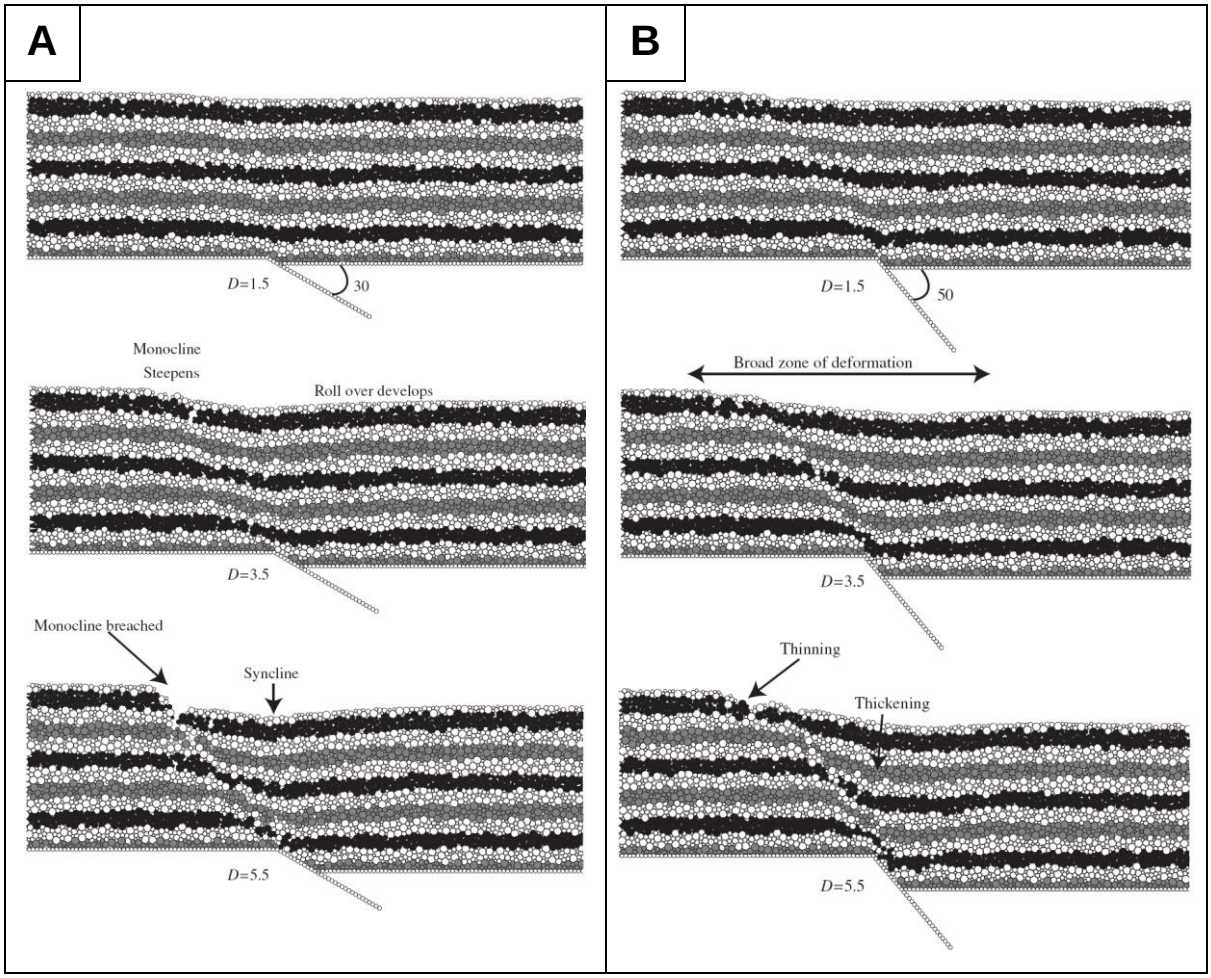

Figure 5.6. Comparison between 50° basement fault dip fault propagation models through (A) standard (0.05*R*) and (B) ultra-weak (0.01*R*) cover materials. Note that (A) is the same model as in Figure 5.5A. The standard model displays surface fracture approximately in line with clear fault propagation through the sedimentary covers whereas the ultraweak model exhibits subtle off-fault surface fracture and deformation (labelled 'Thinning') in the footwall but subsurface deformation is predominantly further to the right, in-line with the basement fault plane. From Finch *et al.* (2004, p. 494, Figure 6 & p. 497, Figure 9).

5.6.3. Comparison with Te Puninga Trench

Shortly after closure of the Ruakura trench, GNS excavated three similar trenches across a strand of the active Kerepehi Fault Zone – the Te Puninga Fault – through *c.* 22.5–17.5 ka Hinuera Formation in the Hauraki Basin. The author was invited to participate in logging of the Arnolds trench during later stages and this afforded a brief visual comparison between the inferred deformation at Ruakura and confirmed on-/near-fault deformation in extremely similar lithology. Major physical differences between the Ruakura and Arnolds trenches included the former being across flat terrain, with purely alluvial deposits (plus tephra covers), whereas the latter crossed a sloping fault scarp (downthrow to the west) with swamp deposits overlying alluvium within the hanging wall. Figures 5.7 and 5.8 illustrate portions of the Arnolds trench sketched by the author which exhibited near-identical deformation.

Figure 5.7 shows the presence of a liquefaction injection structure similar in both morphology and lithology to those in the Ruakura trench. Sand-gravel sized pumiceous sediments (Arnolds unit 2) formed a prominent dike and sill structure which intruded both horizontally and across the top of the breached bed (Arnolds unit 1), with disconnected, semi-imbricate, boudin-like lenses of the liquefied unit occurring toward-fault. Injection structure sediments were very similar, though slightly more gravelly, than secondary unit *j* at Ruakura and the toward-fault, semi-stacked boudin-like lenses were practically identical in form and position (Figure 5.7 *cf.* Figure 5.3). Figure 5.8 highlights structural deformation very similar to Ruakura, though it occurred in the opposite trench wall to, rather than overlying, the major liquefaction. In particular, a marker bed (Arnolds unit 9) had been sheared with a sense of normal displacement but rotated and back-tilted, akin to the western-most pseudo-fold at Ruakura, while discrete units within the section incorporated chaotic rotation and aspects of compressional disruption (Figure 5.8 *cf.* Figures 4.48 & 4.49). Overlying units had subsided across the top of the deformation zone but without brittle failure or obvious internal displacement, as was also the case in the Ruakura trench.

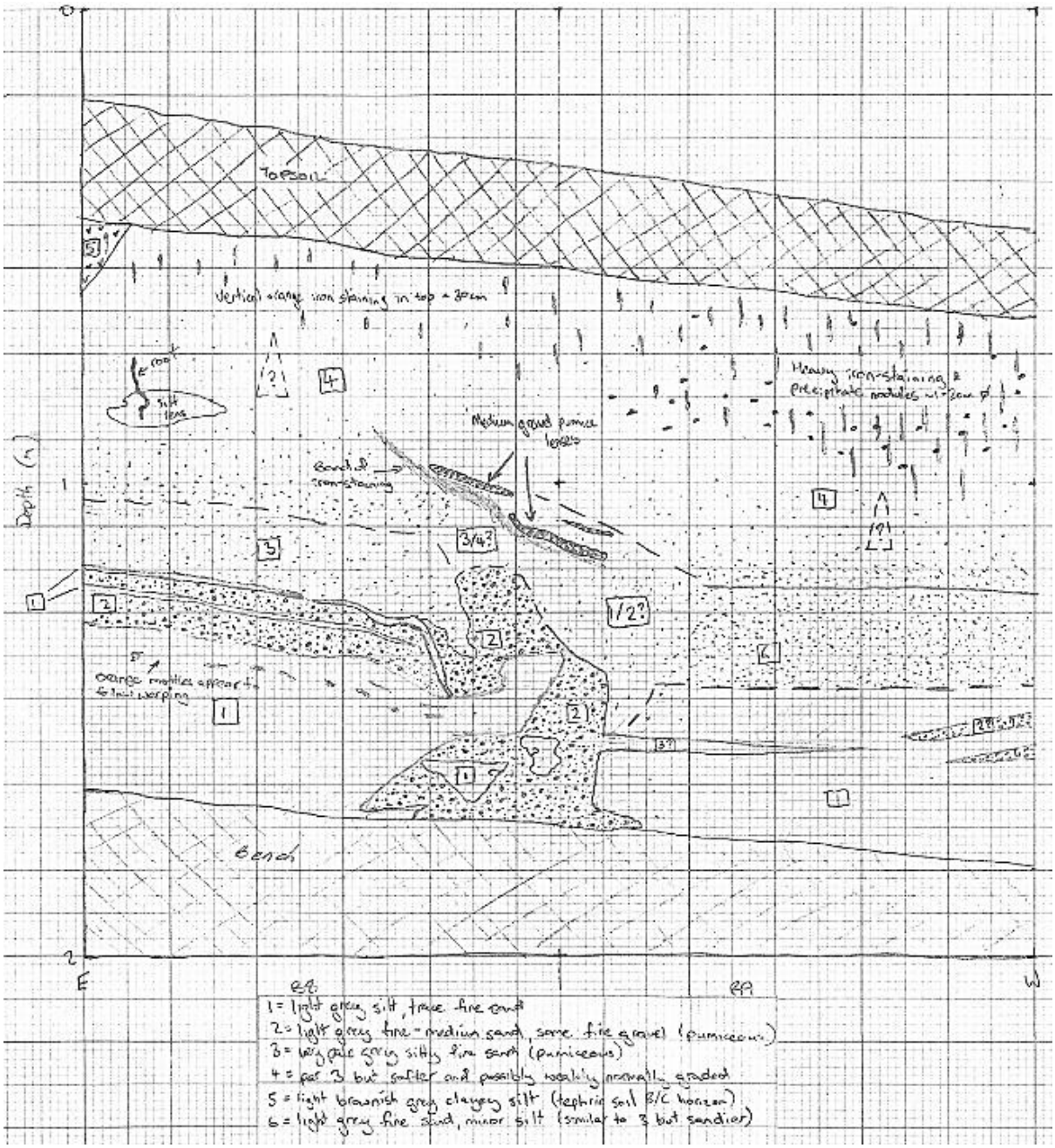

Figure 5.7. Sketch of near-fault deformation in the southern wall of Arnolds trench, across the active Te Puninga Fault in the Hauraki Basin. The section is near the hinge zone of a large monocline dipping down toward the fault (right of frame). Note the lack of brittle failure and obvious offset in beds but the presence of a major paleoliquefaction feature (unit 2) and steepening of dip in units 1 and 3 toward the top of the fault scarp (left of liquefaction).

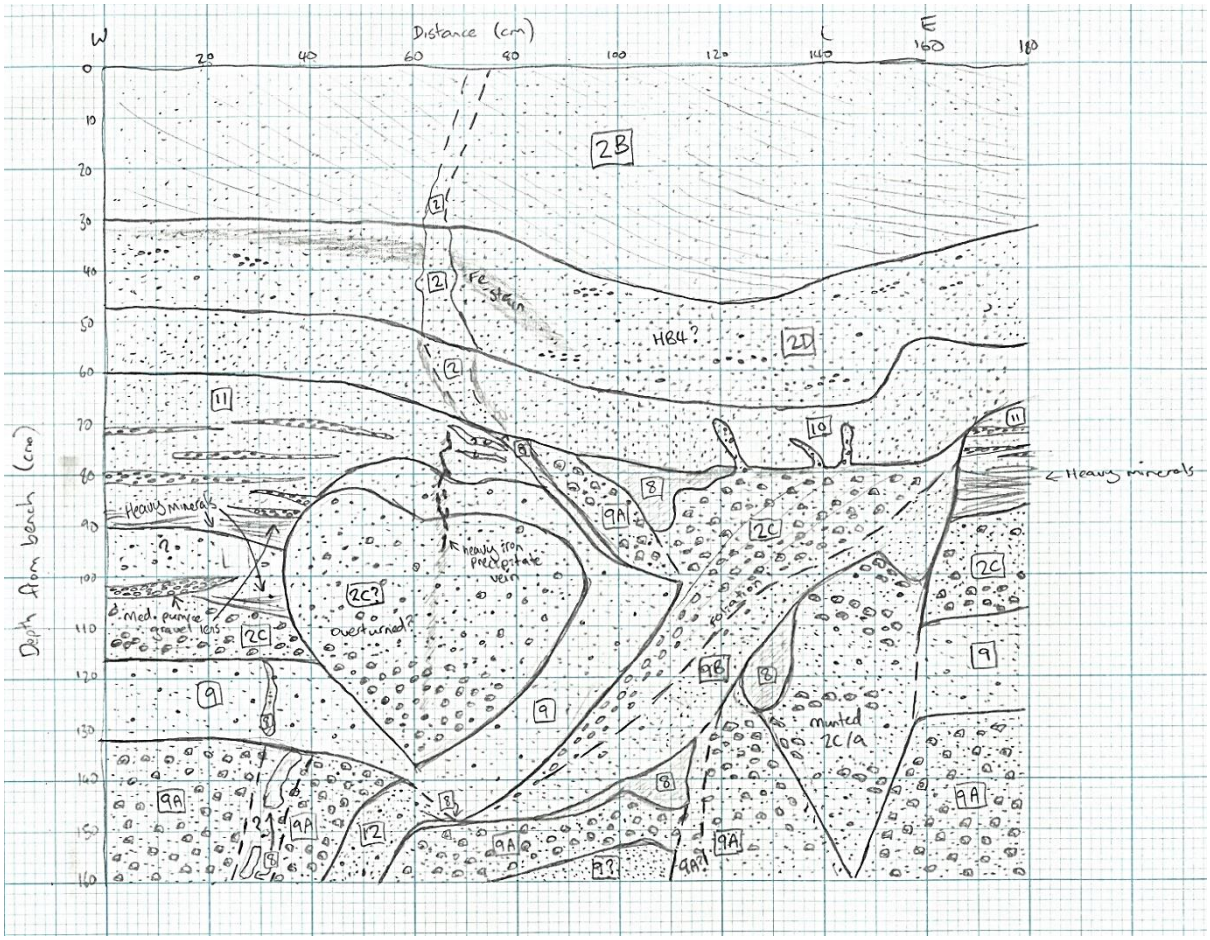

Figure 5.8. Sketch of near-fault deformation in the northern wall of Arnolds trench, across the active Te Puninga trench in the Hauraki Basin. The section is near the hinge zone of a large monocline dipping down toward the fault (left of frame) and is part of the same zone of liquefaction shown in Figure 5.7 but on the opposing (southern) wall. Note the down-warping of upper beds 2B, 2D, and 10, which overlies a chaotic zone that includes shearing and rotation of units 9/9B - forms extraordinarily similar to those seen at Ruakura.

5.7. Possible Alternative Explanations for Deformation in the Ruakura Trench

Deformation in the Ruakura trench is considered evidence of co-seismic deformation, near to the fault-proper, but seismic activity is not the sole possible causal mechanism. The robustness of this hypothesis will therefore be tested by considering alternative explanations; anthropic modification is one obvious such explanation but has been considered unlikely for reasons described as part of the discussion regarding stratigraphy within Section 5.6.1. Consideration is therefore also given to the possibility of the deformation resulting from tree uprooting, a sinkhole, or an impact crater.

5.7.1. Tree Uprooting

Uprooting of established trees, possibly as a result of flooding or strong wind, typically results in an overturned root plate that deforms underlying strata and creates a "pit-mound pair" – a crater-like depression from rip-up of the root plate, with an adjoining hummock of displaced soil (Schaetzl *et al.* 1988). In their review of tree uprooting phenomena across a number of regions, including New Zealand, Schaetzl *et al.* (1988) reported that an average area of 11.9–16 m^2 is disturbed by uprooting of mature trees and provided examples of root plate rotation – illustrating the eventual pit-mound relationship – as shown in Figure 5.9. Although deposition of Hinuera Formation occurred during a glacial period, with little associated soil development, podocarp–hardwood forest is known to have established across the Hamilton Basin following pedogenically-favourable increases in climate temperature and precipitation from *c.* 15 ka BP (Hume *et al.* 1975; Selby & Lowe 1992).

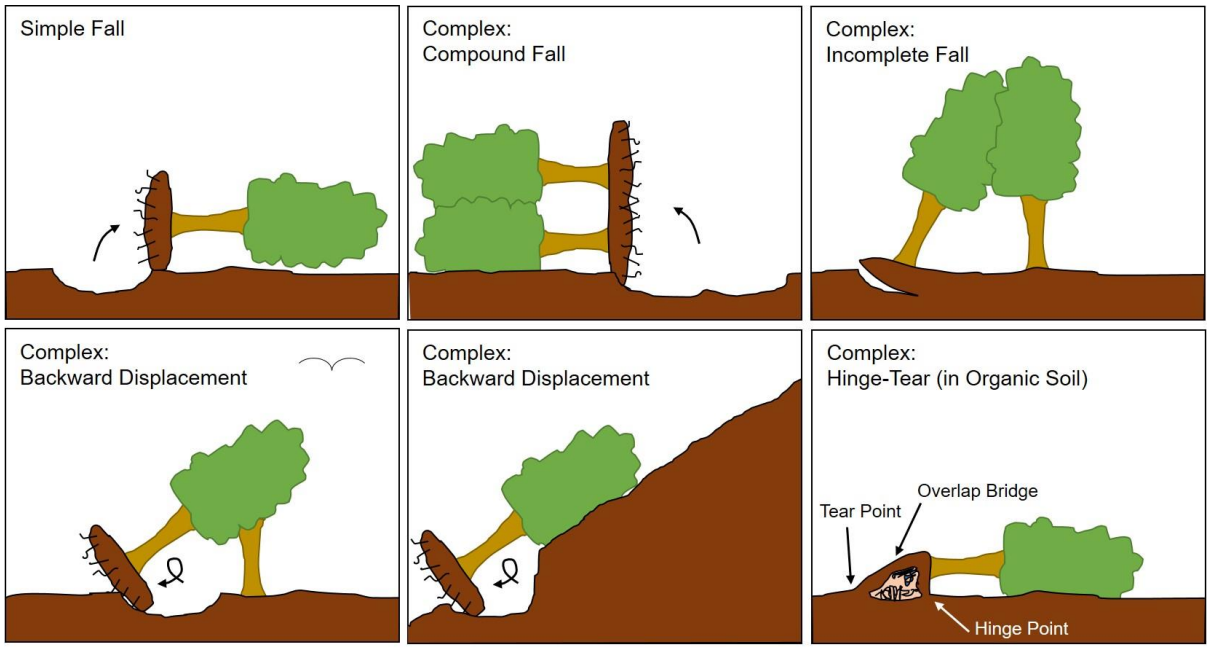

Figure 5.9. Cartoon of representative examples of tree uprooting and root plate displacement. Redrawn from Schaetzl *et al.* (1988, p. 2, Figure 6). Following decomposition or removal of the overturned tree, the resulting crater-like depression and adjacent hummock of displaced soil create a pit-mound pair.

That trees could have grown atop the Hinuera Surface at Ruakura is a distinct possibility but it is reasonable to assume there must firstly have been some soil for them in which to root. As no paleosol exists atop Package II, the presumption must be that Package I constituted that soil (as it does to this day) or an earlier soil existed that was entirely eroded prior to deposition of Package I. If a tree had established and was subsequently overturned in Package I, with deeper roots causing the deformation of Package II, it follows that Package I must also be significantly disturbed. Although the contact between Packages I and II above the deformation zone was indistinct, warped/displaced beds of Package II did not extend into Package I and, if these represent pits, there was no evidence for a mound structure in Package I.

In the absence of deformation through to Package I but if the deformation is indeed attributable to tree uprooting, any tree must have established within a soil atop Package II which has since completely eroded. The graded contact between Packages I and II, suggesting at least partial syn-deposition, combined with the lack of any indication for pre-tephra deposition pedogenesis within Package II lends little support to this theory. In addition, the size and extent of deformation, and potential soil parent material of Package II appear too small, discrete and free-draining to indicate tree-overturn; Schaetzl *et al.* (1988) suggested that key evidence to support the supposition of tree uprooting is pit-mound amplitudes up to 2 m and extensive pit-mound topography (up to 50% of the study area), typically associated with organic, wet or gleyed soils. None of these appear to be the case in the trench area, with deformation being confined to a single <*c.* 4 m area with amplitude <*c.* 0.5 m and in free-draining alluvium.

5.7.2. Sinkhole/Tomo

Sinkholes (often referred to in New Zealand as tomo) are typically associated with karst landscapes, whereby surface deposits collapse into voids created in underlying carbonate strata, but can also be associated in other landscapes subjected to large-scale groundwater extraction (Youssef *et al.* 2016). In an investigation of sinkholes within sandy and gravelly alluvium in modern desert environments of Saudi Arabia, Youssef *et al.* (2016) note that a key associated characteristic is a surficial circular ring structures of fractures and broken scarps, centred on the axis of the sinkhole. Trench logging by Youssef *et al.* (2016) also showed that sinkhole deformation can substantially replicate normal faulting, with bedding being downthrown toward the centre of the void and fissures being filled with vertically/sub-vertically orientated clasts (Figure 5.10).

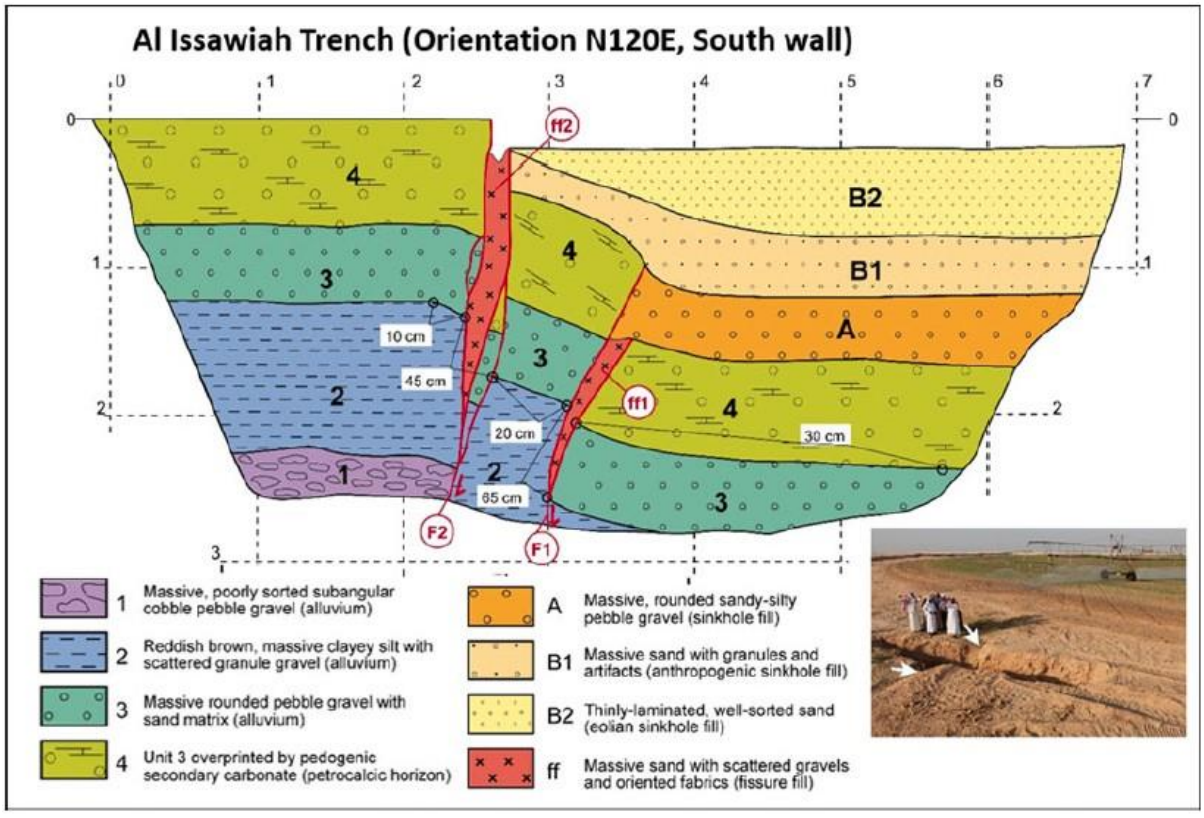

Figure 5.10. Sinkhole log from the Al Issawiah trench reproduced from Youssef *et al.* (2016, p. 636, Figure 9), showing how the sinkhole deformation offsets alluvium bedding and replicates the typical form of a normal fault.

Neither large scale aerial imagery nor high resolution DEM analysis revealed any ring-like structures – fracture or otherwise – around the Ruakura trench or within any nearby area. Bedding offset or any conclusive indication of a footwall/hanging wall relationship akin to normal faulting was not observed in the trench. While some vertical/sub-vertical clast orientations were seen in the Ruakura trench, these were part of warped structures, with adjoining clasts at least partially aligned with the warping rather than simply filling vertical/sub-vertical fissures. The lack of similarities with a comparable stratigraphic environment – in addition to the area not being a karst landscape – does not favour the hypothesis that the Ruakura trench deformation relates to a sinkhole/tomo.

5.7.3. Impact Crater

Impact (predominantly meteorite) craters result from kinetic shock associated with an object striking the Earth at high velocity (Dence *et al.* 1977). Dence *et al.* (1977) noted that although many impact craters measure kilometres in diameter, small meteorite impact craters of approximately 0.5 m wide have been recorded but, crucially, even small craters always share at least one of the following diagnostic characteristics:

- A bowl shape;
- A central high of uplifted material, surrounded by a ring-shaped depression;
- Lithologic brecciation and fracture;
- Shock metamorphosed (glassy) ejecta;
- Fragmented remains of a meteorite (or the complete meteorite, in which case the feature is referred to as an impact pit or impact hole).

Apparently not explored in the years since, experiments in the 1960s and 1970s that sought to understand the impact response of alluvial materials (similar in nature to the Hinuera Formation) showed that crater morphology in alluvium does not greatly differ from that listed above (Jones 1977). In addition to these common features, Jones (1977) described impact craters in alluvium as consistently incorporating conical sand blows (either intra-crater or within ring fractures, with

associated feeder dikes) and – even in loose sand – a coherent, overturned blanket of ejecta with natural stratigraphy inverted upon itself (Figures 5.11 and 5.12).

Figure 5.11. Conical sand blows atop a radial fissure of the experimentally-induced Snowball crater, created by the detonation at-surface of c. 453 tonnes of TNT. Reproduced from Jones (1977, p. 165, Figure 2).

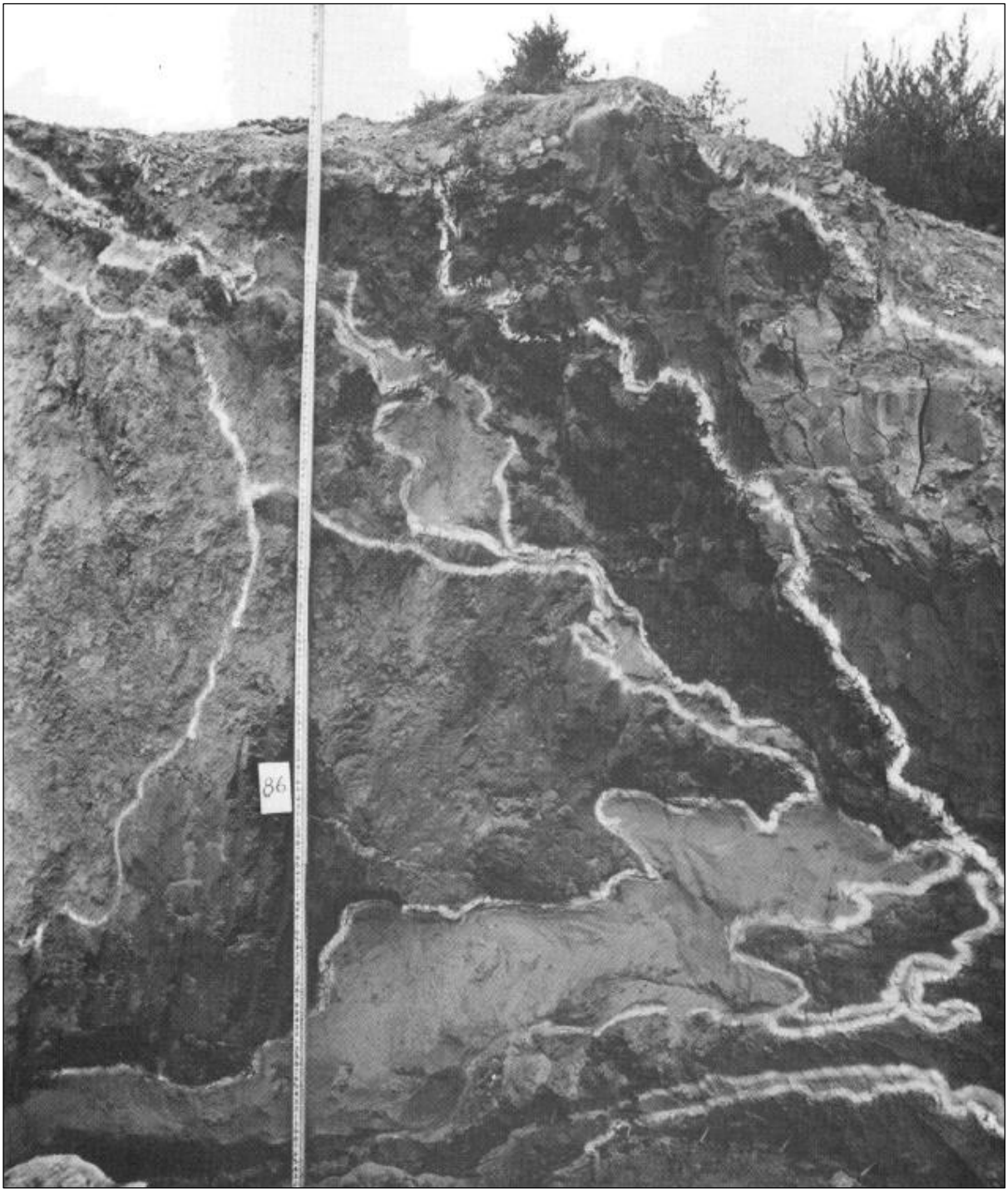

Figure 5.12. Cross-section through Snowball crater showing inversion hinge region of overturned stratigraphy (crater centre to right of frame). Reproduced from Jones (1977, p. 175, Figure 10).

Deformation in the Ruakura trench did not reflect any of the diagnostic features of either Dence *et al.* (1977) or Jones (1977). While the scallops at the top of Package II are somewhat bowl-like, they do not incorporate fractured clasts, are not part of any larger structure with any degree of ring-like symmetry, and there was no evidence for either ejecta or overturned stratigraphy. It is possible that features which may be small seismites could reflect impact-induced liquefaction but this was not prolific and there was no evidence for conical sand blows. As a result, the potential for an impact being the cause of the deformation is considered very low.

5.8. Revised Fault Strike

Potential fault scarps were seen in historic images of the university and research farm areas which seemingly exhibit a general trend north/northwest of the Hillcrest ridge; this is, however, very speculative and if they did exist they are more likely expressions of faulting through Walton Sub-Group and the ash formations. Nevertheless, in conjunction with a lack of in-trench fault evidence but with areas remaining of significant interest directly east of the trench which warrant further exploration, Figure 5.13 suggests a revised interpretation of fault strike incorporating these apparent scarps. The key deviation from the original map of Figure 3.38 is that south of the Ruakura hills, the fault is suggested to swing slightly east and connect with the Hillcrest Road fault (which also coincides with an eastward kink in the Hillcrest ridge). Importantly, this revision reconsiders the originally posited splinter or strand immediately east of the inferred main line of fault as part of the fault-proper, where the longitudinal bar appears offset and ERT sections RUA12–14 showed notable anomalies.

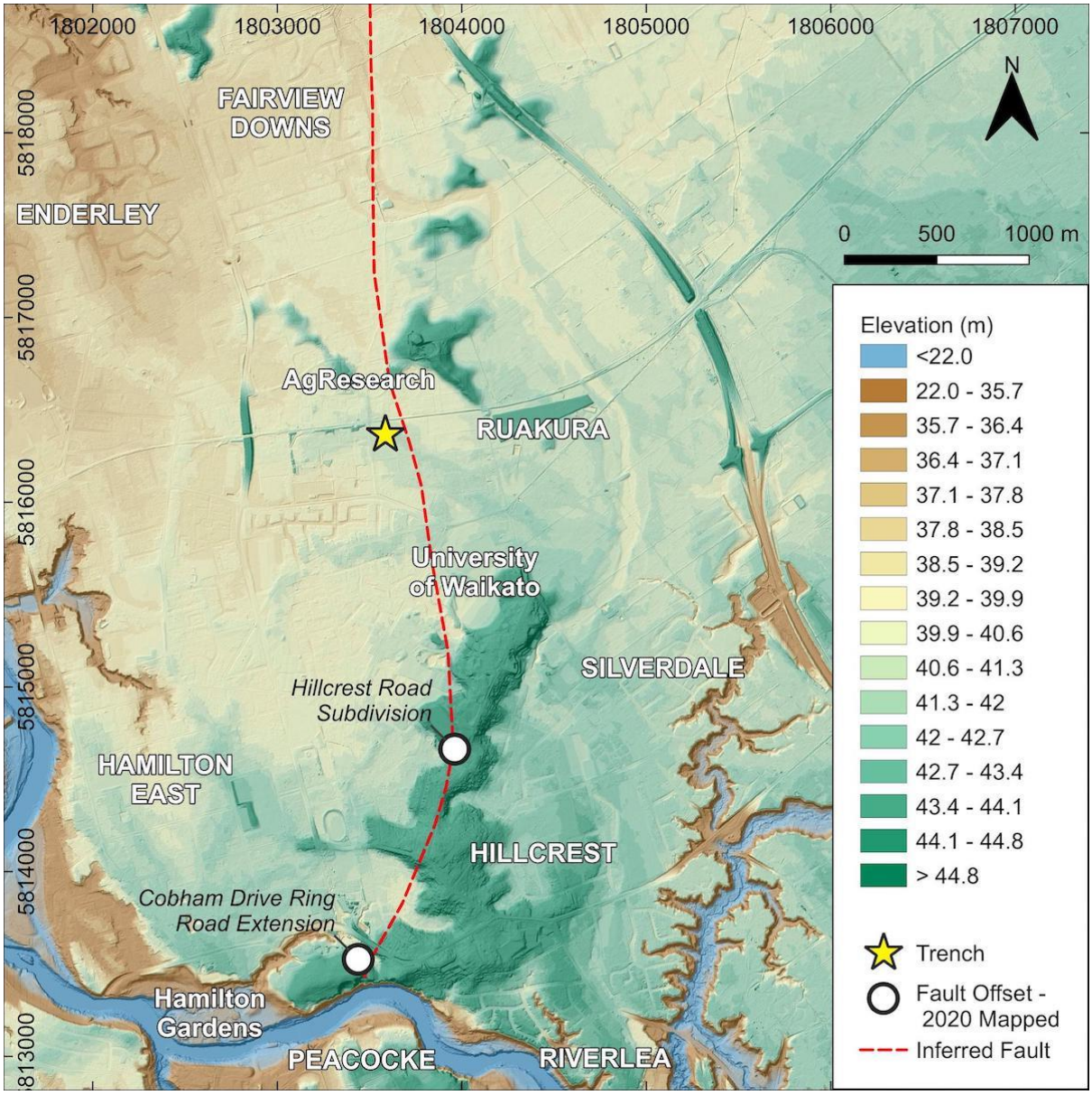

Figure 5.13. DEM of the eastern Hamilton area classified to 0.7 m breaks, overlaid with a hillshade relief, showing revised hypothesised relationship between inferred faulting at Ruakura and faults mapped in 2020 (*cf*. Figure 3.38). Revised strike of fault takes into consideration a conclusion that stratigraphic deformation within the trench is co-seismic near-fault, a geomorphic inference of dextral strike-slip offset to the east of the trench, and an inference that features seen in historic images prior to significant earthworks which removed or obscured them, were fault scarps.

5.9. Summary

While an inferred fault was not directly observable within the Ruakura trench, the cumulative evidence from inferred geomorphology, ERT anomalies, and strong similarity of deformation features to those seen in the Arnolds trench supports a summation that deformation within the Ruakura trench is co-seismic and near-fault. Given the lithological sequences known to exist in the area – primarily sand and gravel alluvial covers, with basement at depth – and previous interpretations of underlying faults in the area, this co-seismic deformation is considered likely to be of similar nature to granular deformation models described by Finch *et al.* (2004), accompanied by liquefaction. Tree uprooting, a sinkhole/tomo, and an impact crater have been considered as possible alternative explanations for the deformation but found to be unlikely. An initially postulated line of faulting, connecting inferred seismogenic geomorphology at Ruakura to confirmed offset at Cobham Drive (with splinters at Ruakura striking SSE towards the Hillcrest ridge), is revised to conclude that the fault strikes slightly further east than originally suggested and cuts through the Hillcrest ridge. This revision reconsiders the splinters as sections of the main fault and incorporates offset at Hillcrest Road recently described by Gibbons (2020), as well as potential evidence in historic imagery for fault scarps along the Hillcrest ridge, whilst maintaining the connection to faulting at Cobham Drive.

6. Conclusion

A multi-disciplinary approach was taken to identify cryptic faulting of the Hinuera Surface at Ruakura, within the northern extent of Te Tātua o Wairere Fault Zone. Desktop analysis began with digital modelling of wider Hamilton Basin geomorphology before scaling down to high resolution interrogation of the alluvial plain around Ruakura. Digital techniques were complemented by field surveys and reviews of aerial imagery. These steps narrowed the area of interest in which to undertake intensive ERT survey, which subsequently identified a particularly anomalous area on the south side of the AgResearch farm that was excavated for a paleoseismic trench. The results of these combined analyses lead to six key conclusions:

1) The predominant concept of the Hinuera Surface forming an alluvial fan is inappropriate. Slope angle across the surface is consistently <0.1° (generally around 0.08°) and the surface does not cover members of the Hamilton Hills towards a fan apex in the basin's east – hills are effectively absent east of Te Tātua o Wairere Fault Zone. The fault zone demarcates the flat plains of the eastern basin from a hillier landscape in the west and the fault zone occurs along the eastern boundary of a *c.* 6 km wide area where surface slope becomes near-horizontal, at only 0.02°.

2) There is no apparent relationship between intra-basin gravity anomalies and earthquake epicentres, or gravity anomalies and fault zone geomorphology. However, low magnitude earthquakes (*c.* 2.5 M_L) have been clustered in a small area just north of Ruakura, around Puketaha. The Puketaha earthquakes occurred in the vicinity of an unconformity upon shallow basement and a major fault inferred at *c.* 350 m depth in a petroleum exploration report from the 1970s. Previous studies using numerical modelling

have shown that shallow, unconsolidated, granular sedimentary sequences – such as the Hinuera Formation – can demonstrate off-fault surface deformation at distance from deeper earthquake-generating faults.

3) Geomorphic signatures suggest that the Hinuera Surface is seismically perturbed, however, fault zone topography has been highly modified by modern land use change and development, and extant geomorphology cannot be relied upon in isolation as diagnostic. Evidence to support seismic influence on the landscape includes abrupt directional changes and constriction of paleochannels, subtle elevation breaks, apparent offset in alluvial bars, and possible fault scarps visible in historic images.

4) Electrical resistivity tomography (ERT) provided non-intrusive insight into broad subsurface zonation and was partly able to be correlated with stratigraphy, to identify apparent deformation. The wide variation in earth material properties and states (i.e. weathered *vs.* unweathered, saturated *vs.* unsaturated) produces imprecision in resistivity survey detail but ERT successfully identified areas along an inferred fault with subsurface anomalies vastly different from an off-fault reference section.

5) Trenching provided unparalleled insight into stratigraphy and structure of the shallow Hinuera Formation at Ruakura but excavation and logging was affected by anthropic impacts. Nevertheless, a *c.* 4 m wide deformation zone in the northern trench wall was sufficiently deeper than and distal from these impacts, and shared such strong similarities with confirmed seismogenic features in the lithostratigraphically similar Arnolds trench, for the trench deformation to be considered co-seismic. The deformation occurred within upper Hinuera Formation materials, deposited more recently than *c.* 20 ka BP and most likely closer to *c.* 15 ka BP.

6) While seismic disturbance is the cause of upper Hinuera Formation deformation, clear evidence of a fault (pseudo-)plane was not observable within the trench. Fault propagation through overlying granular materials is unlikely to accurately reflect true orientation of basement fault planes, with at least

some aspect of (cryptic) horizontal/sub-horizontal stress distribution leading to discrete, small-scale, deformation features occurring near-/off-fault. It is suggested that a main line of fault strikes east of the trench, connecting with the offset at Hillcrest Road described by Gibbons (2020) and extending south-west to confirmed deformation at Cobham Drive. Fault continuation through the northern area of the farm and across Powells Road remains inferred but unconfirmed.

Commencing with the question '*has Te Tātua o Wairere Fault Zone been active within the last 20,000 years?'* this study concludes that features observed within the fault zone, at Ruakura, represent co-seismic disruption of the upper Hinuera Formation and modern Hinuera Surface. Further research is necessary to reach an authoritative age of last activity but as the last (uppermost) Hinuera Formation beds are known to have been deposited *c.* 15,000 years BP, fault activity must have been more recently than then. Understanding the nature of Te Tātua o Wairere Fault Zone is of value both for land use planning purposes as well as building our collective understanding of the Hamilton Basin's geological history. It is recommended that additional investigations be undertaken immediately east of the trenched site, to confirm an inferred line of faulting through the area, as well as in the northern area of the AgResearch farm, to resolve significant ERT anomalies across the left bank of the paleochannel in that location. Interpretations made in the 1970s of faults at *c.* 350 m depth in the Puketaha/Ruakura area should also be revisited in greater detail, to better understand their potential stratigraphic and structural relationships.

References

Advanced Geosciences, Inc. 2017, *Dipole-dipole array: electrical resistivity methods, part 3,* https://www.agiusa.com/dipole-dipole%E2%80%8B-%E2%80%8Barray%E2%80%8B (accessed 5 August 2020).

'Basement', 2003, *McGraw-Hill dictionary of geology & mineralogy*, McGraw-Hill, [n.p.].

Beca Ltd 2016, *Waikato Expressway Hamilton Section, sectors 4 & 5: geological and groundwater longitudinal section string MC10, sheets 25-31* [unpublished technical drawings].

Bowman, D. 2019, *Principles of Alluvial Fan Morphology,* e-book, Springer, Dordrecht, https://doi.org/10.1007/978-94-024-1558-2 (accessed 4 March 2021).

Bradshaw, J. D. 1993, 'A review of the Median Tectonic Zone: terrane boundaries and terrane amalgamation near the Median Tectonic Line', *New Zealand Journal of Geology and Geophysics*, vol. 36, no. 1, pp. 117-125, https://doi.org/10.1080/00288306.1993.9514559

Briggs, R. M., Middleton, M. P. & Nelson, C. S. 2004, 'Provenance history of a Late Triassic-Jurassic Gondwana margin forearc basin, Murihiku Terrane, North Island, New Zealand: petrographic and geochemical constraints', *New Zealand Journal of Geology and Geophysics*, vol. 47, no. 4, pp. 589-602, https://doi.org/10.1080/00288306.2004.9515078

Burbank, D. W. & Anderson, R. S. 2001, *Tectonic Geomorphology*, Blackwell Science, Malden.

Campbell, B. R. 2017, Hamilton's hidden hazard: the characterisation and mapping of zones of tectonic deformation within the Hamilton Basin, M. Sc. Thesis, The University of Waikato, https://hdl.handle.net/10289/11691

Caputo, R., Salviulo, L., Piscitelli, S. & Loperte, A. 2007, 'Late Quaternary activity along the Scorciabuoi Fault (Southern Italy) as inferred from electrical resistivity tomography', *Annals of Geophysics*, vol. 50, no. 2, pp. 213-224, http://hdl.handle.net/2122/3522

Cave, A. 2020, Dynamic site characterisation of the Hamilton Basin, M. Sc. Thesis, The University of Waikato.

Comas, X., Terry, N., Slater, L., Warren, M., Kolka, R., Kristiyono, A., Sudiana, N., Nurjaman, D. & Darusman, T. 2015, 'Imaging tropical peatlands in Indonesia using ground-penetrating radar (GPR) and electrical resistivity imaging (ERI): implications for carbon stock estimates and peat soil characterization', *Biogeosciences*, vol. 12, no. 10, pp. 2995-3007, https://doi.org/10.5194/bg-12-2995-2015

Coop, M. R., Sorensen, K. K., Bodas Freitas, T. & Georgoutsos, G. 2004, 'Particle breakage during shearing of a carbonate sand', *Géotechnique*, vol. 54, no. 3, pp. 157-163, https://doi.org/10.1680/geot.2004.54.3.157

Dence, M. R., Grieve, R. A. F. & Robertson, P. B. 1977, 'Terrestrial impact structures: principal characteristics and energy considerations', *Impact and Explosion Cratering: Planetary and Terrestrial Implications; Proceedings of the Symposium on Planetary Cratering Mechanics, Flagstaff, Arizona*, Pergamon Press, New York, pp. 247-275, https://ui.adsabs.harvard.edu/abs/1977iecp.symp..247D (accessed 2 February 2021).

Eccles, J., Cassidy, J., Locke, C. & Spörli, K. 2005, 'Aeromagnetic imaging of the Dun Mountain Ophiolite Belt in northern New Zealand: insight into the fine structure of a major SW Pacific terrane suture', *Journal of the Geological Society*, vol. 162, pp. 723-735, https://doi.org/10.1144/0016-764904-060

Edbrooke, S. 2005, *Geology of the Waikato area,* 1:250 000, geological map 4 (1 sheet + 68 p.), Institute of Geological and Nuclear Sciences Limited, Lower Hutt.

Edbrooke, S., Ricketts, B. & Leonard, G. 2009, *Opportunities for underground geological storage of CO2 in New Zealand - report CCS-08/2 - the onshore Waikato region: GNS Science report 2009/54*, Institute of Geological and Nuclear Sciences Limited.

Eyles, N. & Clark, B. M. 1986, 'Significance of hummocky and swaley cross-stratification in late Pleistocene lacustrine sediements of the Ontario basin, Canada', *Geology*, vol. 14, no. 8, pp. 679-682, https://doi.org/10.1130/0091-7613(1986)14%3C679:SOHASC%3E2.0.CO;2

Finch, E., Hardy, S. & Gawthorpe, R. 2004, 'Discrete-element modelling of extensional fault-propagation folding above rigid basement fault blocks', *Basin Research*, vol. 16, no. 4, pp. 467-488, https://doi.org/10.1111/j.1365-2117.2004.00241.x

Gibbons, V. 2020, The fault in our hill: characterisation of the Rangitawa Tephra, and insight into tectonic influences at Hillcrest Road, M. Sc. Thesis, The University of Waikato, https://hdl.handle.net/10289/14258

Gill, O. M. & Orense, R. P. 2019, 'Field characterisation and mapping of pumiceous deposits in central North Island, NZ', *Japanese Geotechnical Society Special Publication*, vol. 6, no. 2, pp. 79-87, https://doi.org/10.3208/jgssp.v06.GIZ12

GNS Science n.d., *GROPE,* https://www.geonet.org.nz/data/supplementary/earthquake_location_grope (accessed 24 April 2020).

Gold, R. D., Stephenson, W. J., Odum, J. K., Briggs, R. W., Crone, A. J. & Angster, S. J. 2013, 'Concealed Quaternary strike-slip fault resolved with airborne lidar and seismic reflection: the Grizzly Valley fault system, northern Walker Lane, California', *Journal of Geophysical Research: Solid Earth*, vol. 118, no. 7, pp. 3753-3766, https://doi.org/10.1002/jgrb.50238

Hamilton City Council & LINZ 2020, *Hamilton, Waikato, New Zealand 2019* [data set], distributed by OpenTopography, https://doi.org/10.5069/G9891410

Hardy, S. 2011, 'Cover deformation above steep, basement normal faults: insights from 2D discrete element modelling', *Marine and Petroleum Geology*, vol. 28, no. 5, pp. 966-972, https://doi.org/10.1016/j.marpetgeo.2010.11.005

Hartvich, F. & Valenta, J. 2013, 'Tracing an intra-montane fault: an interdisciplinary approach', *Surveys in Geophysics*, vol. 34, no. 3, pp. 317-347, https://doi.org/10.1007/s10712-012-9216-9

Hatherton, T. & Sibson, R. H. 1970, 'Junction magnetic anomaly north of Waikato River', *New Zealand Journal of Geology and Geophysics*, vol. 13, no. 3, pp. 655-662, https://doi.org/10.1080/00288306.1970.10431336

Hogg, A. G., Lowe, D. J., Palmer, J. G., Boswijk, G. & Bronk Ramsey, C. J. 2012, 'Revised calendar date for the Taupo eruption derived by 14C wiggle-matching using a New Zealand kauri 14C calibration data set', *The Holocene*, vol. 22, no. 4, pp. 439-449, https://doi.org/10.1177%2F0959683611425551

Hume, T. M., Sherwood, A. M. & Nelson, C. S. 1975, 'Alluvial sedimentology of the Upper Pleistocene Hinuera Formation, Hamilton Basin, New Zealand',

Journal of the Royal Society of New Zealand, vol. 5, no. 4, pp. 421-462, https://doi.org/10.1080/03036758.1975.10419362

Jackson, C. A. L., Gawthorpe, R. L. & Sharp, I. R. 2006, 'Style and sequence of deformation during extensional fault-propagation folding: examples from the Hammam Faraun and El-Qaa fault blocks, Suez Rift, Egypt', *Journal of Structural Geology*, vol. 28, no. 3, pp. 519-535, https://doi.org/10.1016/j.jsg.2005.11.009

Jeong, S. & Wotherspoon, L. M. 2019, 'Paper 301: Development of a Waikato Basin T0 and depth model by the H/V spectral ratio method', *2019 Pacific Conference on Earthquake Engineering: Turning Hazard Awareness into Risk Mitigation*, New Zealand Society for Earthquake Engineering, Auckland, https://www.researchgate.net/publication/333340260_Development_of_a_Waikato_Basin_T0_and_depth_model_by_the_HV_spectral_ratio_method (accessed 29 June 2020).

Johnston, M. R. 2019, 'The path to understanding the central terranes of Zealandia', in A. H. F. Robertson (ed.), *Paleozoic-Mesozoic geology of South Island, New Zealand: subduction-related processes adjacent to SE Gondwana*, Geological Society memoir no. 49, The Geological Society of London, London, pp. 16-30, https://doi.org/10.1144/M49.2

Jones, G. H. S. 1977, 'Complex craters in alluvium', *Impact and Explosion Cratering: Planetary and Terrestrial Implications; Proceedings of the Symposium on Planetary Cratering Mechanics, Flagstaff, Arizona*, Pergamon Press, New York, pp. 163-183, https://ui.adsabs.harvard.edu/abs/1977iecp.symp..163J (accessed 2 February 2021).

Kamp, P., Tripathi, A. R. P. & Nelson, C. S. 2014, 'Paleogeography of Late Eocene to earliest Miocene Te Kuiti Group, central-western North Island, New Zealand', *New Zealand Journal of Geology and Geophysics*, vol. 57, no. 2, pp. 128-148, https://doi.org/10.1080/00288306.2014.904384

Kamp, P. J. J. & Lowe, D. J. 1981, 'Quaternary stratigraphy, landscape and soils of the Hamilton Basin', in R. M. Briggs (ed.), *Hamilton conference field trip guides*, Geological Society of New Zealand miscellaneous publication 28B, The University of Waikato, Hamilton, pp. 14-28, https://hdl.handle.net/10289/10207

Kear, D. 1993, 'Reflections on major North Island basement rock assemblages and on megafaults', *Journal of the Royal Society of New Zealand*, vol. 23, no. 1, pp. 29-41, https://doi.org/10.1080/03036758.1993.10721215

Kear, D. & Schofield, J. C. 1978, *Geology of the Ngaruawahia subdivision*, New Zealand Geological Survey bulletin 88, Department of Scientific and Industrial Research, Wellington.

Kellaway, L., Beaumont, L. & Adam, J. P. 2015, *Submission on variation 1 Ruakura: December 2015,* https://www.hamilton.govt.nz/our-council/council-publications/districtplans/ODP/Documents/Ruakura%20Submissions/Kellaway,%20Laura;%20Beaumont,%20Louise;%20and%20Adam,%20John%20P%20-%2049.PDF (accessed 29 August 2020).

Kleyburg, M. A. 2015, Paleoliquefaction in Late Pleistocene alluvial sediments in the Hauraki and Hamilton Basins, M. Sc. Thesis, The University of Waikato, https://hdl.handle.net/10289/9512

Kowalczyk, S., Zukowska, K. A., Mendecki, M. J. & Lukasiak, D. 2017, 'Application of electrical resistivity imaging (ERI) for the assessment of peat properties: a case study of the Całowanie Fen, Central Poland', *Acta Geophysica*, vol. 65, pp. 223-235, https://doi.org/10.1007/s11600-017-0018-9

Kuebler, S., Streich, R., Lück, E., Hoffmann, M., Freidrich, A. M. & Strecker, M. R. 2016, 'Active faulting in a populated low-strain setting (Lower Rhine Graben, Central Europe) identified by geomorphic, geophysical and geological analysis', in A. Landgraf, S. Kuebler, E. Hintersberger & S. Stein (eds.), *Seismicity, fault rupture and earthquake hazards in slowly deforming regions*, Geological Society special publication 432, The Geological Society of London, London, pp. 127-146, https://doi.org/10.1144/SP432.11

Landis, C. A., Campbell, H. J., Aslund, T., Cawood, P. A., Douglas, A., Kimbrough, D. L., Pillai, D. D. L., Raine, J. I. & Willsman, A. 1999, 'Permian-Jurassic strata at Productus Creek, Southland, New Zealand: implications for terrane dynamics of the eastern Gondwanaland margin', *New Zealand Journal of Geology and Geophysics*, vol. 42, no. 2, pp. 255-278, https://doi.org/10.1080/00288306.1999.9514844

Landis, C. A. & Coombs, D. S. 1967, 'Metamorphic belts and orogenesis in southern New Zealand', *Tectonophysics*, vol. 4, no. 4, pp. 501-518, https://doi.org/10.1016/0040-1951(67)90014-5

Langridge, R. M., Ries, W. F., Litchfield, N. J., Villamor, P., Van Dissen, R. J., Barrell, D. J. A., Rattenbury, M. S., Heron, D. W., Haubrock, S., Townsend, D. B., Lee, J. M., Berryman, K. R., Nicol, A., Cox, S. C. & Stirling, M. W. 2016, 'The New Zealand active faults database', *New Zealand Journal of Geology and Geophysics*, vol. 59, no. 1, pp. 86-96, https://doi.org/10.1080/00288306.2015.1112818

Liles, V. E. 1971, *Seismic survey, Waikato Basin 1970-71: unpublished petroleum report PR569*, Ministry of Economic Development New Zealand.

Lowe, D. J., Tippett, J. M., Kamp, P. J. J., Liddell, I. J., Briggs, R. M. & Horrocks, J. L. 2001, 'Ages on weathered Plio-Pleistocene tephra sequences, western North Island, New Zealand', in E. T. Juvigné & J.-P. Raynal (eds.), *Tephras: chronology, archaeology*, Les dossiers de l'Archéo-Logis n° 1, CDERAD éditeur, Goudet, pp. 45-60, https://doi.org/10.13140/2.1.3666.2563

McCraw, J. 2011, *The wandering river: landforms and geological history of the Hamilton Basin*, Geoscience Society of New Zealand, Lower Hutt.

McCraw, J. D. 1967, 'The surface features and soil pattern of the Hamilton Basin', *Earth Science Journal*, vol. 1, no. 1, pp. 59-74, https://hdl.handle.net/10289/9099

McCubbine, J. C., Stagpoole, V., Caratori Tontini, F., Amos, M., Smith, E. & Winefield, R. 2017, 'Gravity anomaly grids for the New Zealand region', *New Zealand Journal of Geology and Geophysics*, vol. 60, no. 4, pp. 381-391, https://doi.org/10.1080/00288306.2017.1346692

McPherson, J. G., Shanmugam, G. & Moiola, R. J. 1987, 'Fan-deltas and braid deltas: varieties of coarse-grained deltas', *Geological Society of America Bulletin*, vol. 99, no. 3, pp. 331-340, https://doi.org/10.1130/0016-7606(1987)99%3C331:FABDVO%3E2.0.CO;2

Meyers, J. 2010, *Mineral prospecting area reduction report: unpublished mineral report MR4571*, Ministry of Economic Development New Zealand.

Moon, V. & de Lange, W. 2017, *Final report on EQC potential shallow seismic sources in the Hamilton Basin: project 16/717*, The University of Waikato, https://www.eqc.govt.nz/research/research-papers/potential-shallow-seismic-sources-in-the-hamilton-basin (accessed 16 March 2020).

Noda, A., Takeuchi, M. & Adachi, M. 2004, 'Provenance of the Murihiku Terrane, New Zealand: evidence from the Jurassic conglomerates and sandstones in Southland', *Sedimentary Geology*, vol. 164, no. 3-4, pp. 203-222, https://doi.org/10.1016/j.sedgeo.2003.10.003

O'Brien, J. P. & Rodgers, K. A. 1973, 'Alpine-type serpentinites from the Auckland province-I. the Wairere Serpentinite', *Journal of the Royal Society of New Zealand*, vol. 3, no. 2, pp. 169-190, https://doi.org/10.1080/03036758.1973.10430599

Opus International Consultants Ltd 2013, *Geotechnical report G3127 Ruakura development stage 1: geotechnical investigation. Tainui Group Holdings Limited; geotechnical interpretive report*, Opus International Consultants Ltd, https://www.epa.govt.nz/assets/FileAPI/proposal/NSP000034/Evidence-Applicants-evidence/41fe0deac8/Applicant-EIC-Geotechnical-REF3-Opus-Geotechnical-Report-G3127-Part01.pdf (accessed 16 September 2020).

Palacky, G. J. 1988, 'Resistivity characteristics of geologic targets', in M. N. Nabighian & J. D. Corbett (eds.), *Electromagnetic methods in applied geophysics: theory*, Investigations in geophysics, vol. 1, Society of Exploration Geologists, pp. 53-125.

Petch, R. A. & Marshall, T. W. 1988, 'Ground water resources of the Tauranga Group sediments in the Hamilton Basin, North Island, New Zealand', *Journal of Hydrology (New Zealand)*, vol. 27, no. 2, pp. 81-98, https://www.jstor.org/stable/43944613

Petty Geophysical Engineering Company 1963, *Reflection seismograph survey, Hamilton Basin: unpublished petroleum report PR536*, Ministry of Economic Development New Zealand.

Roth, W. H., Scott, R. F. & Austin, I. 1981, 'Centrifuge modeling of fault propagation through alluvial soils', *Geophysical Research Letters*, vol. 8, no. 6, pp. 561-564, https://doi.org/10.1029/GL008i006p00561

Saito, K. & Oguchi, T. 2005, 'Slope of alluvial fans in humid regions of Japan, Taiwan and the Philippines', *Geomorphology*, vol. 70, no. 1-2, pp. 147-162, https://doi.org/10.1016/j.geomorph.2005.04.006

Samouëlian, A., Cousin, I., Tabbagh, A., Bruand, A. & Richard, G. 2005, 'Electrical resistivity survey in soil science: a review', *Soil and Tillage Research*, vol. 83, no. 2, pp. 173-193, https://doi.org/10.1016/j.still.2004.10.004

Schaetzl, R. J., Johnson, D. L., Burns, S. F. & Small, T. W. 1988, 'Tree uprooting: review of terminology, process, and environmental implications', *Canadian Journal of Forest Research*, vol. 19, no. 1, pp. 1-11, https://doi.org/10.1139/x89-001

Schofield, J. C. 1965, 'The Hinuera Formation and associated Quaternary events', *New Zealand Journal of Geology and Geophysics*, vol. 8, no. 5, pp. 772-791, https://doi.org/10.1080/00288306.1965.10422116

Selby, M. J. 1967, 'Aspects of the geomorphology of the greywacke ranges bordering the Lower and Middle Waikato Basins', *Earth Science Journal*, vol. 1, no. 1, pp. 37-58, https://hdl.handle.net/10289/9100

Selby, M. J. & Lowe, D. J. 1992, 'The middle Waikato Basin and hills', in J. M. Soons & M. J. Selby (eds.), *Landforms of New Zealand*, 2nd edn, Longman Paul, Auckland, pp. 233-255, https://hdl.handle.net/10289/9272

Seminsky, K. Z., Zaripov, R. M. & Olenchenko, V. V. 2016, 'Interpretation of shallow electrical resistivity images of faults: tectonophysical approach', *Russian Geology and Geophysics*, vol. 57, no. 9, pp. 1349-1358, https://doi.org/10.1016/j.rgg.2016.08.020

Spinardi, F. 2017, A preliminary evaluation of tectonic geomorphological signals within the Hamilton Basin, M. Sc. Thesis, The University of Waikato, https://hdl.handle.net/10289/11824

Spörli, K. 1978, 'Mesozoic tectonics, North Island, New Zealand', *Geological Society of America Bulletin*, vol. 89, no. 3, pp. 415-425, https://doi.org/10.1130/0016-7606(1978)89%3C415:MTNINZ%3E2.0.CO;2

'SSA 2020 Annual Meeting', 2020, *Seismological Research Letters*, vol. 91, no. 2B, pp. 1095-1338, https://doi.org/10.1785/0220200043

Stipp, J. J. & Thompson, B. N. 1971, 'K/Ar ages from the volcanics of Northland, New Zealand', *New Zealand Journal of Geology and Geophysics*, vol. 14, no. 2, pp. 403-413, https://doi.org/10.1080/00288306.1971.10421933

Storz, H., Storz, W. & Jacobs, F. 2000, 'Electrical resistivity tomography to investigate geological structures of the earth's upper crust', *Geophysical Prospecting*, vol. 48, no. 3, pp. 455-471, https://doi.org/10.1046/j.1365-2478.2000.00196.x

Sutherland, R. 1999, 'Basement geology and tectonic development of the greater New Zealand region: an interpretation from regional magnetic data', *Tectonophysics*, vol. 308, no. 3, pp. 341-362, https://doi.org/10.1016/S0040-1951(99)00108-0

Tonkin, P. J. 1970, 'Contorted stratification with clay lobes in volcanic ash beds, Raglan-Hamilton Region, New Zealand', *Earth Science Journal*, vol. 4, no. 2, pp. 129-140, https://hdl.handle.net/10289/9169

Verstraeten, G., Mohamed, I., Notebaert, B. & Willems, H. 2017, 'The dynamic nature of the transition from the Nile floodplain to the desert in Central Egypt since the mid-Holocene: proceedings of the international symposium held at the Johannes Gutenberg-Universität Mainz, 22 & 23 February 2013', in H. Willems & J.-M. Dahms (eds.), *The Nile: natural and cultural landscape in Egypt*, Mainzer Historische Kulturwissenschaften, vol. 36, Transcript Verlag, Bielefeld, pp. 239-254, https://doi.org/10.14361/9783839436158-009

Ward, W. T. 1967, 'Volcanic ash beds of the lower Waikato basin, North Island, New Zealand', *New Zealand Journal of Geology and Geophysics*, vol. 10, no. 4, pp. 1109-1135, https://doi.org/10.1080/00288306.1967.10423211

'Where is the safest place to live in NZ?' 2011, *The Dominion Post*, March 14, http://www.stuff.co.nz/dominion-post/4761061/Where-is-the-safest-place-to-live-in-NZ (accessed 16 March 2020).

White, P. A. 1985, *Handbook on hydrogeological applications of earth resistivity measurements*, Water and soil miscellaneous publication no. 90, Water and Soil Directorate, Ministry of Works and Development, Wellington.

Yasuda, S. & Tohno, I. 1988, 'Sites of reliquefaction caused by the 1983 Nihonkai-Chubu earthquake', *Soils and Foundations*, vol. 28, no. 2, pp. 61-72, https://doi.org/10.3208/sandf1972.28.2_61

Youssef, A. M., Al-Harbi, H. M., Gutiérrez, F., Zabramwi, Y. A., Bulkhi, A. B., Zahrani, S. A., Bahamil, A. M., Zahrani, A. J., Otaibi, Z. A. & El-Haddad, B. A. 2016, 'Natural and human-induced sinkhole hazards in Saudi Arabia: distribution, investigation, causes and impacts', *Hydrogeology Journal*, vol. 24, no. 3, pp. 625-644, https://doi.org/10.1007/s10040-015-1336-0

Appendix A. New Zealand Geological Timescale

Part 1/2

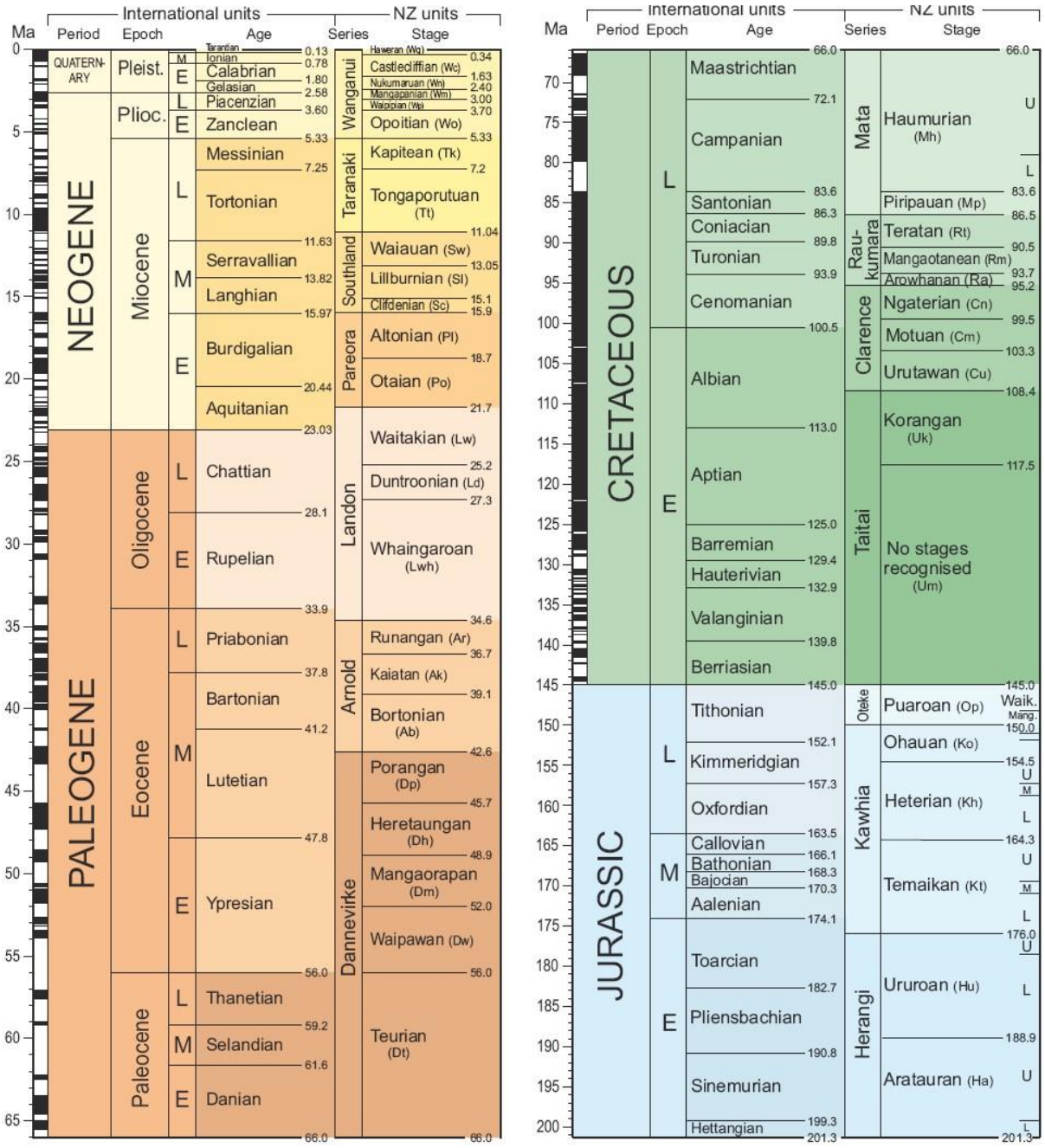

Part 2/2

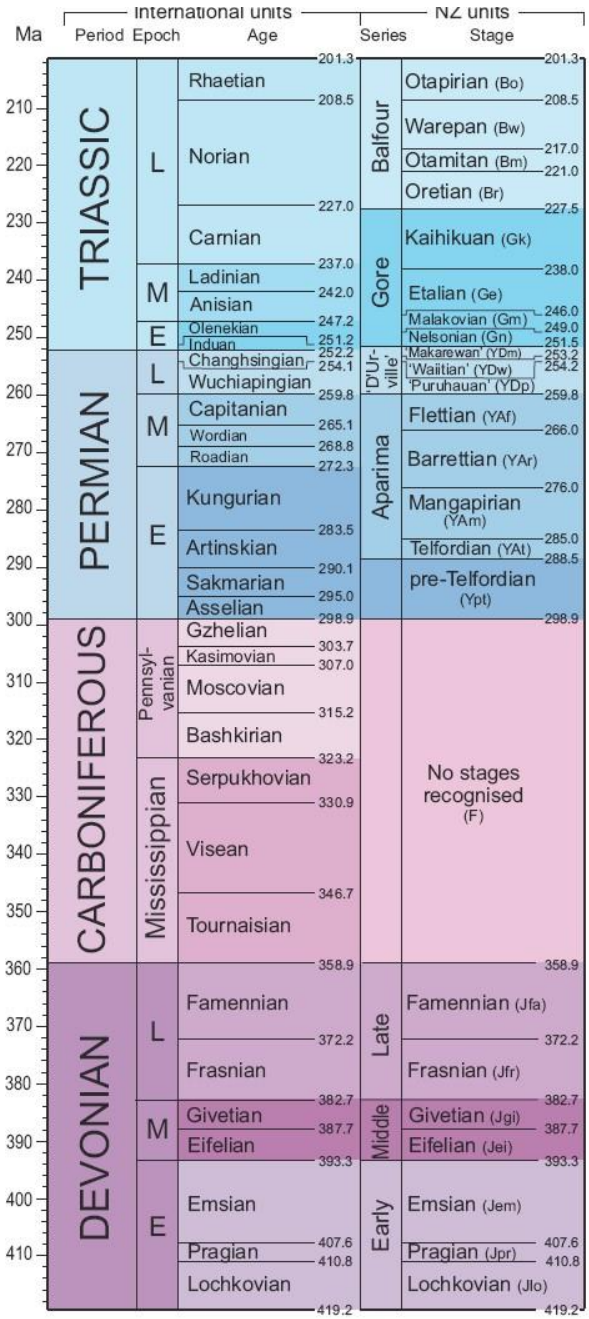

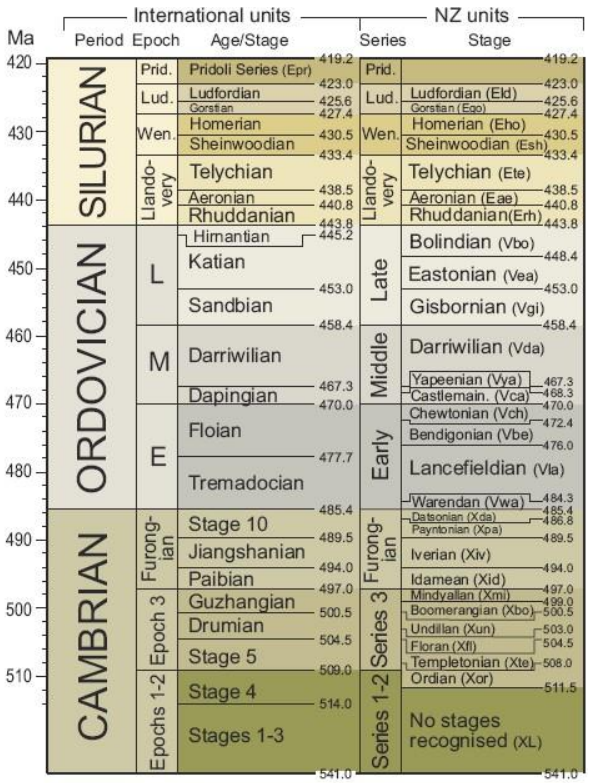

New Zealand Geological Timescale

v. 2015/1

An update of the NZ Geological Timescale (Cooper 2004, GNS Monograph 22), incorporating revised ages from the 2014 International Chronostratigraphic Chart 2014/10 (Cohen *et al.* 2014) and recalibration of NZ stage boundaries (Raine *et al.* 2015, GNS Science Report 2012/39).

Appendix B. Trenched Paddock Utilities

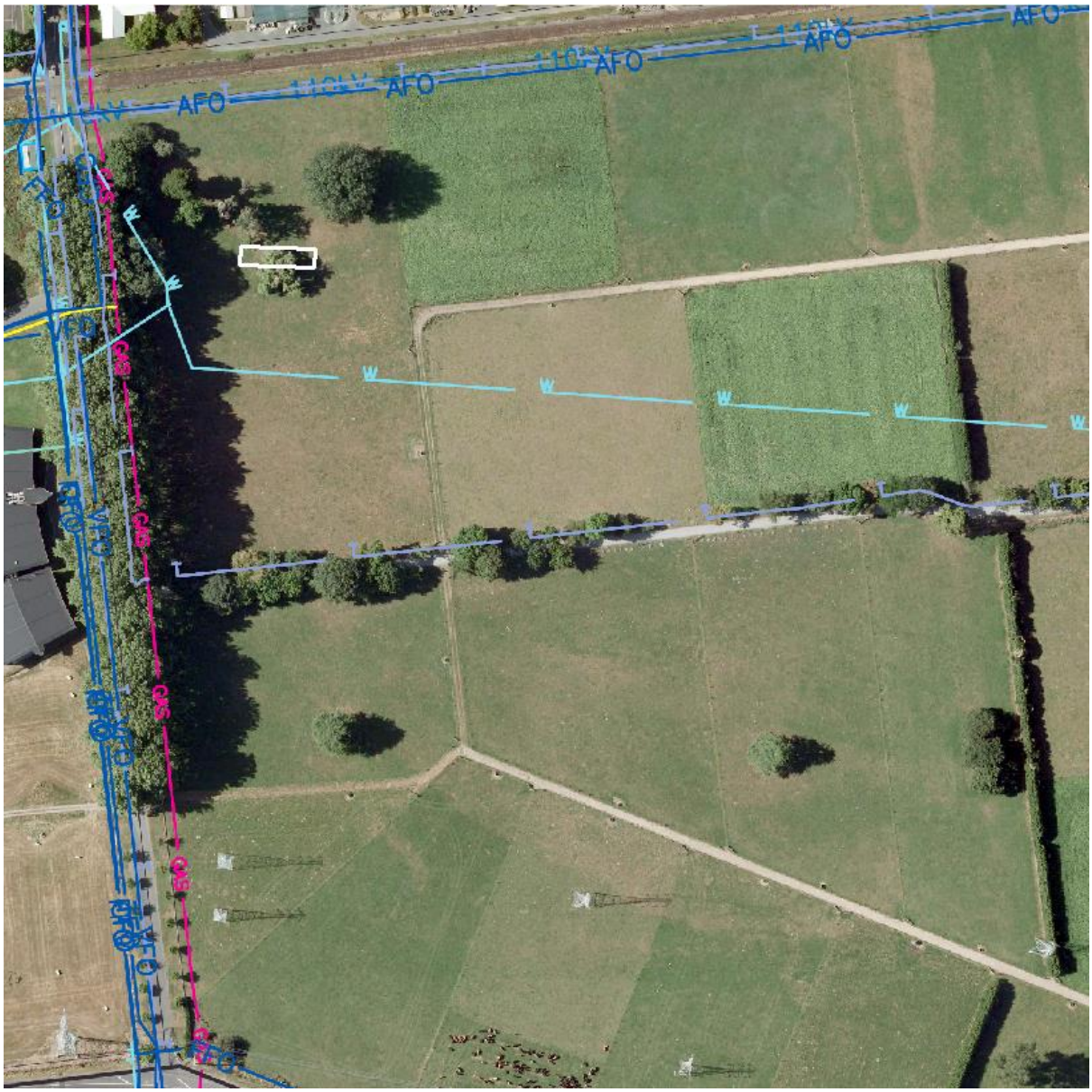

Figure B.1. Cropped selection from the AgResearch services plan[1], issued 31 August 2009, showing positions of buried telephone (T), fibre optic (AFO / VFO), water (W) and Gas connections, and overhead power lines (110 kV – partially obscured by lines showing T and AFO) with trench position outlined in white. Original drawing © 2009 AgResearch.

[1] AgResearch Ltd 2009, *All services: Ruakura Research Centre campus* [unpublished technical drawing].

Figure B.2. Cropped selection from the BCD Group plan[2], issued 17 July 2019, showing position of recently installed buried wastewater line (WW). The thin black line relates to an associated long-section and does not indicate another buried service. Original drawing © 2019 BCD Group.

[2] BCD Group 2019, *Melody Dairies Ltd pumped wastewater main Hamilton: plan & longsection – sheet 1 of 4* [unpublished technical drawing].

Appendix C. ERT Raw Pseudo-sections and Cross-plots

RUA02

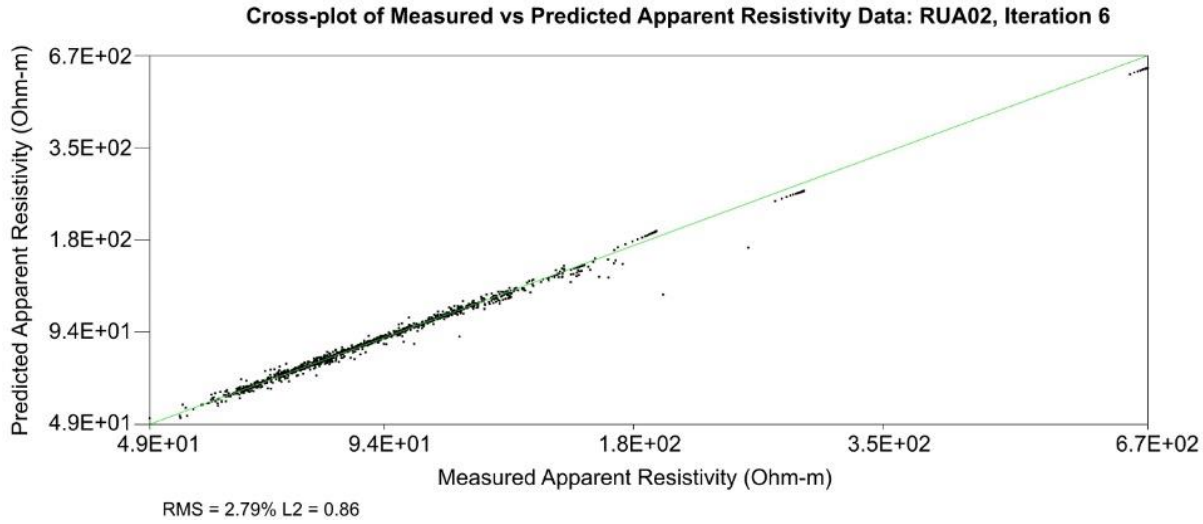

Figure C.1. Cross-plot for RUA02.

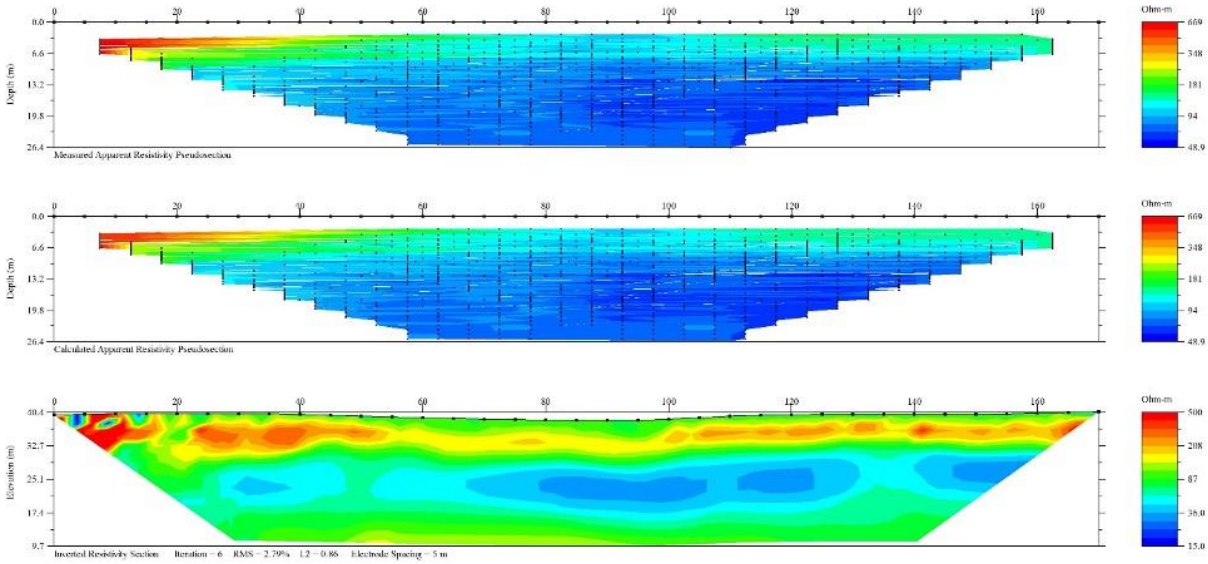

Figure C.2. Pseudo-sections of measured apparent resistivity (top), calculated apparent resistivity (middle), and original inverted resistivity section (bottom) for RUA02.

RUA03

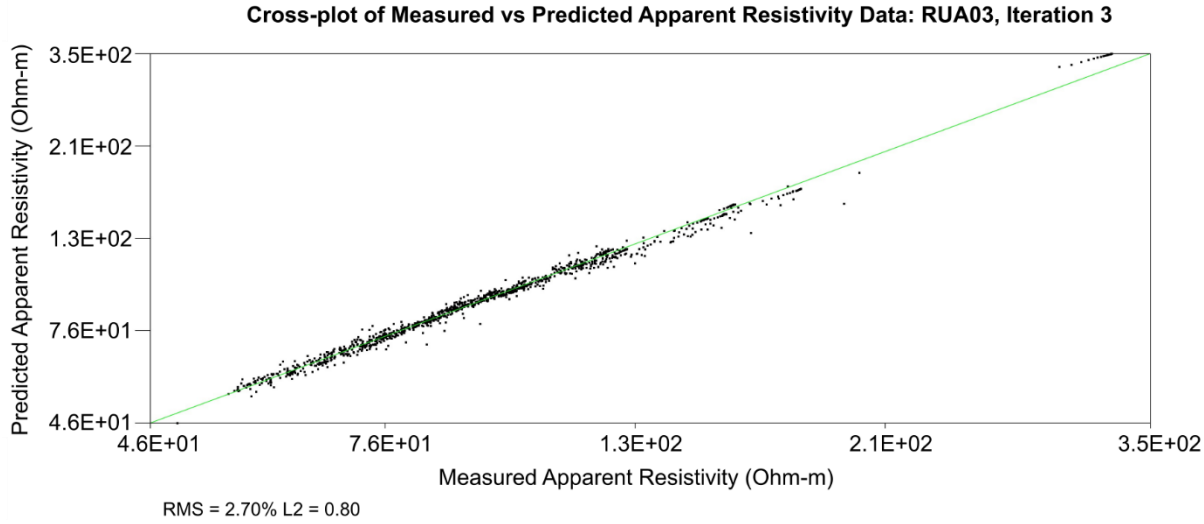

Figure C.3. Cross-plot for RUA03.

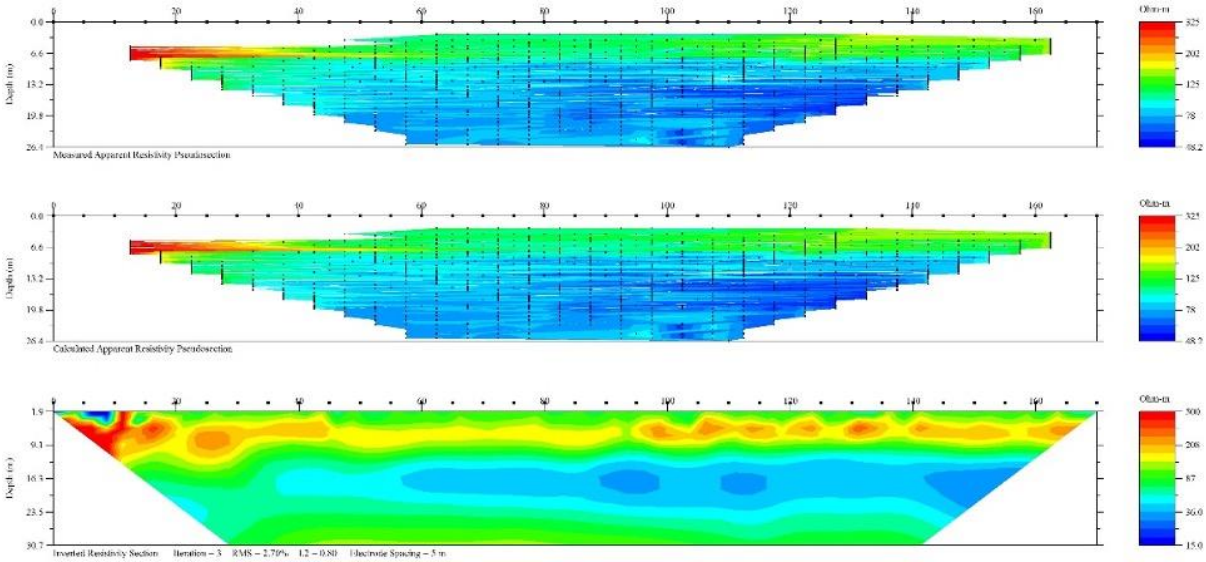

Figure C.4. Pseudo-sections of measured apparent resistivity (top), calculated apparent resistivity (middle), and original inverted resistivity section (bottom) for RUA03.

RUA04

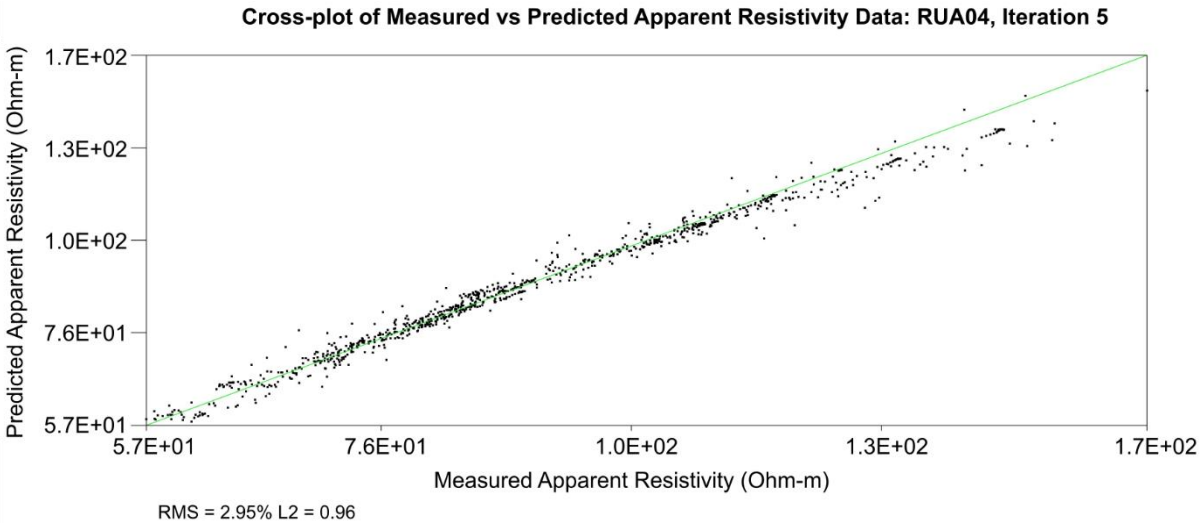

Figure C.5. Cross-plot for RUA04.

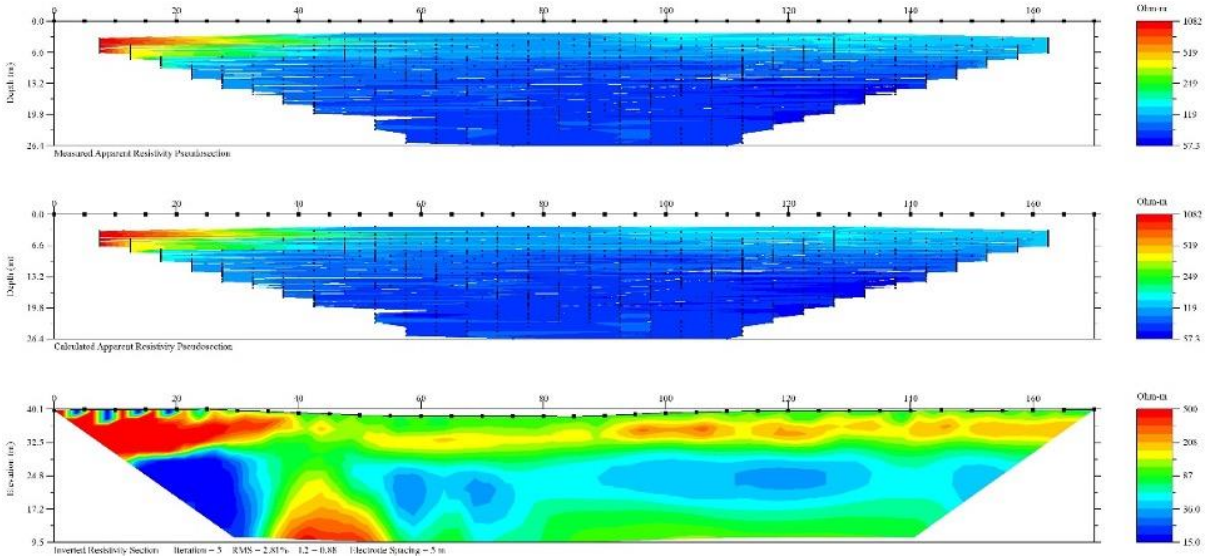

Figure C.6. Pseudo-sections of measured apparent resistivity (top), calculated apparent resistivity (middle), and original inverted resistivity section (bottom) for RUA04.

RUA05

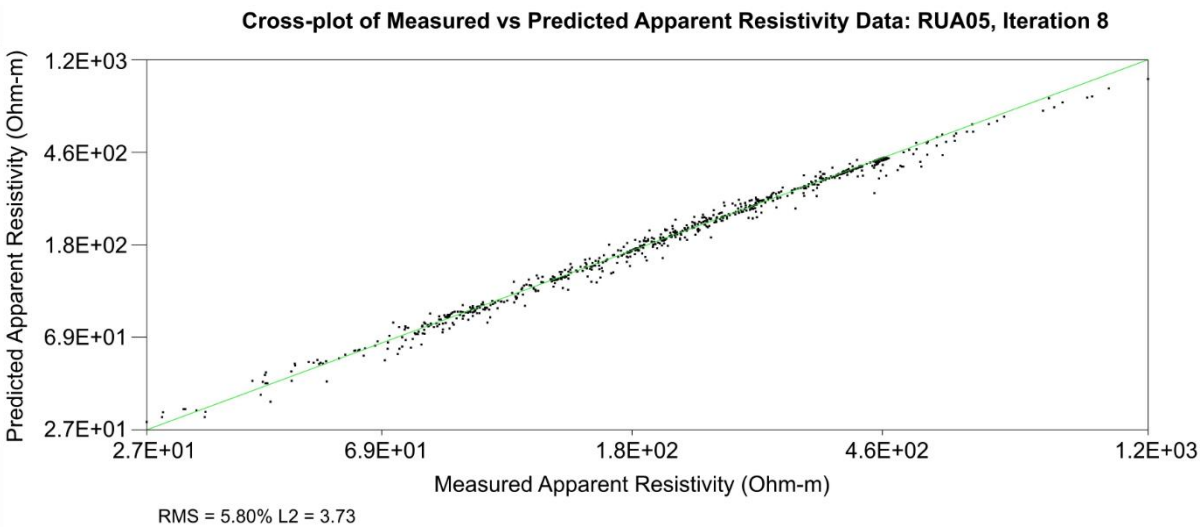

Figure C.7. Cross-plot for RUA05.

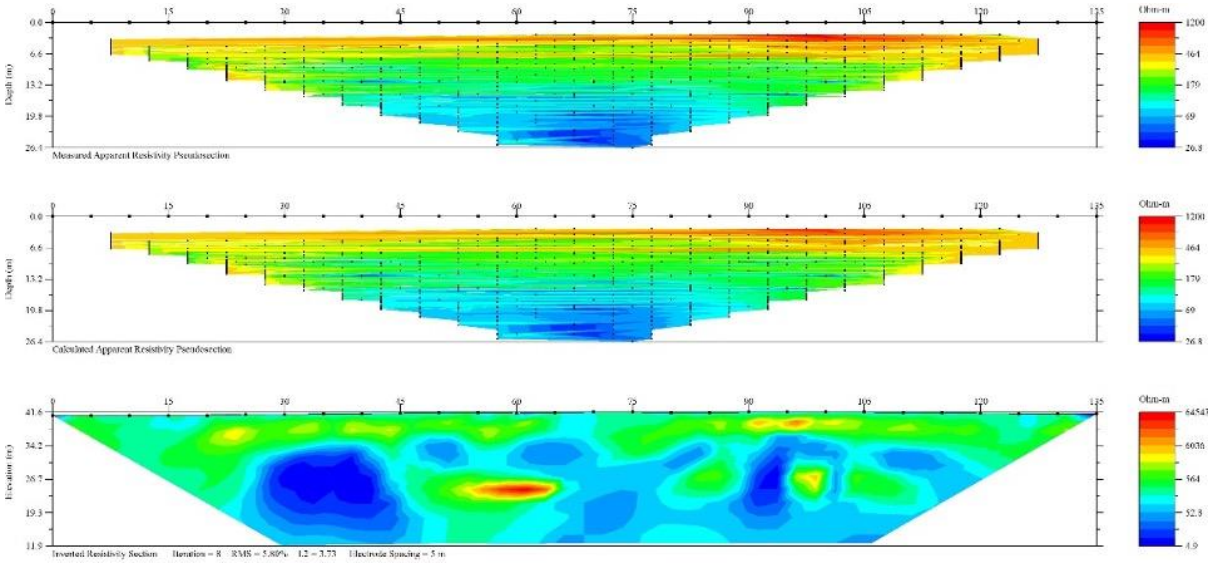

Figure C.8. Pseudo-sections of measured apparent resistivity (top), calculated apparent resistivity (middle), and original inverted resistivity section (bottom) for RUA05.

RUA06

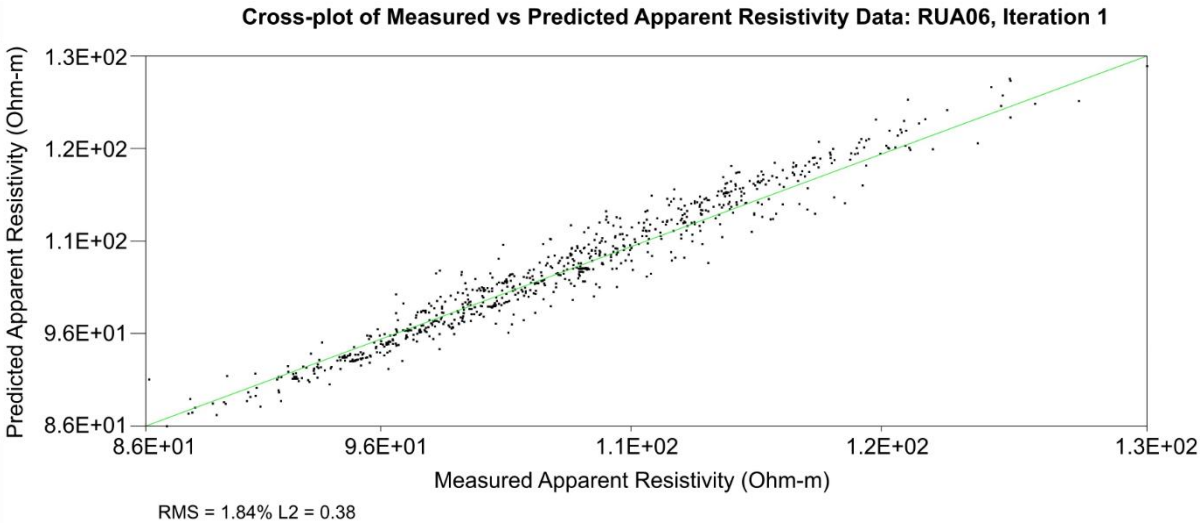

Figure C.9. Cross-plot for RUA06.

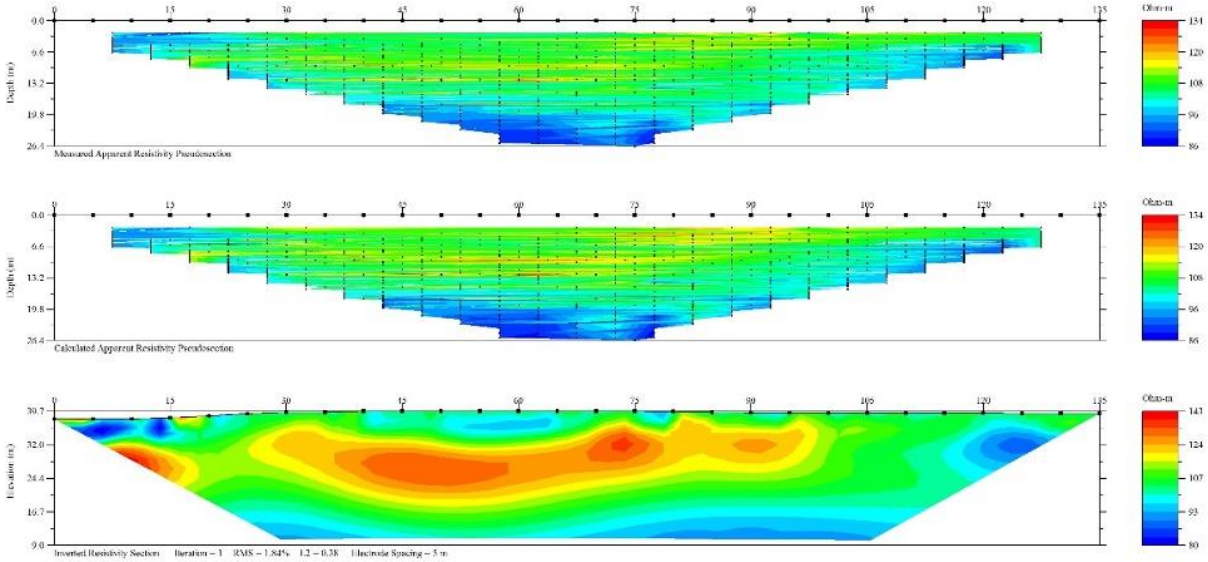

Figure C.10. Pseudo-sections of measured apparent resistivity (top), calculated apparent resistivity (middle), and original inverted resistivity section (bottom) for RUA06.

RUA07

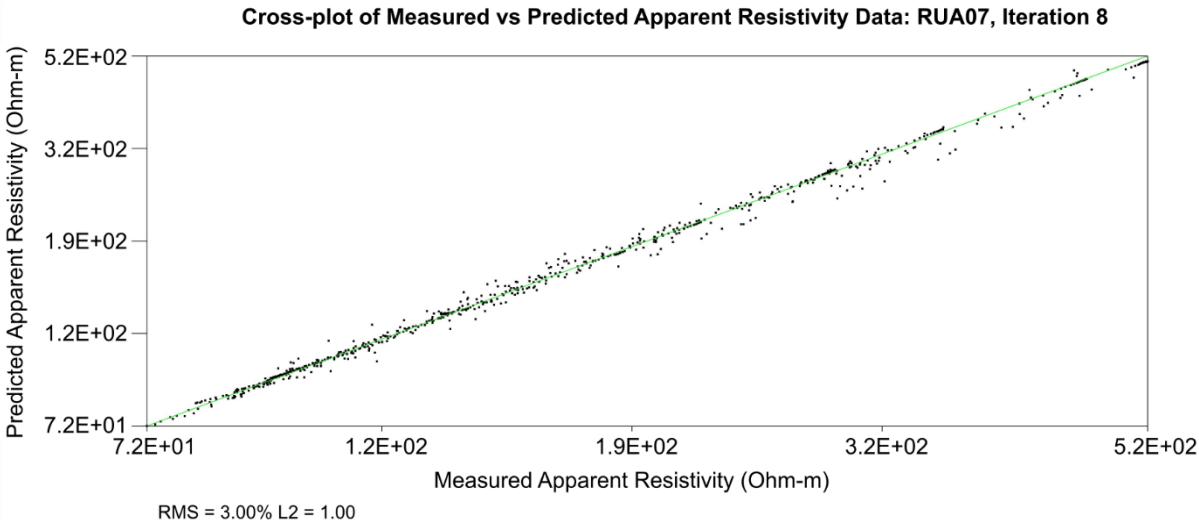

Figure C.11. Cross-plot for RUA07.

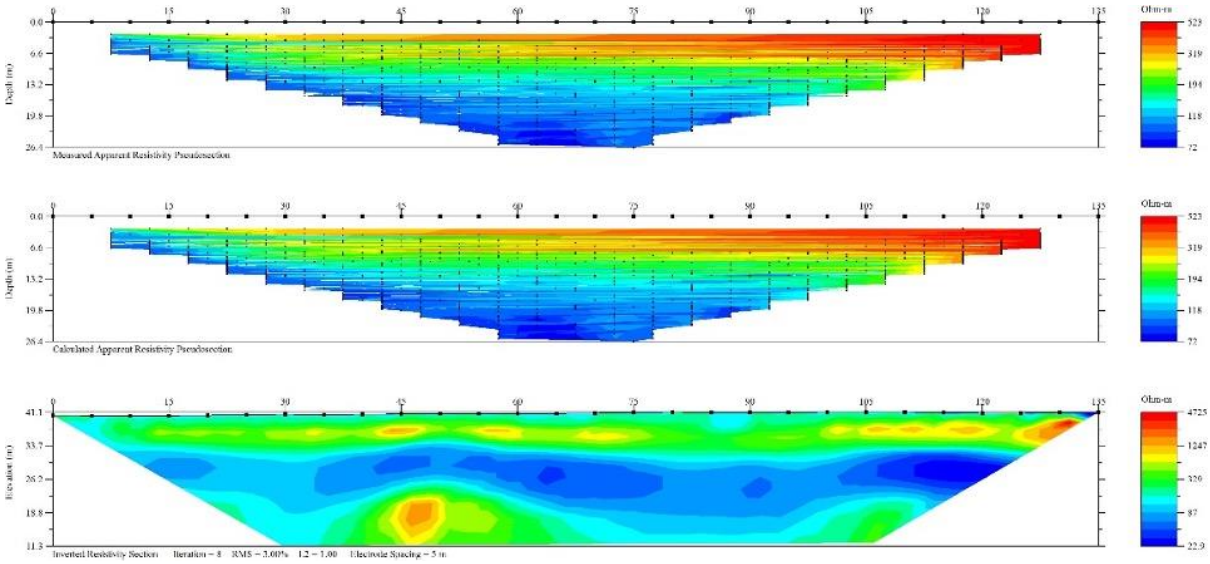

Figure C.12. Pseudo-sections of measured apparent resistivity (top), calculated apparent resistivity (middle), and original inverted resistivity section (bottom) for RUA07.

RUA08

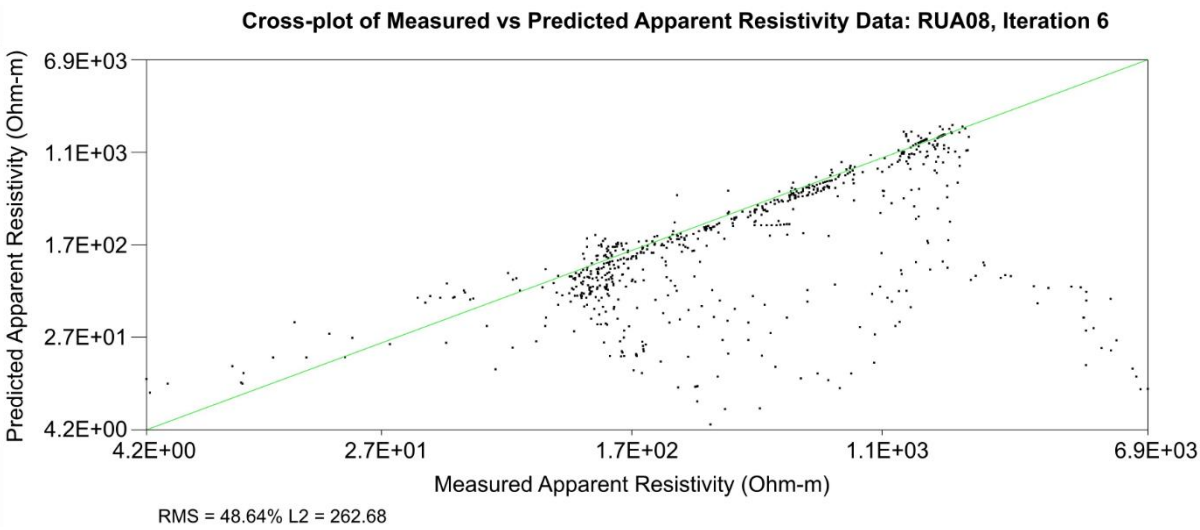

Figure C.13. Cross-plot for RUA08.

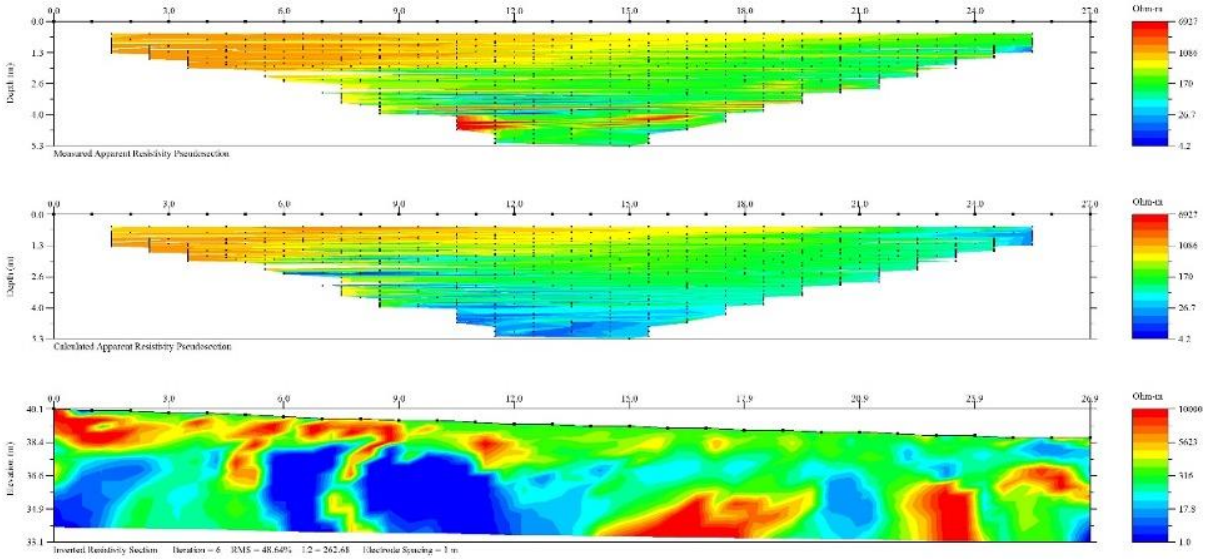

Figure C.14. Pseudo-sections of measured apparent resistivity (top), calculated apparent resistivity (middle), and original inverted resistivity section (bottom) for RUA08.

RUA09

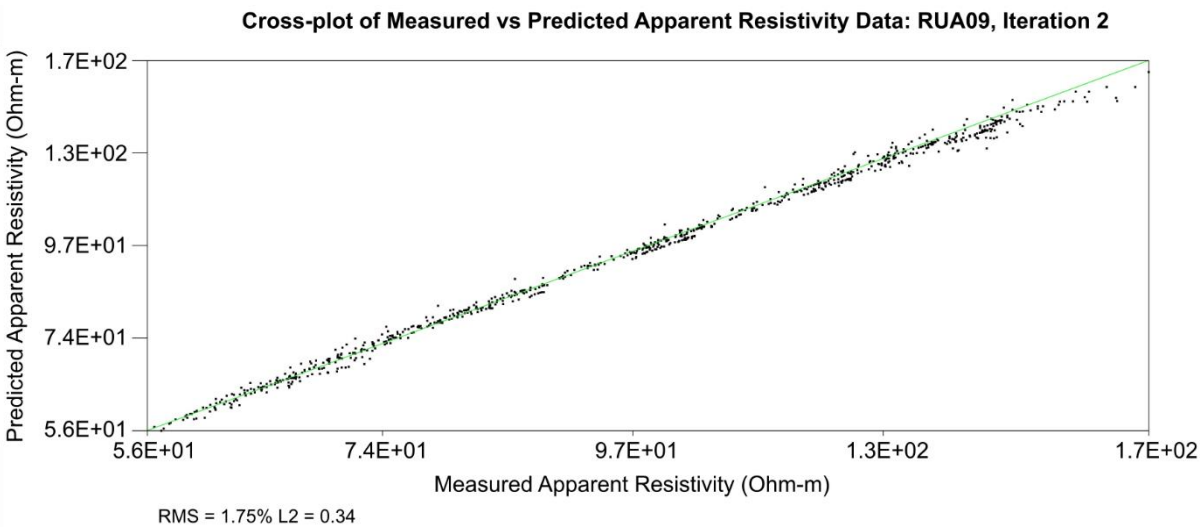

Figure C.15. Cross-plot for RUA09.

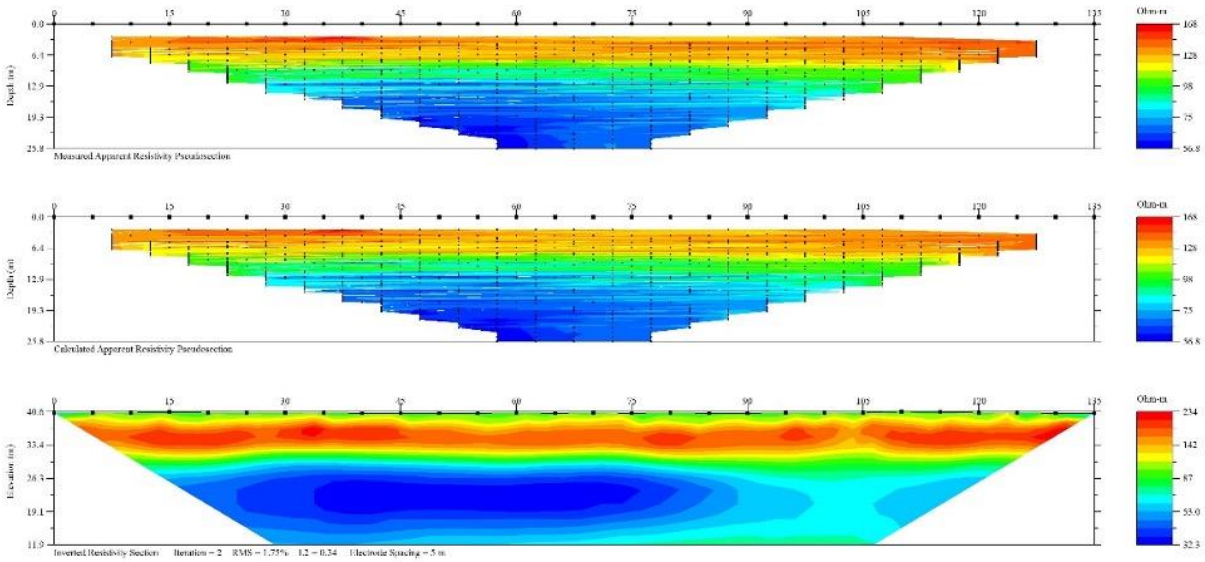

Figure C.16. Pseudo-sections of measured apparent resistivity (top), calculated apparent resistivity (middle), and original inverted resistivity section (bottom) for RUA09.

RUA10

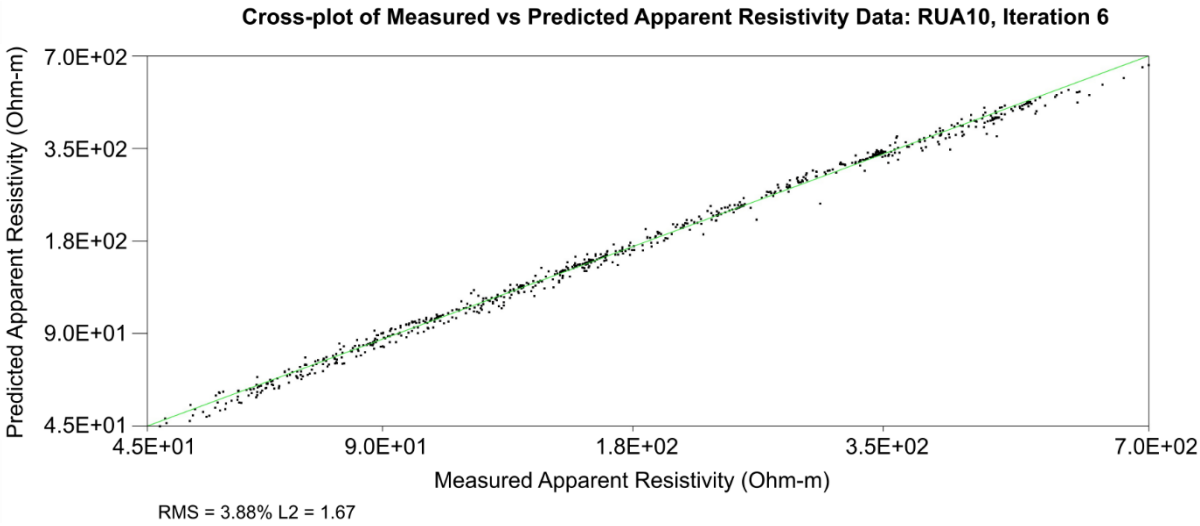

Figure C.17. Cross-plot for RUA10.

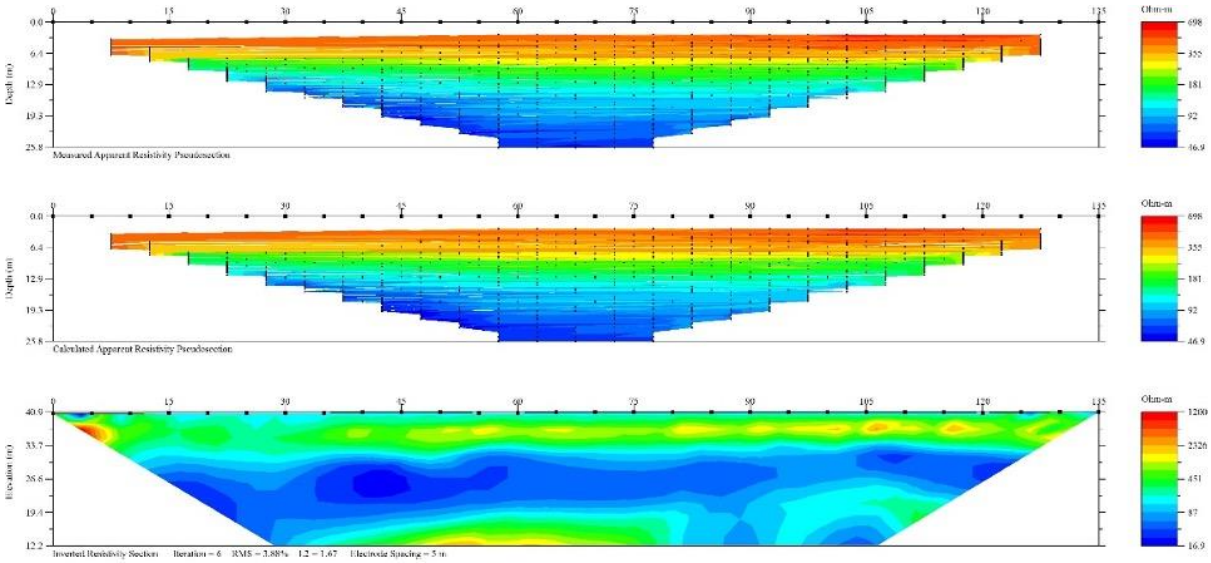

Figure C.18. Pseudo-sections of measured apparent resistivity (top), calculated apparent resistivity (middle), and original inverted resistivity section (bottom) for RUA10.

RUA11

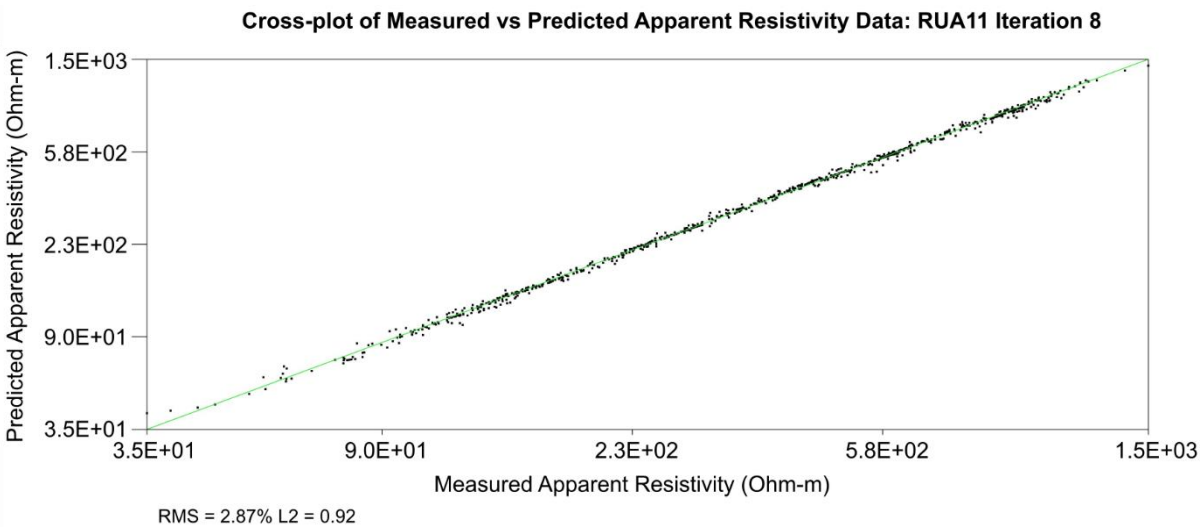

Figure C.19. Cross-plot for RUA11.

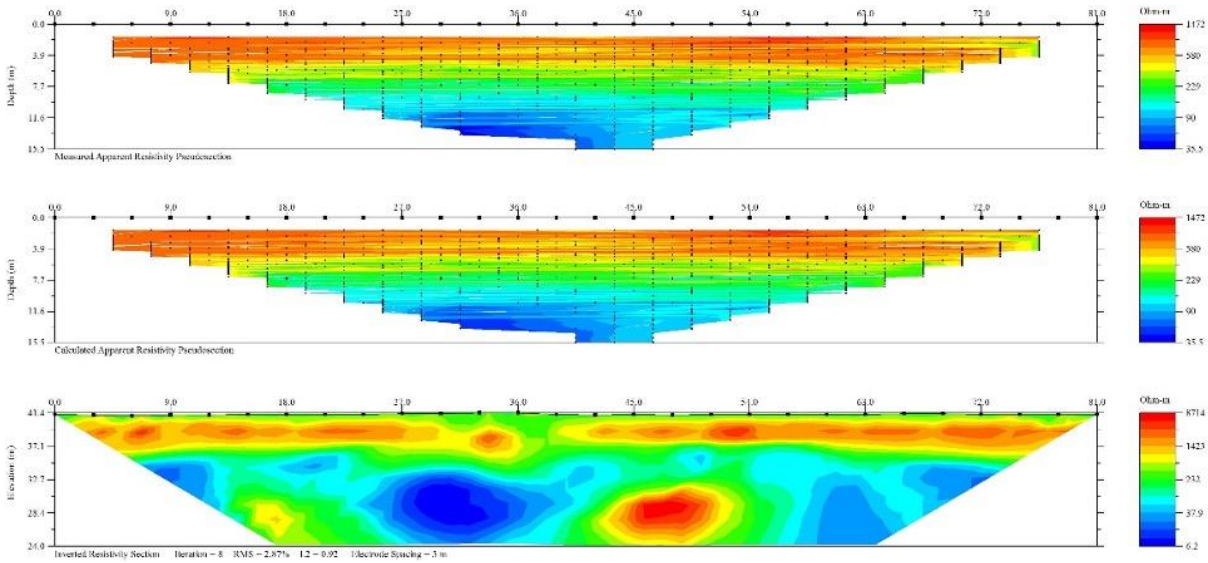

Figure C.20. Pseudo-sections of measured apparent resistivity (top), calculated apparent resistivity (middle), and original inverted resistivity section (bottom) for RUA11.

RUA12

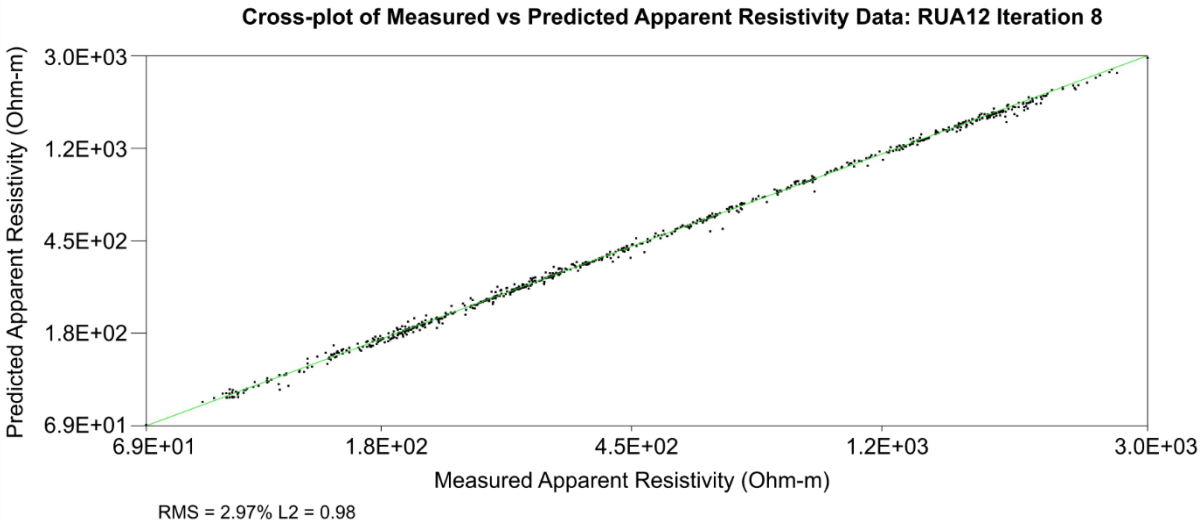

Figure C.21. Cross-plot for RUA12.

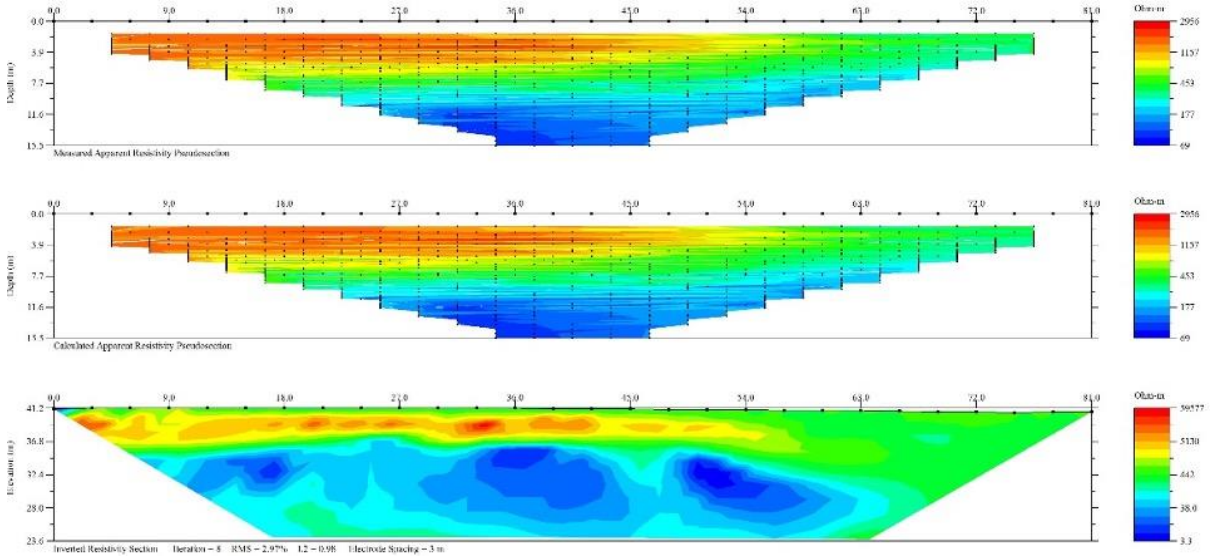

Figure C.22. Pseudo-sections of measured apparent resistivity (top), calculated apparent resistivity (middle), and original inverted resistivity section (bottom) for RUA12.

RUA13

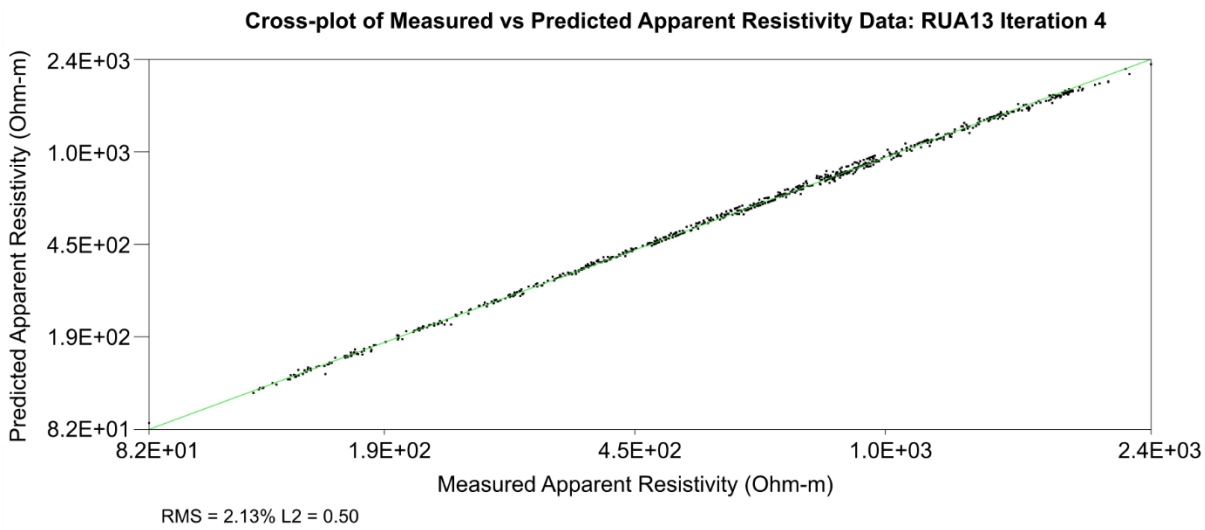

Figure C.23. Cross-plot for RUA13.

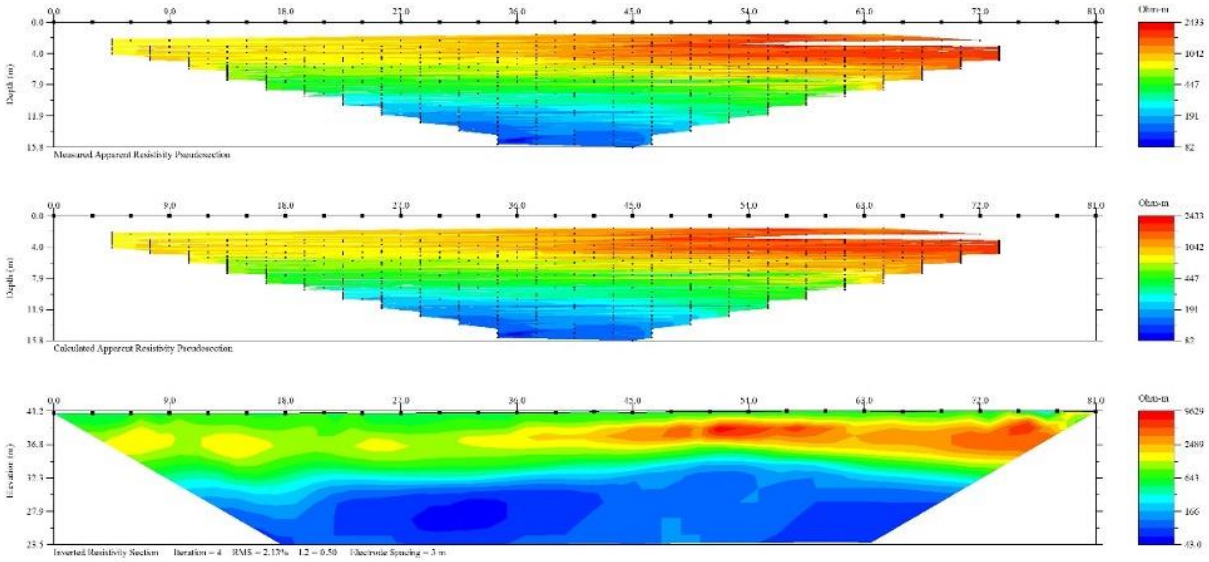

Figure C.24. Pseudo-sections of measured apparent resistivity (top), calculated apparent resistivity (middle), and original inverted resistivity section (bottom) for RUA13.

RUA14

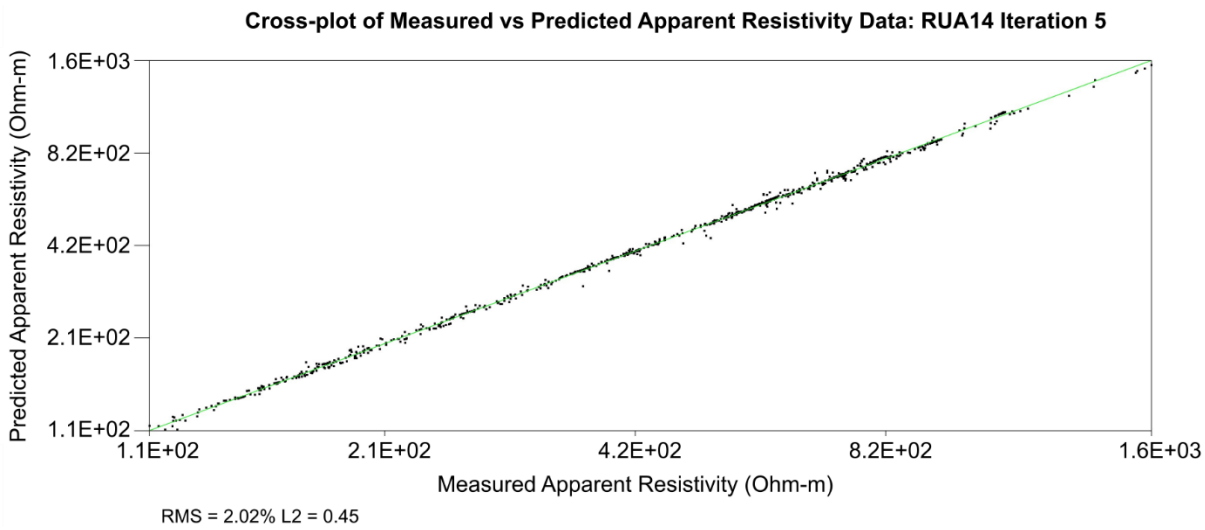

Figure C.25. Cross-plot for RUA14.

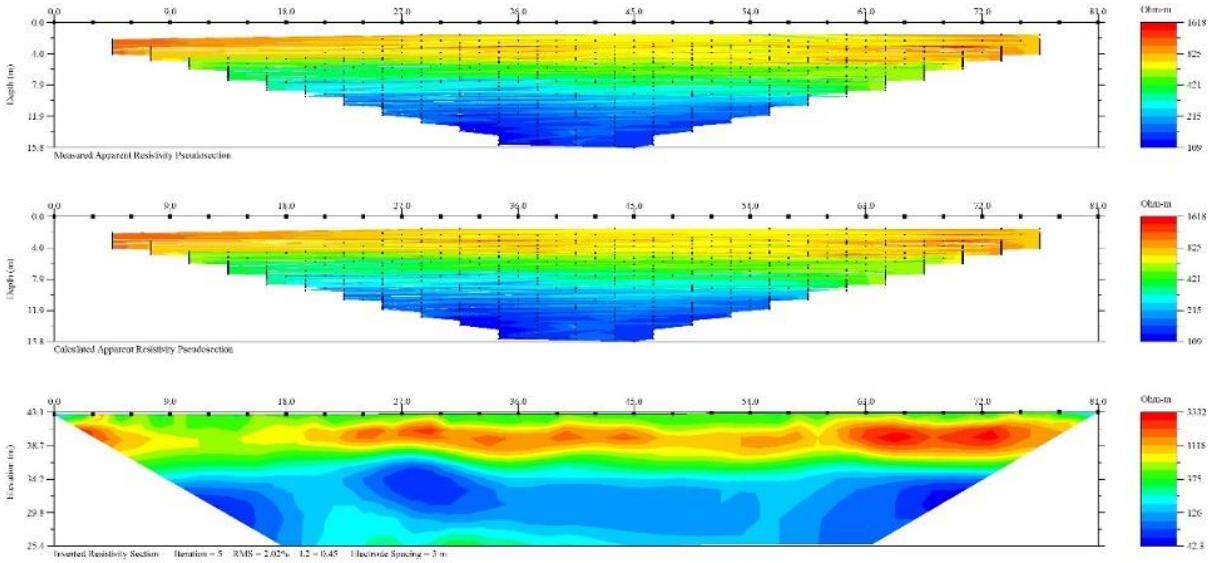

Figure C.26. Pseudo-sections of measured apparent resistivity (top), calculated apparent resistivity (middle), and original inverted resistivity section (bottom) for RUA14.

TGH01

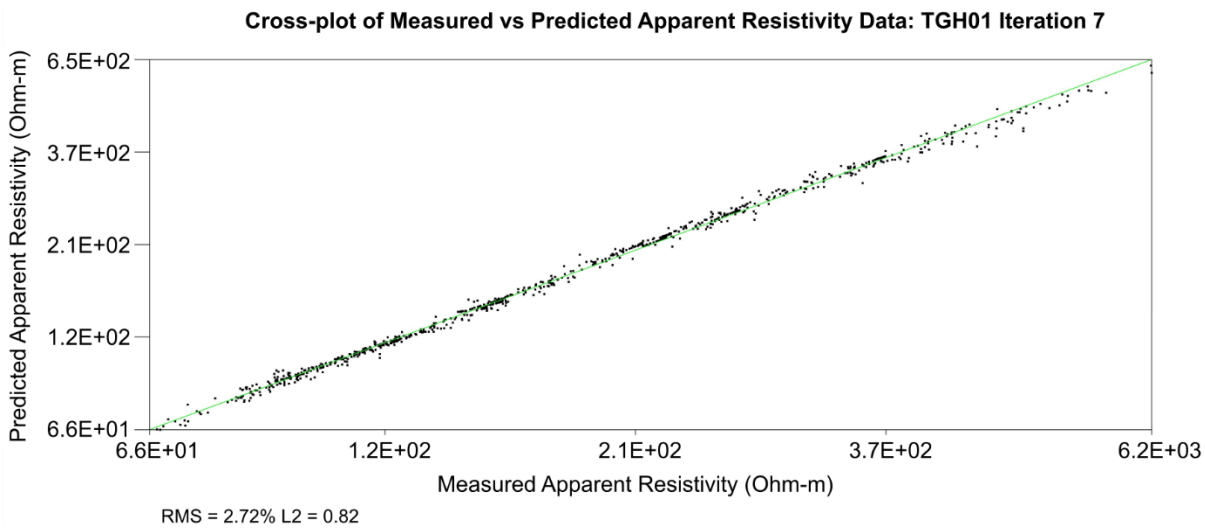

Figure C.27. Cross-plot for TGH01.

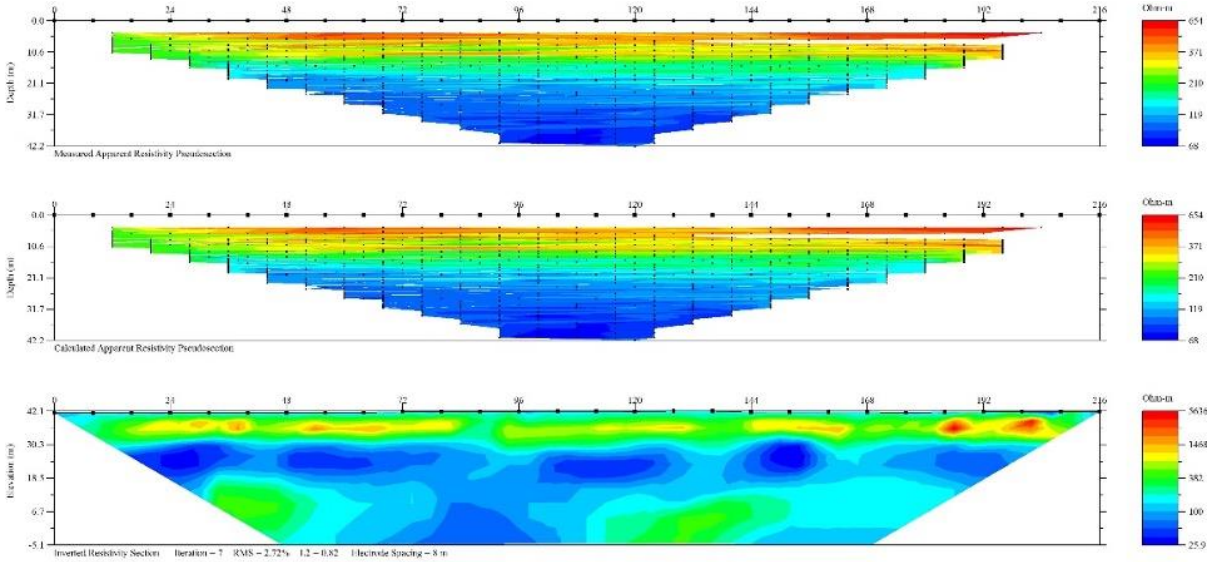

Figure C.28. Pseudo-sections of measured apparent resistivity (top), calculated apparent resistivity (middle), and original inverted resistivity section (bottom) for TGH01.

Appendix D. Hand Auger Logs

AUGER LOG

(Based on Tonkin and Taylor) SHEET 1 of 1

THE UNIVERSITY OF WAIKATO
Te Whare Wānanga o Waikato

PROJECT: MSc Research – Ham. Faults LOCATION: AgResearch Ruakura Farm JOB No: HA01

CO-ORDINATES mN 5817860.335 AUGER TYPE: Dutch HOLE STARTED: 08/09/2020
mE 1803474.063 DATUM: NZGD2000 HOLE FINISHED: 08/09/2020
DIRECTION: Vertical R.L. GROUND: 39.773 m DRILLED BY: GM
ANGLE FROM HORIZONTAL: 90° LOGGED BY: AC CHECKED:

GEOLOGICAL UNIT	DEPTH (m)	GRAPHIC LOG	CLASSIFICATION SYMBOL	MOISTURE CONDITION	STRENGTH / PLASTICITY CONDITION	SOIL DESCRIPTION: Soil NAME; colour, structure. (a) Soil mass qualifications - strength, moisture condition, grading, bedding, plasticity, sensitivity; (b) soil fraction qualifications - major fraction size and shape, weathring of clasts, subordinate fraction, minor fraction; (c) additional information.	SHEAR STRENGTH	PENETROMETER		WATER	
			ML	D		Organic SILT with trace of sand; dark brown. Soft, dry, non-plastic to low plasticity; organics, rootlets; sand, fine [TOPSOIL].					
HINUERA FORMATION			MH	M		Clayey SILT with trace of sand and trace of organics; light brownish orange. Soft to firm, moist, high plasticity; sand, fine, angular to subangular, quartz; organics, rootlets. 0.5 m: becoming light brownish grey with minor sand, no organics.					
			SP	M		Silty fine to medium SAND with some gravel; light grey. Moist, poorly graded; subangular to subrounded, quartz, pumice and lithics; gravel, fine to medium, subrounded, pumice and rhyolite.					
	1		GP	M		Sandy coarse GRAVEL with some silt; light grey. Moist; poorly graded; subangular to subrounded, quartz, pumice and rhyolite; sand, fine to medium, subangular to subrounded, quartz and rhyolite.					1
	2					EOH at 1.1 m: Unable to retain core. *Notes:* Basic properties auger to correlate electrical resistivity tomography, shear vane and penetrometer not used; fine soil strength estimated using field diagnostics per NZGS Field Guide Sheet. Groundwater not encountered. Coordinates and elevation from Leica GS16 GNSS RTK Rover.					2
	3										3

AUGER LOG

(Based on Tonkin and Taylor) SHEET 1 of 1

THE UNIVERSITY OF WAIKATO
Te Whare Wānanga o Waikato

PROJECT: MSc Research – Ham. Faults LOCATION: AgResearch Ruakura Farm JOB No: HA02

CO-ORDINATES mN 5817890.629 AUGER TYPE: Dutch HOLE STARTED: 08/09/2020
mE 1803476.999 DATUM: NZGD2000 HOLE FINISHED: 08/09/2020
DIRECTION: Vertical R.L. GROUND: 40.006 m DRILLED BY: AC
ANGLE FROM HORIZONTAL: 90° LOGGED BY: GM CHECKED:

GEOLOGICAL UNIT	DEPTH (m)	GRAPHIC LOG	CLASSIFICATION SYMBOL	MOISTURE CONDITION	STRENGTH / PLASTICITY CONDITION	SOIL DESCRIPTION: Soil NAME; colour, structure. (a) Soil mass qualifications - strength, moisture condition, grading, bedding, plasticity, sensitivity; (b) soil fraction qualifications - major fraction size and shape, weathring of clasts, subordinate fraction, minor fraction; (c) additional information.	SHEAR STRENGTH	PENETROMETER		WATER	
			ML	D		Organic SILT; dark brown. Soft, dry, non-plastic to low plasticity; organics, rootlets [TOPSOIL].					
HINUERA FORMATION			MH	M		Clayey SILT with minor organics and trace of sand; light brownish grey. Soft to firm, moist, high plasticity; sand, fine, angular to subangular, quartz; organics, rootlets.					
	1		SP	M		Fine to medium SAND with trace of silt and trace of gravel; light brownish grey. Moist; poorly graded; subangular to subrounded, quartz and lithics; gravel, fine to medium, subangular to subrounded, pumice and rhyolite.					1
			SP	M		Fine to medium gravelly SAND with trace of silt; light brownish grey. Moist; poorly graded; subangular to subrounded, quartz and lithics; gravel, medium to coarse, subangular to subrounded, greywacke and rhyolite.					
	2					EOH at 1.2 m: Unable to retain core.					2
	3					*Notes:* Basic properties auger to correlate electrical resistivity tomography, shear vane and penetrometer not used; fine soil strength estimated using field diagnostics per NZGS Field Guide Sheet. Groundwater not encountered. Coordinates and elevation from Leica GS16 GNSS RTK Rover.					3

AUGER LOG

(Based on Tonkin and Taylor) SHEET 1 of 1

THE UNIVERSITY OF WAIKATO
Te Whare Wānanga o Waikato

PROJECT: MSc Research – Ham. Faults LOCATION: AgResearch Ruakura Farm JOB No: HA03

CO-ORDINATES mN 5817905.773 AUGER TYPE: Dutch HOLE STARTED: 08/09/2020
mE 1803574.582 DATUM: NZGD2000 HOLE FINISHED: 08/09/2020
DIRECTION: Vertical R.L. GROUND: 39.574 m DRILLED BY: AC/GM
ANGLE FROM HORIZONTAL: 90° LOGGED BY: GM CHECKED:

GEOLOGICAL UNIT	DEPTH (m)	GRAPHIC LOG	CLASSIFICATION SYMBOL	MOISTURE CONDITION	STRENGTH / PLASTICITY CONDITION	SOIL DESCRIPTION: Soil NAME; colour, structure. (a) Soil mass qualifications - strength, moisture condition, grading, bedding, plasticity, sensitivity; (b) soil fraction qualifications - major fraction size and shape, weathring of clasts, subordinate fraction, minor fraction; (c) additional information.	SHEAR STRENGTH	PENETROMETER		WATER	
			ML	M		Organic SILT; dark brown. Soft to firm, dry, non-plastic to low plasticity; organics, rootlets [TOPSOIL].					
HINUERA FORMATION			MH	M		SILT; light grey, mottled orange. Soft to firm, moist, high plasticity.					
	1		SP	M		Silty fine SAND; light grey, mottled orange. Moist; poorly graded.					1
				W		0.7 m: Silt fraction increases, slight plasticity, wet.					
				S		1.3 m: Saturated.					1.3 ▼
	2					EOH at 1.4 m: Unable to advance due to hole collapse.					2
	3					*Notes:* Basic properties auger to correlate electrical resistivity tomography, shear vane and penetrometer not used; fine soil strength estimated using field diagnostics per NZGS Field Guide Sheet. Coordinates and elevation from Leica GS16 GNSS RTK Rover.					3

AUGER LOG

(Based on Tonkin and Taylor) SHEET 1 of 1

THE UNIVERSITY OF WAIKATO
Te Whare Wānanga o Waikato

PROJECT: MSc Research – Ham. Faults LOCATION: AgResearch Ruakura Farm JOB No: HA04

CO-ORDINATES mN 5816323.135 AUGER TYPE: Dutch HOLE STARTED: 06/10/2020
mE 1803526.181 DATUM: NZGD2000 HOLE FINISHED: 06/10/2020
DIRECTION: Vertical R.L. GROUND: 40.676 m DRILLED BY: GM
ANGLE FROM HORIZONTAL: 90° LOGGED BY: AC CHECKED:

GEOLOGICAL UNIT	DEPTH (m)	GRAPHIC LOG	CLASSIFICATION SYMBOL	MOISTURE CONDITION	STRENGTH / PLASTICITY CONDITION	SOIL DESCRIPTION: Soil NAME; colour, structure. (a) Soil mass qualifications - strength, moisture condition, grading, bedding, plasticity, sensitivity; (b) soil fraction qualifications - major fraction size and shape, weathring of clasts, subordinate fraction, minor fraction; (c) additional information.	SHEAR STRENGTH	PENETROMETER		WATER	
			ML	M		Organic SILT, trace sand; dark brown. Soft, dry, non-plastic to low plasticity; organics, rootlets; sand, fine [TOPSOIL].					
HINUERA FORMATION			ML	M		SILT with minor organics and trace of sand; dark brown, motted orange. Soft, moist, low plasticity, insensitive; organics, rootlets; sand, fine, subangular.	55/39				
	1		SW	M		Silty fine to coarse SAND with some gravel; light brownish grey. Loosely packed, moist; well graded; subangular to subrounded; silt, very slightly plastic; gravel, fine to coarse, subangular to subrounded, greywacke and highly weathered pumice. 1 m: Light brownish grey.					1
			SP	M		Fine to medium gravelly SAND with trace of silt; light brownish grey. Moist; poorly graded; subangular to subrounded, quartz and lithics; gravel, medium to coarse, subangular to subrounded, greywacke and rhyolite.					
	2					EOH at 2.0 m: Unable to advance due to hole collapse. *Notes:* Basic properties auger to correlate electrical resistivity tomography, penetrometer not used; fine soil strength estimated using field diagnostics per NZGS Field Guide Sheet. Shear vane 95039, 19 mm blade. Groundwater not encountered. Coordinates and elevation from Leica GS16 GNSS RTK Rover.					2
	3										3

AUGER LOG

(Based on Tonkin and Taylor) SHEET 1 of 1

THE UNIVERSITY OF WAIKATO
Te Whare Wānanga o Waikato

PROJECT: MSc Research – Ham. Faults LOCATION: AgResearch Ruakura Farm JOB No: HA05

CO-ORDINATES mN 5816333.412 AUGER TYPE: Dutch HOLE STARTED: 06/10/2020
mE 1803537.439 DATUM: NZGD2000 HOLE FINISHED: 06/10/2020
DIRECTION: Vertical R.L. GROUND: 40.982 m DRILLED BY: AC
ANGLE FROM HORIZONTAL: 90° LOGGED BY: GM CHECKED:

GEOLOGICAL UNIT	DEPTH (m)	GRAPHIC LOG	CLASSIFICATION SYMBOL	MOISTURE CONDITION	STRENGTH / PLASTICITY CONDITION	SOIL DESCRIPTION: Soil NAME; colour, structure. (a) Soil mass qualifications - strength, moisture condition, grading, bedding, plasticity, sensitivity; (b) soil fraction qualifications - major fraction size and shape, weathring of clasts, subordinate fraction, minor fraction; (c) additional information.	SHEAR STRENGTH	PENETROMETER		WATER	
			ML	M		Organic SILT, trace sand; dark brown. Soft, dry, non-plastic to low plasticity; organics, rootlets; sand, fine [TOPSOIL].					
FILL			CH	M		CLAY with trace of sand; light reddish brown. Soft, moist, high plasticity, moderately sensitive; sand, medium, subangular to subrounded.	54/20				
			SP	M		Gravelly fine SAND with trace silt; dark reddish brown. Loosely packed, moist; poorly graded; gravel, medium, subangular to subrounded, greywacke; micaceous flakes.					
	1					EOH at 0.9 m: Unable to penetrate.					1
	2					*Notes:* Basic properties auger to correlate electrical resistivity tomography, penetrometer not used; fine soil strength estimated using field diagnostics per NZGS Field Guide Sheet. Shear vane 95039, 19 mm blade. Groundwater not encountered. Coordinates and elevation from Leica GS16 GNSS RTK Rover.					2
	3										3

AUGER LOG

(Based on Tonkin and Taylor) SHEET 1 of 1

THE UNIVERSITY OF WAIKATO
Te Whare Wānanga o Waikato

PROJECT: MSc Research – Ham. Faults LOCATION: AgResearch Ruakura Farm JOB No: HA06

CO-ORDINATES mN 5816342.635 AUGER TYPE: Dutch HOLE STARTED: 06/10/2020
mE 1803549.167 DATUM: NZGD2000 HOLE FINISHED: 06/10/2020
DIRECTION: Vertical R.L. GROUND: 41.222 m DRILLED BY: AC
ANGLE FROM HORIZONTAL: 90° LOGGED BY: GM CHECKED:

GEOLOGICAL UNIT	DEPTH (m)	GRAPHIC LOG	CLASSIFICATION SYMBOL	MOISTURE CONDITION	STRENGTH / PLASTICITY CONDITION	SOIL DESCRIPTION: Soil NAME; colour, structure. (a) Soil mass qualifications - strength, moisture condition, grading, bedding, plasticity, sensitivity; (b) soil fraction qualifications - major fraction size and shape, weathring of clasts, subordinate fraction, minor fraction; (c) additional information.	SHEAR STRENGTH	PENETROMETER		WATER	
	0		ML	M		Organic SILT, trace sand; dark brown. Soft, dry, non-plastic to low plasticity; organics, rootlets; sand, fine [TOPSOIL].					0
HINUERA FORMATION			ML	M		Sandy SILT; light greyish orange. Soft, moist, low plasticity, insensitive; sand, fine.	58/52				
			SP	M		Fine SAND with some silt; light greyish brown. Loosely packed, moist; poorly graded.					
	1		SP	M		Medium to coarse SAND with minor gravel; light greyish brown. Loosely packed, moist; poorly graded; gravel, fine to medium, subangular to subrounded, pumice and rhyolite.					1
	2					EOH at 1.4 m: Unable to advance due to hole collapse. *Notes:* Basic properties auger to correlate electrical resistivity tomography, penetrometer not used; fine soil strength estimated using field diagnostics per NZGS Field Guide Sheet. Shear vane 95039, 19 mm blade. Groundwater not encountered. Coordinates and elevation from Leica GS16 GNSS RTK Rover.					2
	3										3

AUGER LOG

(Based on Tonkin and Taylor) SHEET 1 of 1

THE UNIVERSITY OF WAIKATO
Te Whare Wānanga o Waikato

PROJECT: MSc Research – Ham. Faults LOCATION: AgResearch Ruakura Farm JOB No: HA07

CO-ORDINATES mN 5816351.957 AUGER TYPE: Dutch HOLE STARTED: 06/10/2020
mE 1803560.862 DATUM: NZGD2000 HOLE FINISHED: 06/10/2020
DIRECTION: Vertical R.L. GROUND: 41.520 m DRILLED BY: GM
ANGLE FROM HORIZONTAL: 90° LOGGED BY: AC CHECKED:

GEOLOGICAL UNIT	DEPTH (m)	GRAPHIC LOG	CLASSIFICATION SYMBOL	MOISTURE CONDITION	STRENGTH / PLASTICITY CONDITION	SOIL DESCRIPTION: Soil NAME; colour, structure. (a) Soil mass qualifications - strength, moisture condition, grading, bedding, plasticity, sensitivity; (b) soil fraction qualifications - major fraction size and shape, weathring of clasts, subordinate fraction, minor fraction; (c) additional information.	SHEAR STRENGTH	PENETROMETER		WATER	
			ML	D		Organic SILT, trace sand; dark brown. Soft, dry, non-plastic to low plasticity; organics, rootlets; sand, fine [TOPSOIL].					
HINUERA FORMATION			ML	D		Sandy SILT; light reddish brown. Very soft, dry, low plasticity, insensitive; sand, fine.	68/55				
			SP	M		Silty fine SAND; light reddish brown. Loosely packed, moist; poorly graded.					
			SP	M		Medium to coarse SAND with some gravel; light brownish grey. Loosely packed, moist; poorly graded; sand, subangular to subrounded, quartz and feldspar; gravel, fine to medium, subangular to subrounded, pumice and rhyolite.					
	1		SP	M		Gravelly fine SAND; light brownish grey. Loosely packed, moist; poorly graded; sand, rounded, quartz and feldspar; gravel, medium, subrounded, pumice.					1
			GW	M		Sandy fine to coarse GRAVEL with trace of silt; dark brownish red. Tightly packed, moist; well graded; subangular to subrounded, pumice, rhyolite and greywacke; sand, fine to medium, subangular to subrounded.					
	2					EOH at 1.4 m: Unable to penetrate. *Notes:* Basic properties auger to correlate electrical resistivity tomography, shear vane and penetrometer not used; fine soil strength estimated using field diagnostics per NZGS Field Guide Sheet. Shear vane 95039, 19 mm blade. Groundwater not encountered. Coordinates and elevation from Leica GS16 GNSS RTK Rover.					2
	3										3

AUGER LOG

(Based on Tonkin and Taylor) SHEET 1 of 1

THE UNIVERSITY OF WAIKATO
Te Whare Wānanga o Waikato

PROJECT: MSc Research – Ham. Faults LOCATION: AgResearch Ruakura Farm JOB No: HA08

CO-ORDINATES mN 5816360.564 AUGER TYPE: Dutch HOLE STARTED: 06/10/2020
mE 1803572.991 DATUM: NZGD2000 HOLE FINISHED: 06/10/2020
DIRECTION: Vertical R.L. GROUND: 41.541 m DRILLED BY: GM
ANGLE FROM HORIZONTAL: 90° LOGGED BY: AC CHECKED:

GEOLOGICAL UNIT	DEPTH (m)	GRAPHIC LOG	CLASSIFICATION SYMBOL	MOISTURE CONDITION	STRENGTH / PLASTICITY CONDITION	SOIL DESCRIPTION: Soil NAME; colour, structure. (a) Soil mass qualifications - strength, moisture condition, grading, bedding, plasticity, sensitivity; (b) soil fraction qualifications - major fraction size and shape, weathring of clasts, subordinate fraction, minor fraction; (c) additional information.	SHEAR STRENGTH	PENETROMETER		WATER	
			ML	D		Organic SILT, trace sand; dark brown. Soft, dry, non-plastic to low plasticity; organics, rootlets; sand, fine [TOPSOIL].					
HINUERA FORMATION			ML	D		SILT with trace of sand; dark reddish brown. Firm, dry, low plasticity, moderately sensitive; sand, fine; possibly uncontrolled fill.	77/27				
	1		SP	M		SAND with trace of gravel; dark greyish brown. Loosely packed, moist; poorly graded; fine, angular to subrounded, quartz, feldspar and pumice; gravel, fine to medium, pumice; gravel content increases towards dominant with depth.					1
	2					EOH at 1.0 m: Unable to advance due to hole collapse.					2
	3					*Notes:* Basic properties auger to correlate electrical resistivity tomography, penetrometer not used; fine soil strength estimated using field diagnostics per NZGS Field Guide Sheet. Shear vane 95039, 19 mm blade. Groundwater not encountered. Coordinates and elevation from Leica GS16 GNSS RTK Rover.					3

AUGER LOG

(Based on Tonkin and Taylor) SHEET 1 of 1

THE UNIVERSITY OF WAIKATO
Te Whare Wānanga o Waikato

PROJECT: MSc Research – Ham. Faults LOCATION: AgResearch Ruakura Farm JOB No: HA09

CO-ORDINATES mN 5816370.389 AUGER TYPE: Dutch HOLE STARTED: 06/10/2020
mE 1803584.645 DATUM: NZGD2000 HOLE FINISHED: 06/10/2020
DIRECTION: Vertical R.L. GROUND: 41.385 m DRILLED BY: GM
ANGLE FROM HORIZONTAL: 90° LOGGED BY: AC CHECKED:

GEOLOGICAL UNIT	DEPTH (m)	GRAPHIC LOG	CLASSIFICATION SYMBOL	MOISTURE CONDITION	STRENGTH / PLASTICITY CONDITION	SOIL DESCRIPTION: Soil NAME; colour, structure. (a) Soil mass qualifications - strength, moisture condition, grading, bedding, plasticity, sensitivity; (b) soil fraction qualifications - major fraction size and shape, weathring of clasts, subordinate fraction, minor fraction; (c) additional information.	SHEAR STRENGTH	PENETROMETER		WATER	
			ML	M		Organic SILT, trace sand; dark brown. Soft, dry, non-plastic to low plasticity; organics, rootlets; sand, fine [TOPSOIL].					
HINUERA FORMATION			ML	M		Sandy SILT; light reddish brown. Firm, moist, low plasticity; sand, fine to coarse, some pumice.					
			SP	M		Silty fine SAND, trace gravel; light reddish brown. Loosely packed, moist; poorly graded; sand, rounded, quartz, feldspar; gravel, subrounded, pumice.					
	1		SP	M		Gravelly fine SAND; light brownish grey. Loosely packed, moist; poorly graded; sand, rounded, quartz and feldspar; gravel, medium, subrounded, pumice.					1
	2					EOH at 1.3 m: Unable to advance due to hole collapse. *Notes:* Basic properties auger to correlate electrical resistivity tomography, shear vane and penetrometer not used; fine soil strength estimated using field diagnostics per NZGS Field Guide Sheet. Groundwater not encountered. Coordinates and elevation from Leica GS16 GNSS RTK Rover.					2
	3										3

AUGER LOG

(Based on Tonkin and Taylor) SHEET 1 of 1

THE UNIVERSITY OF WAIKATO
Te Whare Wānanga o Waikato

PROJECT: MSc Research – Ham. Faults LOCATION: AgResearch Ruakura Farm JOB No: HA10

CO-ORDINATES mN 5816379.327 AUGER TYPE: Dutch HOLE STARTED: 06/10/2020
mE 1803596.518 DATUM: NZGD2000 HOLE FINISHED: 06/10/2020
DIRECTION: Vertical R.L. GROUND: 41.568 m DRILLED BY: AC
ANGLE FROM HORIZONTAL: 90° LOGGED BY: GM CHECKED:

GEOLOGICAL UNIT	DEPTH (m)	GRAPHIC LOG	CLASSIFICATION SYMBOL	MOISTURE CONDITION	STRENGTH / PLASTICITY CONDITION	SOIL DESCRIPTION: Soil NAME; colour, structure. (a) Soil mass qualifications - strength, moisture condition, grading, bedding, plasticity, sensitivity; (b) soil fraction qualifications - major fraction size and shape, weathring of clasts, subordinate fraction, minor fraction; (c) additional information.	SHEAR STRENGTH	PENETROMETER		WATER	
			ML	M		Organic SILT, trace sand; dark brown. Soft, dry, non-plastic to low plasticity; organics, rootlets; sand, fine [TOPSOIL].					
HINUERA FORMATION			MH	M		SILT; light brownish orange. Firm, moist, high plasticity, insensitive..	40/22				
			MH	M		SILT, some sand; light brownish orange. Firm, moist, high plasticity; sand, fine, subangular to subrounded. 0.7 m: Some med. to coarse gravel, subangular to subrounded, pumice, lithics.					
	1		SP	M		Gravelly fine SAND; light greyish brown. Loosely packed, moist; poorly graded; sand, subangular to subrounded, quartz, feldspar, pumice; gravel, medium to coarse, subrounded, pumice, rhyolite.					1
	2					EOH at 1.2 m: Unable to advance due to hole collapse. *Notes:* Basic properties auger to correlate electrical resistivity tomography, shear vane and penetrometer not used; fine soil strength estimated using field diagnostics per NZGS Field Guide Sheet. Shear vane 95039, 19 mm blade. Groundwater not encountered. Coordinates and elevation from Leica GS16 GNSS RTK Rover.					2
	3										3

AUGER LOG

(Based on Tonkin and Taylor) SHEET 1 of 1

THE UNIVERSITY OF WAIKATO
Te Whare Wānanga o Waikato

PROJECT: MSc Research – Ham. Faults LOCATION: AgResearch Ruakura Farm JOB No: HA11

CO-ORDINATES mN 5816384.936 AUGER TYPE: Dutch HOLE STARTED: 06/10/2020
mE 1803611.158 DATUM: NZGD2000 HOLE FINISHED: 06/10/2020
DIRECTION: Vertical R.L. GROUND: 41.506 m DRILLED BY: GM
ANGLE FROM HORIZONTAL: 90° LOGGED BY: AC CHECKED:

GEOLOGICAL UNIT	DEPTH (m)	GRAPHIC LOG	CLASSIFICATION SYMBOL	MOISTURE CONDITION	STRENGTH / PLASTICITY CONDITION	SOIL DESCRIPTION Soil NAME; colour, structure. (a) Soil mass qualifications - strength, moisture condition, grading, bedding, plasticity, sensitivity; (b) soil fraction qualifications - major fraction size and shape, weathring of clasts, subordinate fraction, minor fraction; (c) additional information.	SHEAR STRENGTH	PENETROMETER		WATER	
			ML	M		Organic SILT, trace sand; dark brown. Soft, dry, non-plastic to low plasticity; organics, rootlets; sand, fine [TOPSOIL].					
FILL			ML	M		Sandy SILT; light reddish brown. Firm, moist, low plasticity.					
			SP	M		Silty sandy medium to coarse GRAVEL; light reddish brown. Tightly packed, moist; poorly graded; gravel, subangular to subrounded, pumice; sand, subrounded to rounded, pumice;. Becomes light grey toward base.					
	1					EOH at 1.0 m: Unable to penetrate. *Notes:* Basic properties auger to correlate electrical resistivity tomography, shear vane and penetrometer not used; fine soil strength estimated using field diagnostics per NZGS Field Guide Sheet. Groundwater not encountered. Coordinates and elevation from Leica GS16 GNSS RTK Rover.					1
	2										2
	3										3

AUGER LOG

(Based on Tonkin and Taylor) SHEET 1 of 1

THE UNIVERSITY OF WAIKATO
Te Whare Wānanga o Waikato

PROJECT: MSc Research – Ham. Faults LOCATION: AgResearch Ruakura Farm JOB No: HA12

CO-ORDINATES mN 5816361.797 AUGER TYPE: Dutch HOLE STARTED: 14/10/2020
mE 1803574.508 DATUM: NZGD2000 HOLE FINISHED: 14/10/2020
DIRECTION: Vertical R.L. GROUND: 41.311 m DRILLED BY: GM
ANGLE FROM HORIZONTAL: 90° LOGGED BY: GM CHECKED:

GEOLOGICAL UNIT	DEPTH (m)	GRAPHIC LOG	CLASSIFICATION SYMBOL	MOISTURE CONDITION	STRENGTH / PLASTICITY CONDITION	SOIL DESCRIPTION: Soil NAME; colour, structure. (a) Soil mass qualifications - strength, moisture condition, grading, bedding, plasticity, sensitivity; (b) soil fraction qualifications - major fraction size and shape, weathring of clasts, subordinate fraction, minor fraction; (c) additional information.	SHEAR STRENGTH	PENETROMETER		WATER	
			ML	M		Organic SILT, trace sand; dark brown. Soft, moist, low plasticity; sand, medium organics, rootlets; sand, fine [TOPSOIL].					
FILL			ML	M		Gravelly SILT with trace of sand and trace organics; dark brownish orange. Moist, low plasticity; gravel, fine to medium (rare coarse), angular to subangular, limestone; sand, medium; organics, rootlets.					
HINUERA FORMATION			MH	M		SILT with minor sand; dark brownish orange. Moist, low plasticity; sand, fine to medium, subangular to subrounded, quartz, feldspar.	69/19				
			MH	M		SILT with minor sand and minor gravel; light brownish orange. Moist, low plasticity; sand, fine to medium, subangular to subrounded, quartz, feldspar; gravel, medium, subangular to subrounded, pumice, lithics.					
			SP	M		Silty fine SAND with trace of gravel; light brownish orange. Loosely packed, moist, poorly graded; gravel, medium, subangular to subrounded, pumice, lithics.					
	1		SP	M		Gravelly medium to coarse SAND with trace of silt; dark brownish grey. Tightly packed, moist, poorly graded; subangular to subrounded, quartz; gravel, fine to medium, pumice, lithics.					1
						Sandy coarse GRAVEL, dark brownish grey. Tightly packed, moist, poorly graded; subangular to subrounded, pumice, lithics; sand, medium to coarse, subangular to subrounded, quartz.					
						EOH at 1.2 m: Unable to penetrate.					
	2										2
	3										3

Notes:

Basic properties auger to correlate electrical resistivity tomography, penetrometer not used; fine soil strength estimated using field diagnostics per NZGS Field Guide Sheet.

Shear vane 95039, 19 mm blade.

Groundwater not encountered.

Coordinates and elevation from Leica GS16 GNSS RTK Rover.

AUGER LOG

(Based on Tonkin and Taylor) SHEET 1 of 1

THE UNIVERSITY OF WAIKATO
Te Whare Wānanga o Waikato

PROJECT: MSc Research – Ham. Faults LOCATION: AgResearch Ruakura Farm JOB No: HA13

CO-ORDINATES mN 5816362.479 AUGER TYPE: Dutch HOLE STARTED: 14/10/2020
mE 1803576.366 DATUM: NZGD2000 HOLE FINISHED: 14/10/2020
DIRECTION: Vertical R.L. GROUND: 41.334 m DRILLED BY: GM
ANGLE FROM HORIZONTAL: 90° LOGGED BY: GM CHECKED:

GEOLOGICAL UNIT	DEPTH (m)	GRAPHIC LOG	CLASSIFICATION SYMBOL	MOISTURE CONDITION	STRENGTH / PLASTICITY CONDITION	SOIL DESCRIPTION: Soil NAME; colour, structure. (a) Soil mass qualifications - strength, moisture condition, grading, bedding, plasticity, sensitivity; (b) soil fraction qualifications - major fraction size and shape, weathring of clasts, subordinate fraction, minor fraction; (c) additional information.	SHEAR STRENGTH	PENETROMETER		WATER	
			ML	M		Organic SILT, trace sand; dark brown. Moist, low plasticity; organics, rootlets; sand, fine [TOPSOIL]. Very thin bed medium subrounded gravel @ 0.05 m.					
FILL			CL	M		Sandy silty CLAY with trace of organics; light brownish orange. Moist, low plasticity, moderately sensitive; sand, fine to coarse, quartz, lithics; organics, rootlets.	98/48				
			ML	M		Sandy SILT with trace of clay; light brownish orange. Moist, low plasticity; sand, fine to medium, quartz, lithics.					
			SP	M		Silty medium to coarse SAND with some gravel; light greyish orange with dark orange mottles. Loosely packed, moist, poorly graded; sand, subangular to subrounded, quartz, feldspar, lithics; gravel, coarse, subangular, lithics.					
HINUERA FORMATION	1		SP	M		Silty medium to coarse SAND with some gravel; dark red. Loosely packed, moist, poorly graded; sand, subangular to subrounded, quartz, feldspar, rhyolite, lithics; gravel, medium, subrounded, rhyolite, lithics.					1
			GP	W		Sandy coarse GRAVEL; dark red. Tightly packed, moist, poorly graded; gravel subrounded, rhyolite; sand, medium to coarse, subangular to subrounded, quartz, feldspar, rhyolite, lithics.					
	2					EOH at 1.3 m: Unable to penetrate. *Notes:* Basic properties auger to correlate electrical resistivity tomography, shear vane and penetrometer not used; fine soil strength estimated using field diagnostics per NZGS Field Guide Sheet. Shear vane 95039, 19 mm blade. Groundwater not encountered. Coordinates and elevation from Leica GS16 GNSS RTK Rover.					2
	3										3

AUGER LOG

(Based on Tonkin and Taylor) SHEET 1 of 1

THE UNIVERSITY OF WAIKATO
Te Whare Wānanga o Waikato

PROJECT: MSc Research – Ham. Faults LOCATION: AgResearch Ruakura Farm JOB No: HA14

CO-ORDINATES mN 5816362.211 AUGER TYPE: Dutch HOLE STARTED: 14/10/2020
mE 1803578.494 DATUM: NZGD2000 HOLE FINISHED: 14/10/2020
DIRECTION: Vertical R.L. GROUND: 41.331 m DRILLED BY: GM
ANGLE FROM HORIZONTAL: 90° LOGGED BY: GM CHECKED:

GEOLOGICAL UNIT	DEPTH (m)	GRAPHIC LOG	CLASSIFICATION SYMBOL	MOISTURE CONDITION	STRENGTH / PLASTICITY CONDITION	SOIL DESCRIPTION: Soil NAME; colour, structure. (a) Soil mass qualifications - strength, moisture condition, grading, bedding, plasticity, sensitivity; (b) soil fraction qualifications - major fraction size and shape, weathring of clasts, subordinate fraction, minor fraction; (c) additional information.	SHEAR STRENGTH	PENETROMETER		WATER	
			ML	M		Gravelly organic SILT; dark brown. Moist, low plasticity; gravel, fine to medium, subangular, lithics; organics, rootlets [TOPSOIL].					
FILL			CL	M		Sandy silty CLAY with trace of organics; light brownish orange. Moist, low plasticity, sensitive; sand, fine to coarse, quartz, lithics; organics, rootlets.	120/20				
			SP	M		Silty medium to coarse SAND with minor gravel; light greyish orange. Loosely packed, moist, poorly graded; sand, subangular to subrounded, quartz, feldspar, lithics; gravel, fine to medium, subangular, lithics.					
HINUERA FORMATION	1		GW	M		Sandy fine to coarse GRAVEL; light greyish orange. Loosely packed, moist, well graded; gravel subangular to subrounded, pumice, rhyolite, lithics; sand, fine to coarse, subangular to subrounded, quartz, feldspar, rhyolite.					1
	2					EOH at 1.2 m: Unable to advance due to hole collapse. *Notes:* Basic properties auger to correlate electrical resistivity tomography, shear vane and penetrometer not used; fine soil strength estimated using field diagnostics per NZGS Field Guide Sheet. Shear vane 95039, 19 mm blade. Groundwater not encountered. Coordinates and elevation from Leica GS16 GNSS RTK Rover.					2
	3										3

AUGER LOG

(Based on Tonkin and Taylor) SHEET 1 of 1

THE UNIVERSITY OF WAIKATO
Te Whare Wānanga o Waikato

PROJECT: MSc Research – Ham. Faults LOCATION: AgResearch Ruakura Farm JOB No: HA15

CO-ORDINATES mN 5816361.287 AUGER TYPE: Dutch HOLE STARTED: 14/10/2020
mE 1803572.386 DATUM: NZGD2000 HOLE FINISHED: 14/10/2020
DIRECTION: Vertical R.L. GROUND: 41.190 m DRILLED BY: GM
ANGLE FROM HORIZONTAL: 90° LOGGED BY: GM CHECKED:

GEOLOGICAL UNIT	DEPTH (m)	GRAPHIC LOG	CLASSIFICATION SYMBOL	MOISTURE CONDITION	STRENGTH / PLASTICITY CONDITION	SOIL DESCRIPTION: Soil NAME; colour, structure. (a) Soil mass qualifications - strength, moisture condition, grading, bedding, plasticity, sensitivity; (b) soil fraction qualifications - major fraction size and shape, weathring of clasts, subordinate fraction, minor fraction; (c) additional information.	SHEAR STRENGTH	PENETROMETER		WATER	
			ML	M		Gravelly organic SILT; dark brown. Moist, low plasticity; gravel, medium to coarse, angular to subangular, lithics; organics, rootlets [TOPSOIL].					
FILL			MH	M		Clayey SILT with trace of sand and trace of organics; light brownish orange. Moist, high plasticity, moderately sensitive; sand, fine to medium, lithics; organics, rootlets.	66/21				
			SP	M		Silty fine to medium SAND with minor gravel; light greyish orange. Loosely packed, moist, poorly graded; sand, subangular to subrounded, lithics; gravel, fine to medium, subangular to subrounded, lithics.					
HINUERA FORMATION	1		SP	M W		Gravelly medium to coarse SAND with some silt; light greyish orange. Loosely packed, moist, poorly graded; sand, subangular to subrounded, quartz, rhyolite, lithics; gravel, fine to medium, subrounded, rhyolite, lithics. 1.1 m: Gravel becomes coarse. 1.15 m: Wet.					1
	2					EOH at 1.2 m: Unable to penetrate. *Notes:* Basic properties auger to correlate electrical resistivity tomography, shear vane and penetrometer not used; fine soil strength estimated using field diagnostics per NZGS Field Guide Sheet. Shear vane 95039, 19 mm blade. Groundwater not encountered. Coordinates and elevation from Leica GS16 GNSS RTK Rover.					2
	3										3

AUGER LOG

(Based on Tonkin and Taylor) SHEET 1 of 1

THE UNIVERSITY OF WAIKATO
Te Whare Wānanga o Waikato

PROJECT: MSc Research – Ham. Faults LOCATION: AgResearch Ruakura Farm JOB No: HA16

CO-ORDINATES mN 5816361.073 AUGER TYPE: Dutch HOLE STARTED: 14/10/2020
mE 1803570.461 DATUM: NZGD2000 HOLE FINISHED: 14/10/2020
DIRECTION: Vertical R.L. GROUND: 41.202 m DRILLED BY: GM
ANGLE FROM HORIZONTAL: 90° LOGGED BY: GM CHECKED:

GEOLOGICAL UNIT	DEPTH (m)	GRAPHIC LOG	CLASSIFICATION SYMBOL	MOISTURE CONDITION	STRENGTH / PLASTICITY CONDITION	SOIL DESCRIPTION: Soil NAME; colour, structure. (a) Soil mass qualifications - strength, moisture condition, grading, bedding, plasticity, sensitivity; (b) soil fraction qualifications - major fraction size and shape, weathring of clasts, subordinate fraction, minor fraction; (c) additional information.	SHEAR STRENGTH	PENETROMETER		WATER	
			ML	M		Organic SILT with minor gravel; dark brown. Moist, low plasticity; gravel, medium to coarse, angular to subangular, lithics; organics, rootlets [TOPSOIL].					
FILL			MH	M		SILT with some sand and trace of gravel and organics; light brown. Moist, high plasticity, moderately sensitive; sand, fine; gravel, fine, lithics; organics, rootlets.	100/38				
						0.5 m: Mottled orange; larger roots.					
HINUERA FORMATION			SP	M		Fine to medium SAND with some silt and trace of gravel; light greyish orange, mottled orange. Loosely packed, moist, poorly graded; sand, subangular to subrounded, quartz, rhyolite, lithics; gravel, fine to medium, subangular to subrounded, rhyolite, lithics.					
	1		SP	M		Gravelly medium SAND with minor silt; dark reddish brown. Loosely packed, moist, poorly graded; sand, subangular to subrounded, quartz, rhyolite, lithics; gravel, fine to medium, subangular to subrounded, pumice, rhyolite, lithics.					1
				W		1.3 m: Wet.					
	2					EOH at 1.4 m: Unable to advance due to hole collapse.					2
	3					*Notes:* Basic properties auger to correlate electrical resistivity tomography, shear vane and penetrometer not used; fine soil strength estimated using field diagnostics per NZGS Field Guide Sheet. Shear vane 95039, 19 mm blade. Groundwater not encountered. Coordinates and elevation from Leica GS16 GNSS RTK Rover.					3

AUGER LOG

(Based on Tonkin and Taylor) SHEET 1 of 1

THE UNIVERSITY OF WAIKATO
Te Whare Wānanga o Waikato

PROJECT: MSc Research – Ham. Faults LOCATION: AgResearch Ruakura Farm JOB No: HA17

CO-ORDINATES mN 5816361.273 AUGER TYPE: Dutch HOLE STARTED: 14/10/2020
mE 1803568.401 DATUM: NZGD2000 HOLE FINISHED: 14/10/2020
DIRECTION: Vertical R.L. GROUND: 41.207 m DRILLED BY: GM
ANGLE FROM HORIZONTAL: 90° LOGGED BY: GM CHECKED:

GEOLOGICAL UNIT	DEPTH (m)	GRAPHIC LOG	CLASSIFICATION SYMBOL	MOISTURE CONDITION	STRENGTH / PLASTICITY CONDITION	SOIL DESCRIPTION: Soil NAME; colour, structure. (a) Soil mass qualifications - strength, moisture condition, grading, bedding, plasticity, sensitivity; (b) soil fraction qualifications - major fraction size and shape, weathring of clasts, subordinate fraction, minor fraction; (c) additional information.	SHEAR STRENGTH	PENETROMETER		WATER	
			ML	M		Gravelly organic SILT; dark brown. Moist, low plasticity; gravel, medium to coarse, angular to subangular, greywacke, scoria, limestone; organics, rootlets [TOPSOIL].					
FILL			MH	M		Clayey SILT with some sand and trace of organics; light brownish orange. Moist, high plasticity, sensitive; sand, fine; organics, rootlets.	105/18				
			ML	M		Sandy SILT with trace of clay; light brown. Moist, low plasticity, moderately sensitive; sand, fine.	75/20				
HINUERA FORMATION	1		SP	W		Silty fine SAND; light brown. Loosely packed, wet, poorly graded. 0.9 m: Thin bed of coarse gravel, subrounded, pumice, rhyolite.					1
			SP	W		Coarse SAND with minor gravel and trace of silt; light greyish orange. Loosely packed, wet, poorly graded; sand, subangular to subrounded, quartz, rhyolite; gravel, fine to medium, subangular to subrounded, rhyolite, lithics.					
	2					EOH at 1.15 m: Unable to advance due to hole collapse. *Notes:* Basic properties auger to correlate electrical resistivity tomography, shear vane and penetrometer not used; fine soil strength estimated using field diagnostics per NZGS Field Guide Sheet. Shear vane 95039, 19 mm blade. Groundwater not encountered. Coordinates and elevation from Leica GS16 GNSS RTK Rover.					2
	3										3

AUGER LOG

(Based on Tonkin and Taylor) SHEET 1 of 1

THE UNIVERSITY OF WAIKATO
Te Whare Wānanga o Waikato

PROJECT: MSc Research – Ham. Faults LOCATION: AgResearch Ruakura Farm JOB No: HA18

CO-ORDINATES mN 5816362.545 AUGER TYPE: Dutch HOLE STARTED: 16/10/2020
mE 1803573.113 DATUM: NZGD2000 HOLE FINISHED: 16/10/2020
DIRECTION: Vertical R.L. GROUND: 41.270 m DRILLED BY: GM
ANGLE FROM HORIZONTAL: 90° LOGGED BY: GM CHECKED:

GEOLOGICAL UNIT	DEPTH (m)	GRAPHIC LOG	CLASSIFICATION SYMBOL	MOISTURE CONDITION	STRENGTH / PLASTICITY CONDITION	SOIL DESCRIPTION: Soil NAME; colour, structure. (a) Soil mass qualifications - strength, moisture condition, grading, bedding, plasticity, sensitivity; (b) soil fraction qualifications - major fraction size and shape, weathring of clasts, subordinate fraction, minor fraction; (c) additional information.	SHEAR STRENGTH	PENETROMETER		WATER	
			ML	M		Organic SILT with some gravel and minor sand; dark brown. Moist, low plasticity; gravel, fine to medium, subrounded, lithics; sand, fine; organics, rootlets [TOPSOIL].					
FILL			ML	M		Sandy gravelly SILT with trace of organics; dark brownish orange. Moist, low plasticity; sand, fine to medium, subangular to subrounded, quartz; gravel, fine to medium, subangular to subrounded, greywacke; organics, rootlets. 0.6 m: Gravel becomes coarse and angular.					
HINUERA FORMATION	1		SP	M		Silty gravelly fine SAND with trace of organics; light greyish orange. Loosely packed, moist, poorly graded; gravel, medium to coarse, subangular to subrounded, lithics; organics, roots.					1
			SW	M		Gravelly fine to coarse SAND with trace of silt; dark reddish brown. Loosely packed, moist, well graded; sand, subangular to subrounded, quartz, pumice, rhyolite, lithics; gravel, medium to coarse, subangular to subrounded, pumice, rhyolite.					
	2					EOH at 1.6 m: Unable to advance due to hole collapse. *Notes:* Basic properties auger to correlate electrical resistivity tomography, shear vane and penetrometer not used; fine soil strength estimated using field diagnostics per NZGS Field Guide Sheet. Groundwater not encountered. Coordinates and elevation from Leica GS16 GNSS RTK Rover.					2
	3										3

AUGER LOG

(Based on Tonkin and Taylor) SHEET 1 of 1

THE UNIVERSITY OF WAIKATO
Te Whare Wānanga o Waikato

PROJECT: MSc Research – Ham. Faults LOCATION: AgResearch Ruakura Farm JOB No: HA19

CO-ORDINATES mN 5816364.458 AUGER TYPE: Dutch HOLE STARTED: 16/10/2020
mE 1803572.944 DATUM: NZGD2000 HOLE FINISHED: 16/10/2020
DIRECTION: Vertical R.L. GROUND: 41.281 m DRILLED BY: GM
ANGLE FROM HORIZONTAL: 90° LOGGED BY: GM CHECKED:

GEOLOGICAL UNIT	DEPTH (m)	GRAPHIC LOG	CLASSIFICATION SYMBOL	MOISTURE CONDITION	STRENGTH / PLASTICITY CONDITION	SOIL DESCRIPTION: Soil NAME; colour, structure. (a) Soil mass qualifications - strength, moisture condition, grading, bedding, plasticity, sensitivity; (b) soil fraction qualifications - major fraction size and shape, weathring of clasts, subordinate fraction, minor fraction; (c) additional information.	SHEAR STRENGTH	PENETROMETER		WATER	
			ML	M		Organic SILT with some sand and minor sand; dark brown. Moist, low plasticity; sand, fine; gravel, fine to medium, subangular to subrounded, lithics; organics, rootlets [TOPSOIL].					
HINUERA FORMATION			MH	M		Clayey SILT with some sand; light brownish orange. Moist, high plasticity, insensitive to sensitive; sand, fine.	144/22				
						0.7 m: Light grey nodules, ~15 mm dia., semi-brittle – break under pressure.	86/52				
			SP	W		Silty medium to coarse SAND with some gravel and trace of organics; light greyish orange. Loosely packed, wet, poorly graded; sand, subangular to subrounded, rhyolite, lithics; gravel, medium to coarse, subangular, volcanic glass, highly weathered pumice, manganese nodules, lithics (incl. andesite?); organics, decayed roots.					
	1		SW	M		Silty sandy fine to coarse GRAVEL; dark reddish orange. Tightly packed, moist, well graded; gravel, subrounded, rhyolite, lithics; sand, fine to coarse, subangular to subrounded, quartz, feldspar, rhyolite, lithics.					1
						EOH at 1.15 m: Unable to penetrate.					
						Notes:					
						Basic properties auger to correlate electrical resistivity tomography, shear vane and penetrometer not used; fine soil strength estimated using field diagnostics per NZGS Field Guide Sheet.					
						Shear vane 95039, 19 mm blade.					
						Groundwater not encountered.					
						Coordinates and elevation from Leica GS16 GNSS RTK Rover.					
	2										2
	3										3

Appendix E. Additional Trench Photographs and Sketches

Figure E.1. Composite photograph of the trench northern wall on the final day of logging.

Figure E.2. Composite photograph of the trench southern wall on the final day of logging.

Figure E.3. Photograph of the trench northern wall between *c*. 8–16 m. Note the generally darker, redder, coarser nature of Package II above the bench compared with lighter, greyer, finer nature of Package III below.

Figure E.4. Photograph showing nature of 0.5 m x 0.5 m string grid used in the deformation zone of section 4, with coloured flags marking unit contacts.

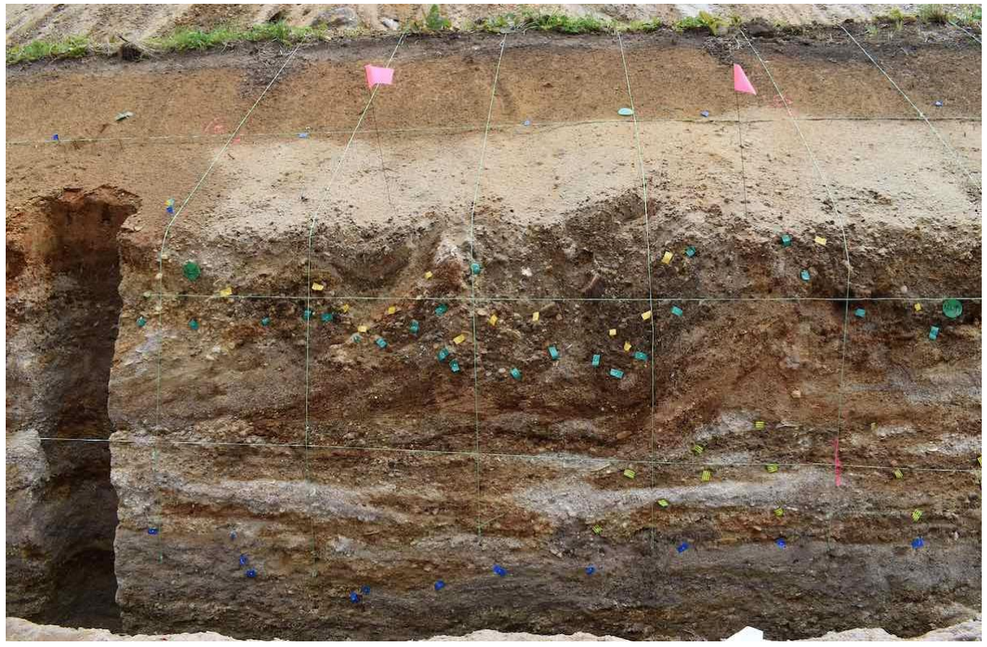

Figure E.5. Photograph of the main part of the deformation zone (to the left of Figure E.4). The vertical slot at left was an attempt at gaining insight into the nature of bedding deeper into the face.

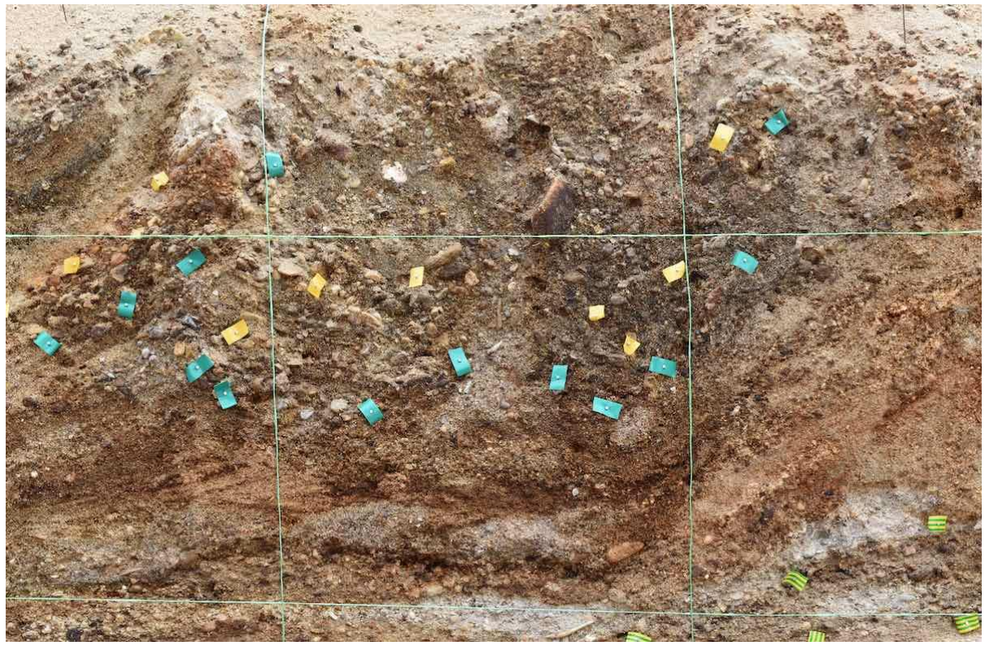

Figure E.6. Photograph showing detail of the two easternmost scallops within the deformation zone. Yellow flags mark the top of Unit 4, green flags the bottom. Note gravel aligning with warping.

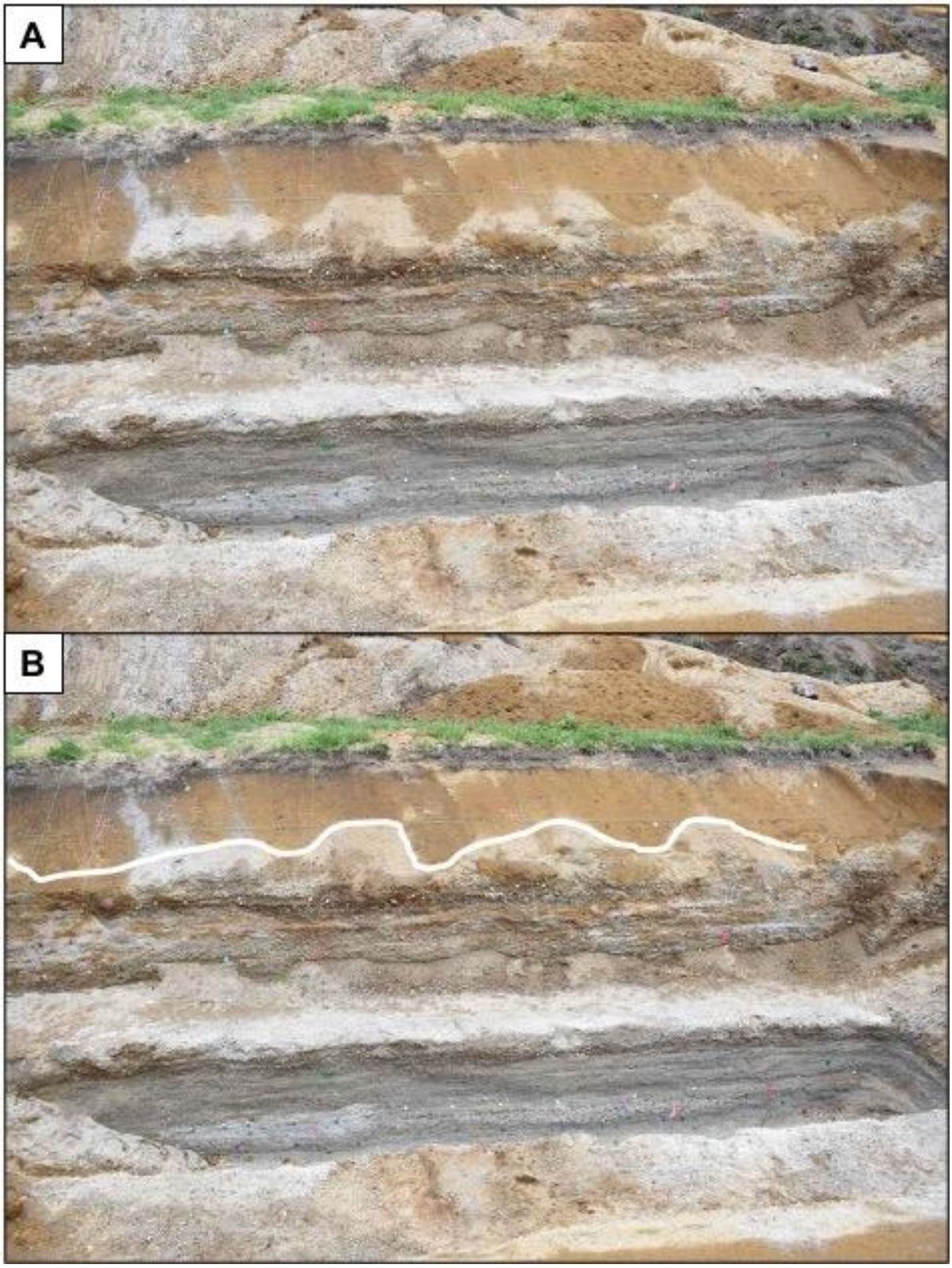

Figure E.7. Photograph of the trench northern wall between *c*. 20–28 m, showing how the contact between Units 1C and 2 was emphasised following rain, as the silty tephra of Unit 1C had greater moisture retention than the more freely draining Unit 2; **(A)** original image, **(B)** white line added.

Figure E.8. Photograph of Package III adjoining the unexcavated western side of the central well, showing cross-bedding and intercalation of various undefined units.

Figure E.9. Photograph showing the inside of the easternmost well.

Figure E.10. Photograph of the trench southern wall showing the unexcavated/unlogged area around the central well.

Figure E.11. Photograph of the trench lower northern wall (Package III) showing a moderately sized relict root casing around the 8 m mark. Whether the root was modern or relict was undetermined but being deeper than any other roots observed in the trench, and appearing to have entrapped larger gravel clasts on the downstream side of apparent paleoflow, suggests it may pre-date deposition of Package II.

Figure E.12. Annotated photograph of the trench upper northern wall showing broken clay pipe and old limestone-chip driveway (Unit 1A) overlying true topsoil (Unit 1B). Depth of clay pipe represents the general maximum depth of impact from most anthropic features.

Figure E.13. Photograph of the trench southern wall showing rubbish pit, highlighting t in-filling which caused much initial confusion as the fill materials closely replicated natural stratigraphy.

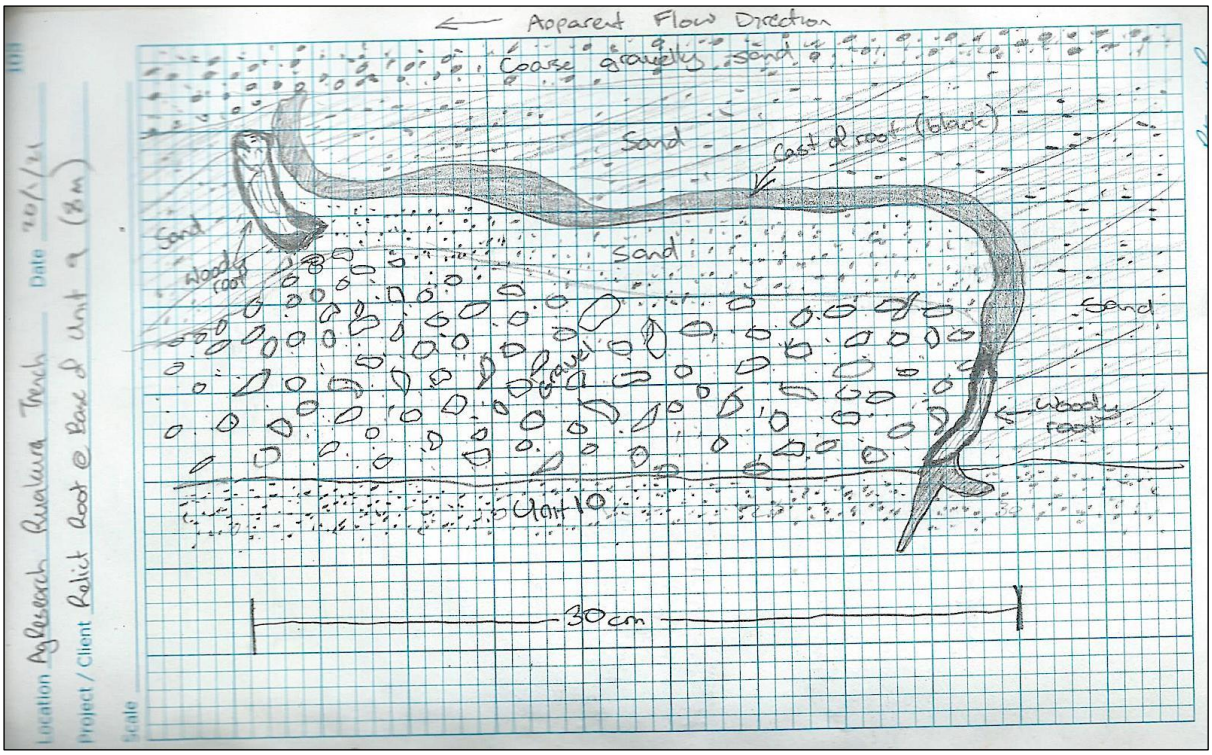

Figure E.14. Sketch of the root casing in Figure E.11.

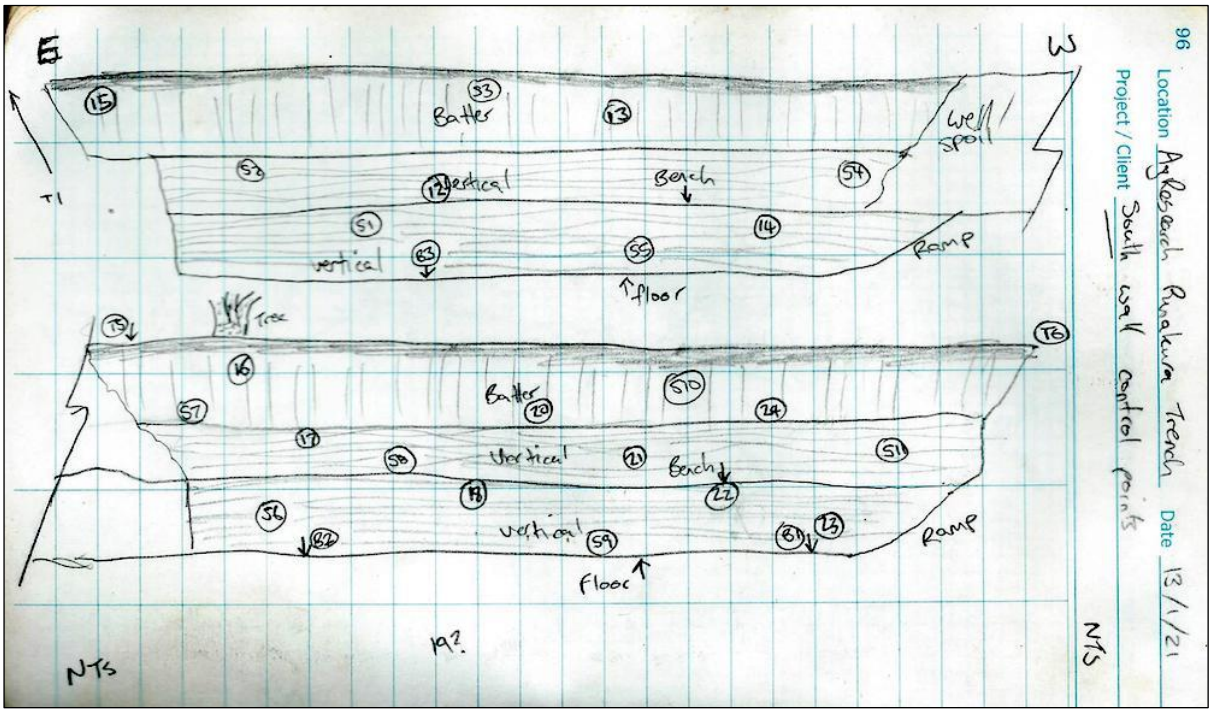

Figure E.15. Sketch of relative positions of trench photogrammetry control points along the southern wall.

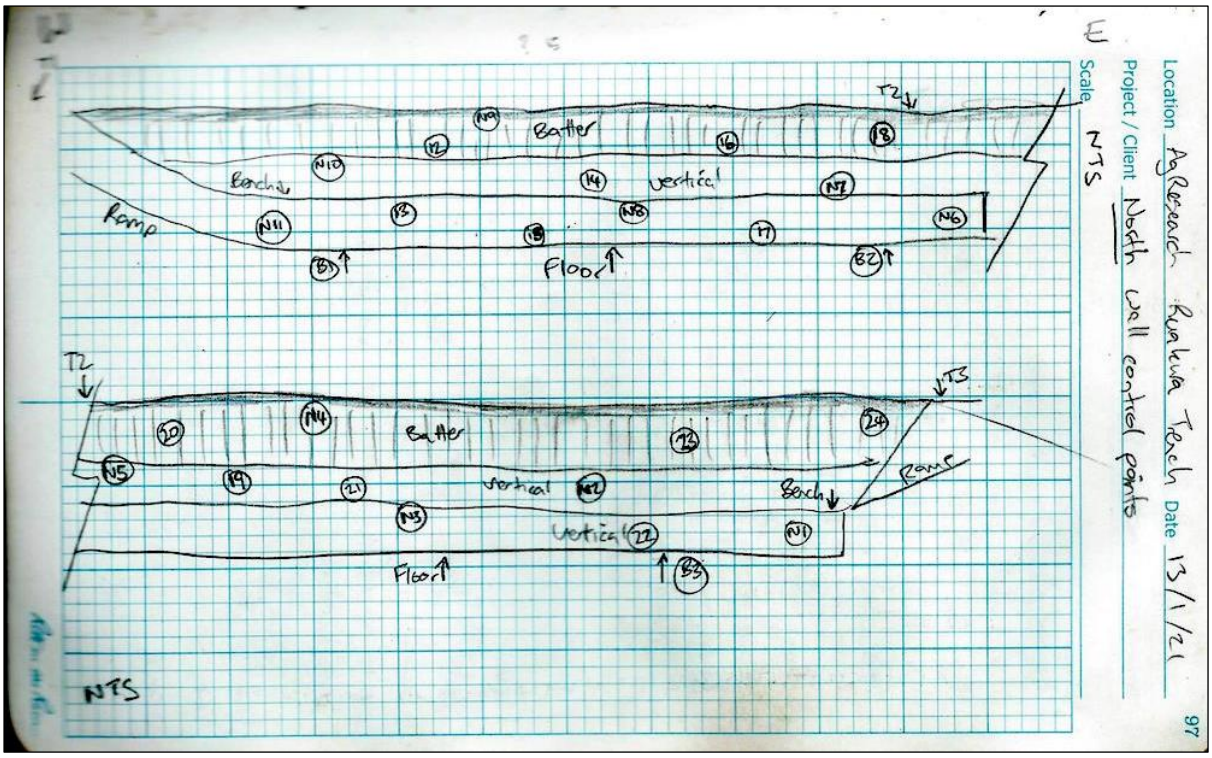

Figure E.16. Sketch of relative positions of trench photogrammetry control points along the northern wall.

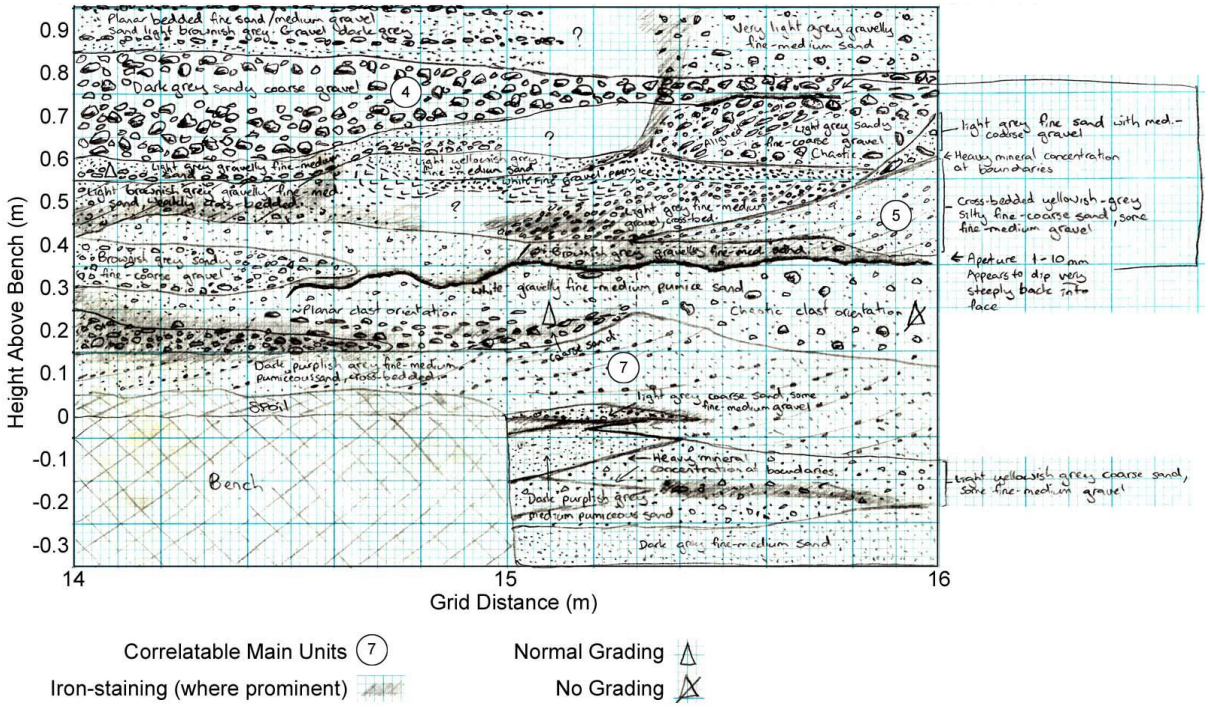

Figure E.17. Original field sketch (with digitally-added elements) of detail from 14–16 m portion of section 3.

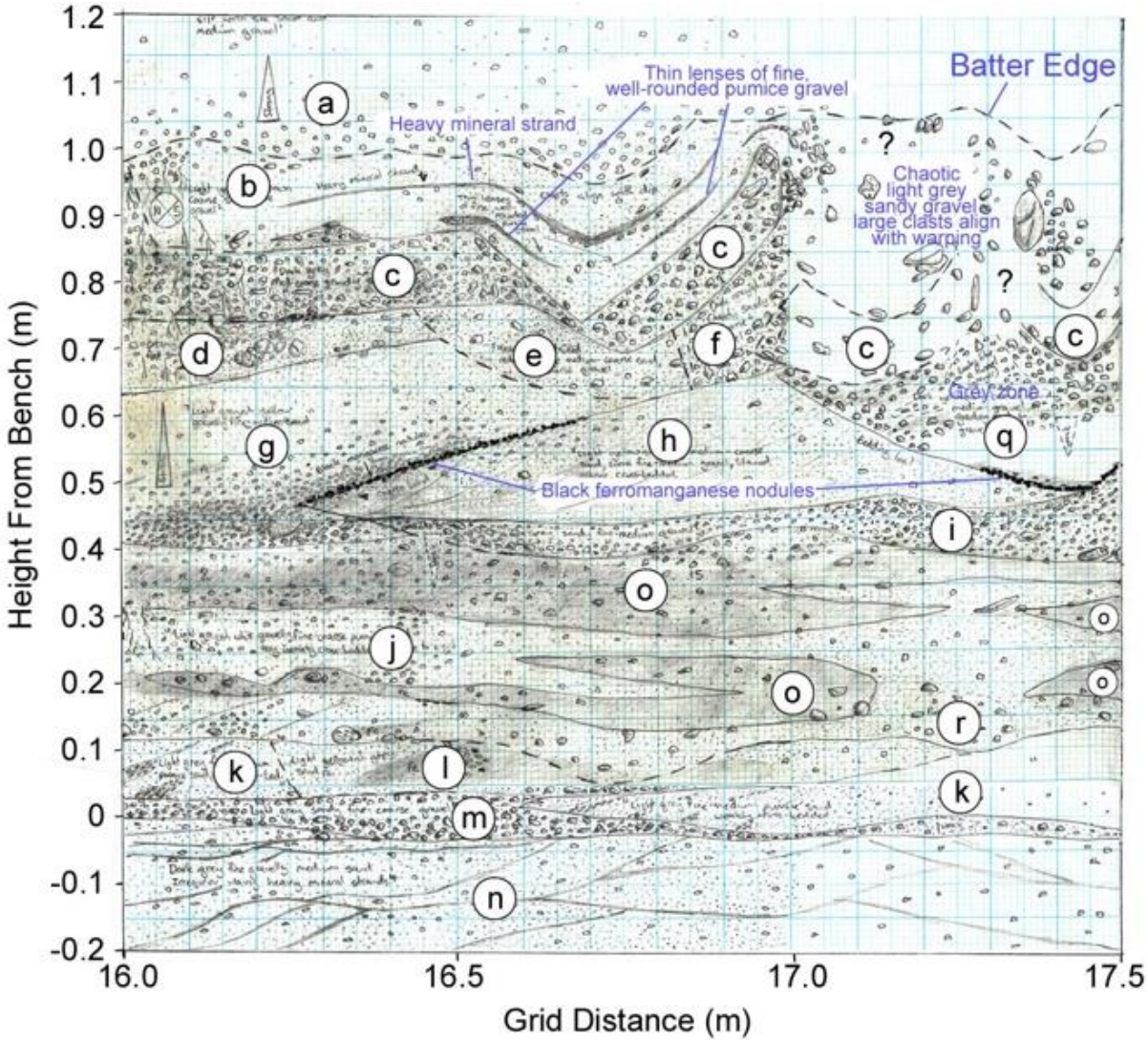

Figure E.18. Original field sketch (with digitally-added elements) of 16–17.5 m portion of section 4.

Figure E.19. Sketch of the completed trench immediately after excavation, looking from W to E.

Figure E.20. (Overleaf) The End.